ALGORITHM THEORETICAL BASIS DOCUMENT

AIRS-TEAM RETRIEVAL FOR CORE PRODUCTS AND GEOPHYSICAL PARAMETERS

Level 2

Chris Barnet, NOAA/NEDIS
Evan Manning, JPL
Phil Rosenkranz, MIT
Larrabee Strow, UMBC
Joel Susskind, GSFC

M. T. Chahine
AIRS Team Leader

Editor

Hartmut H. Aumann
AIRS Project Scientist

Version 4.0 1 March 2007
JPL D-17006

This page intentionally left blank.

Relevant Documents

AIRS Science and Measurement Requirements Document, JPL D-6665, Rev. 1, September 1991, AIRS Brochure

AIRS Instrument Calibration Plan, JPL D-16821, Preliminary, 14 October 1997

AIRS Team Science Data Validation Plan, Core Products, JPL D-16822, Version 1.2, 15 August 1997

AIRS Team Science Data Validation Plan, JPL D-16822, Version 2.1.1, 5 June 2000

AIRS Visible and Infrared In-Flight Calibration Plan, JPL D-18816, Version 3.0, June 2002

AIRS Level 1B Visible, Infrared and Telemetry Algorithms and Quality Assessment (QA) Processing Requirements, JPL D-20046, Version 2.2, 14 February 2003

AIRS Algorithm Theoretical Basis Documents, Level 1B, Part 1: Infrared Spectrometer, JPL D-17003, Version 2.0, 4 January 1999

AIRS Algorithm Theoretical Basis Documents, Level 1B, Part 1: Infrared Spectrometer, JPL D-17003, Version 2.2i, 10 November 2000

AIRS Algorithm Theoretical Basis Document, Level 1B, Part 1: Infrared Spectrometer, JPL D-17003, Version 4.0, 1 March 2007

AIRS Algorithm Theoretical Basis Document, Level 1B, Part 2: Visible/Near-Infrared Channels, JPL D-17004, Version 2, 4 January 1999

AIRS Algorithm Theoretical Basis Document, Level 1B, Part 2: Visible/Near-Infrared Channels, JPL D-17004, Version 2.2, 10 November 2000

AIRS Project Algorithm Theoretical Basis Document, Level 1b, Part 2: Microwave Instruments, JPL D-17005, Version 1.2, 15 November 1996

AIRS Project Algorithm Theoretical Basis Document, Level 1b, Part 2: Microwave Instruments, JPL D-17005, Version 2.1, 10 November 2000

AIRS Algorithm Theoretical Basis Document, AIRS-Team Unified Retrieval For Core Products, Level 2, JPL D-17006, Version 1.7, 18 September 1997

AIRS Algorithm Theoretical Basis Document, AIRS-Team Retrieval For Core Products and Geophysical Parameters, Level 2, JPL D-17006, Version 2.1, 20 December 1999

AIRS Algorithm Theoretical Basis Document, AIRS-Team Retrieval For Core Products and Geophysical Parameters, Level 2, JPL D-17006, Version 2.2, 26 April 2001

Version History

Version 4.0 is the first post-launch Level 2 Algorithm Theoretical Basis Document (ATBD). This version is named 4.0 to synchronize the numbering scheme with the version of the AIRS Product Generation Executive (PGE) that is delivered to the Goddard Space Flight Center (GSFC) Distributed Active Archive Center (DAAC) for routine AIRS data processing. No Version 3.0 was issued. The essential algorithms at the heart of the AIRS Level 2 data PGE have not changed.

Version 2.2 (26 April 2001) was the last pre-launch release of the Level 2 ATBD. This revision incorporated changes in response to the ATBD reviewers.

Version 2.1 (20 December 1999) of the AIRS Level 2 ATBD, 'AIRS-Team Retrieval for Core Products and Geophysical Parameters,' replaced the Version 1.7 (18 September 1997) document, 'AIRS-Team Unified Retrieval for Core Products.'

Prepared By:

Adrienne Harris
AIRS Information Management Engineer

Approved By:

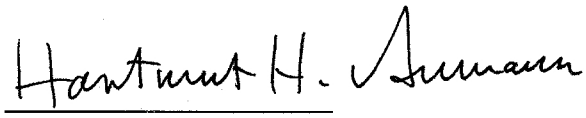

Hartmut H. Aumann
AIRS Project Scientist

M. T. Chahine
AIRS Team Leader

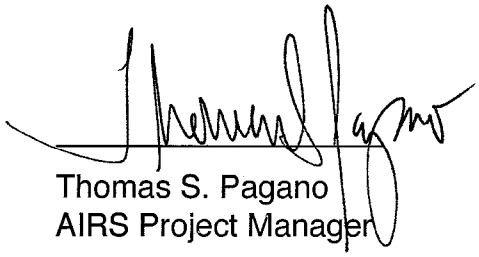

Thomas S. Pagano
AIRS Project Manager

JPL
Jet Propulsion Laboratory
California Institute of Technology
Pasadena, California

JPL D-17006

This page intentionally left blank.

CONTENTS

List of Figures and Tables

This page intentionally left blank.

1. INTRODUCTION

The Atmospheric Infrared Sounder (AIRS) is a facility instrument, selected by NASA to fly on the second, Earth Observing System polar-orbiting platform, EOS-Aqua. The EOS Aqua was launched on 4 May 2002, from Vandenberg, CA, into a 705-km altitude, circular polar orbit, with 1:30 AM ascending node. The same platform also carried the NOAA operational Advanced Microwave Sounding Unit (AMSU) and the microwave Humidity Sounder of Brazil (HSB). AIRS is designed to meet the requirements of the NASA Earth Science Enterprise climate research programs and the NOAA operational weather-forecasting plans. AIRS, AMSU and HSB were put into the operational, routine data-gathering state on 31 August 2002. AIRS and AMSU have worked perfectly since then, but the scan motor of HSB failed in February 2003, causing the loss of the HSB data.

The launch of AIRS on the EOS Aqua spacecraft opened a new era in imaging, hyperspectral infrared sounding. Other hyperspectral infrared sounders have preceded AIRS: the Infrared Interferometer Spectrometer (IRIS) experiment on Nimbus 3 and 4 (Conrath, *et al.*, 1970) collected data from April - July 1969 and April 1970 - January 1971. The Infrared Monitor for Greenhouse Gases (IMG) (Kobayashi, *et al.*, 1999) collected data from October 1996 - June 1997. Both instruments sounded at the sub-spacecraft point only and were Fourier Transform Spectrometers (FTS), which operated for less than one year. The AIRS design, a cooled grating-array spectrometer, with no moving parts, was selected for its exceptional reliability, operational simplicity and radiometric qualities. AIRS is a +/-50-degree cross-track scanner, i.e., the data can be used to create hyperspectral images. Since the start of routine data gathering on 31 August 2002, AIRS has returned 2.9 million spectra of the upwelling radiance each day.

Details of the AIRS design and measurement objectives are provided in Aumann, *et al.*, (2003); details of the prelaunch testing and on-board performance analysis are given in Pagano, *et al.,* (2003); Lambrigtsen (2003) describes the AMSU and HSB instruments. An overview of results, obtained with the first three years of AIRS data, is given in

Chahine, *et al.*, (2006). The accuracy of the geophysical parameters, derived from the Atmospheric Infrared Sounder/Advanced Microwave Sounding Unit as a function of fractional cloud cover, using the V4.0 Level 2 algorithm, is analyzed in Susskind, *et al.*, (2006).

In the following document we present the theoretical basis of the AIRS Level 2 products algorithm. The Level 2 products algorithm is designed such that all AIRS data products will simultaneously satisfy the measurements in a least-squares sense. This requires a complex interaction between algorithms for the various products. For this reason, all products are discussed in one document. The overall flow of data is shown in Figure 1, with reference to chapters in the ATBD. The algorithm described in this document has been implemented as the AIRS Level 2 Product Generation Executive (PGE), Version 4.0, at the Goddard Space Flight Center (GSFC) Distributed Active Archive Center (DAAC).

AIRS is an imaging hyperspectral sounder, which covers 80% of the globe twice per day, during the ascending (day) and the descending (night) overpasses. However, the images are in scan coordinates, with considerable overlap at high latitudes and gaps near the equator. Level 3 products use the position-tagged Level 2 products to create eight-day and monthly mean images, which will ultimately be used to create the AIRS climatology. Separate fields are produced for each of the ascending (day) and descending (night) orbits. The Level 3 algorithm and production rules, using the Level 2 quality flags, are described in Appendix B.

Some results, obtained with the first three years of AIRS data, are shown in Appendix C.

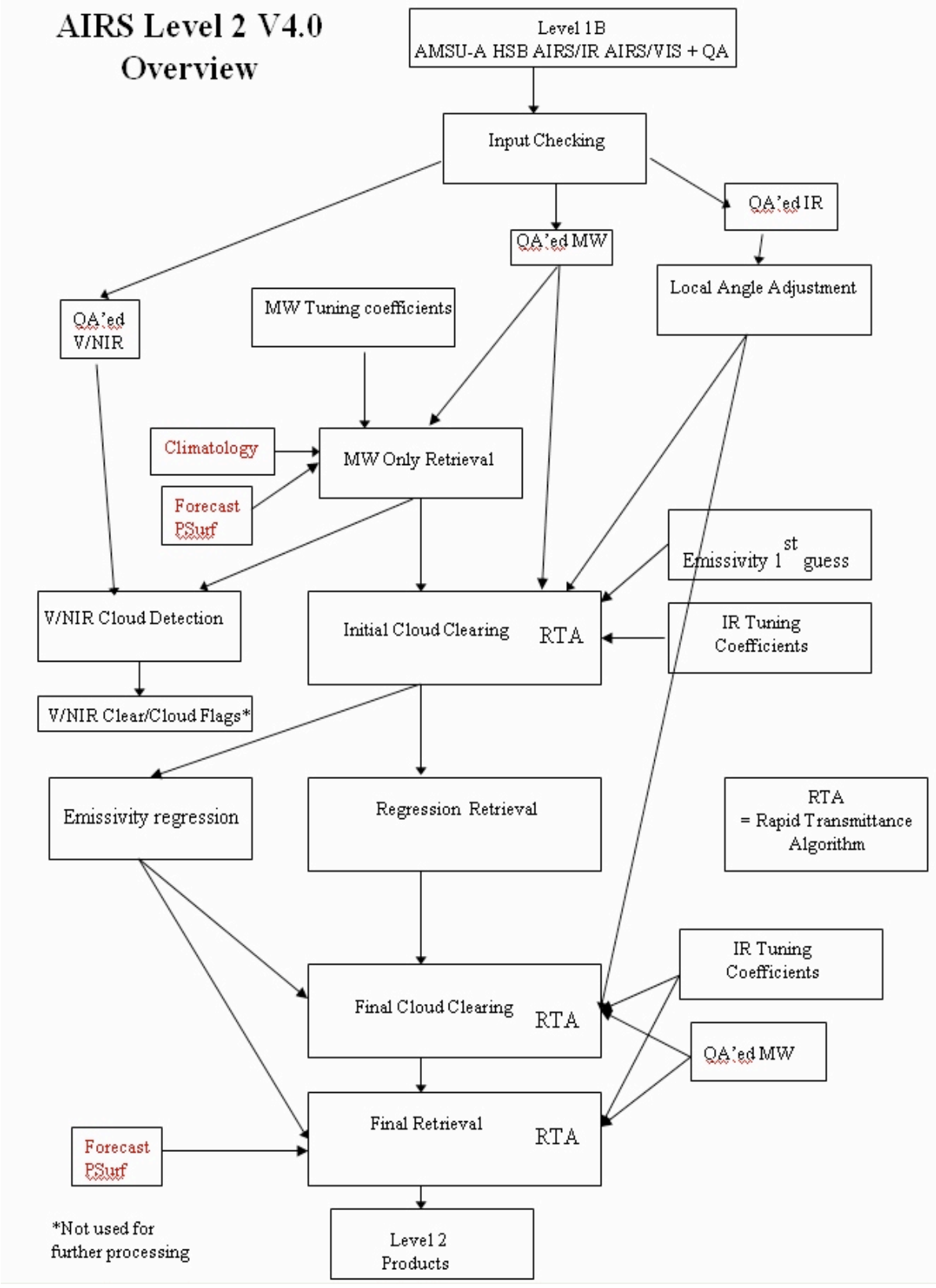

Figure 1. AIRS Level 2 Processing Flowchart

References

Aumann, H.H. , M.T. Chahine, C. Gautier, M. Goldberg, E. Kalnay, L. McMillin, H. Revercomb , P.W. Rosenkranz , W. L. Smith , D. H. Staelin, L. Strow and J. Susskind, (2003a), "AIRS/AMSU/HSB on the Aqua Mission: Design, Science Objectives, Data Products and Processing Systems," IEEE Trans. Geosci. Remote Sens., Vol.41, 253-264.

Chahine, Moustafa T., Thomas S. Pagano, Hartmut H. Aumann, Robert Atlas, Christopher Barnet, John Blaisdell, Luke Chen, Murty Divakarla, Eric J. Fetzer, Mitch Goldberg, Catherine Gautier, Stephanie Granger, Scott Hannon, Fredrick W. Irion, Ramesh Kakar, Eugenia Kalnay, Bjorn H. Lambrigtsen, Sung-Yung Lee, John Le Marshall, W. Wallace McMillan, Larry McMillin, Edward T. Olsen, Henry Revercomb, Philip Rosenkranz, William L. Smith, David Staelin, L. Larrabee Strow, Joel Susskind, David Tobin, Walter Wolf and Lehang Zhou (2006) "The Atmospheric Infrared Sounder (AIRS): IMPROVING WEATHER FORECASTING AND Providing new Data on Greenhouse gases," BAMS 15 July 2006

Conrath, Barney, J., Hanel, R.A., Kunde, V.G., and Prabhakara, C., (1970), "The Infrared Interferometer Experiment on Nimbus 3," JGR Oceans and Atmospheres, Vol. 75, No. 30, Oct. 20, pp. 5831-5857.

Gautier, C., Y. Shiren and M.D. Hofstader (2003 "AIRS/Vis Near IR Instrument", IEEE Transaction on Geoscience and Remote Sensing, Vol.41, 330-342.

Kobayashi, H., A. Shimota, C. Yoshigahara, I. Yoshida, Y. Uehara, and K. Kondo, (1999) "Satellite-borne high resolution FTIR for lower atmosphere sounding and its evaluation," IEEE Trans. Geosci. Remote Sens., 37, 1496-1507.

Lambrigtsen, B. H., (2003) "Calibration of the AIRS Microwave Instruments," IEEE Transaction on Geoscience and Remote Sensing, Vol.41, 369-378.

Pagano, T.S, H. H. Aumann, D. Hagan and Ken Overoye, "Prelaunch and In-Flight Radiometric Calibration of the Atmospheric Infrared Sounder (AIRS)," (2003) IEEE Trans. Geosci. Remote Sens., Vol.41.2, pp.265-273.

Susskind, J., C. Barnet, J. Blaisdell, L. Iredell, F. Keita, L. Kouvaris, G. Molnar, and M. Chahine (2006), "Accuracy of geophysical parameters derived from Atmospheric Infrared Sounder/Advanced Microwave Sounding Unit as a function of fractional cloud cover, " J. Geophys. Res., 111, D09S17, doi:10.1029/2005JD006272.

2. AIRS/AMSU-A/HSB DATA PRODUCTS

2.1 Standard Products

The AIRS Level 2 PGE produces four different files in EOS HDF Swath format:

- Standard Product
- Cloud-Cleared Radiance
- Support Product
- Quality Assessment Support Product

Successive files provide increasingly detailed information about the AIRS Level 2 retrievals.

It is worth noting that each file encompasses one 'granule' of AIRS data. Granules are formally defined as the smallest aggregation of data that is independently managed (i.e., described, inventoried, retrievable). An AIRS granule has been set as 6 minutes of data, corresponding to exactly 45 scanlines of AMSU data or 135 scanlines of AIRS and HSB data. The UTC start time of the N-th granule of each data is (146+(N-1)*360)/3600 hours. The orbit repeat pattern of the EOS Aqua is 16 days, i.e. the spatial coverage of the Nth granule is repeated (almost) exactly 16 days later.

The **Standard Product** consists of retrieved estimates of cloud and surface properties, plus profiles of retrieved temperature, water vapor, ozone and a flag indicating the presence of cloud ice or water. Estimates of the errors associated with these quantities will also be part of the Standard Product. The profile vertical resolution is 30 points total between 1000 mb and .02 mb; WMO pressure levels are used in the troposphere and lower stratosphere. The Standard Product contains quality assessment flags in addition to retrieved quantities. The Standard Product will be generated at all locations atmospheric soundings are taken.

Cloud-Cleared Radiances are produced along with the AIRS Standard Product, as they are the radiances used to retrieve the Standard Product. Nevertheless, they are an order of magnitude larger in data volume than the remainder of the Standard Products and, many Standard Product users are expected to have little interest in the Cloud Cleared

Radiance. For these reasons they are a separate output file, but like the Standard Product will be generated at all locations.

The **Support Product** includes higher vertical resolution profiles of the quantities found in the Standard Product, plus intermediate output (e.g., microwave-only retrieval), research products such as the abundance of trace gases, and detailed quality assessment information. The Support Product profiles contain 100 levels between 1100 and .016 mb; this higher resolution will simplify the generation of radiances using forward models, though the vertical information content is no greater than in the Standard Product profiles. The intended users of the Support Product are researchers interested in generating forward radiance, or in examining research products, and the AIRS algorithm development team. The Support Product will be generated at all locations as Standard Products.

The final AIRS Level 2 data product is the **Quality Assessment Support Product**. This output is intended to provide insight into the detailed workings of the AIRS retrieval algorithm, and will contain a large number of intermediate retrieved quantities, their estimated uncertainties, and associated quality assessment parameters. Because of its large size, the quality assessment Support Product will be generated only at those locations where the AIRS retrieval algorithm is known to be functioning poorly, based upon quality assessment information. The intended users of the Quality Assessment Support Product are the AIRS retrieval algorithm development team, and scientists validating the performance of these algorithms, primarily at the Team Leader Science Computing Facility (TLSCF) at JPL. It will not be generated at the GSFC DAAC.

2.2 Research Products

AIRS will produce a number of research products that will be developed and tested after launch. Primary among these are trace constituent profiles of CO and CH_4, Outgoing Longwave Radiation (OLR) and Clear Sky Outgoing Radiation (COLR), and possibly total CO_2 burden. As opposed to the standard products, research products are more experimental not only for the algorithm, but also for the validation. The intent is to

ultimately upgrade those research algorithms which pass peer review to standard products.

This page intentionally left blank.

3. INPUT QUALITY CONTROL AND ANCILLARY PRODUCTS

Key to the quality of the Level 2 products is careful quality control of the calibrated radiances. The quality control is divided into inter-instrument QC, microwave QC, infrared QC, and visQC.

The inter-instrument QC simply validates that valid data for a 3x3 ensemble of AIRS footprints exist. For all instruments whose data are present and marked valid with state = 0 (PROCESS), the algorithm checks:

1) Time is later than Jan 01, 1994.

2) Latitude is in {-90.1, 90.1}.

3) Longitude is in {-180.1, 180.1}.

If any data are bad, that instrument is marked bad.

Of those that pass the first test, pair-wise comparisons are made of timestamps and locations to make sure the observations are synchronized. If any comparisons fail, then all data for this FOV are considered bad.

4) AMSU distance to central AIRS FOV is greater than 45 km.

5) AMSU distance to central AIRS FOV is greater than 17 + 1/cos(satzen) km.

6) |Time(AMSU) - Time(AIRS) - 0.66667 sec| > 2 sec

7) AMSU distance to central HSB FOV is greater than 45 km.

8) AMSU distance to central HSB FOV is greater than 17 + 1/cos(satzen) km.

9) |Time(AMSU) - Time(HSB) - 0.52167 sec| > 2 sec

10) HSB distance to central AIRS FOV is greater than 45 km.

11) HSB distance to central AIRS FOV is greater than 17 + 1/cos(satzen) km.

12) |Time(HSB) - Time(AIRS) - 0.145 secl > 2 sec

3.1 Microwave QC

AMSU-A data is screened for the following problems:

1) AMSU-A1 State is not 0 (Process)
   Any state other than process indicates data is missing or bad.
   AMSU-A1 data is most important so all AMSU-A data is screened based on it.

2) BT > 350 K or BT < 50 K

If any channel is out of bounds, the entire FOV is discarded.

HSB data is screened for the following problems:

1) HSB State is not 0 (Process)
   Any state other than process indicates data is missing or bad.

2) BT > 350 K or BT < 50 K

If any channel is out of bounds the entire FOV is discarded.

3.2 IR QC and Local Angle Adjustment

The IR QC has three components: QC using flags from Level 1B, missing data fill in, and local angle adjustment.

3.2.1 QC using Flags from Level 1B

Individual IR radiances are excluded from further processing if:

1) AB_state in static channel properties file is > 2.

2) ExcludedChans in L1B input is > 2. (ExcludedChans is a copy of AB_State at the time of L1B processing. Under normal circumstances this check is redundant with #1, but it is possible for L2 to be processed later with different information in the channel properties file.)

3) High noise is indicated by CalChanSummary bit 3.

4) A gain, offset problem, or "pop" is indicated by CalFlag bits 4-6.

5) Radiances converted to BT fall outside [175 K - 10*NEDT, 360K + 10*NEDT + solar], where the solar allowance is:

0 for night data

0.5 * PI*(RADIUS_SUN/DISTANCE_SUN)**2 *Solar_surface_radiance for day data

The entire FOVs are excluded from further processing if:

1) No valid solar zenith angle is available.

2) More than 20 channels fail BT range test in #5 above.

3.2.2 Missing Data Files

The V4.0 physical retrieval uses a relatively small fraction of the available 2378 channels. These channels are identified in a name list. Channels, flagged as bad in the L1B data for a given scene, are not used in the physical retrieval algorithm. The regression step uses a large fixed subset of the 2378 available channels, given in a separate name list. If the IR radiances of some of these channels are excluded, based on the L1B flags, fill-in values are used. Due to the highly redundant nature of the spectrum, the fill-in values can be calculated based on a Principle Components (PCs) approach. The PCs were trained on calculated spectra from standard profiles. If more than TBD of the channels in the name list are filled in, the spectrum is rejected.

3.2.3 Local Angle Adjustment

AIRS makes a 90-degree measurement, cross-track between -49 and +49 degrees. The data analysis, however, uses the data in 3x3 clusters with 30 scan angles between -49 and +49 degrees. A primary assumption of cloud clearing (Section 5.2) is that within a 3x3 array of 9 AIRS FOVs the differences are dominated by differences in clouds. Local angle adjustment removes one potentially confounding source of intra-FOV variation: differences in observing geometry. In each 3x3 there are 3 observations at each of 3 different scan angles. This step makes small adjustments to the spectra for the 3 highest-

angle and 3 lowest-angle FOVs so all FOVs resemble those which would be observed at the central angle. No adjustment is applied to the central FOVs.

The actual adjustment is calculated using a PCs approach. The PCs were trained on calculated spectra from standard profiles at different scan angles. Adjustments are assumed to by symmetric about nadir.

In the L2 system missing or bad data is first filled using the PCs. Then final PCs are calculated, and the radiances are adjusted.

3.3 V/NIR QC and V/NIR Cloud Flags

Any V/NIR data less than 0.0000001 radiance units for any channel and any pixel within a FOV excludes the entire FOV from further processing. The V/NIR channels are for diagnostic purposes only. They are not used in the routine L2 data processing.

3.4 Background Climatology

A background climatology “Clim” is available to all retrievals on a 2.5 degree mercator grid using 100 levels. In L2 V4.0 Clim T, H_2O are used directly only in the MW-Only retrieval step. Reliance on the water climatology is key when HSB data are not available. This is discussed in Section 5.1. The first pass cloud clearing uses the MW product as its input state, and so uses Clim data indirectly.

The climatology is based on two files: "NCEP" and "UARS."

"NCEP" has temperature profiles from the surface to 100 mb and water profiles from the surface to 300 mb as monthly means derived from the 20 year (1979-1998) reanalysis on a 2.5 degree mercator lat/lon grid.

"UARS" has temperature, water vapor and ozone month means and zonal (latitude) means. The information below 100 mbar comes from the NCEP reanalysis, above 100 mbar from the microwave limb sounders (UARS and MLS).

The PGE fills its climatology from these two files as:

1) Temperature profile:

a) below 100 mbar from NCEP, tri-linearly interpolated by month,

lat, lon and then log-pressure interpolated onto the 100 levels.

b) above 100 mbar Temp is extrapolated using P**4 extrapolation

2) H_2O profiles. From the "NCEP" file below 300 mb, tri-linearly interpolated by month, lat, lon. Above 300 mb the "UARS" file is used, linearly interpolated between two latitude zones.

3) Ozone profiles. From "UARS" file, linearly interpolated between two latitude zones. No time interpolation.

4) The AIRS retrievals are based on the absorption by CO_2. The abundance of CO_2 is increasing currently at the rate of 2 ppmv/year. In addition, there is a +/-5 ppmv seasonal and latitudinal variability in the CO_2 column abundance. The AIRS L2 PGE assumes that the abundance of CO_2 is fixed at 370 ppmv globally. This value is appropriate for the year 2002 when AIRS was launched. The next edition of the PGE (V5) will use a linear time dependence from name list, but no seasonal or latitudinal dependence.

3.5 AVN Forecast PSurf

The AVN forecast surface pressure, PSurf, is used by the L2 retrieval. The surface pressure is available on a one-degree grid. The surface pressure is calculated from the 3-, 6-, and 9-hour forecasts from the same model run, interpolated in space and time to match observed location.

Clim T profile is used in the calculation of Psurf when AVN is not available.

3.6 Emissivity First Guess

The V4.0 PGE uses the Masuda emissivity over ocean. Over land the V4.0 PGE uses a regression formulation for the emissivity, which uses the first-pass cloud-cleared radiances as input. No first guess is used.

3.7 Microwave Tuning Coefficients

The microwave brightness temperatures used in the L4.0 PGE are the antenna temperatures. These temperatures are empirically tuned to correct for sidelobes, RTA and other artifacts. The bias is a function of channel and scan angle and is derived from the analysis of obs-cal for ocean using ECMWF temperature and moisture profiles. The microwave tuning coefficients have no time, season, or latitude dependence. Details are discussed in section 5.4.13.3.

3.8 IR Tuning Coefficients

The infrared brightness temperatures used in the L4.0 PGE are empirically tuned to correct for RTA artifacts. The bias is a function of channel and is derived from the analysis of obs-calc for clear ocean spectra, using ECMWF temperature and moisture profiles. There is no scan angle dependence. The IR tuning coefficients have no time, season, or latitude dependence. Details are discussed in section 5.4.13.2.2.

3.9 File Format Reference

The file formats and variable name definitions for all L1A, L1B and L2 products are given in "AIRS Version 4.0 Processing Files Description," Version 1.1, August 2005, JPL D-31231.

References

Kistler, Robert, Eugenia Kalnay, William Collins, Suranjana Saha, Glenn White, John Woollen, Muthuvel Chelliah, Wesley Ebisuzaki, Masao Kanamitsu, Vernon Kousky, Huug van den Dool, Roy Jenne, and Michael Fiorino (2001): The NCEP/NCAR 50-year reanalysis: Monthly means CD ROM and documentation, BAMS 82(2), 247-267.

Swinbank, R., and D. Ortland, 2003: Compilation of wind data for the Upper Atmosphere Research Satellite (UARS) Reference Atmosphere Project, J. Geophys. Res., 108(D19), 4615, doi:10.1029/2002JD003135.

4. THE FORWARD PROBLEM

In the following, atmospheric radiative transfer or the 'forward problem' will be discussed. The physical retrieval methodology utilized by the AIRS team depends on the ability to accurately and rapidly calculate the outgoing radiance based on the state of the surface and the atmosphere. Sections 4.1 and 4.2 discuss the microwave and infrared radiative transfer and error estimates. Almost invariably, the statistical evaluation of calculated brightness temperatures, relative to those observed when the state of the atmosphere is reliably known, differs in the mean by a small, but significant amount, referred to as "bias." This bias may itself be a function of other parameters, such as the scan angle. The process used for the derivation of this bias was described in Section 3.7 for the microwave data and Section 3.8 for the IR data. The application of this bias in the retrieval process is described in Section 5.

4.1 Radiative Transfer of the Atmosphere in the Microwave

At the frequencies measured by AMSU and HSB, the most important absorbing gases in the atmosphere are oxygen and water vapor. The oxygen molecule has only a magnetic dipole moment, and its lines are intrinsically much weaker than those which result from the electric dipole of water vapor; however, the much greater abundance of oxygen in the atmosphere more than compensates for this difference. When clouds are present, liquid water also plays a role in radiative transfer. However, fair-weather cirrus composed of ice particles small compared to the wavelength are generally transparent to AMSU-A and HSB frequencies.

4.1.1 Oxygen

O_2 spin-rotation transitions comprise approximately 30 lines between 50 and 70 GHz and an isolated line at 118.75 GHz (which is not observed by AMSU or HSB). Several groups have measured the pressure-broadened widths of the lines in the 50-70 GHz band. The line parameters used for the forward model are from the Millimeter-wave Propagation Model (MPM92) (Liebe, *et al.,* 1992). The characteristic of oxygen's microwave spectrum that introduces difficulty for construction of models is the significant degree of line mixing. In MPM92, line mixing was treated by a first-order

expansion in pressure. The coefficients for this expansion were determined by a constrained linear fit to laboratory measurements made on an O_2 - N_2 mixture over the frequency range of 49-67 GHz and the temperature range 279-327 K, with a noise level of approximately 0.06 dB/km. Within that range, the model represents the measurements to ≤ 0.2 dB/km (see for example, Figure 4.1.1). It is possible that extrapolation to colder temperatures introduces larger errors. Measurements from the NASA ER-2 at 52-56 GHz (Schwartz, 1997) seem to be in agreement with the model, however.

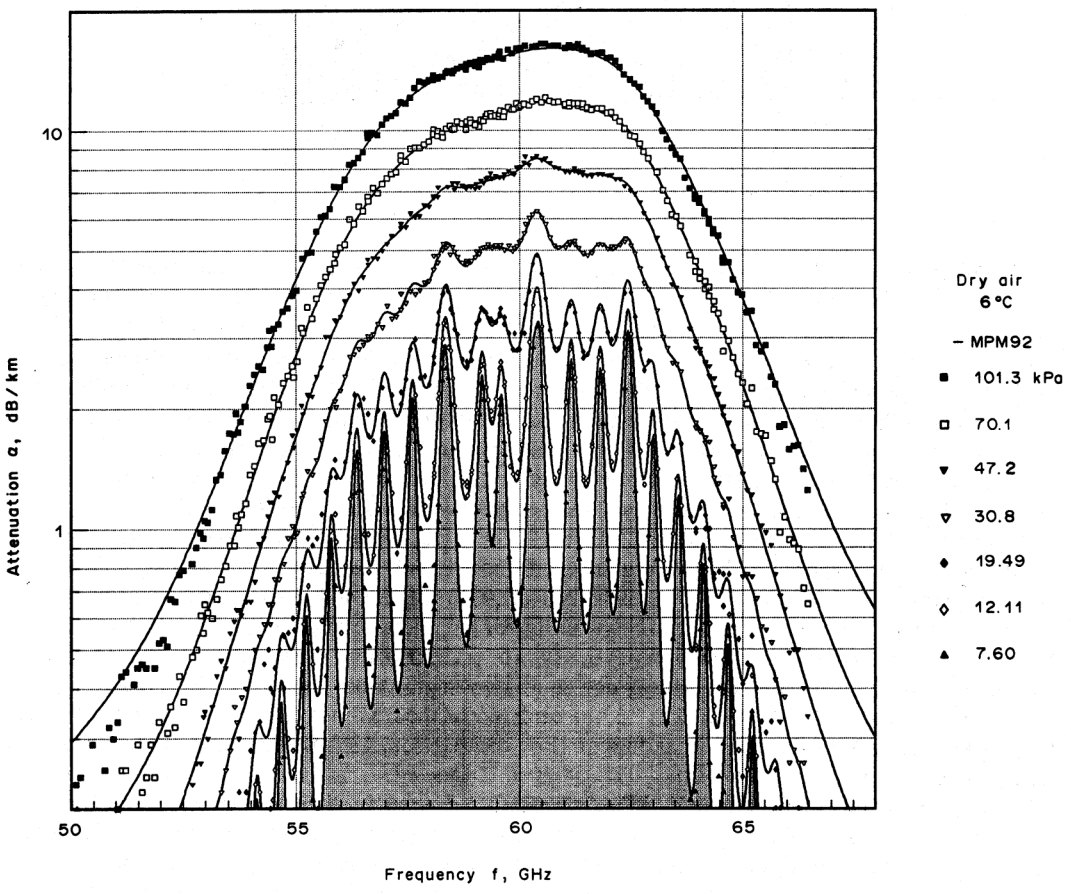

Figure 4.1.1. Millimeter-wave Propagation Model Example

4.1.2 Water Vapor

Water has a weak rotational line at 22.23 GHz that is semi-transparent at normal atmospheric humidity, and a much stronger, opaque line at 183.31 GHz. Intensities of these lines have been calculated and tabulated by Poynter and Pickett (1996 version of JPL line catalog) and Rothman, *et al.*, (1998) (HITRAN), among others. The HITRAN

intensities are used here. For the 22-GHz line, the JPL intensity is higher than the HITRAN value by 0.3%. There is a measurement by Liebe, *et al.*, (1969) (estimated error 0.3%) which is 3.5% lower than the HITRAN value. At 183 GHz, the JPL line intensity is 0.1% higher than HITRAN. Widths have been measured by Liebe, *et al.,* (1969) and Liebe and Dillon (1969) at 22 GHz with estimated uncertainty of 1% for both self and foreign-gas broadening; and by Bauer, *et al.*, (1989) and Tretyakov, *et al.* (2003) at 183 GHz, with uncertainties of 0.5% for self-broadening and 1.0% for foreign-gas broadening, respectively. However, Gamache, *et al.,* (1994) concluded from a survey of measurements of many H_2O lines that, in general, measured line widths should be considered to have uncertainties of 10-15%. The line at 183 GHz is a case in which published measurements of width differ significantly, but the value of Tretyakov, *et al.*, (2003), which is used here, lies near the centroid of the measurements.

At frequencies away from these two lines, microwave absorption by water vapor is predominantly from the continuum, which is attributed to the low-frequency wing of the intense infrared and submillimeter rotational band lines. In the microwave part of the spectrum, the foreign-broadened component of the continuum is stronger than the self-broadened component, for atmospheric mixing ratios. Measurements of continuum absorption as a function of temperature have been made at various frequencies by Liebe and Layton (1987), Godon, *et al.* (1992) and Bauer, *et al.* (1993, 1995). There are also numerous measurements at single temperatures and frequencies in the laboratory, and in the atmosphere where temperature and mixing ratio are variable. The measurements do not present an entirely consistent picture. Rosenkranz (1998) proposed that the most satisfactory overall agreement with laboratory and atmospheric measurements of the water continuum was obtained with a combination of the foreign-broadened component from MPM87 (Liebe and Layton, 1987) with the self-broadened component from MPM93 (Liebe, *et al.*, 1993). The combined model is used here.

4.1.3 Liquid Water

It is useful to distinguish between precipitating and non-precipitating clouds with respect to their interactions with microwaves. Over the range of wavelengths measured by AMSU and HSB, non-precipitating droplets (with diameters of 50 μm or less) can be

treated using the Rayleigh small-droplet approximation. In this regime, absorption is proportional to the liquid water content of the air, and scattering can be neglected. The model for the dielectric constant limits the accuracy of these calculations. The double-Debye model of Liebe, *et al*., (1991) is used here; for temperatures > 0 °C, it has an estimated maximum prediction error of 3% between 5 and 100 GHz, and 10% up to 1 THz. Although some measurements of static dielectric constant at temperatures as low as –20 C were used by Liebe, *et al*. to develop their model, its use for supercooled water must be considered to be an extrapolation, with uncertain accuracy. (The model is implemented using the alternate eq. 2b in Liebe, *et al*.)

Precipitation, on the other hand, requires Mie theory to calculate both absorption and scattering. The latter is generally not negligible, and is the dominant term at some wavelengths. In the case of convective storms, scattering from ice at high altitudes is often the most important process. The rapid transmittance algorithm uses only the small-droplet approximation for cloud liquid water, and scattering is not included. For this reason, retrieved profiles with more than 0.5 kg/m^2 cloud liquid water are rejected, as probably rain-contaminated.

4.1.4 Rapid Transmittance Algorithm

The physical retrieval algorithms used for AIRS/AMSU/HSB do radiative transfer calculations for each profile and hence need a computationally efficient transmittance algorithm. The microwave algorithm computes an effective channel transmittance between two adjacent pressure levels as

$$\langle \tau(P_1, P_2) \rangle = \exp\left[-(\alpha + \beta\rho_V + \gamma\rho_L)\right] \tag{4.1.1}$$

where ρ_V is the water vapor column density of the (P_1, P_2) layer, ρ_L is its liquid water column density, and the coefficients α, β, γ, are calculated for each layer and channel. They implicitly depend on temperature, pressure, and the angle of observation; β also depends implicitly on ρ_V. For AMSU channel 14, α has a weak dependence on the local geomagnetic field. The magnetic field is calculated by a fifth-order spherical-harmonic representation that has an accuracy of a few microteslas. The coefficient α includes the

opacity due to O_2 and a small contribution from pressure-induced absorption by N_2. Parameterization of the coefficients uses approximations described by Rosenkranz (2003) for oxygen-band or window-type channels. In the oxygen band, effective layer opacities are represented by a polynomial in temperature. The opacity profile is computed on a set of fixed pressure levels and then linearly interpolated to the pressure levels of the retrieval, which can be variable (as is the case for the surface pressure). Window-channel coefficients use analytic approximations for far-wing line and continuum absorption. Channels near the two water lines (AMSU channel 1 and HSB channels 3-5) use a Lorentzian-line calculation for the nearby line, with the contributions of other lines treated in the same way as for a window. The local water-line parameters, the water continuum, and the liquid-water absorption are interpolated from a table as functions of temperature.

The retrieval algorithm described in Section 5.2 also makes use of the derivatives $d\alpha/dt$ and $d\beta/d\rho_V$, which are computed in the rapid algorithm by appropriate analytic expressions corresponding to the local-line and continuum components.

The transmittance of multiple layers is calculated by taking the product of the transmittances for each layer. This transmittance is then used in the radiative transfer equation to compute brightness temperature:

$$\Theta_{TOA} = \Theta_{direct} + \tau(0,P_S)\left[\Theta_S + \Theta_{sky}\left(1 - \frac{\Theta_S}{T_S}\right)\right] \tag{4.1.2}$$

where Θ_{TOA} is the brightness temperature emitted from the top of the atmosphere, $\tau(0,P_S)$ is the one-way transmittance of the atmosphere,

$$\Theta_{direct} = \int_0^{P_S} T(P) < d\tau(0,P) > \tag{4.1.3}$$

is the component of brightness temperature emitted from the atmosphere on a direct path to space, Θ_S is the surface brightness (emissivity times temperature),

$$\Theta_{sky} = \int_0^{P_S} T(P) < d\tau(P_S, P) > + \Theta_c < \tau(0, P_S) > \tag{4.1.4}$$

is the sky brightness temperature (including the attenuated cosmic contribution) as it would be observed from the surface, and T_S is the physical surface temperature. T(P) is atmospheric temperature at level P, P_S is the surface pressure, and Θ_c is the cosmic background brightness temperature. The form of (4.1.2) allows separation of the estimation of surface brightness from the estimation of temperature, as described in Section 5.1.1.

Θ_{sky} is computed for a zenith angle θ_{ref} which, due to surface scattering, in general differs from the zenith angle θ for the direct path from surface to satellite. When the surface is classified (see section 5.1.1.1) as either water or coastline, the ratio $\rho_s = \sec(\theta_{ref})/\sec(\theta)$ is estimated as part of the retrieval solution, as described in section 5.1.1.3. For all other surface types, surface scattering is assumed to be Lambertian, and is approximated by

$$\sec(\theta_{ref}) = 1.55 - 0.16 \ln(\kappa_0 + 0.06) \tag{4.1.5}$$

where $\kappa_0 = -\ln(\tau_{zenith}(0,P_S))$is the opacity of the atmosphere at zenith.

Planck's equation for radiant intensity is a nonlinear function of temperature. For microwave frequencies, however, the physical temperatures encountered in the earth's atmosphere lie at the high-temperature asymptote of this function. Hence, as discussed by Janssen (1993), brightness temperature can be used as a surrogate for radiance in the equation of radiative transfer with an accuracy of a few hundredths of a Kelvin, provided that the cosmic background is assigned an effective brightness temperature at frequency ν of

$$\Theta_C = \frac{h\nu}{2k} \times \frac{e^{h\nu/kT_C} + 1}{e^{h\nu/kT_C} - 1} \tag{4.1.6}$$

instead of its actual temperature $T_C = 2.73$ K, in order to linearize Planck's function.

Figures 4.1.2 and 4.1.3 show the derivatives of transmittance with respect to a vertical coordinate which is the logarithm of integrated water vapor for the channels sensitive to moisture, and the logarithm of pressure (a surrogate for integrated oxygen content) for channels in the oxygen band. These weighting functions indicate the atmospheric layers from which the thermal emission measured by each channel originates.

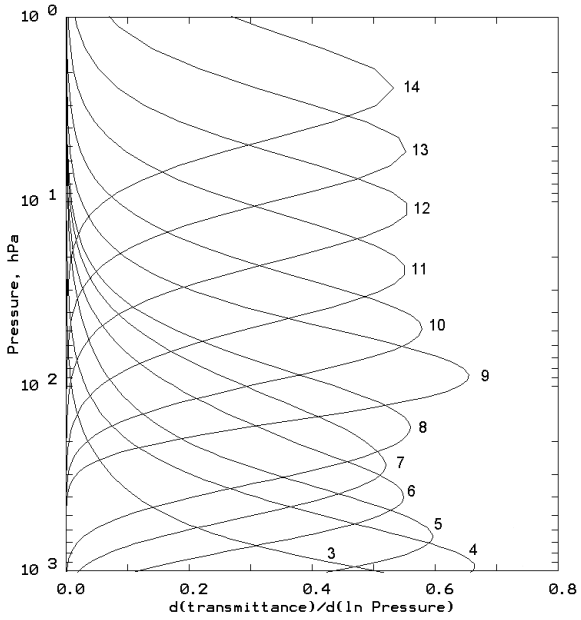

Figure 4.1.2. Oxygen Band Weighting Functions for Unit Surface Emissivity

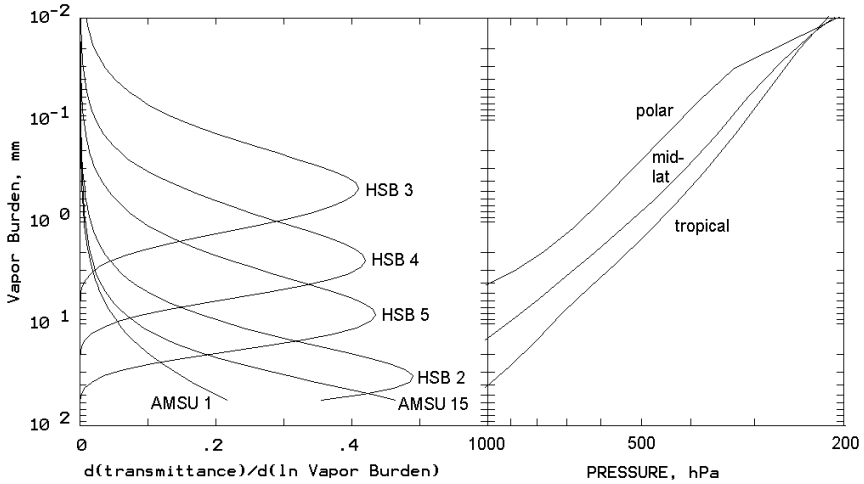

Figure 4.1.3. Water Vapor Weighting Functions for Unit Surface Emissivity (left) and Vapor Burden vs. Pressure in Three Different Climatologies (right)

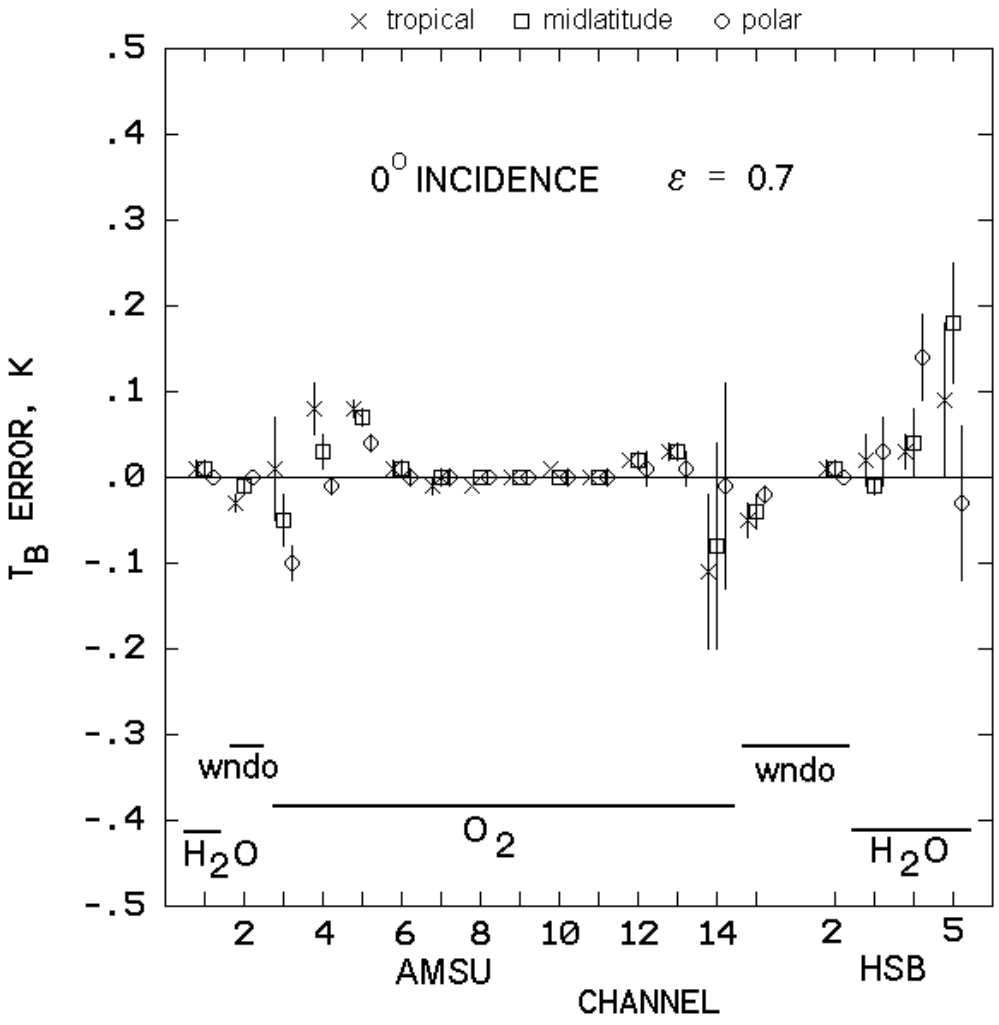

Figure 4.1.4. Brightness Temperature Errors (Rapid Algorithm Minus Line-by-Line Algorithm) for AMSU and HSB Channels. Vertical Lines Indicate ± 1 Standard Deviation; ε is the Surface Emissivity.

The ability of the rapid algorithm to approximate a line-by-line calculation was tested on a set of 300 profiles from the TOVS Initial Guess Retrieval (TIGR) (Chedin, *et al.*, 1985) ensemble. The first 100 profiles from each of the tropical, mid-latitude, and polar groups were used. Figure (4.1.4) shows brightness temperature errors (mean ± 1 standard deviation) at nadir, with surface emissivity = 0.7. For the channels that are not opaque (1-5, 15-17, 19 and 20), these brightness temperature errors depend on surface emissivity. The value ε = 0.7 is typical of ocean at the highest frequencies, and intermediate between ocean and land at the lowest frequencies. Errors for higher-emissivity land surfaces are

smaller than in Figure 4.1.4. The errors for channel 14 include the consequences of the magnetic field approximation. The output files contain a flag structure, MW_tair_range, which indicates whether the final temperature at any pressure level > 0.1 hPa lies outside of the range of profiles for which the rapid algorithm has been found to reproduce a line-by-line calculation within the instrument sensitivity. Different bits are set for temperatures outside the validated range by <10%, 10 to 25%, or >25%.

4.1.5 Microwave Surface Brightness Model

The surface brightness temperature spectrum Θ_S is modeled by a six-parameter (T_0, T_1, T_2, ν_1, ν_2, s) curve, added to an *a priori* surface brightness

$$\Theta_S(\nu) = \varepsilon_0(\nu)\, T_{S0} + T_0 + T_1\, \nu^s / (\nu^s + \nu_1^s) + T_2\, \nu^s / (\nu^s + \nu_2^s) \qquad (4.1.7)$$

where $\varepsilon_0(\nu)$ is a preliminary estimate of emissivity for the surface type obtained from the classification algorithm described in section 5.1.1.1, and T_{S0} is the *a priori* (climatological) surface temperature. The parameters T_0, T_1, T_2 are used in the retrieval solution to adjust the spectrum (they have *a priori* values of zero), while ν_1, ν_2 and s are assigned according to surface type, as in Table 5.1.1. The last three terms in (4.1.7) also help to correct for effects such as ocean surface roughness, errors in the dielectric constant model, misclassification of the surface, or errors in the estimated land fraction within the footprint.

In Figure 4.1.5, the rapid transmittance algorithm is tested against measurements made by the AMSU-A on the NOAA-15 satellite (see Rosenkranz, 2003) and the HSB on Aqua (see Rosenkranz and Barnet, 2006). The calculated brightness temperatures are based on coincident radiosonde profiles, using window channels to infer the surface emissivity, as described in section 5. Sidelobe corrections from Mo (1999) were applied to the AMSU-A measurements in the figure, but no corrections were made to the HSB measurements.

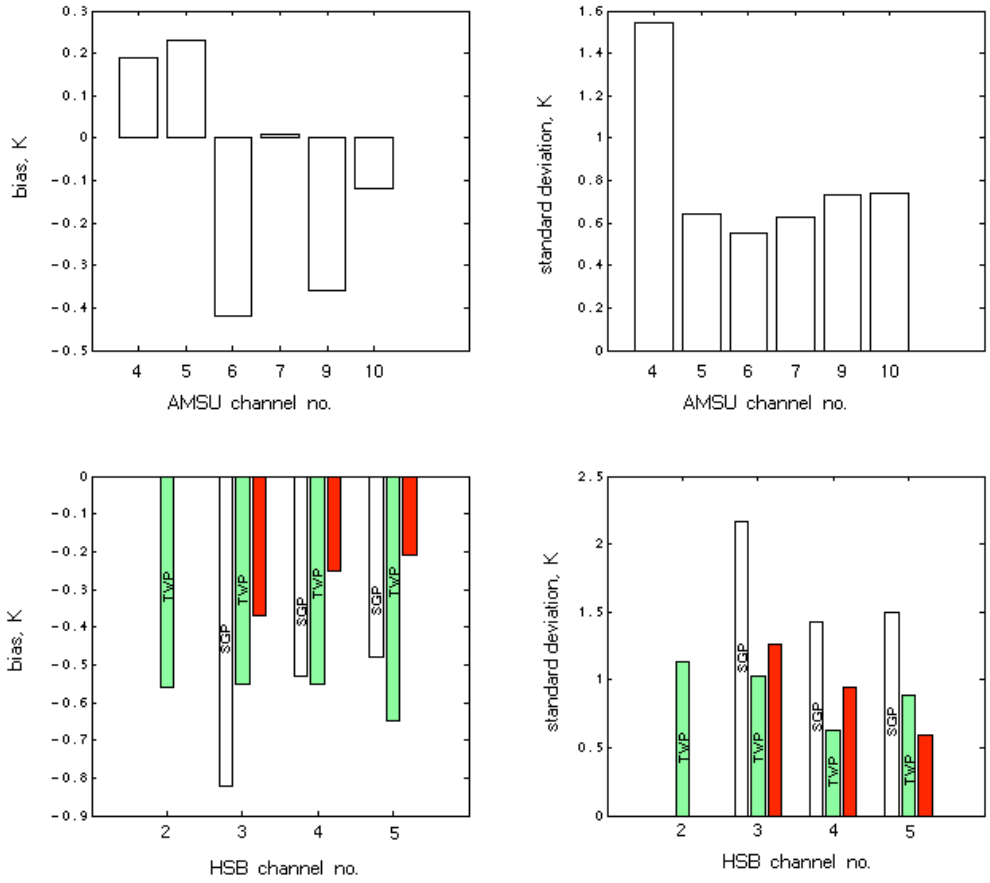

Figure 4.1.5. Statistics of differences between measured brightness temperatures minus brightness temperatures calculated from radiosonde profiles. Three profile ensembles are shown for HSB.

References

Bauer, A., Godon, M., Kheddar, M., and Hartmann, J.M., 1989: Temperature and Perturber Dependences of Water Vapor Line-Broadening. Experiments at 183 GHz; Calculations Below 1000 GHz, *J. Quant. Spectrosc. Radiat. Transfer*, **41**, 49-54.

Bauer, A., Godon, M., Carlier, J., and Ma, Q., 1995: Water Vapor Absorption in the Atmospheric Window at 239 GHz, *J. Quant. Spectrosc. Radiat. Transfer*, **53**, 411-423.

Bauer, A., Godon, M., Carlier, J., Ma, Q., and R.H. Tipping, 1993: Absorption by H_20 and H_20-N_2 Mixtures at 153 GHz, *J. Quant. Spectrosc. Radiat. Transfer*, **50**, 463-475.

Chedin, A., N. A. Scott, C. Wahiche, and P. Moulinier, 1985: The improved initialisation inversion method: A high resolution physical method for temperature retrievals from the TIROS-N series. *J. Clim. Appl. Meteor.*, **24**, 128-143.

Gamache, R.R., J.-M. Hartmann, and L. Rosenmann, 1994: Collisional broadening of water vapor lines- 1. A survey of experimental results. *J. Quant. Spectrosc. Radiat. Transfer*, **52**, 481-499.

Godon, M., Carlier, J. and Bauer, A., 1992: Laboratory Studies of Water Vapor Absorption in the Atmospheric Window at 213 GHz*, J. Quant. Spectrosc. Radiat. Transfer*, **47**, 275-285.

Janssen, M.A. (ed.), 1993: *Atmospheric Remote Sensing by Microwave Radiometry*, Chap. 1, New York: Wiley.

Liebe, H.J. and Dillon, T.A., 1969: Accurate Foreign-Gas-Broadening Parameters of the 22-GHz H20 Line from Refraction Spectroscopy, *J. Chem. Phys.*, **50**(2), 727-732 (1969).

Liebe, H.J., G.A. Hufford, and M.G. Cotton, 1993: Propagation Modeling of Moist Air and Suspended Water/Ice Particles at Frequencies Below 1000 GHz, in *AGARD Conference Proceedings 542*, *Atmospheric Propagation Effects through Natural and Man-Made Obscurants for Visible to MM-Wave Radiation*, pp.3.1-3.10.

Liebe, H.J., Hufford, G.A., and Manabe, T., 1991: A Model for the Complex Permittivity of Water at Frequencies Below 1 THz, *Int. J. of Infrared and Mill. Waves,* **12**(7), pp. 659-675.

Liebe, H.J., and Layton, D.H., Millimeter-Wave Properties of the Atmosphere: Laboratory Studies and Propagation Modeling, NTIA Report 87-224, October 1987.

Liebe, H.J., Rosenkranz, P.W., and Hufford, G.A., 1992: Atmospheric 60-GHz Oxygen Spectrum: New Laboratory Measurement and Line Parameters, *J. Quant. Spectrosc. Radiat. Transfer*, **48**(5/6), 629-643.

Liebe, H.J., Thompson, M.C. Jr., and Dillon, T.A., 1969: Dispersion Studies of the 22 GHz Water Vapor Line Shape*, J. Quant. Spectrosc. Radiat. Transfer*, **9**, 31-47.

Mo, T., "AMSU-A antenna pattern corrections," *IEEE Trans. Geosci. Rem. Sens.*, **37**, 103-112 (1999).

Poynter, R.L. and Pickett, H.M., 1985: Submillimeter, Millimeter, and Microwave Spectral Line Catalog, *Applied Optics*, **24**(14), pp. 2235-2240.

Rothman, L. S., C. P. Rinsland, A. Goldman, S. T. Massie, D. P. Edwards, J.-M. Flaud, A. Perrin, C. Camy-Peyret, V. Dana, J-Y. Mandin, J. Schroeder, A. McCann, R. R. Gamache, R. B. Wattson, K. Yoshino, K. V. Chance, K. W. Jucks, L. R. Brown, V. Nemtchinov, P. Varanasi, 1998: "The HITRAN Molecular Spectroscopic Database and HAWKS (HITRAN Atmospheric WorKStation):1996 Edition," *J. Quant. Spectrosc. Radiat. Transfer* **60**, 665-710.

Rosenkranz, P. W., 1998: Water vapor microwave continuum absorption: A comparison of measurements and models. *Radio Science*, **33**, 919-928. (Correction, *Radio Science*, **34**, 1025, 1999).

Rosenkranz, P. W., 2003: "Rapid radiative transfer model for AMSU/HSB channels", *IEEE Trans. Geosci. Rem. Sens.*, **41**, 362-368.

Rosenkranz, P. W., and C. D. Barnet, 2006: "Microwave radiative transfer model validation", *J. Geophys. Res.*, **111**, D09S07, doi:10.1029/2005JD006008.

Schwartz, M. J., 1997: Observations and Modeling of Atmospheric Oxygen Millimeter-wave Transmittance, Ph.D. Thesis, Mass. Inst. Of Tech., Dept. of Physics, Cambridge, MA.

Tretyakov, M., V. V. Parshin, M. A. Koshelev, V. N. Shanin, S. E. Myasnikova, and A. F. Krupnov, 2003: "Studies of 183 GHz water line: broadening and shifting by air, N_2 and O_2 and integral intensity measurements", *J. Molec. Spectros.*, **218**, 239-245.

4.2 Radiative Transfer of the Atmosphere in the Infrared

Physical retrievals of atmospheric parameters attempt to minimize the difference between computed and observed channel radiances. The accuracy of the retrieval is therefore directly related to the accuracy of the computed radiances. AIRS measures the convolution of the up-welling monochromatic radiances with the instrument spectral response function (SRF). An exact calculation of the observed radiances therefore requires the convolution of simulated monochromatic radiances. These computed radiances are complicated functions of the atmospheric state (temperature, pressure, gas amount), the gas transmittances, and the AIRS SRFs. Since the atmospheric emission lines can have widths as small as ~ 0.001 cm^{-1}, the wavenumber grid scale for the radiance calculation must have a similar spacing. This small grid spacing, combined with the time- consuming SRF convolutions, makes a monochromatic calculation of radiances orders of magnitude too slow for practical use. Instead, we must use a fast radiative transfer model that is based on appropriately convolved atmospheric transmittances for each spectral channel. Then the radiative transfer can be performed on a per-channel basis rather than on a finely spaced monochromatic wavenumber grid.

The starting point for understanding the AIRS radiative transfer algorithm (AIRS-RTA) is the monochromatic radiative transfer equation. The monochromatic radiance leaving the top of a nonscattering atmosphere is

$$R(\nu,\theta) = \varepsilon_s(\nu)B(\nu,T_s)\tau(\nu,p_s,\theta) + \int_{p_s}^{0} B(\nu,T)\frac{d\tau(\nu,p,\theta)}{dp}dp + \rho_s(\nu)H_{sun}(\nu)\tau(\nu,p_s,\theta)\tau(\nu,p_s\theta_{sun})\cos(\theta_{sun}) + R_d \qquad (4.2.1)$$

where $B(\upsilon, T)$ is the Planck function emission at frequency and temperature T, $\tau(\upsilon, p, \theta)$ is the transmittance between pressure p and the satellite at viewing angle θ, and T_s, ε_s, and ρ_s refer to the Earth's surface temperature, emissivity, and reflectivity respectively. The

solar radiance incident at the top of the atmosphere is represented by H_{sun}, while R_d is a relatively small radiance contribution arising from the reflection of the downwelling atmospheric thermal emission

$$R_d(\nu) = 2\pi\rho_s\tau(\nu, p_s, \theta)\int_{p=0}^{p_s} B(\nu,T)\int_{\theta_i=0}^{\frac{\pi}{2}} \sin(\theta_i)\cos(\theta_i)\frac{d\tau_d(\nu, p, \theta_i)}{dp}dpd\theta_i \qquad (4.2.2)$$

where τ_d is the transmittance between pressure p and the surface. The dependence of temperature and angle on pressure (altitude) has been suppressed in the above equations, as well as the dependence of the transmittances on temperature and gas abundance.

The AIRS-RTA allows the integration of the radiative transfer equation over 100 atmospheric layers to be performed in a discrete form. For reasons of clarity and brevity we omit further discussion of the last two terms in Equation (4.2.1), except to note that they are included in the AIRS-RTA by simplified approximations. A discrete form of the radiative transfer equation can then be written conveniently as

$$R_{meas} = \int R(\nu)f(\nu - \nu_0)d\nu = \int(\varepsilon_s B(T_s)\tau_N + \sum_{i=1}^{N} B(T_i)(\tau_{i-1} - \tau_i))f(\nu - \nu_0)d\nu \qquad (4.2.3)$$

where the atmospheric layers are numbered from space to the surface, 1 to N respectively. $B(T_i)$ is the Planck emission for layer i at temperature T_i, τ_i is the transmittance from layer i to space, inclusive, and $f(\upsilon - \upsilon_0)$ is the AIRS SRF for the channel centered at υ_0. The emissivity and Planck function are nearly constant over the narrow width $\Delta\upsilon$ of the AIRS channels, so they may be moved outside the integral. After integrating the transmittances, we are left with the channel-averaged form of the radiative transfer equation,

$$R_{meas} = \varepsilon_s B(T_s)\tau_N + \sum_{i=1}^{N} B(T_i)(\tau_{i-1} - \tau_i) \qquad (4.2.4)$$

where all terms now represent appropriate channel-averaged quantities.

The polychromatic approximation introduced in the above relation replaces the monochromatic layer-to-space transmittances with transmittances convolved with the SRFs. This in effect convolves the outgoing radiances, allowing us to do radiative transfer at just a single frequency per channel. In most cases, the AIRS channel radiances

calculated from the above equation using convolved layer-to-space transmittances differ from the convolved monochromatic AIRS channel radiances by ≤ 0.05 K, assuming one has perfect layer-to-space convolved transmittances in hand.

Figure 4.2.1 illustrates the large difference in spectral resolution between the upwelling monochromatic radiation and an AIRS brightness temperature spectrum. Because of this large difference in spectral resolution one cannot derive the layer-to-space transmittances directly from the product of the convolved layer transmittances since Beer's law is no longer valid. Overcoming this problem is one of the major issues in the development of a model for fast, parameterized, convolved layer transmittances.

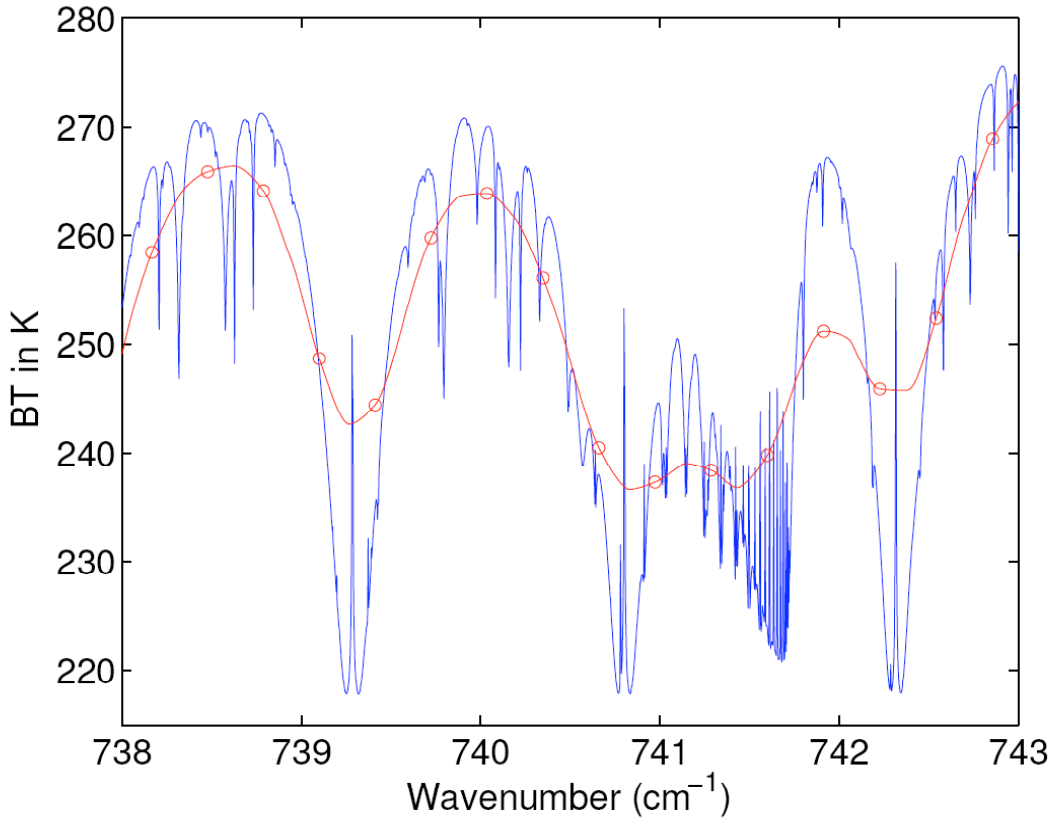

Figure 4.2.1. Simulated Monochromatic (Blue) and AIRS SRF Convolved (Red) Brightness Temperature Spectra. The red circles indicate the actual AIRS channel centroids.

In the following sections we discuss the major issues in developing the AIRS-RTA, which include: (1) forming a discrete grid for integrating the radiative transfer equation, (2) parameterizing the layer transmittances as a function of the atmospheric state, (3) the spectroscopy needed to compute atmospheric transmittances, (4) the line-by-line algorithm used to generate the monochromatic transmittances (5) the AIRS spectral response functions.

The flowchart shown in Figure 4.2.2 outlines the flow of activities needed to develop the AIRS-RTA, which is discussed in the following text.

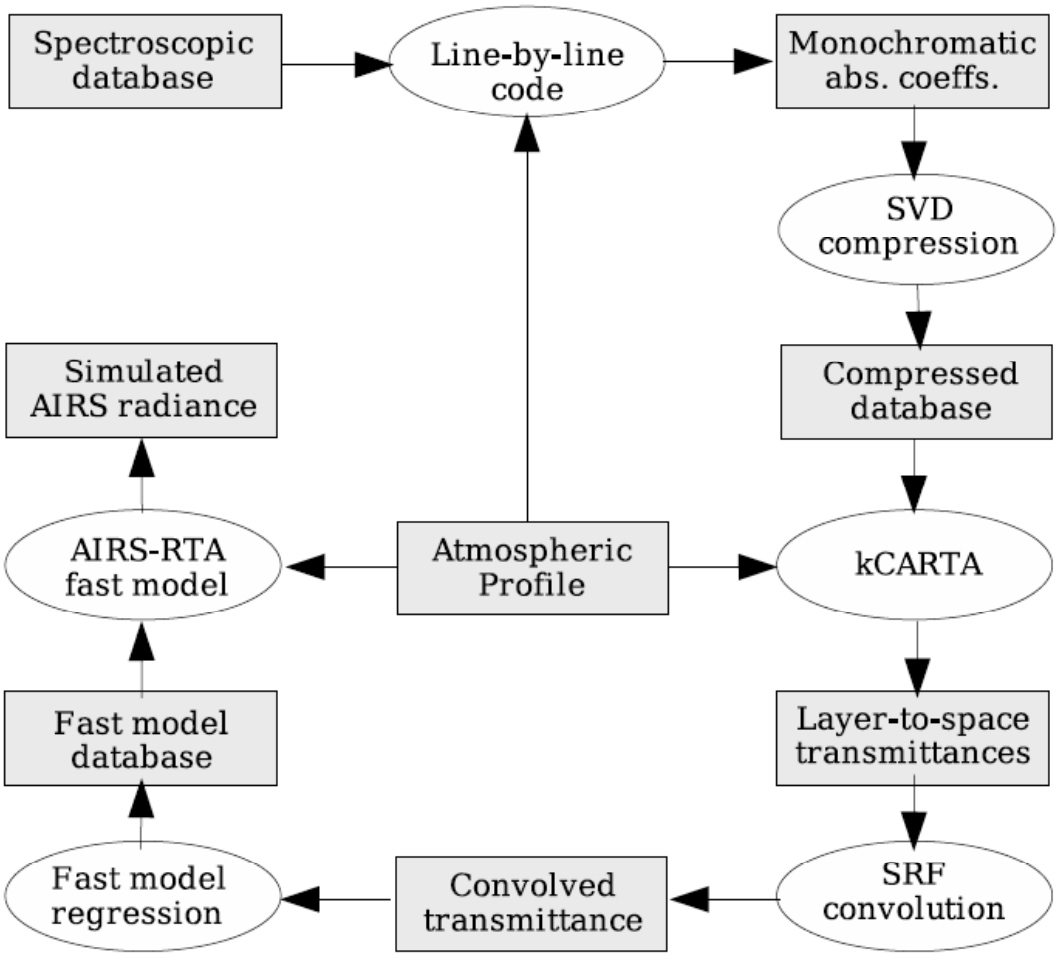

Figure 4.2.2. Flow Diagram for Development of the AIRS-RTA

4.2.1 AIRS Atmospheric Layering Grid

The atmospheric pressure layering grid for the AIRS-RTA model was selected to keep radiative transfer errors below the instrument noise. Grid characteristics are a function of the spectral region(s) of observation, the instrument resolution, and instrument noise. The speed of the final fast transmittance model will depend on the number of layers, so excessive layering should be avoided.

Line-by-line simulations indicate some channels need a top layer with pressures as small as 0.01 mb (an altitude of ~ 80 km). The region of primary importance to AIRS is the troposphere and lower stratosphere, where layers on the order of 1/3 of the nominal 1-km vertical resolution of AIRS retrievals are desired. Smoothly varying layers facilitate interpolation and avoid large changes in layer effective transmittances. The following relation defines the pressure layer boundaries selected for AIRS

$$P_i = (ai^2 + bi + c)^{7/2} \tag{4.2.5}$$

where P is the pressure in millibars; i is the layer boundary index and ranges from 1 to 101; and the parameters a, b, and c were determined by solving this equation with the following fixed values: P_1 = 1100 mb, P_{38} = 300 mb, and P_{101} = 0.005 mb. The 101 pressure layer boundaries in turn define the 100 AIRS layers. These layers vary smoothly in thickness from several tenths of a kilometer near the surface to several kilometers at the highest altitudes. Figure 4.2.3 is a plot of the layer mean pressure for the 100 AIRS layers.

4.2.2 Fast Transmittance Modeling

Over the years, a number of fast transmittance models have been developed for various satellite instruments. However, some of these models only have been applied to the microwave region where the measured radiances are essentially monochromatic and easier to model. AIRS required a major new effort in the development of its RTA. Some of the details of our model can be found in Strow, *et al.*, (2003).

The AIRS-RTA most closely follows Susskind, *et al.*, (1983) by parameterizing the optical depths rather than transmittances for channels where the influence of water vapor

is small. Channels sensitive to water vapor are modeled using a variant of the Optical Path TRANsmittance (OPTRAN) algorithm developed by McMillin, *et al*., (1979, 1995). The AIRS infrared fast model is thus a hybrid of both Susskind's approach and OPTRAN.

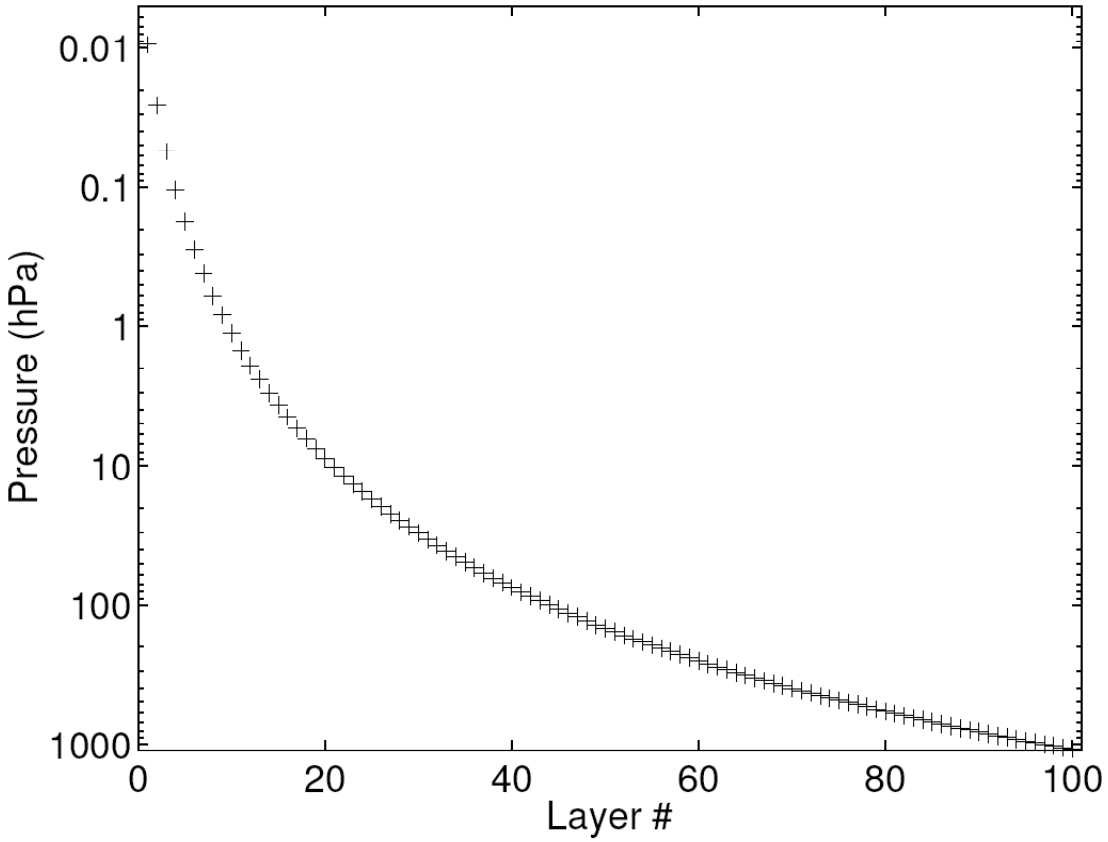

Figure 4.2.3. Mean Pressure of the AIRS-RTA 100 Layers

The AIRS-RTA model actually produces equivalent channel averaged optical depths, k, which are related to the layer transmittances, τ, by $\tau = \exp(-k)$. The optical depth is the product of the absorption coefficient and the optical path. For AIRS, a fast model for k is much more accurate than a model that directly returns layer τ. k is computed for each of the 100 atmospheric layers used for AIRS radiative transfer. The current AIRS-RTA model allows water, ozone, methane, carbon monoxide, carbon dioxide, the temperature, and local scan angle to vary. All other gases are treated as "fixed" gases. These gases are "fixed" in the sense that we only need to parameterize their dependence on temperature, not amount. Although the observed radiances are primarily sensitive to temperature via the Planck function, the temperature dependence of the transmittances is also important.

The following discussion outlines the development of a parameterization of the convolved layer transmittances as a function of the atmospheric state. Most of the complications of this parameterization arise from the loss of Beer's law, which forces us to introduce terms in the transmittance parameterization for a given atmospheric layer that depend on layers above the particular layer under consideration. These parameterizations, which are functions of the atmospheric profile, are derived from least-squares fits to a statistical set of atmospheric profiles in order to ensure that we can faithfully produce the appropriate transmittances under all atmospheric conditions. We call this statistical set of profiles our "regression profiles."

Breakout of Gases Once the atmospheric layering grid and regression profiles (see later discussion) are selected, the monochromatic layer-to-space transmittance can be calculated. The gases are distributed into sub-groups that are either fixed or variable. The details of how the transmittance model simultaneously handles several variable gases is somewhat complicated and beyond the scope of this document. For simplicity, this discussion is restricted to fixed gases (F), water vapor (W), and ozone (O). The breakout of the other variable gases is similar. The monochromatic layer-to-space transmittances for the 48 regression profiles are calculated for each pressure layer, grouped into the following three sets, and convolved with the AIRS SRF

$$\begin{aligned} F_l &= \tau_l(fixed) \\ FO_l &= \tau_l(fixed + ozone) \\ FOW_l &= \tau_l(fixed + ozone + water) \end{aligned} \qquad (4.2.6)$$

Water continuum absorption is excluded since it varies slowly with wavenumber and does not need to be convolved with the AIRS SRF. In addition, separating out the water continuum improves our fit of the local line water transmittance. Later, the water continuum is factored into the total transmittance as a separate term.

For each layer l, the convolved layer-to-space transmittances are ratioed with transmittances in the layer above, $l - 1$, to form effective layer transmittances for fixed (F), water (W), and ozone (O) as

$$
\begin{aligned}
F_l^{eff} &= \frac{F_l}{F_{l-1}} \\
O_l^{eff} &= \frac{FO_l}{FO_{l-1}} \div \frac{F_l}{F_{l-1}} \\
W_l^{eff} &= \frac{FOW_l}{FOW_{l-1}} \div \frac{FO_l}{FO_{l-1}}
\end{aligned}
\tag{4.2.7}
$$

Forming these ratios in the above manner reduce the errors inherent in separating the gas transmittances after the convolution with the instrument spectral response function. The total effective layer transmittance can be recovered as

$$
FOW_l^{eff} = F_l^{eff} \times O_l^{eff} \times W_l^{eff} = \frac{FOW_l}{FOW_{l-1}} \tag{4.2.8}
$$

The convolution of a product of terms is in general not the same as the product of the terms convolved individually. However, the above formulation guarantees the product of all the layer transmittances from layer l to N exactly returns FOW_l, if the layer transmittances are exact.

The zeroth layer transmittance (i.e., when $l - 1 = 0$) is taken to be exactly 1.0. The negative logarithm of these layer effective transmittances is taken to get effective layer optical depths

$$
\begin{aligned}
k_{fixed} &= -\ln(F^{eff}) \\
k_{ozone} &= -\ln(O^{eff}) \\
k_{water} &= -\ln(W^{eff})
\end{aligned}
\tag{4.2.9}
$$

which become the dependent variables in the fast model regression.

Predictors The independent variables in the fast model regression, called the predictors, are a set of variables relating to the atmospheric profile. The optimal set of predictors used to parameterize the effective layer optical depth depends upon the gas, the instrument SRFs, the range of viewing angles, the spectral region, and even the layer thicknesses. In short, no one set of predictors is likely to work well in every case. Finding the set of predictors which give the best results is, in part, a matter of trial and error. However, there are some general trends.

For an instrument such as AIRS with thousands of channels, it is difficult to develop individual optimal predictors for each channel. The AIRS-RTA uses seven sets of predictors, each corresponding with a subset of channels. These sets of predictors were determined by extensive trial and error testing, as well as consideration of the relative importance of the variable gases in each channel. Supplemental sets of predictors are used for OPTRAN water, the water continuum, and variable CO_2.

The regression is prone to numerical instabilities if the values of the predictors vary too greatly. Consequently, we follow the usual practice of defining the predictors with respect to the values of a reference profile, either by taking a ratio or an offset. There is also a danger of numerical instability in the results of the regression, due to the interaction of some of the predictors. Sensitivity of the output to small perturbations in the predictors is avoided by systematic testing, but there are practical difficulties in detecting small problems since we are performing on the order of 1 million regressions.

As an example, the predictors for the fixed gases for one of the seven sets are

$$1)a \quad 2)a^2 \quad 3)aT_r \quad 4)aT_r^2 \quad 5)T_r \quad 6)T_r^2 \quad 7)aT_z \quad 8)aT_z/T_r \tag{4.2.10}$$

where a is the secant of the local path angle, T_r is the temperature ratio $T_{profile}/T_{reference}$, and T_z is the pressure weighted temperature ratio above the layer

$$T_z(l) = \sum_{i=2}^{l} P(i)P(i) - P(i-1)T_r(i-1) \tag{4.2.11}$$

where *P(i)* is the average layer pressure for layer *i*. The predictors for the variable gases can involve more complicated dependencies on the gas and the pressure weighted gas ratios above the layer, similar to the temperature term defined above. Note that terms like T_z (or W_z, etc. for the variable gases) make the layer l transmittance dependent on the temperature (or gas amounts) in the layers above l.

Regressions for Fast Transmittance Parameters The accuracy of radiative transfer calculations made with the AIRS-RTA model was improved significantly by weighting the variables prior to performing the regression. Radiative transfer is insensitive to layers for which the change in layer-to-space transmittance across the layer is approximately

zero. This occurs when either the layer effective transmittance is approximately unity, or the layer- to-space transmittance is approximately zero. Therefore, the data going into the regression is not all of equal importance to the final accuracy of radiative transfer calculations made with the model. We found it useful to weight the data in terms of both its effective layer optical depth as well as the total optical depth of all the layers above the layer under consideration.

The spectral dependence of the fitting errors are shown in Figure 4.2.4 and a histogram of these errors in Figure 4.2.5. The errors are calculated with respect to the regression profile set, comparing the RMS errors between the brightness temperatures of input data and the AIRS-RTA model calculated values. These graphs including errors from all six angles used for regression profiles. They do not include errors associated with the parameterization of the reflected thermal and reflected solar radiation.

During the development of the AIRS-RTA, the RMS errors were computed for a large independent set of profiles. The RMS errors for the independent profiles were generally similar to those for the regression profiles. The regression profiles represent a wide range of possible conditions, with a number of extreme cases. It is important to recognize, however, that the AIRS-RTA does have a statistical component that comes from the selection of the regression profiles.

Regression Profiles One other necessary pre-processing step is the selection of a set of profiles for calculation of the layer-to-space transmittances. The transmittances for these profiles become the regression data for the fast transmittance coefficients. These profiles should span the range of atmospheric variation, but, on the whole, should be weighted towards the more typical cases. The range of variation provides the regression with data points covering the range of possible atmospheric behavior, while the weighting of the mix of profiles towards more typical cases produces a transmittance model that works best on more statistically common profiles.

The process of calculating and convolving monochromatic layer-to-space transmittances is generally computationally intensive, thus imposing a practical limit on the number of profiles one can calculate for use in the regression. As discussed earlier, 48 regression

profiles (at 6 viewing angles each) are sufficient to cover most of the profile behavior. This number is a compromise between the available time and computing resources and the need to cover a wide range of profile behavior in the regression. Choosing too few profiles leads to accuracy problems for profiles outside the range of behaviors considered. Choosing more profiles than necessary does not hurt the fast model, but does consume extra time and computer resources.

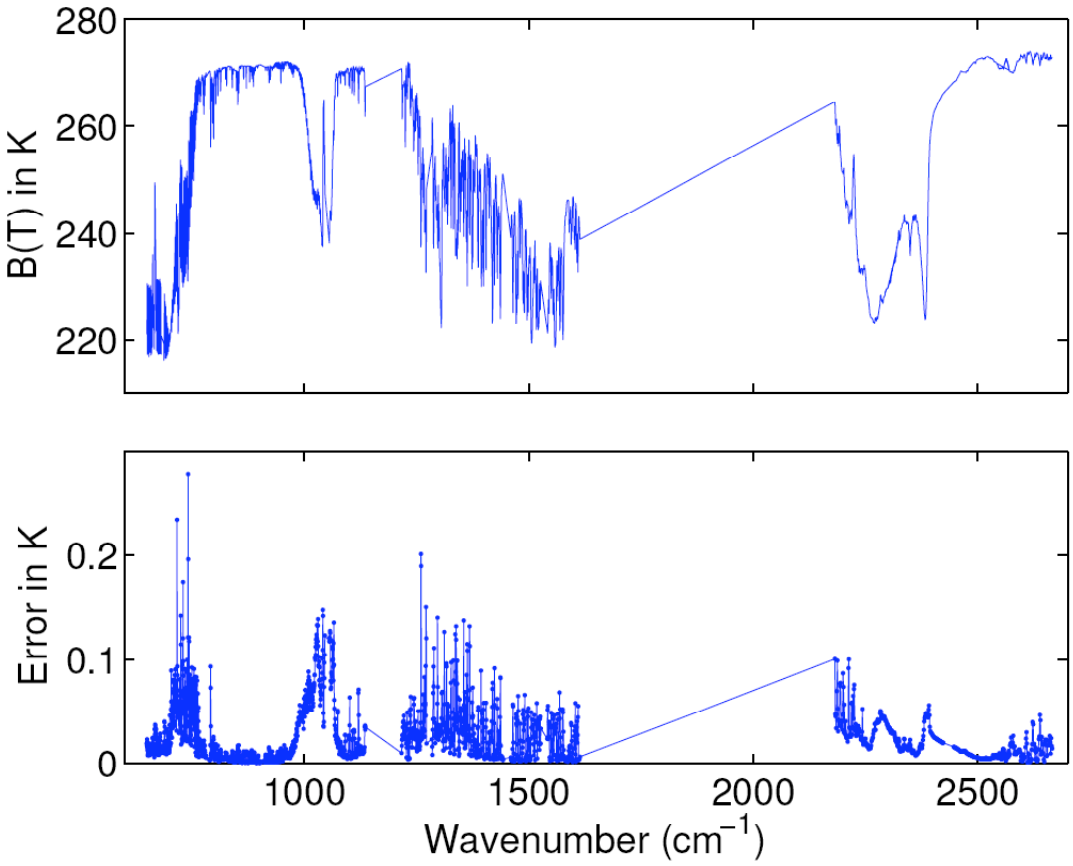

Figure 4.2.4. RMS Errors of the AIRS-RTA Model

Each profile should cover the necessary pressure (altitude) range with data for temperature as well as absorber amount for each of the gases allowed to vary. The fixed gases include all whose spatial and temporal concentration variations have a negligible impact on the observed radiances. As previously mentioned, the variable gases are H_2O, O_3, CO, CH_4, and CO_2. All other gases are included in the "fixed gases." CO_2 is handled differently than the other variable gases, and only two CO_2 absorber amount profiles are used: a standard amount profile and a perturbed amount profile. The standard amount

CO_2 profile is treated as a fixed gas. A very simple and accurate parameterization is used to model the difference in transmittance between the standard CO_2 profile transmittances and the perturbed CO_2 profile transmittances.

For those satellite-viewing angles relevant to the AIRS instrument (0 to 49 degrees), the effects of viewing angle can be approximated fairly well by multiplying the nadir optical depth by the secant of the local path angle. This approximation neglects the minor refractive effect at large angles. Due to the curvature of the Earth, the local path angle is in general not the same as the satellite viewing angle, but is related to it by a fairly simple equation. Local atmospheric path angles of 0, 32, 45, 53, 60, and 63 degrees are used in the regression profiles to cover the 0-49 degree satellite view angle range. An additional six angles between 69-84 degrees are used for the shortwave channels where transmittances at large angles are need to model the reflected solar radiance.

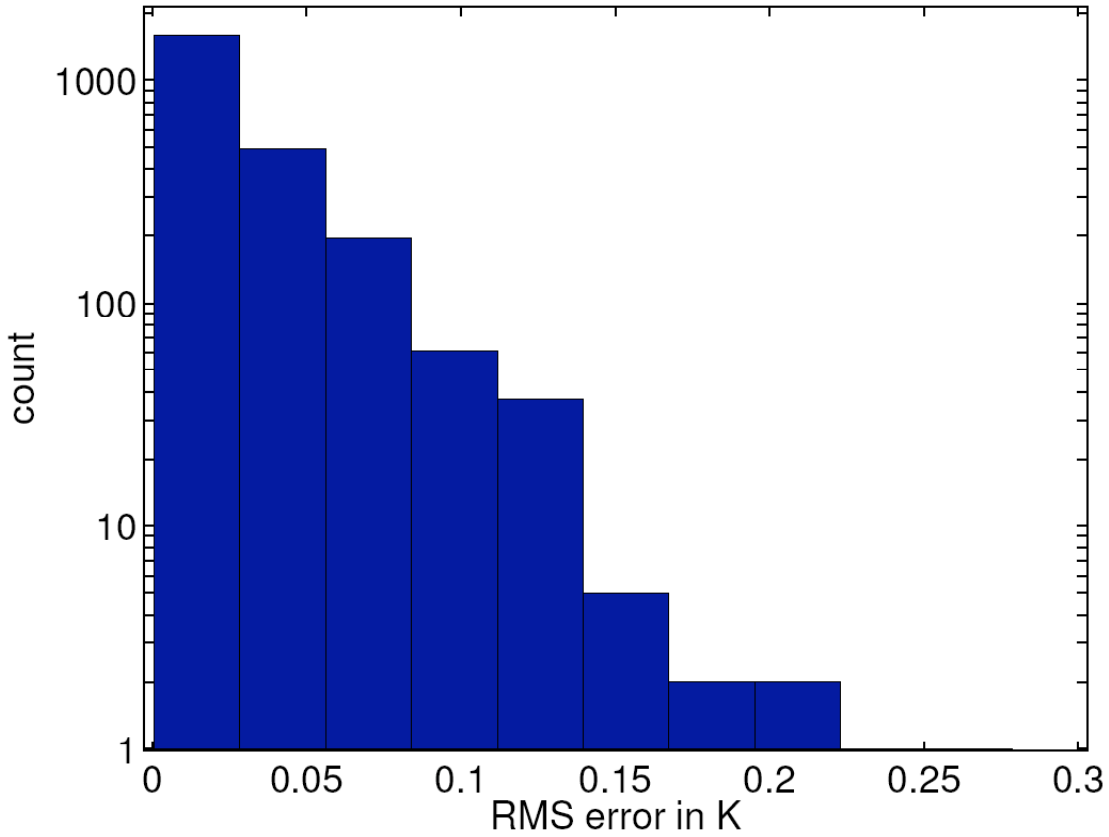

Figure 4.2.5. Histogram of the AIRS-RTA Model, Fitting Errors for All Channels

4.2.3 Spectroscopy

The ultimate goal is to produce an AIRS-RTA that does not introduce significant errors in AIRS computed radiances. This requires a fast model that can compute accurate transmittances. Even if the fast model RMS fitting errors are zero, the accuracy of the transmittances are dependent upon the quality of the spectroscopic line parameters and lineshape models used to compute the monochromatic transmittances.

Due to the dominance of either CO_2 or H_2O absorption in the majority of AIRS channels, the most important spectroscopy errors are associated with errors in the line parameters and line shapes of these two gases. The line parameters most likely to introduce spectroscopy errors into the fast forward model for AIRS are the line strengths, line widths, and the temperature dependence of the line widths. However, errors in spectral lineshapes and continuum absorption probably are generally more troublesome than line parameter errors.

Currently, the HITRAN-2000 (Rothman, *et al.*, 2003) database is used for most atmospheric line parameters. As so many bands and molecules contribute to the observed radiances, the accuracy of the existing line parameters is difficult to judge in detail. Based upon our analysis of AIRS observations and calcuated radiances, we estimate the combined effects of line parameter and lineshape model errors in the computed optical depth of the stronger absorbing "fixed" gases (which in most spectral regions is dominated by CO_2) are typically at the 5% level, while for water the optical depth errors are at the 10% level.

Errors in the spectral line shapes of CO_2 and H_2O are much more problematic than line parameter errors. Because of the large optical depths of CO_2 and H_2O in the atmosphere, their spectral line wings can be important, especially for remote sensing of temperature and humidity. For example, AIRS channels with the sharpest weighting functions are located in between lines or in the line wings where knowledge of the spectral line shape is most important. Moreover, accurate measurements of the line wing absorption are exceedingly difficult due to problems simulating atmospheric optical depths in a

laboratory cell, especially for H_2O. It is also tedious and expensive to make these large optical depth measurements at the low temperatures found in the upper troposphere.

Figure 4.2.6 shows the optical depth "tuning" used with the AIRS-RTA in version 4 processing. These multipliers are used to scale the indicated component of the optical depth inside the AIRS-RTA. These are empirically determined values, and some small portion of these adjustment may be due to error sources other than spectroscopy. Tracing these adjustments back to line parameter errors is no simple task and has not yet been attempted.

Figure 4.2.7 shows the effects of our optical depth tuning on AIRS radiances. The data set consists of the clearest night-time AIRS observations matched with sondes launched as part of the AIRS validation campaign. The sonde profiles were used with the AIRS-RTA to compute simulated radiances, which were then differenced with the observations. The sonde data did not extend to the stratosphere, so ignore the bias in the 15-μm and 4.3-μm stratospheric channels. We solved for an effective surface skin temperature using the AIRS super-window channel at 2616 cm^{-1}, so the bias there has been forced to zero.

4.2.4 Monochromatic Transmittance Calculations

The monochromatic layer-to-space transmittances used to determine the parameters of the AIRS-RTA model are indirectly generated using our custom line-by-line code (UMBC-LBL). Building a custom LBL code allowed us to incorporate those features we deemed desireable, include our Q-, P-, and R-branch CO_2 line-mixing model which has a significant effect on the optical depths in the 15-μm and 4-μm regions.

Currently, 48 profiles are used in the regressions for the fast transmittance parameters. Because line-by-line (and especially Q/P/R branch line mixing) calculations are very slow, we developed a new pseudo line-by-line algorithm called the kCompressed Atmospheric Radiative Transfer Algorithm (kCARTA) to allow the (relatively) fast computation of almost monochromatic transmittances and radiances. The UMBC-LBL was used to compute a very large look-up table of monochromatic layer optical depths for a set of 11 reference atmospheric profiles. The kCARTA program interpolates the lookup

table optical depths for temperature and scales for absorber amount to compute the optical depths for the desired profile. Any change in the physics of the line-by-line code or line parameter database requires a recalculation of the affected portion of the look-up table.

The kCARTA database consists of many individual look-up tables each covering a 25-cm^{-1} interval with 10,000 points (0.0025-cm^{-1}spacing) for 100 pressure layers (0.009492 to 1085 mb) and 11 temperatures. The 11 temperature profiles are the U.S. Standard profile, and 10 profiles offset from it in ± 10 K increments. On average, 7 gases must be included per 25-cm^{-1} region. The continua due to gases such as N_2 and O_2 are also included in these tables. Optical depths are computed using a 0.0005 cm^{-1}grid and then averaged to the database grid spacing of 0.0025 cm^{-1}.

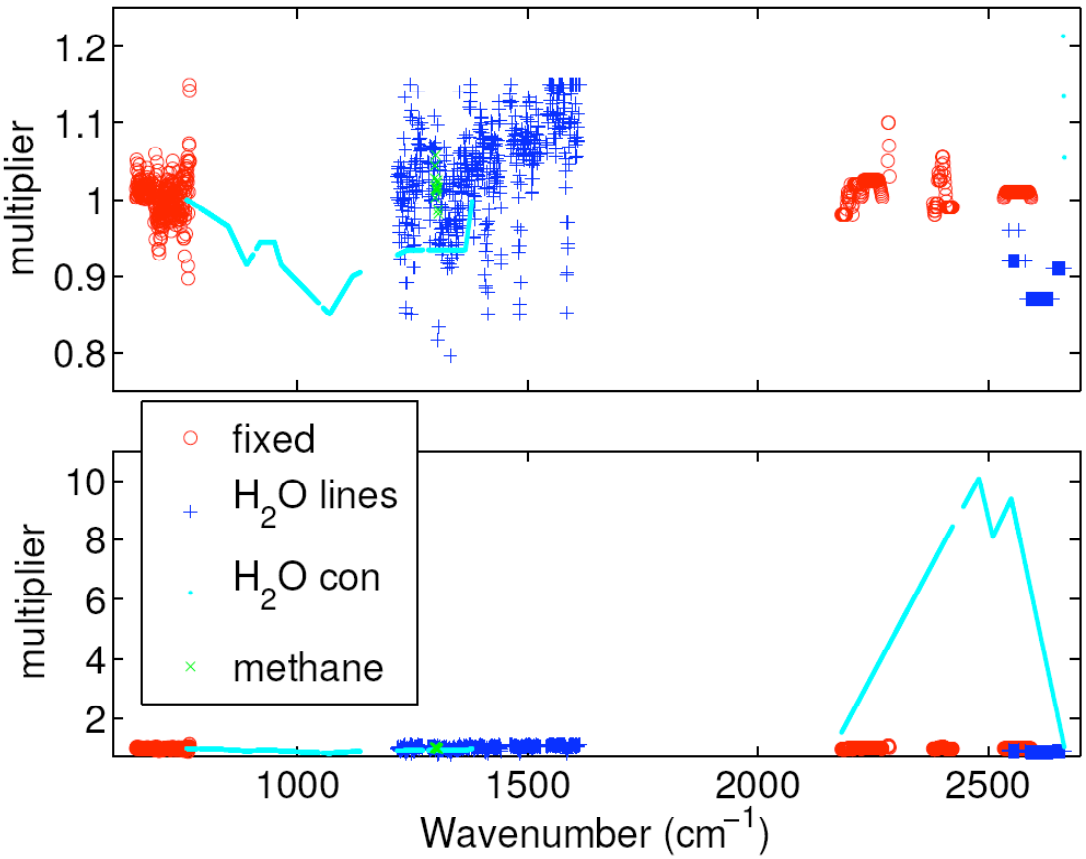

Figure 4.2.6. Optical Depth Tuning used in the V4 AIRS-RTA. The bottom panel shows the same data as the top panel, but with the vertical range expanded to illustrate the large adjustment to the water continuum in the shortwave channels.

Consequently, the highest altitude optical depths are not truly monochromatic, but exhibit good integrated optical depths. The relatively large width of the AIRS Spectral Response Function (SRF) results in negligible errors due to this averaging.

This large look-up table has been compressed using a Singular Value Decomposition (SVD) method. The approximately 50 times compression achieved in kCARTA is lossy, but the accuracy of the transmittances remains very high. kCARTA bridges the gap between slow but accurate line-by-line codes, and fast but special purpose fast transmittance codes. kCARTA is used to calculate the 48 profile transmittances we use as regression data for the AIRS fast transmittance model. The computation time for these transmittances is not a significant fraction of the time involved in creation of a new fastmodel. However, the transmittance data files are very large, and the convolution of these monochromatic transmittances with the AIRS SRFs is a time consuming process.

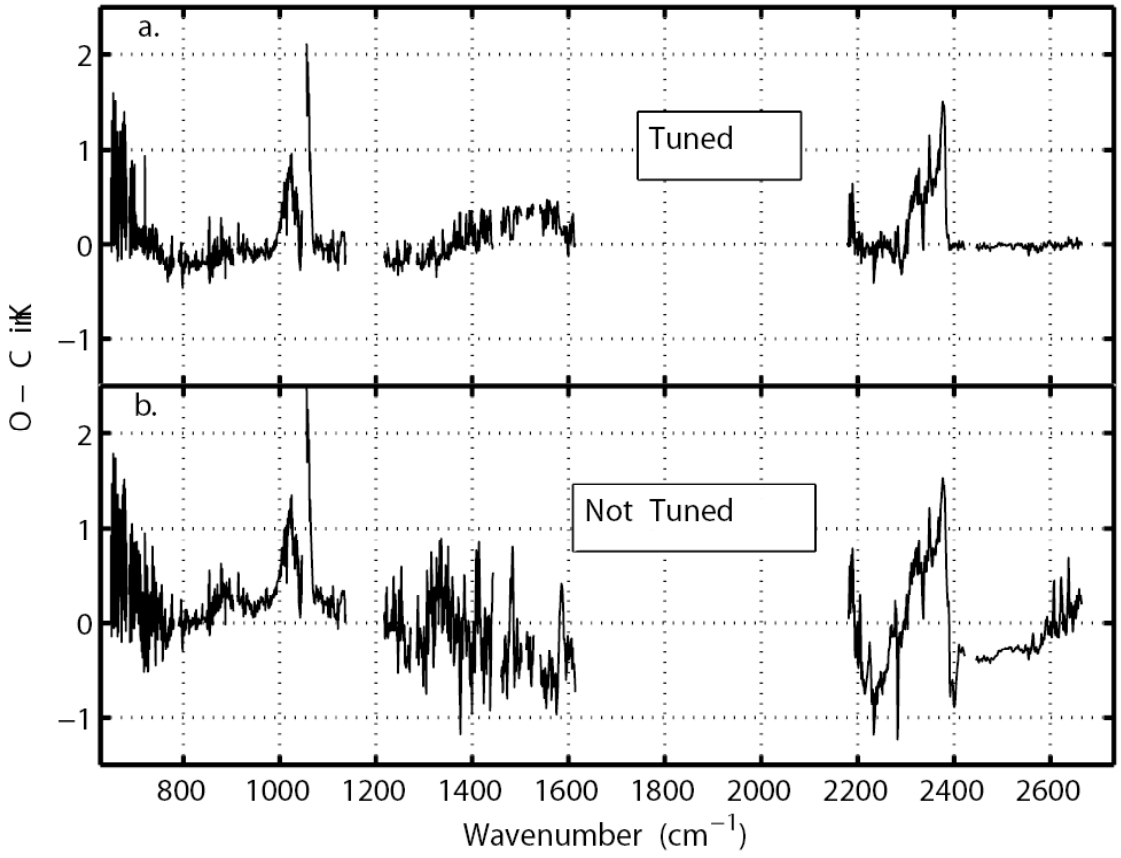

Figure 4.2.7. Comparison of Observed - Calculated Brightness Temperatures with and without Optical Depth Tuning

4.2.5 Spectral Response Function Measurements and Modeling

Inaccuracies in the AIRS spectral response function directly impact the accuracy of the AIRS-RTA, and consequently the accuracy of the AIRS retrieved products. The AIRS SRFs are not Level 1 products, so it is appropriate to discuss the determination of the SRF functions in this document. Complete knowledge of the AIRS SRFs derived solely from ground calibration was not possible for two reasons; (1) small changes in the alignment of the AIRS spectrometer/focal plane since launch have shifted the centroids of the AIRS SRFs, and (2) the spectral location of fringes produced by the AIRS entrance aperture filters are dependent on the thermal environment of AIRS in orbit. Both of these effects are relatively small, but our requirements on SRF knowledge are quite stringent.

Since becoming operational in late August 2002, the AIRS channel centroids have remained stable to within 1% of a channel Full Width at Half Maximum (FWHM). An extreme solar event in late October 2003 led mission control to shut off the AIRS coolers temporarily. When AIRS was switched back on in early November 2003, it required a few weeks to cool down, and then be re-calibrated back to approximately the same configuration as before the shutdown. While it was possible to adjust the channels back to their pre-shutdown centroids, this required a small change to the operating temperature, which resulted in a small relative shift of the fringes. The effects of this shift are small enough to ignore for retrieval purposes, but may need to be accounted for when looking at radiance biases for climate purposes.

Figure 4.2.8 shows the estimated change to the AIRS observed brightness temperatures due to the change in fringe position in November 2003. The effects are negligible in most channels, but not everywhere. The largest change is in 2200-cm^{-1} region which affects the CO sounding channels. The inset plot shows a blowup of this region, and the good agreement between the model and observed change is evidence the fringe and SRF models are fairly accurate.

While we can not measure the SRFs in orbit, we can measure the channel centroids to fairly high accuracy. Careful analysis of AIRS data indicates the channel centroids drift

back and forth by 0.5% of a FWHM (peak-to-peak) over each orbit. The exact reason for this drift is uncertain, but it is probably related to solar heating effects. There is also a long term drift, with the channels having drifted 0.3% of a FWHM in the first two years since launch. This slow drift appears to be slowing and it may not be necessary to take action to maintain the current channel centroids. If it is eventually deemed necessary, it should be possible to again "dial in" the original channel centroids by adjusting the temperature of the focal plane, but this would again cause another relative shift in the fringe positions.

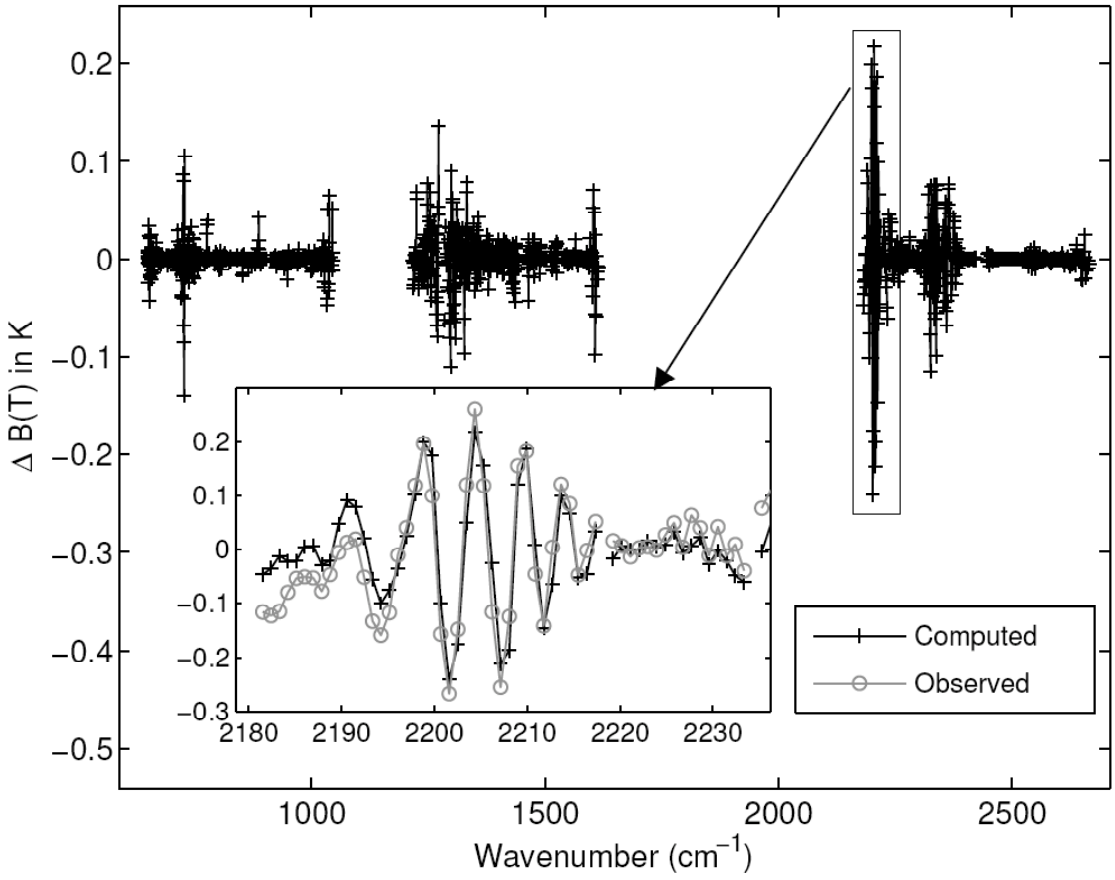

Figure 4.2.8. Estimated Change to AIRS Observed Brightness Temperatures due to the Offset in Fringe Position in November 2003

Figure 4.2.9 shows the drift in the AIRS channel centroids as a function of time as well as latitude during the ascending (day-time) portion of Aqua's orbit. The back-and-forth shift of the centroids with each orbit shows up in this plot as the latitude dependence of the shift. The data used for this plot does not extend to high latitudes, so the full range of

the shift with latitude is not shown. The Version 4 AIRS-RTA and Level 1B data does not account for this small orbital and long-term centroid drift. The effects of a 0.5% error in the channel centroids is shown in Figure 4.2.10. It is possible to apply an approximate correction for a small centroid error by interpolating the forward model radiances, but that requires knowledge of the centroid position.

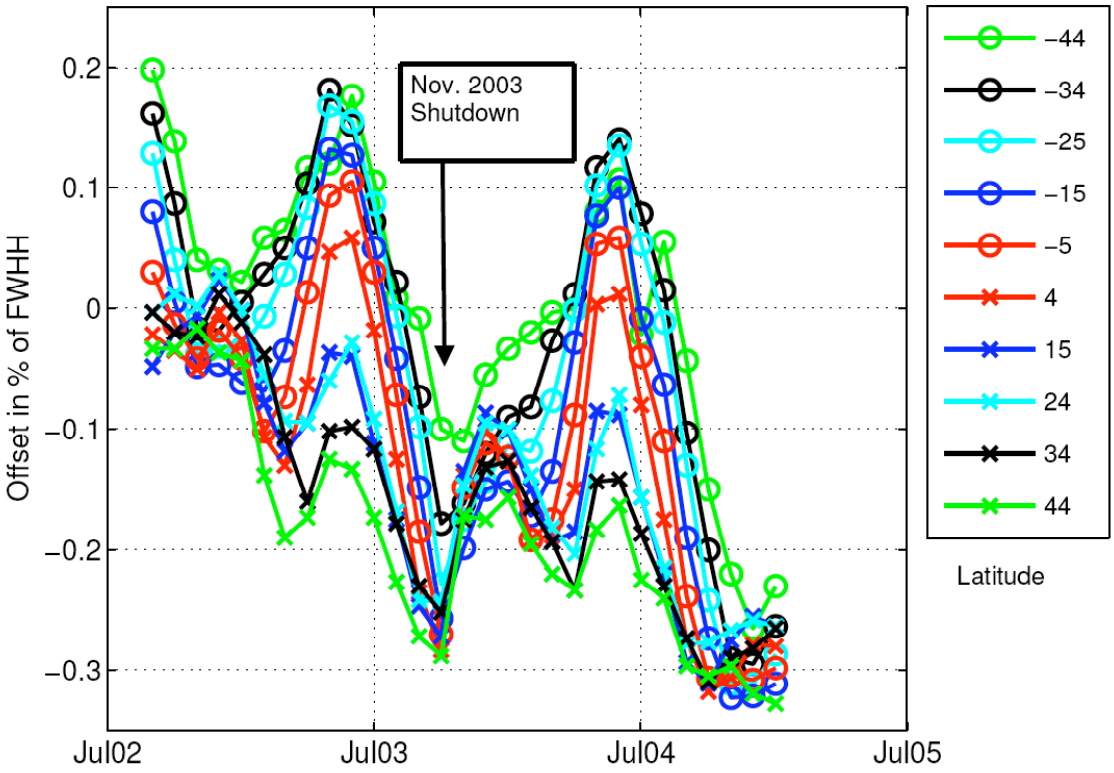

Figure 4.2.9. Centroid Drift versus Time and Latitude, Ascending (Day) Orbit

4.2.6 AIRS-RTA Error Analysis

The following table contains rough estimates of the errors in the AIRS-RTA in units of brightness temperature. They are separated into radiative transfer/spectroscopy errors and SRF knowledge errors. In many cases these errors will be correlated, sometimes of opposite sign. Consequently it is very difficult to properly combine the errors in Table 4.2.1 into a single AIRS-RTA error budget. In addition, most of these errors are highly channel dependent. They have been estimated conservatively and represent upper bounds.

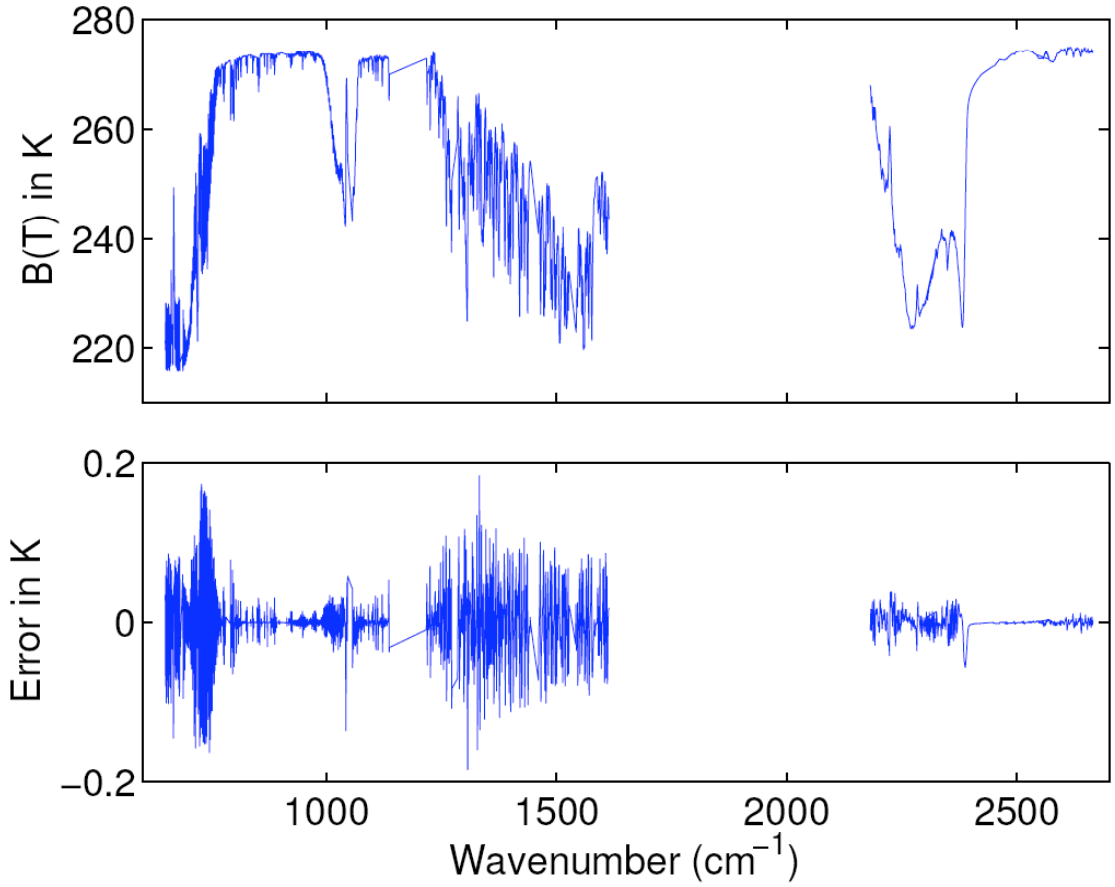

Figure 4.2.10. Brightness Temperature Error for a 0.5% Error in Channel Centroids

Table 4.2.1. AIRS-RTA Error Estimates

Radiative Errors	**Error (K)**	**Comment**
Fast model fit	0.05 - 0.3	Can be larger for individual profiles
Spectroscopy	0.2 - 0.6	Errors are more likely for water
Reflected thermal	0.0 - 0.2	Proportional to reflectivity
Solar	0.0 - 0.1	Can be much larger if ρ is off
Layering	0.05	Most channel have lower errors
Polychromatic approximation	0.05	Most channel have lower errors
Aerosols	0.0 - 1	Dust can make it through cloud clearing
SRF Errors		
Centroids	0.0 - 0.1	Possible to corrected for
Widths	0.0 - 0.2	Negligible for most channels
Fringes	0.0 - 0.2	Negligible for most channels
Wings	0.0 - 0.2	Negligible for most channels

This page intentionally left blank.

5. DESCRIPTION OF THE CORE RETRIEVAL ALGORITHM

5.1 Microwave Initial Guess Algorithms

5.1.1 Profile Retrieval Algorithm

The microwave initial guess profile retrieval algorithm derives temperature, water vapor and non-precipitating cloud liquid water profiles from AMSU-A/HSB brightness temperatures. It is intended to provide the starting point for the AIRS cloud clearing and retrieval. This is an iterative algorithm in which the profile increments are obtained by the minimum-variance method, using weighting functions computed for the current temperature and moisture profiles with the rapid transmittance algorithm described in Section 4.1. A block diagram is shown in Figure 5.1.1.

The input vector of measured brightness temperatures is accompanied by an input validity vector whose elements are either one or zero. This provides a way of handling missing or bad data (for example, during the period after HSB failed on Feb. 5, 2003).

5.1.1.1 Preliminary Surface Type Classification

The surface classification algorithm is diagrammed in Figure 5.1.2. The classification rules are from Grody, *et al.,* (2000), and make use of discriminant functions that are linear combinations of AMSU-A channels 1, 2, 3, and 15. If sea ice is indicated by the classification algorithm, then its concentration fraction is estimated from a linear operation on channels 1, 2, and 3. If the surface type is glacier or snow-covered land, then the snow or ice fraction is estimated using AMSU-A channels 3 and 15. Parameters of the surface brightness model (Equation 4.1.7) are assigned according to surface type as in Table 5.1.1. *A priori* emissivities for the ice and snow types were estimated from NOAA-15 and Aqua data. For land, $\varepsilon_0(\nu) = 0.95$ at all frequencies; for seawater, the dielectric constant model of Ellison, *et al.,* (2003) was used to compute the emissivity of a flat surface viewed in the polarization of the AMSU-A and HSB radiometers.

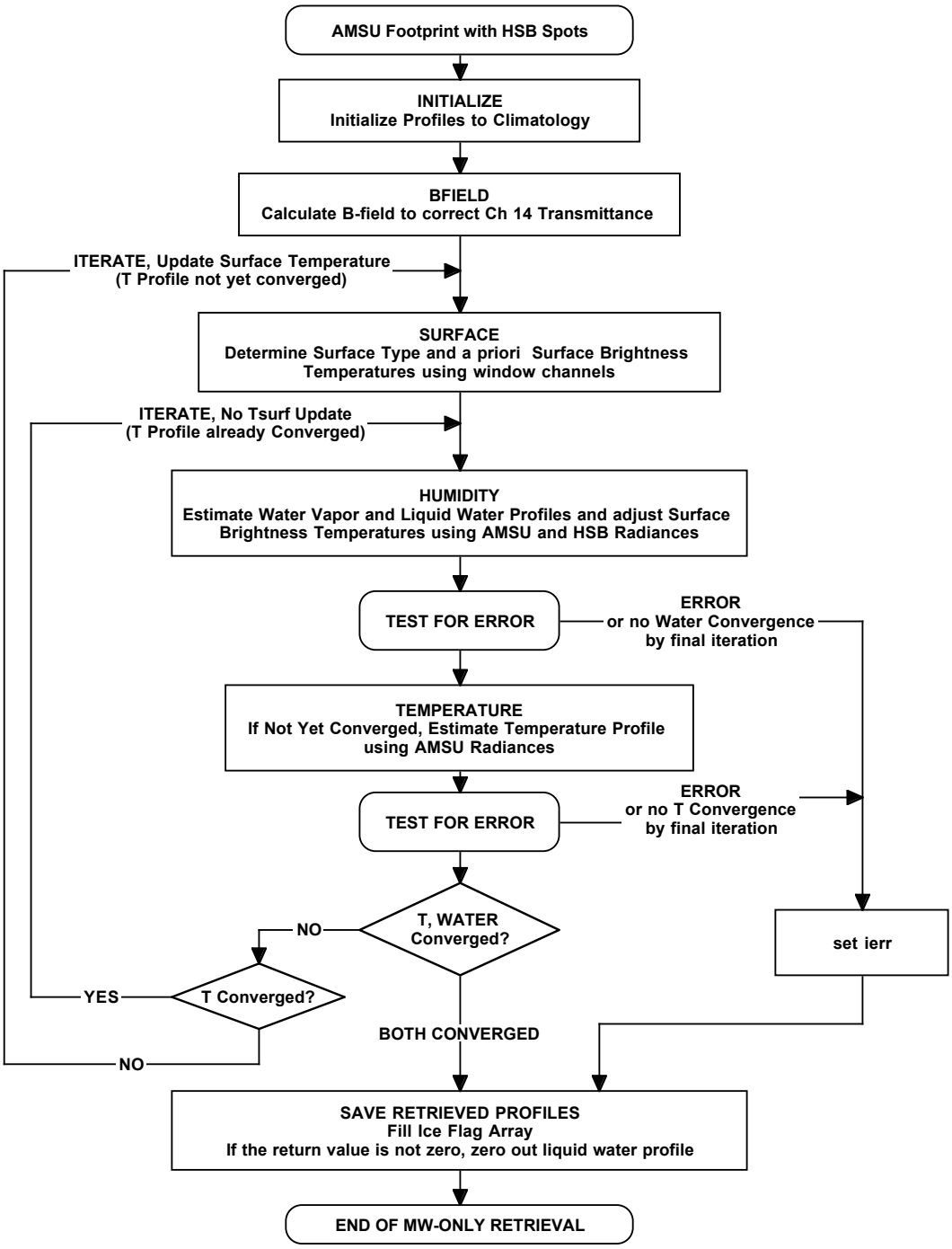

Figure 5.1.1. AMSU-A/HSB Initial Guess Profile Retrieval

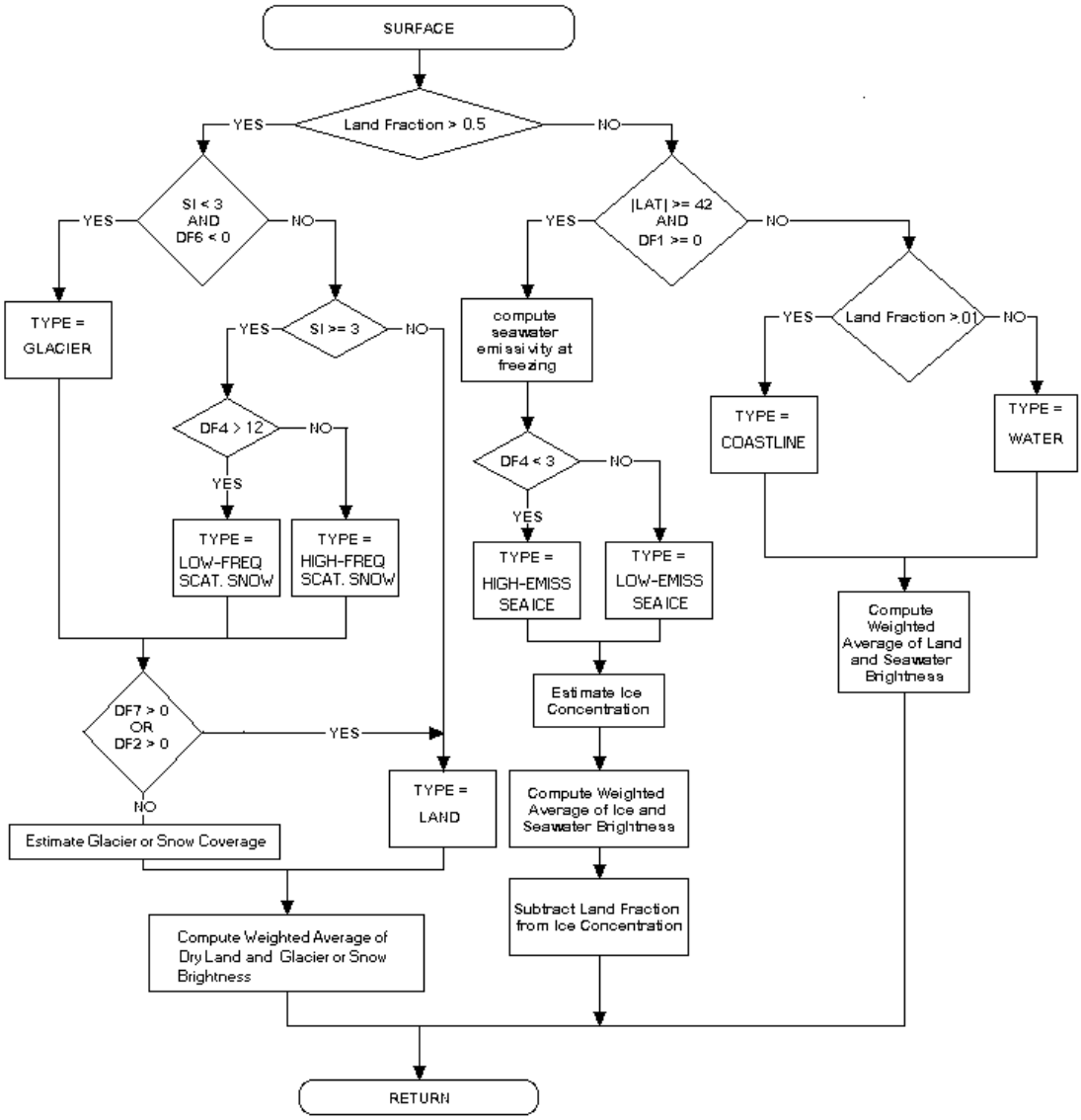

Figure 5.1.2. Surface Classification Algorithm

5.1.1.2 Atmospheric Moisture and Condensation Model

Measurements of brightness temperature at the HSB frequencies are a result of the vertical profile of atmospheric opacity relative to temperature and hence do not by themselves distinguish, at any given altitude, between opacity due to water vapor and opacity due to liquid water. However, the physics of water vapor condensation add some *a priori* information or constraints. Wilheit (1990) suggested that liquid water should be placed at the altitudes where the measurements force relative humidity into saturation. Although the water vapor profile is saturated within the cloudy part of the field of view, it

is assumed here that the condensation process is not spatially resolved, hence the threshold for condensation, denoted by H_L, may be less than 100%. The saturation vapor pressure depends on temperature, and due to errors in the estimated temperature profile, H_L may also be greater than 100%. Therefore, H_L is retrieved as an atmospheric parameter, along with a profile H, which is a generalization of relative humidity to encompass both vapor and liquid water, as illustrated in Figure 5.1.3. It is important to note that because convergence is determined from the brightness temperature residuals, which, in turn, are computed using the vapor and liquid mixing ratios (or column densities), the role of H in this algorithm is only to introduce the *a priori* statistics and constraints.

The average vapor mixing ratio in the field of view is

$$\rho_V = \rho_S [\text{ramp}(H, 10) - f(H)] / 100 \tag{5.1.1}$$

where ρ_S is the saturation value of mixing ratio,

$$\text{ramp}(x,c) = \begin{cases} x & \text{for } x \geq c; \\ c \exp(x/c - 1) & \text{for } x < c, \end{cases} \tag{5.1.2}$$

and

$$f(H) = \text{ramp}(H - H_L, 6) \tag{5.1.3}$$

Thus, the value of ρ_V/ρ_S lies between zero and $H_L/100$. The liquid water mixing ratio averaged over the field of view is assumed to be given by

$$\rho_L = c_1 f(H) \tag{5.1.4}$$

where c_1 is a coefficient equivalent to a liquid/air mass mixing ratio of 10^{-5} per percent.

The saturation vapor mixing ratio is computed from the temperature profile by the formula of Liebe (1981). Saturation is calculated with respect to liquid water (by extrapolation) even when the temperature is below 273 K. This model therefore allows supercooled liquid water and water vapor greater than the saturation value with respect to ice.

Table 5.1.1. Surface-Model Parameters Fixed by Classification. ($\sigma_{0,\,1,\,2,\,\rho,\,HL}$ = *a priori* standard deviation of T_0, T_1, T_2, p_ρ, H_L)

Surface type	s	ν_1 (GHz)	ν_2 (GHz)	σ_0 (K)	σ_1 (K)	σ_2 (K)	σ_ρ	σ_{HL}(%)
0. Coastline	1.2	90	-	note 1	note 1	0	0.12	8
1. Land	1.2	90	-	15	20	0	0	8
2. Water	1.5	50	-	note 1	note 1	0	0.12	8
3. High-emissivity sea ice	3	40	120	10	10	10	0	0
4. Low-emissivity sea ice	3	40	120	10	10	10	0	0
5. Snow (high-frequency scattering)	3	50	150	20	20	20	0	0
6. Glacier/snow (very low-frequency scattering)	3	40	120	20	20	20	0	0
7. Snow (low-frequency scattering)	3	33	90	20	20	20	0	0

Note 1: For water or coastline, $\sigma_0^2 = 25 + (0.55\ T_s\ \sigma_{LF})^2$ and $\sigma_1^2 = 100 + (0.25\ T_s\ \sigma_{LF})^2$, where σ_{LF} is the estimated uncertainty in the land fraction.

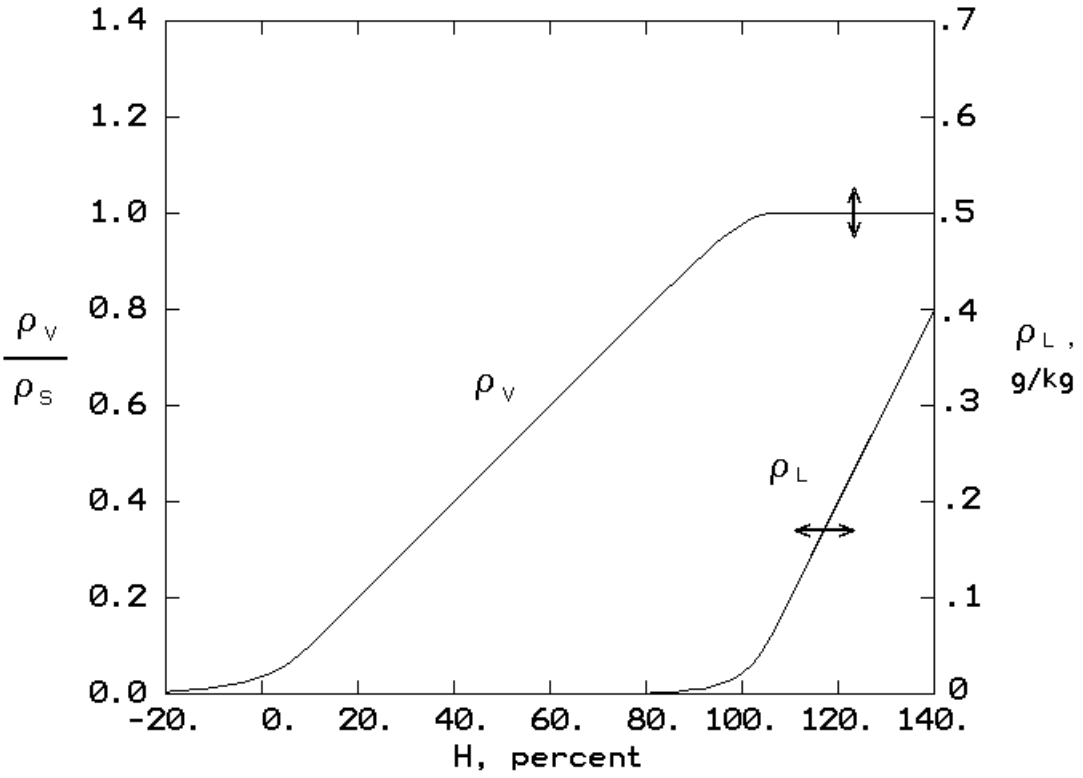

Figure 5.1.3. Water Vapor(ρ_v) and Cloud Liquid (ρ_L) Mixing Ratios as Functions of H_L = 100. The Arrows Indicate How the curves Change as H_L Varies

5.1.1.3 Estimation of Surface Brightness and Atmospheric Moisture

This part of the algorithm is based on retrieval methods described by Wilheit (1990), Kuo, *et al.,* (1994), Wilheit and Hutchison (1997), and Rosenkranz (2006). It uses the four channels of HSB and channels 1, 2, 3 and 15 of AMSU-A. The HSB measurements are weighted averages over 3x3 spatial arrays which approximate the AMSU-A field of view. The H profile, H_L, and four surface parameters T_0, T_1, T_2, and p_ρ are concatenated into a vector $\vec{Y}$. The parameter p_ρ, when the surface type is either water or coastline, determines the secant ratio ρ by

$$\rho = \sec(\theta_{ref})/\sec(\theta) = 1 + \text{ramp}(p_\rho, 0.02) \tag{5.1.5}$$

The cost function to be minimized is

$$(Y_{est}-Y_o)^T \mathbf{S}_Y^{-1} (Y_{est}-Y_o) + (\Theta_{obs}-\Theta-\Theta')^T (\mathbf{S}_e+\mathbf{S}_f)^{-1} (\Theta_{obs}-\Theta-\Theta') \tag{5.1.6}$$

in which Y_{est} is the estimate of Y, Y_o is its *a priori* value and $\mathbf{S_Y}$ is its covariance matrix with respect to Y_o, Θ_{obs} is a vector of the eight measured antenna temperatures, $\mathbf{S_e}$ is their error covariance matrix (assumed to be diagonal), Θ' is the tuning correction for sidelobe effects and possible transmittance error, and Θ is a brightness temperature vector computed from the current values of temperature, moisture, and surface brightness. $\mathbf{S}_f$ is a diagonal covariance matrix which approximately represents errors in Θ resulting from errors in the temperature profile retrieval and tuning.

The estimate of Y is obtained by Newtonian iteration (see Rodgers, 1976), except that Eyre's (1989) method of damping is used to avoid large relative humidity increments, because of the nonlinearity of the problem:

$$Y_{est_n} = Y_{est_{n-1}} - \delta [\, Y_{est_{n-1}} - Y_o \,] + \delta \, \mathbf{S}_Y \, \mathbf{W}_Y^T \, X_Y \tag{5.1.7}$$

in which $(\mathbf{W_Y})_{ij} = \partial\Theta_i/\partial Y_j$, superscript T indicates transpose, and X_Y is the solution vector to

$$[\mathbf{W}_Y \, \delta \, \mathbf{S}_Y \, \mathbf{W}_Y^T + \mathbf{S}_e + \mathbf{S}_f \,] \, X_Y = \Theta_{obs} - \Theta - \Theta' + \mathbf{W}_Y \, \delta [\, Y_{est_{n-1}} - Y_o \,] \tag{5.1.8}$$

where

$$\delta = \begin{cases} 1.0 \text{ if } (\Theta_{i_{obs}} - \Theta_i - \Theta') < 10 \text{ K for all channels i, or } n \geq 10; \\ 0.1 \text{ otherwise.} \end{cases} \quad (5.1.9)$$

Here δ is a scalar rather than a matrix as in Eyre's paper. The Jacobian matrix $\mathbf{W}_Y$ is computed for the state represented as $Y_{est_{n-1}}$ by application of the chain rule for differentiation to the forward model equations. This is sometimes referred to as a "tangent linear" method. For example, the elements of $\mathbf{W}_Y$ corresponding to H values are

$$\frac{\partial \Theta}{\partial H} = G \bullet \left(\frac{\partial \kappa}{\partial \rho_v} \bullet \frac{\partial \rho_v}{\partial H} + \gamma \frac{\partial \rho_L}{\partial H} \right) \quad (5.1.10)$$

in which $G = \partial\Theta/\partial\kappa$ where κ represents the opacity of the layer at the viewing angle, and $\gamma = \partial\kappa/\partial\rho_L$. G is equal to the integral over an atmospheric layer of the function G(h) for which an expression is given by Schaerer and Wilheit (1979). The rapid transmittance algorithm computes the coefficient γ in the small-droplet (Rayleigh) approximation. Hence, it is intended to be applied only to non-precipitating cloud situations. Differentiation of (5.1.1) and (5.1.4) yields $\partial\rho_v/\partial H$ and $\partial\rho_L/\partial H$.

The elements of $\mathbf{S}_Y$ corresponding to relative humidity were calculated from the TIGR profile ensemble (Chedin, *et al.*, 1985). For the surface, it is necessary to postulate statistics based on physical plausibility and observed ranges of variation. The standard deviations of parameters depend on surface type, and are listed in Table 5.1.1. The *a priori* relative humidity is obtained from climatological databases (NCEP 50-year reanalysis, Kistler, *et al.*, 2001) of temperature and vapor mixing ratio, but limited to < 90%. Hence the initial cloud liquid-water profile always has very small values. The *a priori* values of T_0, T_1 and T_2 are set to zero, and H_L to 100, in all cases; the *a priori* value of p_ρ is assumed to be 0.02. For water surfaces, the parameters T_0, T_1, and p_ρ are all related to roughness, and therefore the *a priori* statistics assigned to them assume correlation coefficients of 0.2. As indicated by the standard deviations in Table 5.1.1, at most three of the four surface-roughness parameters are allowed to vary for any surface type.

After update of Y by (5.1.7-8), the water vapor and liquid water profiles are computed from (5.1.1-4), and surface brightness is computed for both window and sounding frequencies from (4.1.7), using the new estimate.

5.1.1.4 Estimation of Temperature Profile

The atmospheric temperature vector is augmented by T_S, which is considered to be distinct from the air temperature near the surface. The measured Θ's used in the temperature profile retrieval are channels 4-14 of AMSU-A. Given an existing estimate $T_{est_{n-1}}$, the new estimated profile is to be determined from a vector Θ_{obs} of observed brightness temperatures. A cost function similar to (5.1.6), with Y replaced by T, is to be minimized separately for the temperature profile. Hence, the retrieved profiles are not influenced by statistical correlations between temperature and relative humidity.

Initially, the temperature profile, including surface temperature, is set to a climatological profile T_o which depends on latitude and season. The new, minimum-variance estimate of T is obtained by Newtonian iteration (Rodgers, 1976, eq. 101):

$$T_{est_{n-1}} = T_o + \mathbf{S_T}\,\mathbf{W_T}^{\mathbf{T}}\,X_T \qquad (5.1.11)$$

where S_T is the temperature covariance matrix and X_T is the solution vector to

$$[\mathbf{W}_T\,\mathbf{S}_T\,\mathbf{W}_T^{\,T} + \mathbf{S}_e + \mathbf{S}_f]\,X_T = \Theta_{obs} - \Theta - \Theta' + \mathbf{W}_T[\,T_{est_{n-1}} - T_o\,] \qquad (5.1.12)$$

The error covariance matrix ($\mathbf{S}_e$+$\mathbf{S}_f$) includes the effects of surface brightness uncertainty, water vapor, liquid water, and instrument noise.

The elements of the Jacobian matrix $\mathbf{W}_T$ corresponding to the atmospheric part of the temperature vector are given by

$$\partial\Theta/\partial T = K + G\,\partial\kappa/\partial T \qquad (5.1.13)$$

where K is equal to the temperature weighting function as defined by Schaerer and Wilheit (1979) integrated over the given atmospheric layer, $G = \partial\theta/\partial\kappa$, and $\partial\kappa/\partial T$ is computed by the rapid transmittance algorithm. The second term on the right side of (5.1.13) is a small correction to the temperature weighting function.

The elements of $\mathbf{W}_T$ corresponding to T_S are obtained by partial differentiation of Eq. (4.1.2):

$$\frac{\partial \Theta}{\partial T_s} = \frac{\tau \, \Theta_{sky} \, \Theta_s}{T_s^2} \tag{5.1.14}$$

The dependence on T_S is nonlinear here because Θ_S is considered to be a known input from the moisture algorithm. If the validity of a channel is zero, then the row of $\mathbf{W}_T$ corresponding to that channel is set to zeros. The dimensions of the matrix remain the same.

The covariance of the temperature vector was computed from the TIGR ensemble (Chedin, *et al.*, 1985). T_S is assumed to have the same *a priori* mean and variance as the air temperature near the surface, but the covariances of T_S with atmospheric temperatures are assumed to be reduced by a factor of 0.9 from those of the surface air temperature.

5.1.1.5 Iteration Procedure and Convergence Tests

After the temperature profile is updated using (5.1.11-12), the algorithm returns to the moisture and surface-brightness section for another iteration of (5.1.7-8), using weighting functions computed for the updated temperature and moisture profiles. Convergence is tested separately for the temperature channels and for the moisture/surface channels; iteration of either part of the algorithm is suspended when one of the following conditions is met : (1) the computed brightness temperature vector Θ meets the closure criterion

$$\sum_{i=1}^{N_B} \frac{\left[\Theta_{obs_i} - \Theta_i - \Theta'_i\right]^2}{\Delta T_i^2} \quad \leq \quad N_B \tag{5.1.15}$$

where ΔT_i is the instrument noise (not the total measurement error) on channel i and N_B is the number of valid elements in Θ_{obs}; or (2) when successive computations of the left side of (5.1.15) change by less than 1% of the right side, for the temperature channels, or 2% for the moisture/surface channels; or (3) when the number of iterations exceeds a preset limit, which is 12 for the temperature channels and 16 for the moisture/surface channels. Typically, iteration of the temperature profile ceases after one or two iterations, but the moisture profile often requires six or more iterations.

5.1.1.6 Output Flags

Several error flags are produced by the microwave retrieval algorithm. The 'mw_ret_code' may contain any of the following values (or sums of values if more than one condition applies):

0: No error.

1: Moisture variables rejected. Test of residuals for channels AMSU1-8,15 and HSB2-5.

2: Troposphere temperature profile rejected. Test of residuals for moisture-related channels when integrated vapor > 6 mm or integrated cloud liquid > 0.1 mm, or for channels AMSU3-8 under any conditions.

4: Integrated cloud liquid water > 0.5 mm.

8: Insufficient valid channels to do the retrieval.

32: Derived surface emissivity > 1 for any AMSU frequency.

64: Stratosphere temperature profile rejected. Test of residuals for channels AMSU9-14.

In polar regions, error value 1 may occur without 2, and is then considered nonfatal; i.e., processing continues to the IR retrieval stages.

The Qual_MW_Only_Temp_Tropo flag is a summary of the bits in mw_ret_code that affect the tropospheric temperature quality (2, 4, 8, 32) and can have values 0: usable, or 2: not usable.

The Qual_MW_Only_Temp_Strat flag is a summary of the bits in mw_ret_code that affect the stratospheric temperature quality (8, 64) and can have values 0: usable, or 2: not usable.

The Qual_MW_Only_H2O flag is a summary of the bits in mw_ret_code that affect the moisture variables (1, 4, 8, 32) and in addition tests the surface type when HSB is not operating, because with AMSU alone, integrated vapor and liquid water can be retrieved, but only over a water surface (ocean or coastline). Possible values are 0: moisture profiles and integrals usable; 1: only integrals usable; 2: not usable.

If the mean square of brightness temperature residuals for the HSB channels is greater than 64 (i.e., 8K rms per channel), then an ice-scattering flag ('cloud_ice') is set at all altitudes for which clouds are present and the temperature estimate is below 273 K. This typically flags intense precipitation systems like thunderstorms.

5.1.2 Precipitation Flags, Rate Retrieval, and AMSU Corrections

The precipitation algorithm produces the following: (1) flags indicating possible precipitation-induced perturbations impacting AMSU-A Channels 4, 5, 6, 7, and 8, (2) estimates of corrections that may, at the user's option, be applied to AMSU-A brightness temperatures for channels 4, 5, 6, 7, and 8, to compensate for precipitation, if present, and (3) a precipitation-rate retrieval (mm/h) for each ~50-km AMSU-A and ~15-km AMSU-B spot which was tuned for mid-latitudes using all-season NEXRAD data. Inputs to the algorithm are fields of AMSU-A data for channels 1-12 and 15, the data for all four HSB channels, and topographical data. Figures 5.1.4 and 5.1.5 are block diagrams of the algorithm.

5.1.2.1 Precipitation Flags

The objective of the flags for each of AMSU-A channels 4-8 is to alert users of this data to the possibility that retrievals based on these microwave channels might be impacted by precipitation. The four possible flag states are:

0 The magnitude of the detected precipitation perturbations (if any) are less than 0.5 K

1 Small perturbations are present (nominally between 0.5 and 2 K), which are approximately correctable

2 Estimated AMSU-A precipitation-induced brightness temperature perturbations for this channel may exceed 2 K in magnitude, so perturbation corrections are less reliable

-1 It is unknown whether perturbations due to precipitation are present (e.g., surface elevation >2 km)

These perturbations are discussed further in section 5.1.2.4.

5.1.2.2 Perturbation Corrections

Perturbation corrections are estimated for AMSU Channels 4, 5, 6, 7, and 8. In addition, for each AMSU-A beam position a precipitation-rate estimate (mm/h) is provided when flag states 0, 1, or 2 exist for AMSU channel 4 (52.8 GHz). Users of AMSU data for temperature profile retrievals should use brightness temperatures flagged with 2 or -1 with caution, even if the suggested perturbation corrections are employed. These perturbations are computed for AMSU-A channels 4-8 at ~50-km resolution using the algorithm diagrammed in Figure 5.1.4 and discussed in Section 5.1.2.4. It should be noted that 52.8-GHz brightness temperatures can suffer warm perturbations over ocean due to low altitude absorption and emission by clouds or precipitation. Such warm perturbations could be flagged and corrected as are the cold perturbations. The 23.8/31.4 GHz combination could be used to validate the locations of such excess absorption and perturbations over ocean.

5.1.2.3 General Description of the Rain Rate Retrieval Algorithm

Accurate remote sensing of precipitation rate is challenging because the radiometric signatures of irregularly formed hydrometeors can depend strongly on their distributions in size, temperature, ice content and structure. As a result, all active and passive microwave remote sensing methods rely on the statistical regularity of precipitation characteristics. Experimental validation typically involves comparisons with rain gauges, radar, and other sensors, each of which has its own limitations. Ultimately, precipitation retrieval methods are best validated by comparing several independent sensing techniques such as those to be tested with the Aqua mission and its co-orbiting satellites. For example, CLOUDSAT will carry a 94-GHz precipitation imaging radar (G.L. Stephens et

al, *Bull. Amer. Meteor. Soc.*, vol. 83, no. 12, pp. 1771-1790, 2002). Relevant instruments on Aqua include the Advanced Microwave Scanning Radiometer-EOS (AMSR-E), the Moderate Resolution Imaging Spectrometer (MODIS), and AIRS itself.

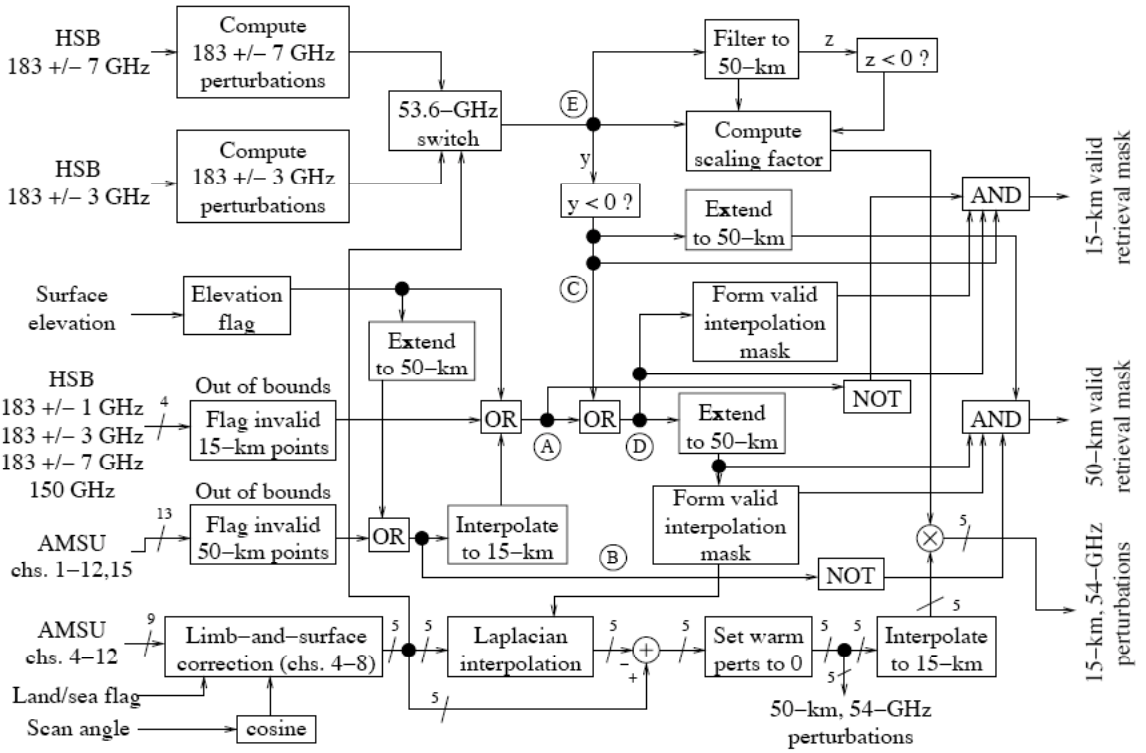

Figure 5.1.4. Precipitation-Rate Retrieval Algorithm, First Stage

The primary precipitation-rate retrieval products of AMSU/HSB are ~15- and ~50-km resolution contiguous retrievals over the viewing positions of AMSU within 43º of nadir. The two outermost 50-km viewing positions (six outermost for 15-km) on each side of the swath are currently omitted due to their grazing angles. The algorithm architectures for these two retrieval methods are presented below.

5.1.2.4 Elaboration of 15- and 50-km Retrieval Algorithms

The 15-km resolution precipitation-rate retrieval algorithm, summarized in Figures 5.1.4 and 5.1.5, begins with identification of potentially precipitating pixels. All 15-km pixels with brightness temperatures at 183 ± 7 GHz that are below a threshold T_7 are flagged as potentially precipitating, where

$$T_7 = 0.667\ (T_{53.6} - 248) + 252 + 6 \cos \theta \qquad (5.1.16)$$

and where θ is the satellite zenith angle. If, however, the spatially filtered brightness temperature $T_{53.6}$ at 53.6 GHz is below 249 K, then the brightness temperature at 183 ± 3 GHz is compared instead to a different threshold T_3, where:

$$T_3 = 242.5 + 5 \cos \theta \qquad (5.1.17)$$

This spatial filter picks the warmest spot within a 7×7 array of AMSU-B pixels. The 183±3-GHz band is used to flag potential precipitation when the 183±7-GHz flag could be erroneously set by low surface emissivity in very cold dry atmospheres, as indicated by $T_{53.6}$. These thresholds T_7 and T_3 are slightly colder than a saturated atmosphere would be, therefore lower brightness temperatures imply the presence of a microwave-absorbing cloud. If the locally filtered $T_{53.6}$ is less than 242 K, then the pixel is assumed not to be precipitating.

Within these flagged regions strong precipitation is generally characterized by cold cloud-induced perturbations of the AMSU-A tropospheric temperature sounding channels in the range 52.5-55.6 GHz. Examples of 183±7-GHz data and the corresponding cold perturbations at 52.8 GHz are illustrated in Figures 5.1.6(a) and (c), respectively. These 50-km resolution 52.8-GHz perturbations $\Delta T_{50,\ 52.8}$ are then used to infer the perturbations $\Delta T_{15,\ 52.8}$ (see Figure 5.1.6(d)) that might have been observed at 52.8 GHz with 15-km resolution had those perturbations been distributed spatially in the same way as the cold perturbations observed at either 183 ± 7 GHz or 183 ± 3 GHz, the choice between these two channels being the same as described above. This requires the bi-linearly interpolated 50-km AMSU data to be resampled at the HSB beam positions. These inferred 15-km perturbations are computed for five AMSU-A channels using:

$$\Delta T_{15,54} = (\Delta T_{15,183} / \Delta T_{50,183})\ \Delta T_{50,54} \qquad (5.1.18)$$

The perturbation $\Delta T_{15,183}$ near 183 GHz is defined to be the difference between the observed brightness temperature and the appropriate threshold given by (5.1.16) or (5.1.17). The perturbation $\Delta T_{50,54}$ near 54 GHz is defined to be the difference between

the limb-and-surface-corrected brightness temperature and its Laplacian-interpolated brightness temperature based on those pixels surrounding the flagged region (Staelin and Chen, *IEEE Trans. Geosci. Remote Sensing*, vol. 38, pp. 2232-2332, Sept. 2000). Limb and surface-emissivity corrections to nadir for the five 54-GHz channels are produced by neural networks for each channel; they operate on nine AMSU-A channels above 52 GHz, the cosine of the viewing angle ϕ from nadir, and a land-sea flag (see Figure 5.1.4). They were trained on 7 orbits spaced over one year for latitudes up to $\pm 55^{o}$. Inferred 50- and 15-km precipitation-induced perturbations at 52.8-GHz are shown in Figures 5.1.6 (c) and (d), respectively, for a frontal system. Such estimates of 15-km perturbations near 54 GHz help characterize heavily precipitating small cells.

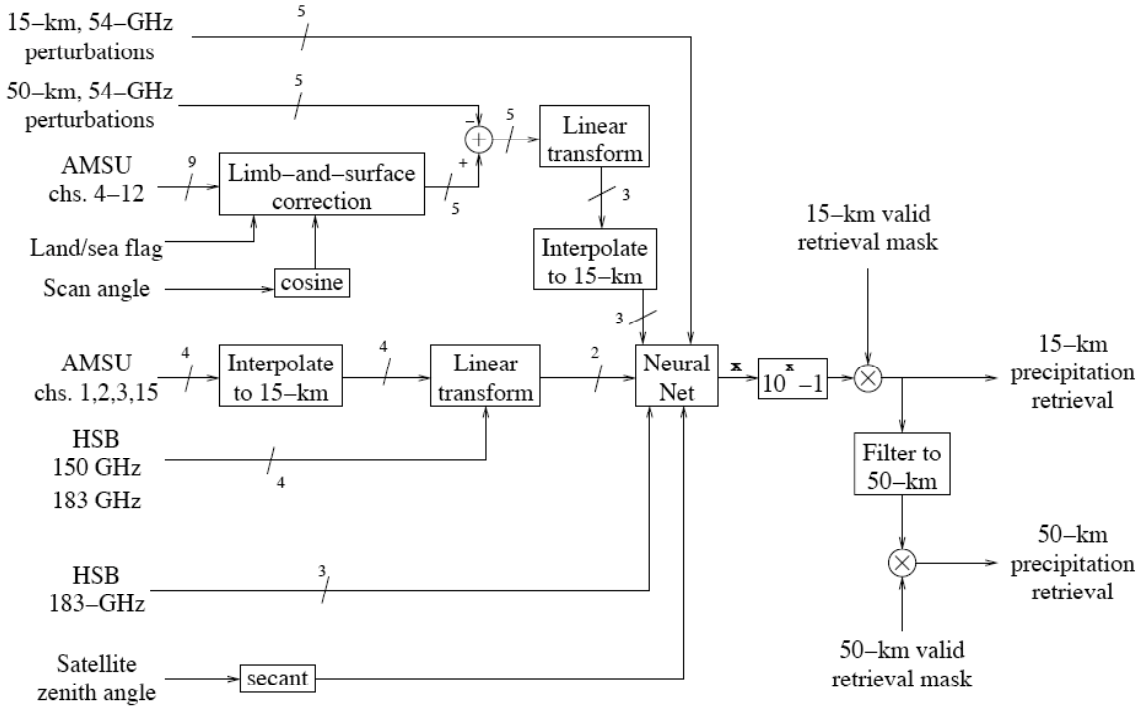

Figure 5.1.5. Precipitation-Rate Retrieval Algorithm, Final Stage

Such inferred 15-km resolution perturbations at 52.8, 53.6, 54.4, 54.9, and 55.5 GHz are then combined with 1) the 183±1-, ±3-, and ±7-GHz 15-km HSB data, 2) the leading three principal components characterizing the original five corrected 50-km AMSU-A temperature brightness temperatures, and 3) two surface-insensitive principal components that characterize the window channels at 23.8, 31.4, 50.3, and 89 GHz, plus the four HSB channels. All 13 of these variables, plus the secant of the satellite zenith angle θ, are

input to the neural net used for 15-km precipitation rate retrievals, as shown in Figure 5.1.5.

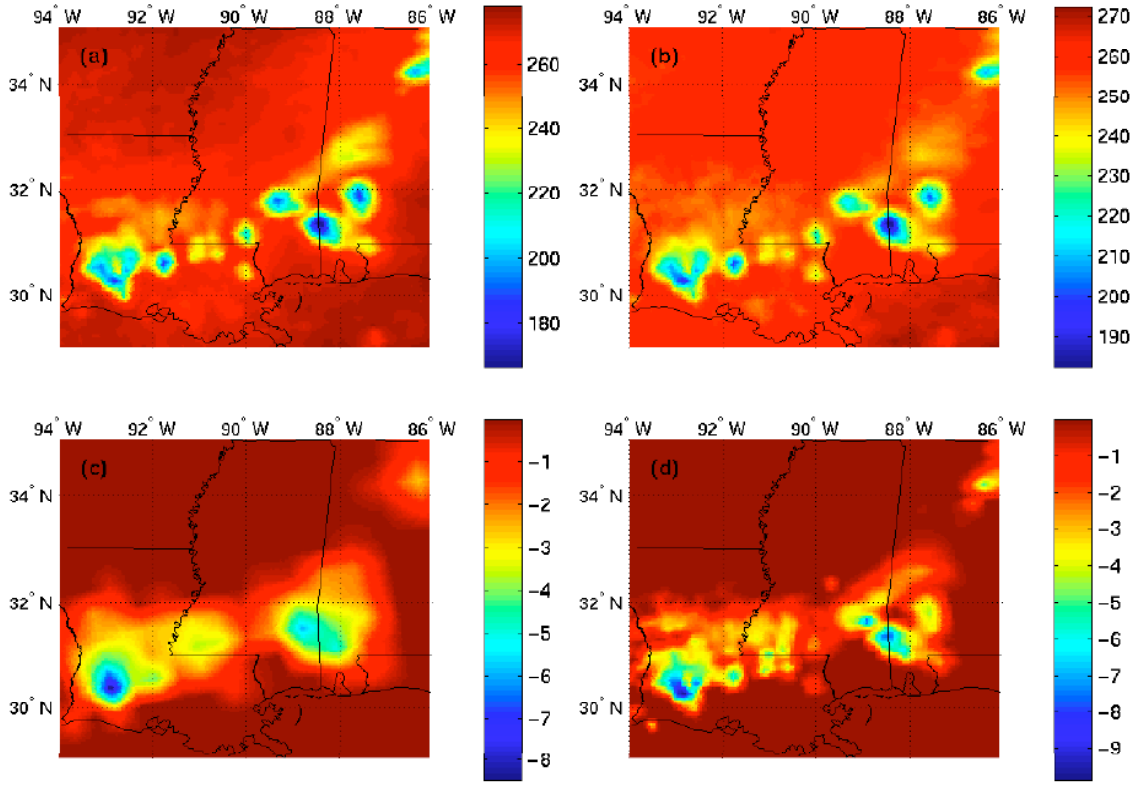

Figure 5.1.6. Frontal System September 13, 2000, 0130 UTC; (a) brightness temperature near 183±7 GHZ, (b) brightness temperatures near 183±3 GHz, (c) brightness temperature perturbations near 52.8 GHz, (d) inferred 15-km resolution brightness temperature perturbations near 52.8 GHz

This network was trained to minimize the rms value of the difference between the logarithms of the (AMSU+1 mm/h) and (NEXRAD+1 mm/h) retrievals; use of logarithms prevented undue emphasis on the heaviest rain rates, which were roughly three orders of magnitude greater than the lightest rates. Adding 1 mm/h prevented undue emphasis on the lightest rates. NEXRAD precipitation retrievals with 2-km resolution were smoothed to approximate Gaussian spatial averages that were centered on and approximated the view-angle distorted 15- or 50-km antenna beam patterns. The accuracy of NEXRAD precipitation observations are known to vary with distance, so only points beyond 30 km but within 110 km of each NEXRAD radar site were included in the data used to train and test the neural nets. Eighty different networks were trained

using the Levenberg-Marquardt algorithm, each with different numbers of nodes and water vapor principal components. A network with nearly the best performance over the testing data set was chosen; it used two surface-blind water vapor principal components, and only slightly better performance was achieved with five water vapor principal components with increased surface sensitivity. The final network had one hidden layer with 5 nodes that used the tanh sigmoid function. These neural networks are similar to those described by Staelin and Chen (IEEE TGARS, vol. 38, no. 5, pp. 2232-2332, 2000). The resulting 15-km resolution precipitation retrievals are then smoothed to yield 50-km retrievals.

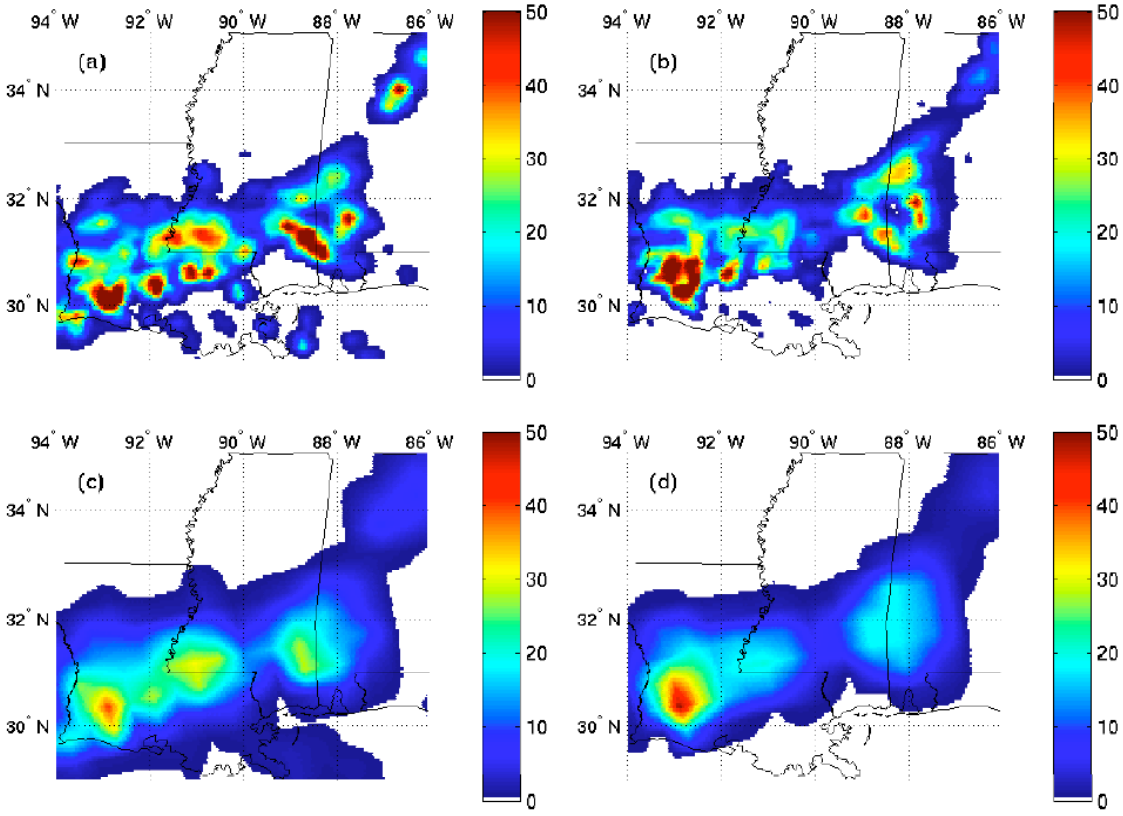

Figure 5.1.7. Precipitation Rates (mm/h) Observe September 13, 2000, 0130 UTC: (a) 15-km resolution NEXRAD retrieval, (b) 15-km resolution AMSU retrieval, (c) 50-km resolution NEXRAD retrieval, (d) 50-km resolution AMSU retrieval

The 15-km retrieval neural network was trained using precipitation data from the 38 orbits listed in Table 5.1.2. Each 15-km pixel flagged as potentially precipitating using 183 ± 7 GHz or 183 ± 3 GHz brightness temperatures (see Equations 5.1.16 and 5.1.17)

was used either for training, validation, or testing of the neural network. For these 38 orbits over the United States, 15,160 15-km pixels were flagged and considered suitable for training, validation, and testing; half were used for training, and one-quarter were used for each of validation and testing, where the validation pixels were used to determine when the training of the neural network should cease. Based on the final AMSU and NEXRAD 15-km retrievals, approximately 14 and 38 percent, respectively, of the flagged 15-km pixels appear to have been precipitating less than 0.1 mm/h for the test set.

Table 5.1.2. List of Rainy Orbits used for Training, Validation, and Testing

16 Oct 1999, 0030 UTC	30 Apr 2000, 1430 UTC
31 Oct 1999, 0130 UTC	14 May 2000, 0030 UTC
2 Nov 1999, 0045 UTC	19 May 2000, 0015 UTC
4 Dec 1999, 1445 UTC	19 May 2000, 0145 UTC
12 Dec 1999, 0100 UTC	20 May 2000, 0130 UTC
28 Jan 2000, 0200 UTC	25 May 2000, 0115 UTC
31 Jan 2000, 0045 UTC	10 Jun 2000, 0200 UTC
14 Feb 2000, 0045 UTC	16 Jun 2000, 0130 UTC
27 Feb 2000, 0045 UTC	30 Jun 2000, 0115 UTC
11 Mar 2000, 0100 UTC	4 Jul 2000, 0115 UTC
17 Mar 2000, 0015 UTC	15 Jul 2000, 0030 UTC
17 Mar 2000, 0200 UTC	1 Aug 2000, 0045 UTC
19 Mar 2000, 0115 UTC	8 Aug 2000, 0145 UTC
2 Apr 2000, 0100 UTC	18 Aug 2000, 0115 UTC
4 Apr 2000, 0015 UTC	23 Aug 2000, 1315 UTC
8 Apr 2000, 0030 UTC	23 Sep 2000, 1315 UTC
12 Apr 2000, 0045 UTC	5 Oct 2000, 0130 UTC
12 Apr 2000, 0215 UTC	6 Oct 2000, 0100 UTC

5.1.2.5 Preliminary Validation of Retrieval Accuracy

This section presents three forms of validation for this initial precipitation-rate retrieval algorithm: 1) representative quantitative comparisons of AMSU and NEXRAD precipitation rate images, 2) quantitative comparisons of AMSU and NEXRAD retrievals stratified by NEXRAD rain rate, and 3) representative precipitation images at more extreme latitudes beyond the NEXRAD training zone. For the results reported in this section, the threshold below which the retrieval algorithm used the 183±3-GHz channel to flag potentially precipitating pixels was 248 K instead of 249 K as reported in the first paragraph of 5.1.2.4. The threshold was changed from 248 K to 249 K in order to reduce the probability of false precipitation around high-altitude regions.

Figures 5.1.7(a) and (b) presents 15-km resolution precipitation retrieval images for 13 September 2000 obtained from NEXRAD and AMSU, respectively. On this occasion both sensors yield rain rates over 50 mm/h at similar locations, and lower rain rates down to 1 mm/h over similar areas. The revealed morphology is very similar, despite the fact that AMSU is observing approximately 6 minutes before NEXRAD, and they are sensing altitudes that may be separated by several kilometers; rain falling at a nominal rate of 10 m/s takes 10 minutes to fall 6 kilometers. Similar agreement is obtained at 50-km resolution, as suggested in Figures 5.1.7(c) and (d).

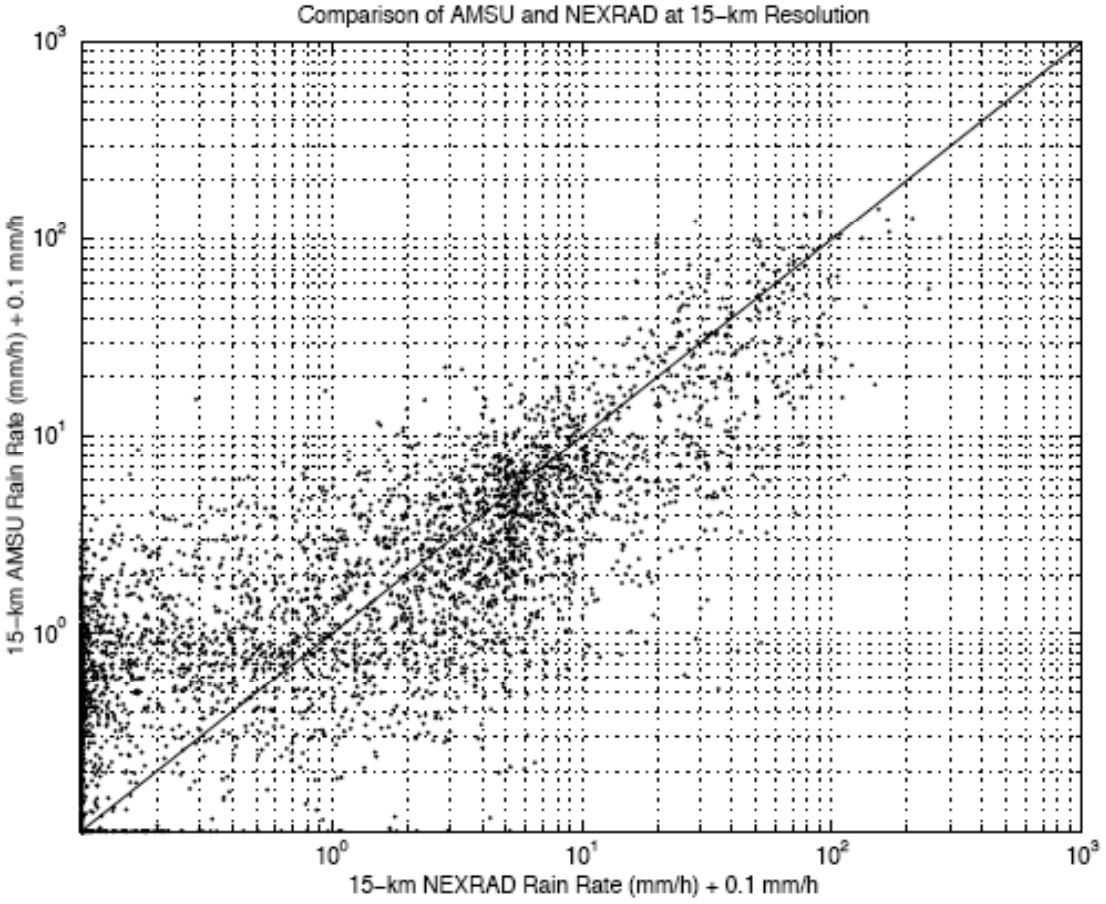

Figure 5.1.8. Comparison of H, for AMSU and NEXRAD Estimates of Rain Rate at 15-km Resolution

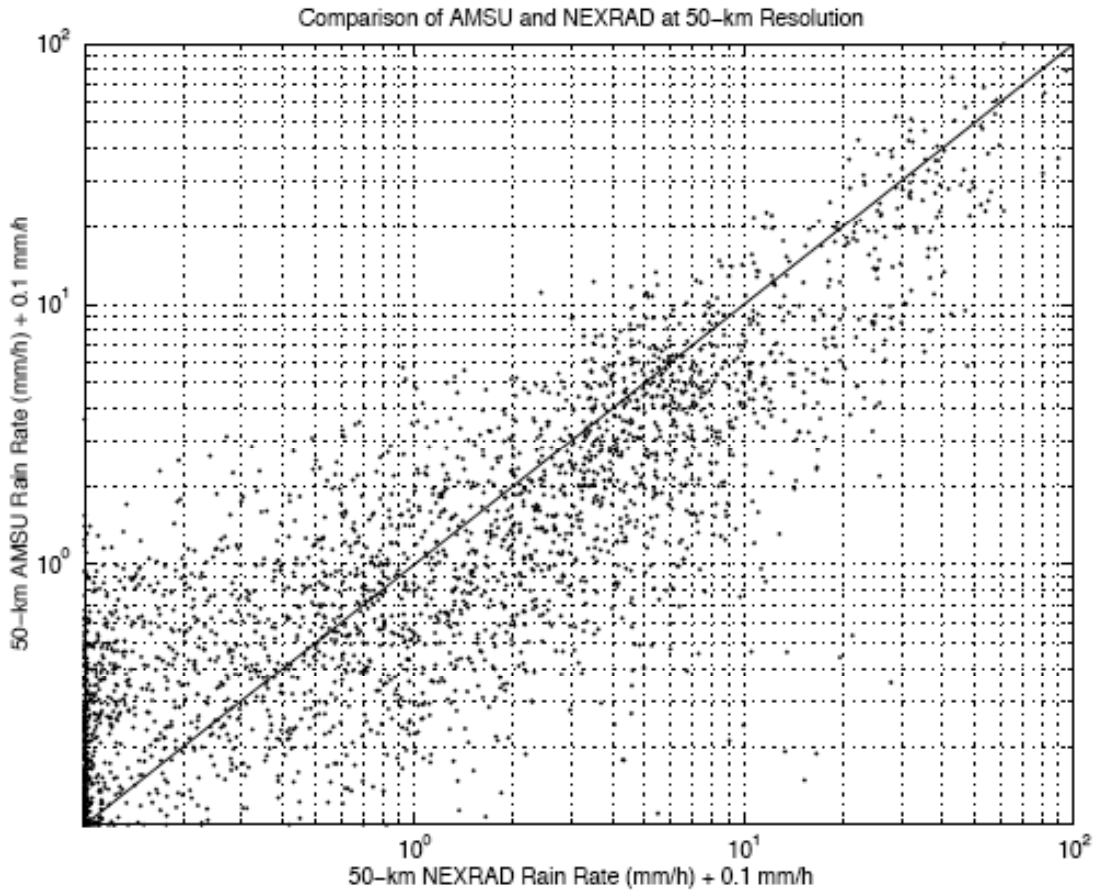

Figure 5.1.9. Comparison of AMSU and NEXRAD Estimates of Rain Rate at 50-km Resolution

Figure 5.1.8 shows the scatter between the 15-km AMSU and NEXRAD rain-rate retrievals for the test pixels not used for training or validation. Figure 5.1.6 shows the scatter between the 50-km AMSU and NEXRAD rain-rate retrievals over all points flagged as precipitating. First, we note that the maximum rain rates retrieved by AMSU and NEXRAD over all points where retrievals are possible at 15-km resolution were 159 and 270 mm/h, respectively, and that these maxima were 100 and 95 mm/h for 50-km resolution. These rates can be compared to the rain rate distributions found in GATE where more than 99 percent of all rain fell at rates less than 100 mm/h (Bell and Sushani, *J. Applied Meteorology*, vol. 33, pp.1067-1078, Sept. 1994).

Next, it is interesting to see to what degree each sensor retrieves rain when the other does not, and how much rain each sensor misses. For example, of the 73 NEXRAD 15-km

rain rate retrievals in Figure 5.1.5 above 54 mm/h, none were found by AMSU to be below 3 mm/h, and of the 61 AMSU 15-km retrievals above 45 mm/h, none were found by NEXRAD to be below 16 mm/h. Also, of the 69 NEXRAD 50-km rain rate retrievals in Figure 5.1.6 above 30 mm/h, none were found by AMSU to be below 5 mm/h, and of the 102 AMSU 50-km retrievals above 16 mm/h, none were found by NEXRAD to be below 10 mm/h.

The relative sensitivity of AMSU and NEXRAD to light and heavy rain can be seen from Figure 5.1.9. In general, the figure suggests that AMSU is relatively less sensitive to high rain rates. The risk of overestimating rain rate also appears to be limited. Only 3.3 percent of the total AMSU-derived rainfall was in areas where AMSU saw more than 1 mm/h and NEXRAD saw less than 1 mm/h. Only 7.6 percent of the total NEXRAD-derived rainfall was in areas where NEXRAD saw more than 1 mm/h and AMSU saw less than 1 mm/h. These percentages can be compared to the total percentages of AMSU and NEXRAD rain that fell at rates above 1 mm/h, which are 94 and 97, respectively.

Perhaps the most significant AMSU precipitation performance metric is the rms difference between the NEXRAD and AMSU rain rate retrievals for those 15-km pixels not used for training or validation; these are grouped by retrieved NEXRAD rain rates in octaves. The central 26 AMSU-A scan angles and the central 78 AMSU-B scan angles were included in these evaluations; only the outermost angles on each side were omitted. The results are listed in Table 5.1.3 for both 15- and 50-km retrievals. The smoothing of the 15-km NEXRAD and AMSU results to nominal 50-km resolution was consistent with an AMSU-A Gaussian beamwidth of 3.3 degrees.

The rms agreement between these two very different precipitation-rate sensors appears surprisingly good, particularly since a single AMSU neural network is used over all seasons and latitudes. The 3-GHz radar retrievals respond most strongly to the largest hydrometeors, especially those below the bright band near the freezing level, while AMSU interacts with the general population of hydrometeors in the top few kilometers of the precipitation cell, which may lie several kilometers above the freezing level. Much of the agreement between AMSU and NEXRAD rain-rate retrievals must therefore result

from the statistical consistency of the relations between rain rate and its various electromagnetic signatures. It is difficult to say how much of the observed discrepancy is due to each sensor, or to say how well each correlates with precipitation reaching the ground.

This study furthermore provided an opportunity for evaluation of radar data. The rms discrepancies between AMSU and NEXRAD retrievals were separately calculated over all points at ranges from 110 to 230 km from any radar. For NEXRAD precipitation rates below 16 mm/h, these rms discrepancies were approximately 40 percent greater than those computed for test points at 30-110 km range. At rain rates greater than 16 mm/h, the accuracies beyond 110 km were more comparable. Most points in the eastern U.S. are more than 110 km from any NEXRAD radar site.

Table 5.1.3. RMS AMSU/NEXRAD Discrepancies (mm/h)

NEXRAD range	15-km resolution	50-km resolution
<0.5 mm/h	1.0	0.5
0.5-1 mm/h	2.0	0.9
1-2 mm/h	2.3	1.1
2-4 mm/h	2.7	1.8
4-8 mm/h	3.5	3.2
8-16 mm/h	6.9	6.6
16-32 mm/h	19.0	12.9
>32 mm/h	42.9	22.1

5.1.2.6 Global Retrievals of Rain and Snow

Figure 5.1.10 illustrates precipitation-rate retrievals at points around the globe where radar confirmation data is scarce. In each case the results are plausible and meteorologically revealing. Figure 5.1.10(a) shows precipitation retrievals in the tropics over a mix of land and sea, while Figure 5.1.10(b) shows a more intense tropical event. Figure 5.1.10(c) illustrates strong precipitation near 72-74° N, again over both land and sea. Finally, Figure 5.1.10(d) illustrates the March 5, 2001, New England snowstorm that deposited roughly a foot of snow within a few hours. This accumulation is somewhat greater than is indicated by the rain rates of ~1.2 mm/h that were inferred by the same algorithm. This applicability of the algorithm to snowfall rate should be expected

because the observed radio emission originates exclusively at high altitudes. Whether the hydrometeors are rain or snow upon impact depends only on air temperatures near the surface, far below those altitudes being probed. One of the principal Aqua validation activities will involve testing and tuning of the precipitation retrievals for climates not adequately represented in the NEXRAD training data set. For example, polar stratiform precipitation is expected to exhibit relatively weaker radiometric signatures in winter when the temperature lapse rates are lower.

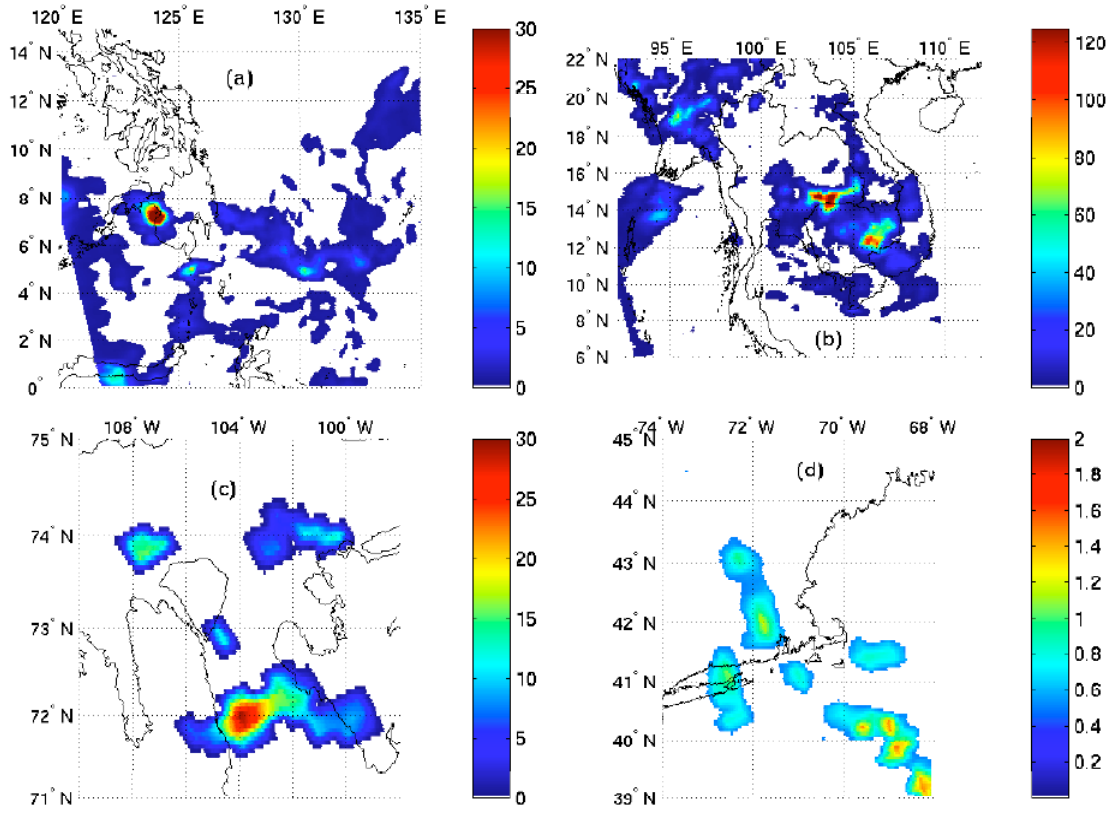

Figure 5.1.10. AMSU Precipitation Rate Retrievals (mm/h) with 15-km Resolution: (a) Philippines on 16 April 2000, (b) Indochina on 5 July 2000, (c) Canada on 2 August 2000, and (d) New England snowstorm on 5 March 2000

5.1.2.7 Conclusions

These evaluations of rain rate with 15- and 50-km nominal resolution suggest that AIRS/AMSU/HSB rain rate retrievals will usefully supplement other global precipitation data sets over both land and sea at rates up to 100 mm/h or more, and that an early scientific objective of the Aqua program should be to reconcile and inter-calibrate these

various approaches. They also suggest that most 15-km spots precipitating more than 1 mm/h should be readily identifiable. It also appears likely that further training and validation would be helpful for atmospheric conditions remote from those occurring in the eastern United States.

References

Chedin, A., N. A. Scott, C. Wahiche, and P. Moulinier, 1985: The improved initialisation inversion method: A high resolution physical method for temperature retrievals from the TIROS-N series. *J. Clim. Appl. Meteor.*, **24**, 128-143.

Ellison, W. J., S. J. English , K. Lamkaouchi, A. Balana, E. Obligis, G. Deblonde, T. J. Hewison, P. Bauer, G. Kelly and L. Eymard, 2003: "A comparison of ocean emissivity models using the Advanced Microwave Sounding Unit, the Special Sensor Microwave Imager, the TRMM Microwave Imager, and airborne radiometer observations," *J. Geophys. Res.*, **108**(D21), 4663, doi:10.1029/2002JD003213.

Eyre, J. R., 1989: Inversion of cloudy satellite sounding radiances by nonlinear optimal estimation. I: Theory and simulation for TOVS. *Q. J. R. Meteorol. Soc.* , **115**, 1001-1026.

Grody, N., F. Weng, and R. Ferraro, 2000: "Application of AMSU for obtaining hydrological parameters." In *Microwave Radiometry and Remore Sensing of the Earth's Surface and Atmosphere*, (P. Pampaloni and S. Paloscia, eds.) VSP (ISBN 90-6764-318-1), pp. 339-352.

Kistler, R., E. Kalnay, W. Collins, S. Saha, G. White, J. Woollen, M. Chelliah, W. Ebisuzaki, M. Kanamitsu, V. Kousky, H. van den Dool, R. Jenne, and M. Fiorino, 2001: "The NCEP-NCAR 50-Year Reanalysis: Monthly Means CD-ROM and Documentation," *Bull. Am. Meteor. Soc.* **82**, 247-267.

Kuo, C. C., D. H. Staelin and P. W. Rosenkranz, 1994: "Statistical Iterative Scheme for Estimating Atmospheric Relative Humidity Profiles," *IEEE Trans. Geosci. and Remote Sensing ,* **32**, 254-260.

Liebe, H. J., 1981: "Modeling attenuation and phase of radio waves in air at frequencies below 1000 GHz," *Radio Sci.*, **16**, 1183-1199.

Rodgers, C. D., 1976: Retrieval of atmospheric temperature and composition from remote measurements of thermal radiation. *Rev. Geophys. and Space Phys.*, **14**, 609-624.

Rosenkranz, P. W., 2006: "Cloud liquid-water profile retrieval algorithm and validation," *J. Geophys. Res.*, **111**, D09S08, doi:10.1029/2005JD005832.

Schaerer, G. and T. T. Wilheit, 1979: A passive microwave technique for profiling of atmospheric water vapor. *Radio Science*, **14**, 371-375.

Wilheit, T. T., 1990: An algorithm for retrieving water vapor profiles in clear and cloudy atmospheres from 183 GHz radiometric measurements: Simulation studies. *J. App. Meteor.,* **29**, 508-515.

Wilheit, T. T., and K. D. Hutchinson, 1997: Water vapour profile retrievals from the SSM/T-2 data constrained by infrared-based cloud parameters. *Int. J. Remote Sensing*, **18**, 3263-3277.

5.2 Cloud Clearing

5.2.1 Overview

Cloud clearing refers to the process of determination of the clear-column radiances for AIRS channel i, $\hat{R}_i$, which represent what channel i "would have observed" if the entire scene were cloud free. In the context of AIRS Version 4.0, the entire scene is the AMSU A Field of Regard (FOR), in which observations in a 3 x 3 array of AIRS Fields of View (FOV's) are present. Observations in the 3 x 3 array of AIRS FOV's are taken at 3 different zenith angles. The cloud-clearing methodology attributes differences in these radiances to differing cloud conditions within the FOR. Therefore, a process referred to as local angle adjustment is applied to these observed radiances, channel by channel, to generate angle adjusted radiances $R_{i,k}$, representative of the radiances AIRS channel i would have observed in FOV k if the observation were taken at the satellite zenith angle of the center FOV within the FOR, rather than at its actual satellite zenith angle. Details of the methodology to perform this adjustment are given in Section 5.2.2.

The basic inputs to the cloud-clearing process are $R_{i,k}$ and an (nth) estimate of the surface and atmospheric state. Auxiliary fields needed are the AIRS channel-tuning coefficients, channel noise file, and RTA coefficients. These are used together to generate the nth estimate of cloud-clearing coefficients $\eta_k^{(n)}$ which can be used to determine $\hat{R}_i^{(n)}$. Radiances in some channels are not sensitive to clouds in the Field of View, and for these channels, it is better to average the observations $R_{i,k}$ over the 9 fields of view to obtain $\hat{R}_i^{(n)}$. Other important parameters obtained in the cloud-clearing process are the channel-noise amplification factor, $A^{(n)}$, the effective channel-noise amplification factor, $A_{eff}^{(n)}$, and the clear-column-radiance noise covariance matrix, $\hat{M}_{ij}^{(n)}$.

Figure 5.2.1 gives a flow diagram showing the basic steps involved in the cloud-clearing process. Details are given in Section 5.2.4.

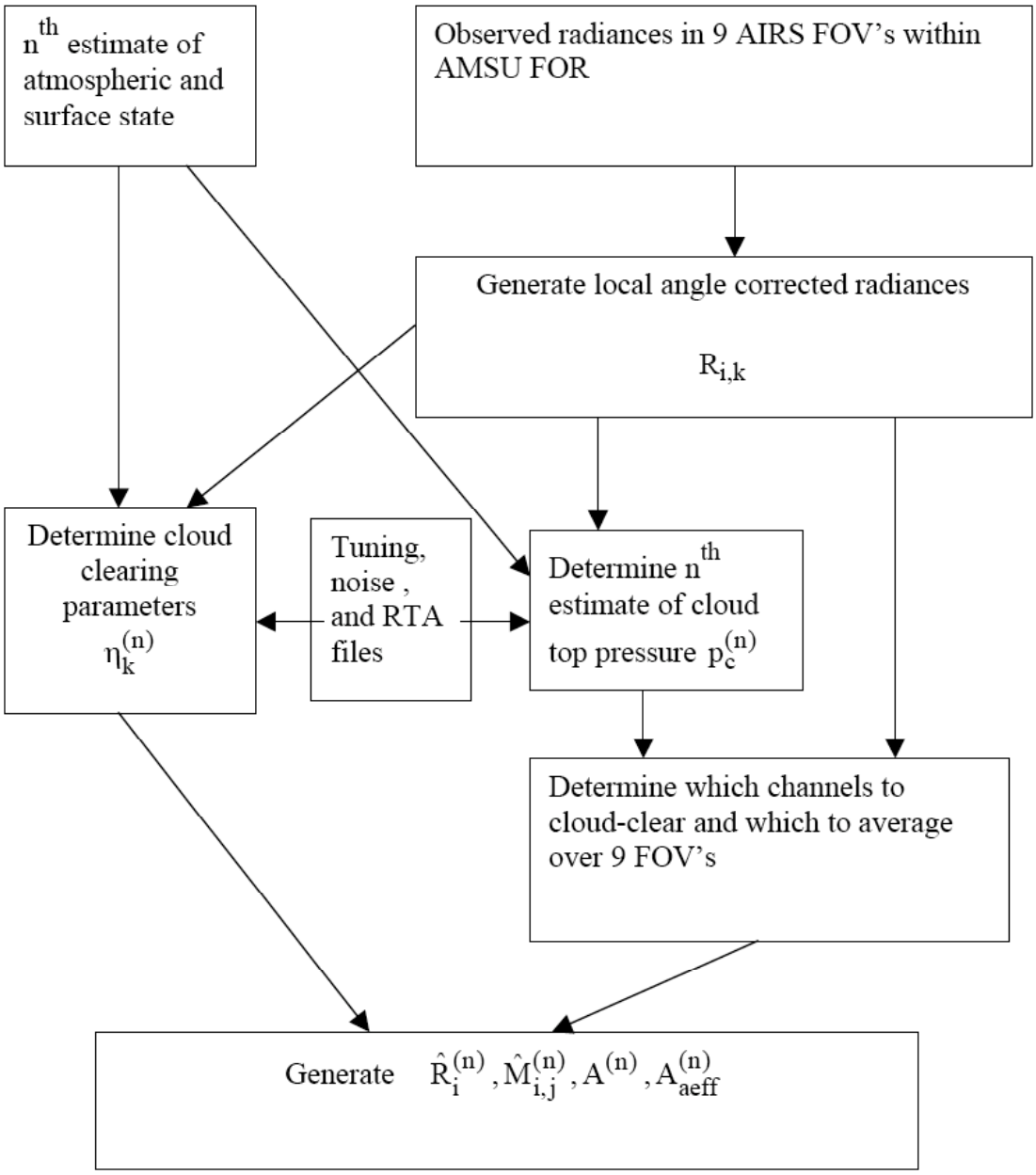

Figure 5.2.1. Cloud Clearing Overview

5.2.2 Local Angle Adjustment of AIRS Observations

The cloud-clearing algorithm assumes that the observed AIRS radiances in footprints falling within the composite AMSU-A retrieval footprint differ only because of different cloud characteristics within the footprints. Other parameters, such as the viewing angle, are assumed constant over the 3 x 3 array of AIRS footprints being used. This means the

radiances in the 9 AIRS footprints at 3 different zenith angles (φ) must be adjusted to what they would have been if they observed otherwise the same scene but at a common central zenith angle (φ_{cen}) before cloud clearing is attempted. The procedure used to achieve this adjustment is described below.

The coefficients of the correction are based on synthetic regression, a process in which regression coefficients are generated using radiances that are simulated for a range of cloud conditions and profiles that cover the expected atmospheric range. AIRS radiances are calculated for each of the 90 AIRS viewing angles and AMSU-A radiances are calculated for the AMSU-A footprint viewing angle. Noise is added, but care must be taken that it be treated properly. The radiances being calculated are an attempt to simulate the measurements that would have been observed if the viewing angles were different. Thus all other factors, including the noise, do not change with angle. What this means for the simulation is that the added noise is random over the set of profiles and for each channel, but is constant over the viewing angle. In other words, once the noise is determined for a channel and a profile, that same noise is used for all 90 AIRS viewing angles. It must only be constant over the 3 viewing angles that cover each AMSU-A footprint, but it is easier to keep it constant over all 90 spots.

Let prof be the profile index, fp be the footprint number, νbe channel frequency and

be the zenith angle, respectively; the noisy radiance for a given profile, footprint,

channel and local zenith angle is:

$$R(prof, fp, \nu, \varphi) = R_o(prof, fp, \nu, \varphi) + \varepsilon(prof, fp, \nu) \qquad (5.2.1)$$

where $R(prof, fp, \nu, \varphi)$ is the noise free radiance, and $\varepsilon(prof, fp, \nu)$ is the noise for the particular profile, spot, and channel. The consequence of not treating the noise properly is to cause large errors in the predictants used to generate the coefficients, with a corresponding adverse effect on the resulting coefficients. Many angle adjustment procedures currently in use do not properly handle the instrumental noise.

In the following discussion, the term "weighting function" is used to denote the contribution function that describes the region of the atmosphere being viewed by a

particular channel. The observed radiance for a particular channel changes with angle in two ways. One is that the weighting function peaks in a higher region of the atmosphere when the angle moves away from nadir. The other is that the weighting function becomes slightly narrower. This occurs because, to a first approximation, the majority contribution to the observed radiance for a particular channel arises within a confined slab of the atmosphere. When viewed at an angle, the slab is thinner in atmospheric height. For the small angles under consideration, the second effect is small. If the weighting function peak for a channel is raised slightly in the atmosphere, there is a linear combination of the given channel with nearby channels that, for a given profile, provides the same radiance at the observed angle as the given channel would have provided if observed at nadir. The correction procedure employed here seeks to find and use that linear combination.

For a given channel, regression coefficients are generated that give the change in radiance as a linear function of observed radiances. Radiances are used rather than brightness temperatures to avoid Planck equation calculations. The exponentiation within the Planck equation is computationally intensive. Furthermore, an error can result if a low temperature coupled with noise causes the calculated value to go negative. For daytime conditions, the predictors are principal component scores of the eigenvectors of the radiances plus the difference of cosines of the solar zenith angles between the AIRS and AMSU-A observations. For nighttime conditions the predictors are the principal component scores of the eigenvectors of the radiances. The additional term for daytime conditions is proportional to the change in solar energy falling on a horizontal surface due to the change in viewing angle. This term is important for the shortwave channels.

In applying the angle correction, the first step is to normalize the observed radiances by dividing by the instrumental noise for the given channel. The next step is to generate the eigenvectors of the predictors. In practice, the regression uses the 45 principal component scores for the 45 eigenvectors with the highest eigenvalues as predictors. Use of the eigenvectors prevents the solution from becoming singular. For daytime, the matrix of predictors is given by:

$$X_{day} = \left[\frac{R_o(prof, fp, \nu, \varphi)}{\varepsilon(\nu)} + (\cos(\phi) - \cos(\phi_{cen})) \right] x\, E \tag{5.2.2}$$

for nighttime, the matrix of predictors is given by:

$$X_{night} = \left[\frac{R_o(prof, fp, \nu, \varphi)}{\varepsilon(\nu)} \right] x\, E \tag{5.2.3}$$

where **E** denotes the matrix of eigenvectors and εν)denotes the instrumental noise for the channel. Once the predictors are available, the regression is given by:

$$\bar{A}(\nu, \varphi) = \bar{C}_o(\nu, \varphi) + \bar{C}(\nu, \varphi)\bar{X}(\varphi) \tag{5.2.4}$$

where $\bar{C}(\nu, \varphi)$ denotes the vector of regression coefficients.

The vector of adjusted radiances may then be computed:

$$\bar{R}(\nu, \varphi)_{angle\_adjusted} = \bar{R}(\nu, \varphi)_{obs} + \bar{A}(\nu, \varphi) \tag{5.2.5}$$

where $\bar{R}(\nu, \varphi)_{obs}$ denotes the vector of original measured radiances.

Separate coefficients are generated for day and night. Although the daytime coefficients may be used to calculate the adjusted radiances at night, the errors that are generated are of the same magnitude as those produced during the day and thus larger than they would otherwise be. While the errors in the daytime corrections are small, nighttime corrections produced with nighttime coefficients are much more accurate. This is an important consideration because in daylight, the visible channels can be used to help cloud detection. At night, cloud detection has to rely on relationships between channels at different wavelengths. The increased accuracy for the short wavelength channels is an important factor in the ability to detect clouds.

5.2.3 Principles of Cloud Clearing

Infrared observations at most wavelengths are affected by clouds in the field-of-view. Three basic approaches used for accounting for effects of clouds in satellite remote sensing are: 1) identify clear areas and only perform retrievals in those areas, with no cloud correction needed; 2) use channel observations in adjacent potentially partially cloudy scenes to reconstruct what the channel radiances would have been if the scenes were clear, and use these reconstructed observations to determine geophysical parameters; and 3) determine both surface and atmospheric geophysical parameters, as well as cloud properties, from the radiance observations themselves. An example of the first approach is given by Cuomo, *et al.,* (1993). Eyre (1989a, 1990) has used the third approach in simulation by assuming an unknown homogeneous amount of black clouds at an unknown pressure, and attempted it with real TOVS data as well (Eyre, 1989b). Our approach, like that used in Susskind (1993), is of the second type and is an extension of that used by Smith (1968), Chahine (1974), and Chahine (1977). This approach utilizes satellite observed radiances, $R_{i,k}$, corresponding to channel i and field-of-view k, made over adjacent fields-of-view. In this approach, there is no need to model the radiative and reflective properties of the clouds. The only assumption made is that the fields-of-view are homogeneous except for the amount of cloud cover in K different cloud formations in each field-of-view. $\hat{R}_{i,}$ the radiance which would be observed if the entire field of view were clear, and $R_{i,clr,\ell}$, the radiance which would be observed if the entire field of view were covered by cloud formation ℓ, are therefore assumed to have the same respective values in each field-of-view. If the observed radiances in each field-of-view are different, the differences in the observed radiances are then attributed to the differences in $\alpha_{\ell k}$, the fractional cloudiness for cloud formation ℓ in field-of-view k. In the following discussion, $R_{i,k}$ represents the observed channel i radiance in FOV k <u>after</u> it has been adjusted to what it would have been if it were observed at the central zenith angle of the FOR, as shown in Section 5.2.2.

Using the assumption described above, Chahine (1977) showed that the reconstructed clear-column radiance for channel i, $\hat{R}_{i,}$ can be written as a linear combination of the measured radiances in K+1 fields-of-view, $R_{i,1} \cdot \cdot R_{i,K+1}$, according to

$$\hat{R}_i = R_{i,1} + \eta_1 \left[R_{i,1} - R_{i;K+1} \right] + \cdots \eta_k \left[R_{i,1} - R_{i,(K+2)-k} \right] + \cdots \eta_K \left[R_{i,1} - R_{i,2} \right] \qquad (5.2.6)$$

where $\eta_1 \cdots \eta_K$ are unknown channel independent constants, and K+1 fields-of-view (FOV's) are needed to solve for K cloud formations (with K lineaerly independent values of η).

Cloud formations should be distinguished from cloud types. For example, if three fields of view are considered, and two cloud types exist, with cloud top pressures at 300 mb and 700 mb, and the respective cloud fractions as seen from above are (10%, 20%), (20%, 40%), and (30%, 60%) in each field of view, then only a single cloud formation exists with cloud fractions of 30%, 60%, and 90% in each field of view respectively. If instead, the third field of view had cloud fractions of 30% and 65%, then 5% of a second cloud formation exists in the third field of view only. The above discussion applies only to cases in which the upper cloud type is opaque, and a portion of the scene, as observed from above, corresponds to cloud type 1, cloud type 2, or the surface. If the upper cloud type is semi-transparent, then a portion of the scene can correspond to cloud type 1 overlaying the surface, cloud type 1 overlaying cloud type 2, cloud type 2, and the surface. In such a case, three cloud formations will exist in general even if the relative amounts of each cloud type are as initially stated above.

In Chahine (1977), the fields-of-view are ordered such that FOV 1 is the clearest field-of-view based on observations in the 11 μm window (the field-of-view with the highest 11 μm radiances is assumed to be FOV 1) and FOV K+1 is the cloudiest. Thus η_1 multiplies the largest radiance differences and η_K the smallest. Once $\eta_1 \cdots \eta_K$ are determined, Equation (5.2.6) is used to produce the reconstructed clear column radiances for all channels used in the retrieval process. The reconstructed clear column radiances are then used when solving for the geophysical parameters. This approach has been successfully applied to fields-of-view, assuming one cloud formation, in the analysis of

HIRS2/MSU operational sounding data by several authors (McMillin and Dean, (1982), Susskind, *et al.,* (1984), Susskind and Reuter (1985a) and Chahine and Susskind (1989)) and is the method used by NOAA/NESDIS in production of their clear column radiances used in generation of operational HIRS2/MSU retrievals (McMillin and Dean, 1982). Chahine and Susskind (1989) show that retrieval accuracy using this approach, verified by co-located radiosondes, does not degrade appreciably with increasing cloud cover, for retrieved cloud fractions of up to 80%. Susskind and Reuter (1985b) have performed simulations with two cloud formations and three fields-of-view for the AMTS instrument, an earlier version of AIRS (Chahine, *et al.*, 1984), used in conjunction with MSU. Susskind, *et al.*, (2003) describe an improved cloud clearing methodology for use with AIRS/AMSU data and show, via simulation, that sounding accuracy does not degrade appreciably with increasing cloudiness up to 80% effective fractional cloud cover. The methodology we use to analyze AIRS/AMSU data is identical to that of Susskind, *et al.* ,(2003) and is described in detail in Section 5.2.4.

5.2.4 Cloud Clearing Methodology

As in Susskind et al. (2003), one sounding is generated for the 3x3 array of AIRS footprints (FOV's) within a given AMSU A footprint (FOR). The basic equation is analogous to Equation (5.2.6), but we have found it is advantageous (as suggested by L. McMillin) to extrapolate the radiances in the K fields of view according to a similar equation of the form

$$\hat{R}_i = R_{i,AVG} + \sum_{k=1}^{K} \eta_k (R_{i,AVG} - R_{i,k}) \qquad (5.2.7)$$

where $R_{i,AVG}$ is the average radiance of all K fields of view. Optimal values of η_k will give true values of $\hat{R}_i$ up to instrumental noise effects. Only K-1 linearly independent values of η are obtainable from Equation (5.2.7), to the extent that K-1 cloud formations exist within the FOR.

Susskind, *et al.*, (1998) used the 9 AIRS spots within an AMSU A footprint to construct 3 fields of view used to determine 2 values of η to be used in Equation 5.2.6. Field of view 1 was comprised of the average of the observations in the 3 warmest spots in an 8 μm window channel, and field of view 3 was the average of 3 coldest spots. We now use

all radiances in all spots separately and determine 9 values of η, up to 8 of which are linearly independent. Given η_k, clear column radiances for all channels can be obtained from Equation 5.2.7. As in Susskind, *et al.*, (1998), we determine the values η from observations in a selected set of I(= 44) cloud filtering channels which are primarily in between lines in the 15 μm CO_2 band with some additional channels in the long wave and short wave window regions. If, for each channel i, one substitutes an estimated value of the expected clear column radiance for channel i, $R_{i,CLR}$, for $\hat{R}_i$ in Equation 5.2.7, this gives I (44) equations for K (9) unknowns. The unconstrained weighted least square solution to this multilinear problem is given by

$$\eta_{Kx1} = \left[\Delta R' N^{-1} \Delta R \right]^{-1}_{KxK} \Delta R' N^{-1} \Delta R_{CLR} \qquad (5.2.8)$$

where ΔR is a IxK matrix with $\Delta R_{i,k} = R_{AVG} - R_{i,k}$, ΔR_{CLR} is an Ix1 matrix given by $\Delta R_{i,CLR} = R_{i,CLR} - R_{i,AVG}$, and N is an IxI channel noise covariance matrix.

The key to the accurate determination of η is obtaining the best values of $\Delta R_{i,CLR}$, along with an accurate treatment of the noise covariance matrix N. As in Susskind, *et al.*, (1998), we assume the noise in channel i used to determine η is dominated by errors in $\Delta R_{i,CLR}$. The values of $\Delta R_{i,CLR}$ which we use to determine η (and $\hat{R}_i$) are iterative and are computed based on the current best estimate of all relevant surface and atmospheric properties.

For optimal results, it is important for the estimates of geophysical parameters used to obtain $\Delta R_{i,CLR}$ to be unbiased over large regions of the atmosphere. For example, if the estimated temperature profile were uniformly too warm, values of $\Delta R_{i,CLR}$ computed from this profile would all be too high and incorrect values of η_k would be obtained which would reconstruct too high values of $\hat{R}_i$. To avoid this, we make sure that the profile used to estimate $\Delta R_{i,CLR}$ is consistent with observations in all AMSU A (and HSB) channels, thus insuring an unbiased temperature and moisture profile over coarse layers in the atmosphere. It would be a mistake to use a GCM generated analysis or a

forecast field directly to compute $R_{i,CLR}$ because this field, while potentially accurate, could be biased in the vertical.

The iterative methodology to determine clear column radiances consists of four passes to determine η^n (n = 1, 2, 3, 4), using four sets of conditions, described later, to compute $R^n_{i,CLR}$, in which $R^n_{i,CLR}$ and hence η^n, become increasingly more accurate for each iteration. Each set of conditions has its own N^n, reflecting expected errors in $R^n_{i,CLR} - R_{i,1}$. The diagonal term of the noise covariance matrix is modeled according to

$$N^n_{ii} = NE\Delta N_i^2 + \left[\frac{\partial R_i}{\partial T_s}\delta T_s^n\right]^2 + \left[\frac{\partial R_i}{\partial \varepsilon_{\nu_i}}\delta \varepsilon^n_{\nu_i}\right]^2$$
$$+ \left[\frac{\partial R_i}{\partial \rho_{\nu_i}}\delta \rho^n_{\nu_i}\right]^2 + \left[\frac{\partial R_i}{\partial T(p)}\ \delta T(p)^n\right]^2$$
$$+ \left[\frac{\partial R_i}{\frac{\partial q(p)}{q}}\frac{\delta q(p)^n}{q}\right]^2 + 0.1^2\left(\frac{dB}{dT}\right)^2_{\Theta_{i,CLR}} + \bar{N}_{ii}{}^2\left(\frac{dB}{dT}\right)^2_{\Theta_{i,CLR}} \qquad (5.2.9a)$$

where $NE\Delta N_i$ is the channel i instrumental noise and the next 5 terms are contributions to errors in the computed value $R_{i,CLR}$ resulting from errors in estimated surface skin temperature, surface spectral emissivity, surface spectral bi-directional reflectance of solar radiation, and temperature and moisture profile respectively. Two additional sources of radiance uncertainty are included in Equation 5.2.9a, representative of the physics error estimate, $\bar{N}_{ii}$ (see Section 5.4.11.3), and an additional radiance uncertainty term. Both terms ($\bar{N}_{ii}$ and 0.1) are in brightness temperature units. The off diagonal term of the noise covariance matrix is given by

$$N_{ij}^{n} = \frac{\partial R_i}{\partial T_s}\frac{\partial R_j}{\partial T_s}\left(\delta T_s^n\right)^2 + \frac{\partial R_i}{\partial \varepsilon_{\nu_i}}\frac{\partial R_j}{\partial \varepsilon_{\nu_j}}\left(\delta\varepsilon_{\nu_i}^n \delta\varepsilon_{\nu_j}^n\right) + \ldots. \qquad (5.2.9b)$$

The partial derivatives in Equations 5.2.9a and 5.2.9b are determined empirically by computing the radiance using the current estimate of each parameter and recomputing it after a small change in that parameter. In Susskind, *et al*., (1998), the uncertainties, such as δT_s^n, are specified so as to be indicative of the expected errors for that parameter in pass n. We now predict these errors on a profile-by-profile basis for each pass by propagation of expected sources of error through the retrieval process in a manner described in Section 5.4.9. A principal source of retrieval error arises from errors in the reconstructed clear column radiances.

5.2.4.1 Selection of Optimal Fields of View

The effects of instrumental noise on the clear column radiances will in general be amplified from single spot noise values because the clear column radiances are expressed as a linear combination of the observations in different fields of view. If there were no other sources of error, the diagonal term of the clear column radiance noise covariance matrix in a given pass, referring to the error in $\hat{R}_i$ obtained by Equation (5.2.7), would be

$$\left[\delta\hat{R}\cdot\delta\hat{R}'\right]_{ii} = NE\Delta N_i^2 \cdot A\left(\eta_k\right)^2 \qquad (5.2.10)$$

where $A\left(\eta_k\right)$ is the noise amplification factor, given by

$$A\left(\eta_k\right) = \left[\sum_{k=1}^{9}\left(\frac{1}{9}\cdot\left(1+\sum_{k'=1}^{9}\eta_{k'}\right)-\eta_k\right)^2\right]^{1/2}. \qquad (5.2.11)$$

$A\left(\eta_k\right)$ is approximately equal to $\left[\sum\eta_k{}^2\right]^{1/2}$ because the first term, containing the factor 1/9, is small. It is desirable to find an accurate expression for clear column

radiance which minimizes $A(\eta_k)$. We can minimize $A(\eta_k)$ by expressing Equation (5.2.7) in terms of radiances in an optimal set of fields of view, given by linear combinations of the original set. The optimal $A(\eta_k)$ can be found by transforming the original contrast terms ΔR_k to a new set, ΔR_k^T, according to

$$\Delta R_{i,k}^T \equiv \sum_{k'} U_{k,k'} \cdot \Delta R_{i,k'} \tag{5.2.12}$$

where U is the unitary transformation which diagonalizes $\Delta R' \cdot N^{-1} \cdot \Delta R$

$$\left[U' \cdot \left(\Delta R' \cdot N^{-1} \cdot \Delta R \right) \cdot U \right]_{k,k'} = \lambda_k \cdot \delta_{k,k'}. \tag{5.2.13}$$

This is equivalent to having originally selected fields of view in which

$$R_k^T = R_{AVG} - \sum_{k'} U_{k,k'} \left(R_{AVG} - R_{k'} \right). \tag{5.2.14}$$

One eigenvalue λ_k is always zero because only 8 linearly independent values of $\Delta R_{i,k}$ exist. In transformed space,

$$\hat{R}_i = R_{i,AVG} + \sum_{k=1}^{K_{max}} \zeta_k \cdot \Delta R_{i,k}^T \tag{5.2.15}$$

and the solution for ζ_k is given by

$$\zeta_k = \lambda_k^{-1} \cdot \left(\Delta R^{T'} \cdot N^{-1} \cdot \Delta R_{CLR} \right) \tag{5.2.16}$$

where $\Delta R_{i,k}^{T'}$ is the transpose of $\Delta R_{i,k}^{T}$.

It is apparent that large eigenvalues λ_k imply low values of ζ_k while small eigenvalues imply large (and undesirable) values of ζ_k. The eigenvalues themselves indicate the degrees of freedom in the radiances in the different fields of view corresponding to the different number of cloud formations. Typical cloud formation eigenvalues are the order of 1000. We discard all eigenvalues less than 25 and set K_{max} accordingly, with the constraint that K_{max} is never greater than 4. We also do not include any eigenfunction whose eigenvalue is less than the uncertainty in ζ_k, given later in Equation (5.2.19). Discarding low eigenvalues reduces the noise amplification factor by suppressing noise in the solution for η, according to

$$\eta_k = \sum_{k'=1}^{K_{max}} U_{k,k'} \cdot \zeta_{k'} \tag{5.2.17}$$

resulting in lower values of η. The values of η_k obtained from Equation 5.2.17 are then used in Equation 5.2.7 to give $\hat{R}_i$.

Under certain pathological conditions, one or more cloud formations may not result in significant eigenvalues of $\Delta R' N^{-1} \Delta R$ and cannot be solved for, resulting in a poor solution. The most obvious example of this is a single cloud formation with a constant cloud fraction in each field of view. Here ΔR is not influenced by cloud contrast and is comprised of noise only. The most common examples of this are all fields of view are clear, which is a benign case, or all fields of view are overcast, which is a case which must be otherwise identified and rejected. Likewise, with two cloud formations, if the lower cloud deck is overcast, a proper reconstruction of the clear column radiances cannot be obtained. In this case, if the cloud fraction of the upper cloud in field of view k

is α_{1k}, then the lower cloud fraction as seen from above, α_{2k}, is $1-\alpha_{1k}$. In general, if $\alpha_{2k} = A + B\alpha_{1k}$ for all k, then cloud formation 2 will have a zero eigenvalue of $\Delta R' N^{-1} \Delta R$ up to noise effects. The benign case occurs when A=0, corresponding to a truly single cloud formation.

5.2.4.2 Contribution of Clouds to the Retrieval Channel Noise Covariance Matrix

The physically based retrieval methodology described in section 5.4 requires a channel noise covariance matrix M representing channel correlated errors in the terms $\left(\hat{R}_i - R_i^m\right)$ and $\left(\hat{R}_j - R_j^m\right)$ where R_i^m is the radiance computed for channel i based on the m^{th} iterative solution. The channel noise covariance matrix is the sum of two parts, resulting from noise in the reconstructed clear column radiances $\delta\hat{R}_i$ with noise covariance $\hat{M}$, and noise in the computed radiances δR_i^m due to uncertainty in the parameters assumed known, with noise covariance $\tilde{M}$.

$\hat{M}_{ij} = \left[\delta\hat{R}\delta\hat{R}'\right]_{ij}$ is the expected noise covariance matrix for the channel clear column radiances. The noise in $\hat{R}_i$ obtained from Equation (5.2.7) has two parts, arising from instrumental noise $NE\Delta N_i$, and from cloud clearing errors coming from errors in ζ_k. Errors in ζ_k will cause channel correlated clear column radiance errors. Clear column radiances for those channels affected by clouds will have this additional error due to errors in ζ. For the AIRS instrument, the channel noise is spectrally uncorrelated, giving the final result

$$\left[\delta\hat{R}\,\delta\hat{R}'\right]_{ii} = NE\Delta N_i^2\, A\,(\eta_k)^2 + \left[\Delta R^T \delta\zeta\,\delta\zeta'\Delta R^{T'}\right]_{ii} \qquad (5.2.18a)$$

and

$$\left[\delta\hat{R}\delta\hat{R}'\right]_{ij} = \left[\Delta R^T \delta\zeta\,\delta\zeta'\Delta R^{T'}\right]_{ij} \qquad (5.2.18b)$$

where $\delta\zeta\,\delta\zeta'$ is the error covariance of ζ. If N, as defined in Equation (5.2.9), is indeed representative of the noise in the determination of η, then it can be shown (see Equation 5.4.17) that

$$\left[\delta\zeta\,\delta\zeta'\right]_{kk'} = \left[\Delta R^{T'} N^{-1} \Delta R^{T}\right]^{-1} = \lambda_k^{-1}\delta_{kk'}. \tag{5.2.19}$$

In the special case for which we determine that channel i does not "see" the clouds (i.e., stratospheric sounding channels or tropospheric sounding channels peaking significantly above the highest cloud top), the clear column radiance is best described as the average radiance in all fields of view. For these channels, the scene appears to be clear and we can define effective values of η^{CLR} for "clear" channels as $\eta_k{}^{CLR} = 0$ for all k. For these channels (see Equation 5.2.11),

$$A\left(\eta_k^{CLR}\right) = \frac{1}{3} \tag{5.2.20}$$

which is a noise reducer. For "clear" channel i, one can write

$$\hat{M}_{ij} = \frac{1}{9} NE\Delta N_i^2\ \delta_{ij} \tag{5.2.21}$$

where j is any other channel and δ_{ij} is the Kronecker delta function.

In a given FOR, a channel to be determined not to see clouds according to our algorithm, it must be included in a list showing a 95% probability of not seeing a cloud, which is pre-computed as a function of cloud top pressure and zenith angle. In addition, the standard deviation of the radiances in the 3x3 array of AIRS spots must be less than twice the channel noise. Otherwise, it is assumed to channel sees clouds in this FOR.

For channels which see clouds, the clear column noise covariance can now be expressed as

$$\hat{M}_{ij} = NE\Delta N_i\, NE\Delta N_j\, A\left(\eta_k\right)^2 \delta_{ij} + \sum_{k=1}^{K_{max}} \left(\Delta R_{ik}^{T} \Delta R_{jk}^{T} \lambda_k^{-1}\right). \tag{5.2.22}$$

Errors in clear column radiances can be larger than predicted by Equation (5.2.22), however, because λ_k^{-1} is just an estimate of $(\delta\zeta\delta\zeta')_{kk'}$. Moreover, Equation (5.2.22) does not take into account contributions to the noise covariance matrix arising from higher components of ζ not solved for ($k > K_{max}$) as well as fitting errors due to a poor first guess. Another estimate of the error in the ζ parameters can be computed using weighted radiance residuals in the channels used in the cloud clearing retrieval, $R_{i,CLR} - \hat{R}_i$. If we take $R_{i,CLR} - \hat{R}_i$ as the uncertainty of $\Delta R_{i,CLR}$, then using Equation (5.2.16), we estimate the uncertainty in ζ_k according to

$$\left[\delta\hat{\zeta}\delta\hat{\zeta}'\right]_{kk} = \left(\frac{1}{\lambda_k}\right)^2 \sum_i \left(\Delta R_{k,i}^T N_{ii}^{-1}\right)^2 \left(R_{i,CLR} - \hat{R}_i\right)^2 \tag{5.2.23}$$

which we evaluate for all significant functions k with $\lambda_k > 10^{-3}$. This includes eigen functions with $\lambda_k < 25$ and therefore not included in the solution for $\hat{R}_i$. For values of $k \le K_{max}$, we take

$$\left[\delta\zeta\delta\zeta'\right]_{kk} = MAX\left[\lambda_k^{-1}, \left[\delta\hat{\zeta}\delta\hat{\zeta}'\right]_{kk}\right] \tag{5.2.24}$$

and for values of k between K_{max} and K_{sig} (significant eigenvalues $\lambda_k > 10^{-3}$) we set

$$\left[\delta\zeta\delta\zeta'\right]_{kk} = \left[\delta\hat{\zeta}\delta\hat{\zeta}'\right]_{kk} \tag{5.2.25}$$

and write

$$\begin{aligned}\hat{M}_{ij} &= NE\Delta N_i \, NE\Delta N_j \, A(\eta_k)^2 \, \delta_{ij} \\ &+ \sum_{k=1}^{K_{sig}} \Delta R_{ik}^T \, \Delta R_{jk}^T \left[\delta\zeta\delta\zeta'\right]_{kk}\end{aligned} \quad . \tag{5.2.26}$$

One can think of Equation (5.2.26) in terms of a different effective noise amplification factor $A_{i,eff}$ for each channel i

$$\hat{M}_{ii} = NE\Delta N_i^2 \, A^2_{i,eff} \tag{5.2.27}$$

where

$$A_{i,eff} = \left[A(\eta_k)^2 + \sum_{k=1}^{k_{sig}} \frac{\Delta R_{i,k}^{T^2} \left[\delta\zeta\delta\zeta' \right]_{kk}}{NE\Delta N_i^{\,2}} \right]^{1/2} . \qquad (5.2.28)$$

The channel effective noise amplification factor is largest for channels which see the surface and have potentially large values of the scene contrast $\Delta R_{i,k}$. We find it convenient to define an effective noise amplification factor relevant to the surface channel retrieval step as the RMS value of $A_{i,eff}$ over all NSURF infrared channels used in the surface retrieval step

$$A_{eff} = \frac{1}{NSURF} \left[\sum_{i=1}^{NSURF} A_{i,eff}^{\,2} \right]^{1/2} . \qquad (5.2.29)$$

Very large values of A_{eff} can arise when $\delta\zeta\delta\zeta'$ is large (A_{eff} is sometimes 100 or more) and indicate a large uncertainty in the determination of the clear column radiances. These large uncertainties are sometimes caused by hidden, or nearly hidden cloud formations, and often correlate with poor solutions. Alternatively, A_{eff} can be large if there are significant errors in the geophysical parameters used to compute $R_{i,CLR}$ even if the cloud conditions are relatively simple.

5.3 AIRS Post-Launch First Guess Regression Procedure

The NOAA/NESDIS eigenvector regression product derives temperature, moisture, ozone profiles, skin temperature, and emissivity from the AIRS cloud-cleared radiances and is used as a first guess for the physical retrieval. In general, a regression is derived from a ”training dataset” that are geophysical states compiled from radiosonde profiles, satellite retrieved profiles, a numerical weather prediction model, or climatologies, or some combination of the above. Satellite radiances corresponding to the geophysical training dataset are used to derived a linear statistical relationship between radiances and the geophysical state. A regression provides fast and accurate initial guesses for temperature, moisture, and ozone profiles as well as surface parameters (Goldberg, *et al*., 2003).

definition of additional symbols in post-launch eigenvector algorithm	
symbol	description
n	channel number, AIRS original channel index, $n = 1, 2378$
M_e	number of channels used in eigenvector computation
M_ϵ	number of channels used in emissivity computation
m	channel sub-set index number
$n(m)$	sub-set of AIRS channels used in regression
$\mathrm{NE}\Delta\mathrm{N}_{n(m)}$	Noise Equivalent Difference Radiance for AIRS channel n
$R_{n(m),j}$	Radiance (observations) for channel n, case j
$\Delta\Theta_{m,j}$	Argument of Radiance
i	geophysical parameter index
L	vertical grid index, $L = 1, 100$
$X_{i,j}$	geophysical parameter, *e.g.* $T(L), q(L)$, etc for case j and geophysical index i
j	index for a scene of radiances and/or geophysical parameters
α	AIRS view (scan) angle, $-48.95° \leq \alpha \leq 48.95°$
v	index for the view angle regime (see Table 5.1)
J_e	ensemble of cases ($j = 1, J_e$) used for training of EOF's
$J_r(v, L)$	ensemble of cases ($j = 1, J_r(v, L)$) used for training of profile regressions for view angle regime = v and atmospheric layer L
$J_\epsilon(l)$	ensemble of cases ($j = 1, J_\epsilon$) used for training of emissivity regression for surface type = l
k	Eigenvalue index (k=1 is largest (most significant) eigenvalue)
λ_k	Eigenvalue
$E_{k,m}$	Eigenvector for channel $n(m)$
v	view angle index
$P^v(k, j)$	Predictor array at view angle v for a single scene j, contains k elements of PCS's and 2 additional predictors
$A^v_{L,k}$	regression coefficients at view angle v

Eigenvector regression for atmospheric sounding was first demonstrated by Smith and Woolf (1976). Eigenvectors are also commonly referred to as empirical orthogonal functions (EOF's) in the literature. Because of the large number of channels measured by AIRS, the eigenvector form of regression is crucial for exploiting the information content of all channels in a computationally efficient way. By representing radiometric information in terms of a reduced set of eigenvectors (much fewer in number than the total number of instrument channels, described in sub-section 5.3.1), the dimension of the regression problem is reduced by approximately one order of magnitude. Another advantage of using a reduced set of eigenvectors is that the influence of random noise is reduced by elimination of higher order eigenfunctions which are dominated by noise structure. It should be noted that if all eigenvectors are retained as basis functions, the

eigenvector regression reduces to the ordinary least squares regression solution in which satellite measurements are used directly as predictors.

Eigenvectors of the radiance covariance matrix are computed from AIRS cloudy radiance and are used as basis functions to represent the AIRS radiometric information. The generation of the covariance matrix and derivation of the eigenvector coefficients is discussed in sub-section 5.3.1. The use of principal component analysis reduces the data into fewer components that still retain the information content of the original data.

These components are commonly referred to by statisticians as Principal Component Scores (PCSs). AIRS cloud cleared radiances are converted to PCSs and then used to solve for atmospheric temperature, moisture, ozone, surface temperature. The training of these geophysical regressions is discussed in sub-section 5.3.3.

The application of these coefficients to compute PCSs from AIRS cloud cleared radiances is discussed in sub-section 5.3.5 and the use of those PCSs to compute temperature, $T(p)$, moisture mixing ratio, $r_w(p)$, and ozone mixing ratio, $r_o(p)$, is discussed in sub-sections 5.3.7, 5.3.8, 5.3.9, respectively.

A synthetic regression (simulated AIRS radiances) is used to derive the surface emissivity coefficients and is discussed in sub-section 5.3.10.

5.3.1 Generating the Radiance Covariance Matrix and Eigenvectors

The covariance matrix of radiance is derived from an ensemble of AIRS spectra. Radiances span two orders of magnitude between the long-wave and short-wave channels, therefore, we normalized the AIRS spectra by the AIRS instrument noise, $NEDN_{n(m)}$, to minimize numerical effects associated with round-off error.

For version 4.0 a single day of AIRS radiances was determined to be adequate to describe the entire variance of radiances. A global ensemble of AIRS cloudy radiances from 15 January 2003 was used as the ”training” data for eigenvector coefficients. Since there is a large redundancy in the AIRS granules, a subset was constructed from the AIRS FOV’s. In each of granule every 9_{th} FOV (1_{st},10_{th},19_{th},. . .,82_{nd}) from every 45_{th} scan line

(45_{th},90_{th},135_{th}) was used. This resulted in $J_e = 240 \cdot 10 \cdot 3 = 7200$ spectra to be used for training.

In the version 4.0 regression a total of $M_e = 1680$ channels were considered to be reliable for all post launch epochs based on the AIRS science team channel property files (v6.6.x) and a summary list of channel behavior over two years, compiled by Margaret Weiler. In addition, channels that are affected by non thermodynamic equilibrium (P-branch side of the 4.3 μm CO_2 band) were also removed. The AIRS channel numbers used are listed in Table 5.3.8 for reference.

Detector arrays can experience spurious events that can alter the noise characteristics. The AIRS L1b calibration can mark certain channels as bad on any arbitrary scan line. For training of eigenvectors and regression coefficients any spectra containing bad channels are removed from the training ensemble.

The deviations of the normalized radiances from their sample mean is denoted as $\Delta\tilde{\Theta}_{m,j}$, a matrix of dimensions [m = 1,M_e j = 1, J_e], where M_e = 1680 is the total number of instrument channels and J_e = 7200 is the sample size of the training data set for eigenvector coefficients. The deviation matrix is given by

$$\Delta\tilde{\Theta}_{m,j} \equiv \frac{R_{n(m),j}}{\mathrm{NE}\Delta\mathrm{N}_{n(m)}} - \frac{< R_{n(m),j} >_{J_e}}{\mathrm{NE}\Delta\mathrm{N}_{n(m)}} \equiv \frac{R_{n(m),j}}{\mathrm{NE}\Delta\mathrm{N}_{n(m)}} - < \tilde{\Theta}_{m,j} >_{J_e} \quad (5.3.1)$$

The covariance matrix of the normalized radiances, $\Delta\tilde{\Theta}_{cov}$, is a square matrix of order M_e = 1680 and is given by

$$\Delta\tilde{\Theta}_{\mathrm{cov}} \equiv \frac{1}{J_e} \sum_{j=1}^{J_e} \Delta\tilde{\Theta}_{m,j} \cdot \Delta\tilde{\Theta}_{j,m}^{T} \quad (5.3.2)$$

The diagonal elements of $\Delta\tilde{\Theta}_{cov}$ represent the variance of the respective channel noise scaled radiance while the off diagonal elements represent the covariance between pairs of channels. We normalize $\Delta\Theta_{cov}$ by the number of observations J_e so that the magnitude of the eigenvalues does not change with the size of the training ensemble.

The relationship between the radiance covariance and eigenvectors and eigenvalues is given by:

$$\Delta\tilde{\Theta}_{\mathrm{cov}} \equiv E^{T}_{m,k} \cdot \Lambda_{k,k'} \cdot E_{k',m} \tag{5.3.3}$$

where $\Lambda_{k,k}$ is a diagonal matrix with elements equal to λ_k. We use the routines TRED2, TQLI in Press, *et al.,* 1986, pgs. 350-363, to derive $E_{k,m}$ and λ_k and the routine EIGSRT to order the eigenvalues in terms of the amount of the total data variance. The largest λ_k explains the most variance and each successive eigenvector explains progressively less of the total data variance. The square root of eigenvalues is equivalent to the standard deviation of the principal component scores (PCSs, see Eqn. 5.3.6) of the training ensemble. Since we are using normalized radiances, the square root of the eigenvalues can be interpreted as signal-to-noise; however, this is only an approximation since the AIRS short-wave band noise is a function of the scene radiance.

In Figure 5.3.1 the eigenvalues are shown for the training day used in the v4.0 PGE. Also shown are eigenfunctions of a 3-day (9/6/02, 9/29/02, and 1/25/03) ensemble of synthetic AIRS radiances in which we used models for temperature, moisture, ozone, and carbon trace gases, and instrument noise models to compute radiances. The difference between these two curves represents the information not contained within the synthetic radiances, most likely due to clouds. The fact that the eigenvalues beyond k = 1000 decrease and become smaller than the eigenvalues from the simulated clear radiances is an indication that we may need more than J_e = 7200 cases for the training of the EOF's or that we need more than one training day. In version 5.0 this will be addressed. In Figure 5.3.2 the first 100 eigenvalues are shown for the v4.0 PGE training day. Again, eigenvalues from synthetic clear radiances is shown for comparison.

In this formalism, the significant eigenvalues are those that are above the noise "floor". Random noise should generate constant eigenvalues, thus we examine Figure 5.3.1 to find the "knee" in the curve. To the right of this "knee" the information content is dominated by noise. The optimal number ($K_{\max}$) has been determined to be 85 for capturing the information content of the measurements from AIRS. Using a greater number of eigenvectors tends to make the regression result more sensitive to noise. Once

K_{max} is determined, those eigenfunctions are used as basis functions to represent the original radiance information in terms of PCS's. The EOF training procedure produces the following coefficients:

1. The average radiance of the J_e scenes used in the training ensemble, $< R_{n(m),j} >_{J_e}$
2. The eigenvalues, λ_k
3. The most significant eigenfunctions, $E_{k,m}$.
4. and the noise used in the computation $NE\Delta N_{n(m)}$

The file format for these coefficients is described in Sec. 5.3.2.

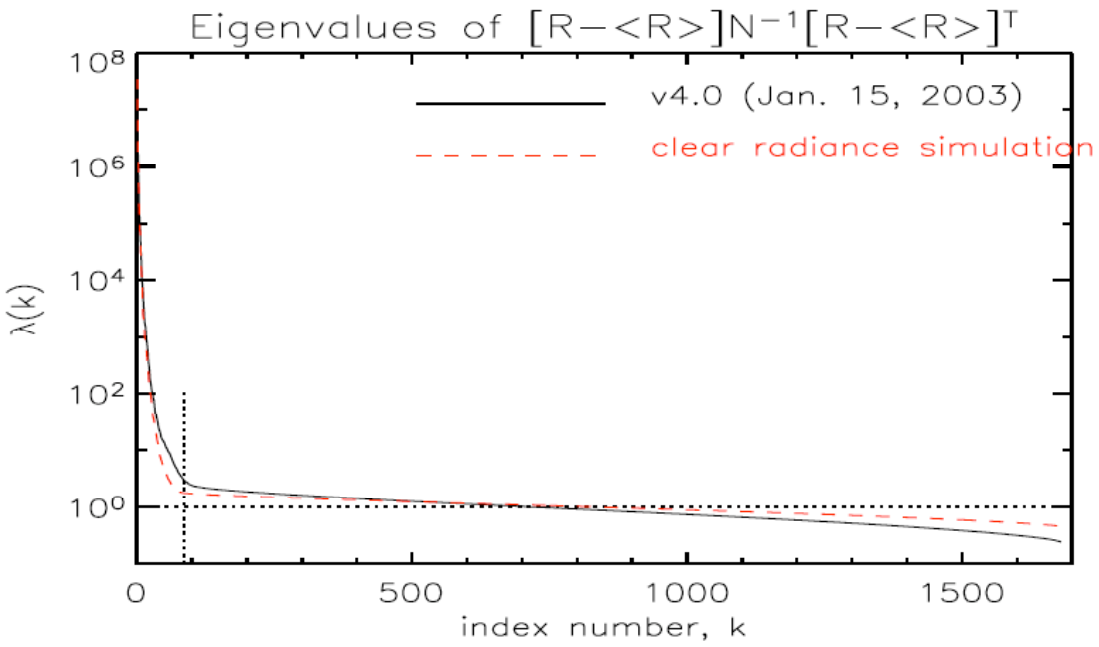

Figure 5.3.1. The values of λ_k for AIRS cloudy radiances (solid line) and simulated AIRS clear radiances (dashed line)

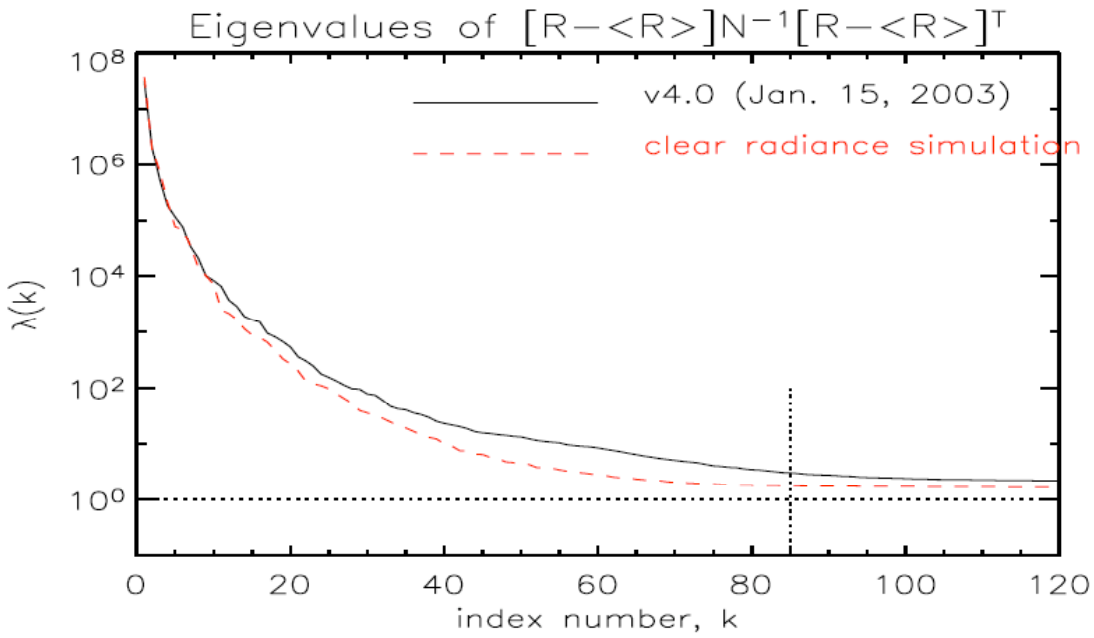

Figure 5.3.2. The first 100 values of λ_k for AIRS cloudy radiances (solid line) and simulated AIRS clear radiances (dashed line)

5.3.2 NOAA Eigenvector File Format

The eigenvector file is written out with the following components using FORTRAN formatted I/O.

- A header block with
  - the number of channels in the subset, M_e = 1680, format(i13)
  - the number of eigenvectors, K_{store} = 200, format(i13)
  - A flag if radiances are used (set to T), format(2x,L1)
  - A flag is the mean is subtracted (set to T), format(2x,L1)
- The average of $\tilde{\Theta}$ for the M_e channels, format(1x,5g15.7)

$$< \tilde{\Theta} >_m \equiv \frac{< R_{n(m),j} >_{J_e}}{\mathrm{NE}\Delta\mathrm{N}_{n(m)}} \tag{5.3.4}$$

- Each eigenvector, $E_{k,m}$, is written out as a single record of M_e elements for each value of $k = 1, K_{store}$,

format(1x,5g15.7)

• The value of $\lambda(k)$ for $k = 1,M_e$, format(1x,5g15.7)

• The value of $NE\Delta N_{n(m)}$ for $m = 1,M_e$, format(1x,5g15.7)

• The value of channel wavenumber, $\nu_{n(m)}$, for $m = 1,M_e$. format(1x,5g15.7)

• The value of $n(m)$ for $m = 1,M_e$. format(1x,6i12)

5.3.3 Generating Regression Coefficients from Principal Component Scores

AIRS viewing geometry changes along the scan-line from $-48.95^\circ \le \alpha \le 48.95^\circ$. The regression could have been trained at each of the 30 view angles, or with the assumption of symmetry about nadir we could have used 15 view angles; however, this creates the need for a large volume of coefficients and memory requirements. After some analysis it was decided to train the regression in four view angle regimes, defined in Table 5.3.1, and use two additional predictors; one for which side of nadir the observation is made, and the other is the view angle of the observation. In this way, the regression is allowed to fit the radiances as a function of angular variability over a narrow range of angles and can adjust the fit for scan asymmetry.

Table 5.3.1. View-angle Regimes in the NOAA Regression

v	$\alpha_1(v)$	$\alpha_2(v)$	$J_r(v)$
1	53.130	42.269	$\approx$ 3,000
2	42.269	31.788	$\approx$ 6,000
3	31.788	19.948	$\approx$ 7,000
4	19.948	0.000	$\approx$ 10,000

In our algorithm, we normalize PCSs by the square root of the eigenvalue to minimize numerical roundoff error in the computation. Again we employ Eqn. 5.3.1, reproduced below, to convert our spectrum of M_e channels, for an ensemble of scenes, into PCSs to be used for training the regression coefficients. The J_r scenes used for training the regression coefficients are not the same scenes as used in training the eigenvectors, that is $J_r = J_e$. In the AIRS science team algorithm we will apply the regression coefficients to cloud cleared radiances, therefore, cloud cleared radiances are used to compute the

regression coefficients. Each spectrum $R_{n(m),j}$, is first converted to a signal-to-noise departure from the average of the *eigenvector* training ensemble, $< R_{n(m),j} >_{J_e}$

$$\Delta\tilde{\Theta}_{m,j} \equiv \frac{R_{n(m),j}}{\mathrm{NE}\Delta\mathrm{N}_{n(m)}} - \frac{< R_{n(m),j} >_{J_e}}{\mathrm{NE}\Delta\mathrm{N}_{n(m)}} \equiv \frac{R_{n(m),j}}{\mathrm{NE}\Delta\mathrm{N}_{n(m)}} - < \tilde{\Theta}_{m,j} >_{J_e} \tag{5.3.5}$$

and then converted into PCS's

$$P_{k,j} = \frac{1}{\sqrt{\lambda_k}} \cdot E_{k,m} \cdot \Delta\tilde{\Theta}_{m,j} \tag{5.3.6}$$

Only k = 1,$K_{\max}$ principal components are kept, where $K_{\max}$ = 85 is the number of significant eigenvalues determined in sub-section 5.3.1.

A predictor array is constructed using the PCSs for those cases with $\alpha_1(v) < |\alpha| \leq \alpha_2(v)$, where α is the instrument view angle. The predictor argument for the sub-set of cases is assembled with the first $K_{\max}$ elements being set equal to $P_{k,j}$. The element $i = K_{\max} + 1$ is set equal to one if $\alpha < 0$ or zero if $\alpha \geq 0$. The element $i = K_{\max} + 2$ is set equal to $1-\cos\left(\frac{\pi\cdot\alpha}{180}\right)$. Therefore, the complete predictor vector used in this regression can be given by

$$P_{k,j} = \begin{pmatrix} P_{1,j} \\ P_{2,j} \\ \cdots \\ P_{K_{\max},j} \\ \frac{1-\mathrm{sign}(\alpha_j)}{2} \\ 1-\cos(\frac{\pi\cdot\alpha_j}{180}) \end{pmatrix} \qquad i = 1, K_{\max}+2 \tag{5.3.7}$$

For AIRS, we use $K_{\max}$ = 85 principal component scores for predictors and solve for atmospheric temperature, moisture, ozone profiles, and surface temperature. Initially, only one day of data was thought to be sufficient to generate regression coefficients; however, we found that the analysis field may have large errors in certain regions. Currently, three days from AIRS observations for the generating regression coefficients are 6 September 2002, 25 January 2003, 8 June 2003, collocated with estimates of the true atmospheric profiles (*i.e.*, ECMWF). Data are selected by screening out cases where

the AIRS cloud cleared radiances may be affected by clouds and where there may be problems with the geophysical states used as "truth" using the following tests:

1. The brightness temperature of the AIRS observation in channel # 2112, $B_\upsilon^{-1}(R_{n(m)})$ must be within ± 5 K of the predicted brightness temperature, Θ(2212), computed from AMSU radiances, $\Theta_A(n)$. We use AMSU channels n = 4, 5, and 6 to compute the predicted AIRS radiance, Θ(2112), as follows

$$\Theta(2112) = a_1 + a_2 \cdot \Theta_A(4) + a_3 \cdot \Theta_A(5) + a_4 \cdot \Theta_A(6) + a_5 \cdot \cos(\theta) + a_6 \cdot (1 - \cos(\alpha)) \quad (5.3.8)$$

   where the coefficients of the AMSU screening test used to predict AIRS channel #2112 (f = 2390.53cm^{-1}) are

coef	value	multiplied by
a_1	18.653	constant
a_2	-0.169	AMSU chl.4
a_3	+1.975	AMSU chl.5
a_4	-0.865	AMSU chl.6
a_5	+4.529	cosine of satellite zenith angle
a_6	-0.608	1-cosine of view angle

2. The reconstruction score, given in Eqn. 5.26, is less than 1.25.

3. Compare the brightness temperatures, computed from the training ensemble geophysical states with the AIRS cloud cleared radiances for a set of channels given below. The difference between observed and computed brightness temperature for all 12 channels must be within 2 K. The 12 channels are

NOAA index	AIRS channel	freq.	reason for test
84	186	702.18	200 mb T
87	198	706.14	300 mb T
92	215	711.00	400 mb T
94	221	712.74	500 mb T
97	232	715.94	600 mb T
103	262	724.82	700 mb T
113	333	746.01	800 mb T, cloud contamination
117	375	759.57	900 mb T, cloud contamination
129	914	965.43	surface, cloud contamination
190	1669	1468.83	450 mb water
201	1763	1542.45	200 mb water
203	1771	1547.88	400 mb water

There are approximately 2,700,000 total spectral samples for the three training days and about 26,000 passed the three threshold tests above. The approximate number in each view angle regime, $J_r(v)$ is given in Table 5.3.1.

Another issue for the regression is that topography limits the available training ensemble for some altitude layers. For each case, j, there is a maximum number of vertical levels defined by the surface pressure (that is,some of the 100^{th} layer grid is below the surface). If this lower level is given as L_{bot} then the number of cases in the training ensemble, J_r, is a function of how many cases have surface pressure above that level, that is, each profile is only valid over the range of $L = 1, L_{bot}$. Therefore, the number of cases in the regression training ensemble is a function of both view angle regime, v, and the vertical atmospheric layer, L. Regression is a linear operator and, as such, each layer and view angle regime is a separate regression.

We can write the total number of cases used for training the regression in each layer of the atmosphere and each view-angle regime as $J_r(v,L)$. These are the cases that satisfy the view-angle criteria in Table 5.3.1 and have valid geophysical parameters in the layer under consideration in X_i. We can compute the average predictor argument for this subset ensemble and subtract that from the training ensemble

$$\Delta P_{k,j} = P_{k,j} - < P_{k,j} >_{J_r(v,L)} \tag{5.3.9}$$

For temperature we train the regression on the layer mean temperature for atmospheric layer L and also for surface skin temperature. For moisture the regression is trained on both the $\log_e(r_w(L))$ and $r_w(L)$, where $r_w(L)$ is the mass mixing ratio of water in grams/kilo-gram (g/kg) within layer L. For ozone the regression is only trained on $\log_e(r_o(L))$ where $r_o(L)$ is the mass mixing ratio within layer L. The generalized equation we will solve, for $X_i = T(L), X_i = T_{surf}, X_i = r_w(L), X_i = \log_e(r_w(L))$, *and* $X_i = \log_e(O_3(L))$, is given by

$$X_{i,j} = < X_{i,j} >_{J_r(v,L)} + A^v_{i,k} \cdot \Delta P_{k,j} \tag{5.3.10}$$

where we can write,

$$\Delta X_{i,j} = X_{i,j} - < X_{i,j} >_{J_(v,L)} \tag{5.3.11}$$

See Table 5.3.2 for a translation from our parameter space, X_i, to geophysical layer parameter X_L. We can solve Eqn. 5.3.10 for the regression coefficients, $A^v_{i,k}$, as follows:

$$A_{i,k}^{v} = \Delta X_{i,j} \cdot \Delta P_{j,k}^{T} \cdot \left[\Delta P_{k,j} \cdot \Delta P_{j,k}^{T}\right]^{-1} \tag{5.3.12}$$

No additional regularization is needed in Eqn. 5.3.12 since the principal components have been regularized by selecting only K_{max} = 85 of the principal components. Once $A_{i,k}^{v}$ is determined we can combine the average of the geophysical parameter given in Eqn. 5.3.11,

$$\overline{X}_j \equiv < X_{i,j} >_{J_r(v,L)}$$

and the average of the predictor given in Eqn. 5.3.9,

$$\overline{P}_k \equiv < P_{k,j} >_{J_r(v,L)}$$

into a single value, called

$$\overline{A}_i = \overline{X}_i + A_{i,k} \cdot \overline{P}_k$$

so that our regression equation can utilize the un-normalized predictors. We can rewrite Eqn. 5.3.11 as

$$X_{i,j} = \overline{A^v}_i + A_{i,k}^{v} \cdot P_{k,j} \tag{5.3.13}$$

where A_i^v is defined as

$$\overline{A^v}_i \equiv < X_{i,j} >_{J_r(v,L)} - A_{i,k}^{v} \cdot < P_{k,j} >_{J_r(v,L)} \tag{5.3.14}$$

Once the regression matrix is known it is useful to compute the mean and standard deviation of the error between the regression, applied to the training ensemble radiances, and the geophysical value in the training ensemble. This is the fitting error. Each case has an error, δX, given by

$$\delta X_{i,j} = X_{i,j} - \left[\overline{A^v}_i + A_{i,k}^{v} \cdot P_{k,j}\right] \tag{5.3.15}$$

For each geophysical parameter we can compute a mean and standard deviation of the regression error (difference of regression from the training values). The mean error is given by

$$\overline{\delta X_i} \equiv \frac{1}{J_r(v,L)} \sum_j \delta X_{i,j} \tag{5.3.16}$$

and should be zero for the training ensemble. The standard deviation of the error is given by

$$\sigma(\delta X_i) \equiv \left[\frac{1}{J_r(v,L)} \sum_j \left(\delta X_{i,j} - \overline{\delta X_i} \right)^2 \right]^{\frac{1}{2}} \tag{5.3.17}$$

The standard deviation can be compared to the standard deviation of the training ensemble's departure from its mean, given in Eqn. 5.3.11.

$$\sigma(\Delta X_i) \equiv \left[\frac{1}{J_r(v,L)} \sum_j \left(\Delta X_{i,j} \right)^2 \right]^{\frac{1}{2}} \tag{5.3.18}$$

The mean and standard deviation of the regression error and the standard deviation of training ensemble are all written into the regression coefficient file (see section 5.3.4).

Table5.3.2. Geophysical parameters, X_i, solved in NOAA real-time regression (NOTE: r_w = mass mixing ratioof water, r_o = mass mixing ratio of ozone). The index i is used in the data file and the index L =1+(i−1)/4 is used in a storage vector in the retrieval code.

i	L	eigenvector regression parameter
1	1	$T(1)$
2	1	$r_w(1)$
3	1	$\log_e(r_w(1))$
4	1	$\log_e(r_o(1))$
5	2	$T(2)$
6	2	$r_w(2)$
7	2	$\log_e(r_w(2))$
8	2	$\log_e(r_o(2))$
...	...	
385	97	$T(97)$
386	97	$r_w(97)$
387	97	$\log_e(r_w(97))$
388	97	$\log_e(r_o(97))$
393	99	$T(P_s)$
394	99	$r_w(P_s)$
395	99	$\log_e(r_w(P_s))$
396	99	$\log_e(r_o(P_s))$
397	100	T_s

i	n	synthetic regression parameter
401	1	$\epsilon(1)$
402	2	$\epsilon(2)$
...	...	...
439	39	$\epsilon(39)$

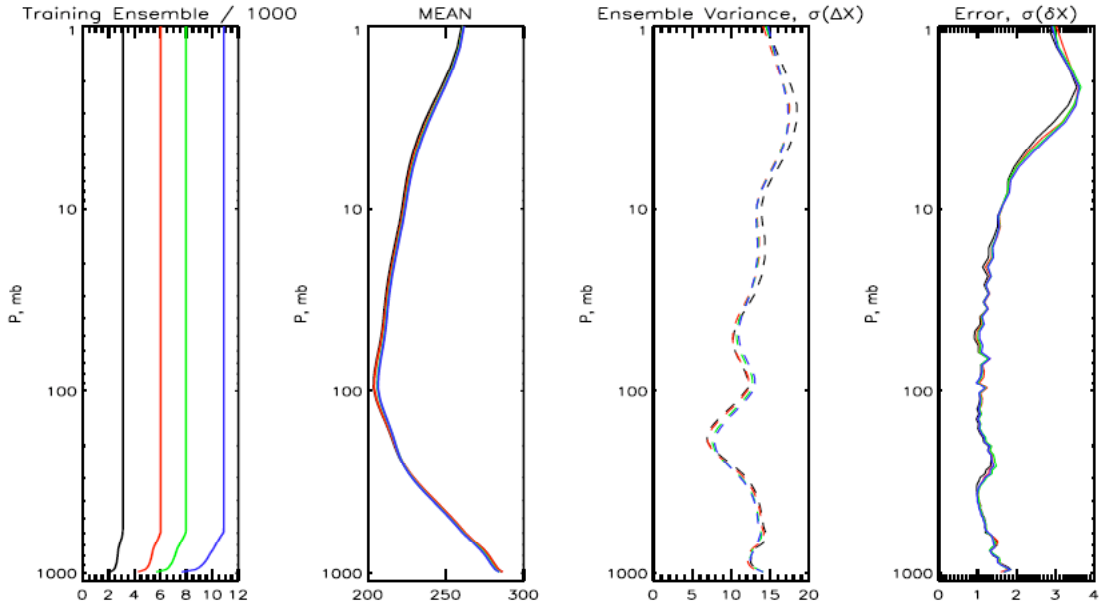

Figure 5.3.3. Regression Statistics for the V4.0 Temperature Regression. In each panel there are 4 lines corresponding to $v = 1$ (black), $v = 2$ (red), $v = 3$ (green) and $v = 4$ (blue). From left to $v = 1$ (black), $v = 2$ (red), $v = 3$ (green) and $v = 4$ (blue). From left to right the panels are $J_r(\upsilon,L)$, $<X_{i,j}>_{Jr(\upsilon,L)}$, $\sigma(\Delta X_i)$, using Eqn. 5.3.18, and $\sigma(\delta X_i)$ using Eqn. 5.3.17.

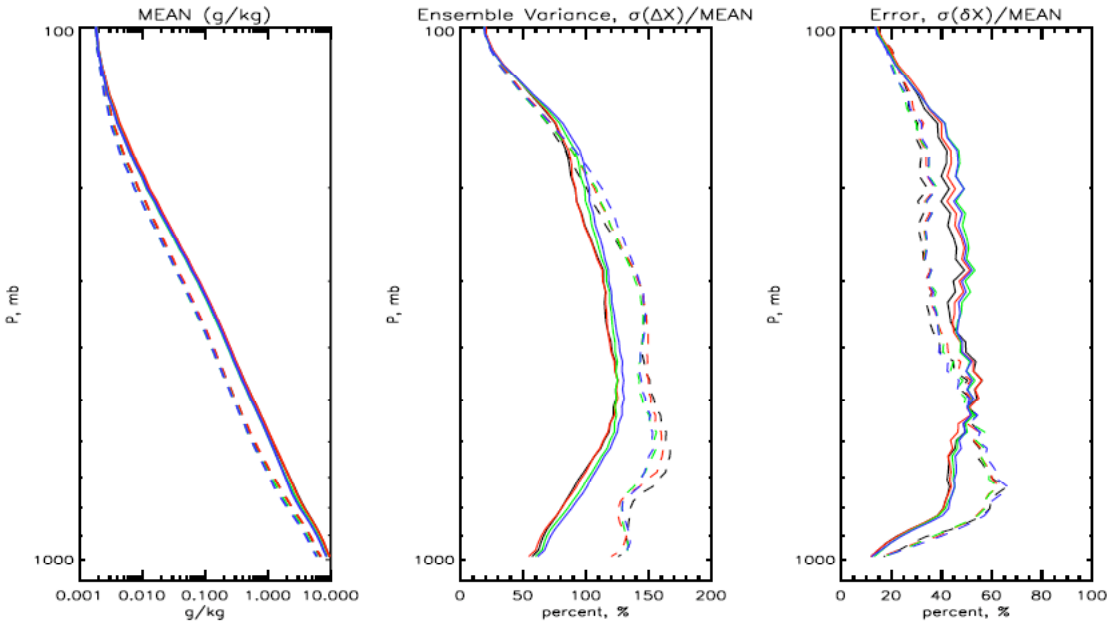

Figure 5.3.4. Regression Statistics for the V4.0 Water Regression. In each panel there are 4 lines corresponding to $v = 1$ (black), $v = 2$ (red), $v = 3$ (green) and $v = 4$ (blue). From left to right the panels are

$$\overline{X}_j \equiv < X_{i,j} >_{J_r(v,L)},$$

$\sigma(\Delta X_i)/X$, using Eqn. 5.3.18, and $\sigma(\delta X_i)/X$, using Eqn. 5.3.17. Solid lines are the linear water regression and dashed lines are the logarithmic water regression, in which exponentials of X are computed to convert $\log(r_w(L)$ into $r_w(L)$.

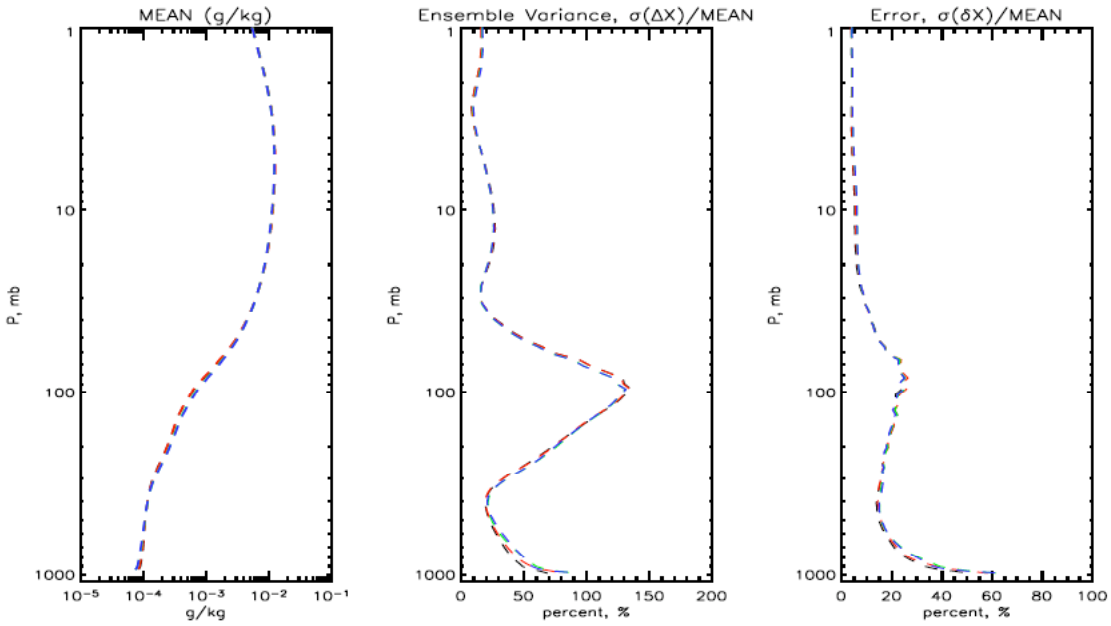

Figure 5.3.5. Regression Statistics for V4.0 Ozone Regression. In each panel there are 4 lines corresponding to $v = 1$ (black), $v = 2$ (red), $v = 3$ (green) and $v = 4$ (blue). From left to right the panels are

$$\overline{X}_j \equiv < X_{i,j} >_{J_r(v,L)},$$

$\sigma(\Delta X_i)/X$, using Eqn. 5.3.18, and $\sigma(\delta X_i)/X$, using Eqn. 5.3.17. Exponentials of X are computed to convert $\log(r_o(L)$ into $r_o(L)$.

5.3.4 NOAA Regression File Format

In the NOAA regression file each set of geophysical parameters is written for a view angle block. The index number system for the geophysical parameters is given in Table 5.3.2 or 5.2. In the profile regression, the 393 parameters (1-388,393-397) are written out in 4 sequential blocks in the regression file. In the surface regression the 39 emissivity regressions are written out for the 4 land types. The overall structure of the data file looks like

- Header Block for Profile Regression
- 393 regression sets for view angle regime number 1

• 393 regression sets for view angle regime number 2

• 393 regression sets for view angle regime number 3

• 393 regression sets for view angle regime number 4

• Header Block for Synthetic Emissivity Regression

• 39 regression sets for land surface type 1 (non-frozen land)

• 39 regression sets for land surface type 2 (non-frozen ocean)

• 39 regression sets for land surface type 3 (ice)

• 39 regression sets for land surface type 4 (snow)

Each regression set includes the following:

• The header line, format(2i4,a10,i6,4f10.5), for the profile and emissivity regression set contains

– The parameter number (see Table 5.3.2)

– The number of predictors, $I = K_{max} + 2$

– The pressure at level L or frequency at emissivity n.

– The number of cases in training ensemble, $J_r(v,L)$ or $J(l)$.

– The mean of the training ensemble,

$$< X_j >_{J_r(v,L)} \text{ or } < X_j >_{J_\epsilon(l)}$$

– The standard deviation of the training ensemble, $\sigma(\Delta X(L))$

– the standard deviation of the error of the regression applied to the training ensemble, $\sigma(\delta X(L))$

• A block of $I + 1 = K_{max} + 3$ coefficients, starting with

$$\overline{A^v}_i$$

and then the I values of $A_i(L)$ are written with format(8g15.7)

5.3.5 Computing Principal Component Scores from AIRS Radiances

We begin by computing the radiance argument from AIRS cloud-cleared or clear radiances for our single spectrum for scene *j* using Eqn. 5.1 for the M_e channels used in the eigenvector array.

$$\Delta\tilde{\Theta}_{m,j} \equiv \frac{R_{n(m),j}}{\mathrm{NE}\Delta\mathrm{N}_{n(m)}} - <\tilde{\Theta}>_m \tag{5.3.19}$$

The channel list, $n(m)$, noise values, $\mathrm{NE}\Delta\mathrm{N}_{n(m)}$, and average radiance, $<\tilde{\Theta}>_m$, are all read in from the eigenvector coefficient file.

We then convert the radiance argument into principal component scores; however, some of the AIRS HgTeCd detectors may suffer from a phenomena described as "popping" in which the detector has a non-Gaussian noise event that can be many NEΔN units. This "popping" occurs for any arbitrary channel about 1:10,000,000 measurements. When training eigenvectors or regression coefficients any spectra containing bad channels are simply removed from the training ensemble. When applying the regression operationally the use of a bad channel can be quite detrimental, therefore, we need a dynamic ability to remove BAD channels from our algorithm. In the physical algorithm, the channel is simply removed from consideration; however, in regression algorithms a bad channel cannot be removed.

Bad channels can be found by monitoring the reconstruction scores (see Eqn. 5.3.26) and the difference between the reconstructed and the observed radiances. If AIRS level1B radiance quality flags indicated the radiance is sub-optimal (*i.e.*, the CalFlag bit 4,5,6 is set), we compute the PCSs by using the mean deviations of the neighboring good channels of the bad channels (using the average of the 10 neighboring channels). Then we use this set of PCSs to reconstruct those channels that are marked bad. After that we recomputed the PCS, substituting the reconstructed radiances for the bad channel(s) and use that PCS for regression retrieval.

For example, if channel m_0 is BAD in radiance set $R_{n(m_0),j}$ for case j it can be *crudely estimated* by the average value of the neighboring radiances.

$$\Delta\tilde{\Theta}_{m_0,j} = \frac{1}{10}\sum_{i=1,5}\left(\Delta\tilde{\Theta}_{m_0-i,j} + \Delta\tilde{\Theta}_{m_0+i,j}\right) \tag{5.3.20}$$

where $m_0 - i$ is the i_{th} closest valid radiance, within our channel list, on the low wavenumber side of m_0 and $m_0 + i$ is the the i_{th} closest valid radiance on the high wavenumber side. In the PGE code we exclude any of the i channels that are marked bad, so there can be less than 10 channels in Eqn. 5.3.20; however, this event is incredibly rare. We begin by using this estimate in place of the bad radiance(s) to compute an initial guess for the principal component score, $P^0_{k,j}$

$$P^0_{k,j} = \frac{1}{\sqrt{\lambda(k)}} \cdot E_{k,m} \cdot \Delta\tilde{\Theta}_{m,j} \tag{5.3.21}$$

Once $P^0_{k,j}$ is computed, the BAD radiance for channel m_0 can be estimated from all the remaining good radiances and our estimate of the bad radiance. This approach can only work if there is redundant information contained within the spectrum. For AIRS the 1680 channels can be represented by approximately 85 principal components, therefore, the is approximately a 20:1 redundancy in the AIRS spectrum. The radiance argument for the bad channels is replaced by one computed from our entire spectrum as follows

$\Delta\tilde{\Theta}_{m_0,j} = \sqrt{\lambda(k)} \cdot E^T_{m_0,k} \cdot P^0_{k,j}$, where, m_0 is the index of the BAD channel (5.3.22)

Then the PCSs can be recomputed from the improved estimate of the bad radiance along with the good radiances.

$$P^1_{k,j} = \frac{1}{\sqrt{\lambda(k)}} \cdot E_{k,m} \cdot \Delta\tilde{\Theta}_{m,j} \tag{5.3.23}$$

This process could be iterated until $P^i_{k,j}$ converges; however, the first iteration appears to be adequate in operation. Basically, we use principal components to generate reconstructed radiances and to compute the Root Mean Square (RMS) between the

reconstructed radiances and the observed radiances. It appears that the RMS for most cases is comparable with the instrument noise level, therefore AIRS observations can be reconstructed very accurately by using about 85 PCSs.

We use the first iteration of the PCSs, $P^1_{k,j}$, in all our regression applications in the next three sections.

5.3.6 Computing Radiance Reconstruction Scores

Reconstructed radiances are computed from the principal component scores (PCSs) and inverting Eqn. 5.3.19 to obtain a radiance.

$$\hat{R}_{n(m),j} = \mathrm{NE\Delta N}_{n(m)} \cdot \left(< \tilde{\Theta} >_m + \sqrt{\lambda(k)} \cdot E^T_{m,k} \cdot P^1_{k,j} \right) \tag{5.3.24}$$

The reconstructed radiances can be thought of as noise free radiances, therefore, we can estimate the noise in the spectrum by taking the difference between the radiance argument and the reconstructed radiance argument as follows

$$CS_{m,j} = \frac{R_{n(m),j} - \hat{R}_{n(m),j}}{\mathrm{NE\Delta N}_{n(m)}} \quad \equiv \quad \Delta\tilde{\Theta}_{m,j} - \sqrt{\lambda(k)} \cdot E^T_{m,k} \cdot P^1_{k,j} \tag{5.3.25}$$

If we take the root-sum-square of *RS* then we have a single parameter that describes the quality of the spectrum.

$$RS_j \equiv \frac{1}{M} \sum_{m=1}^{M} CS_{m,j} \tag{5.3.26}$$

A value reconstruction score equal to one is an indication that the radiance noise is statistically equal to the our noise estimate, $\mathrm{NE\Delta N}_{n(m)}$. The reasons that a reconstruction score is different than one could be due to:

- The spectrum has bad channels that were not identified.
- Instrument problems, such as incorrect detector temperatures, scan mirror not pointing toward the Earth, etc.
- The instrument noise has changed or is significantly different that NEΔN (*e.g.*, in warm scenes the AIRS noise in the short wave becomes larger, hence, RS_j will be larger than 1).

• The spectrum contains information that was not in the eigenvector training ensemble, J_e. For example, a volcano can produce trace gases, such as sulfur dioxide, which has a unique spectral structure that is not represented in our K_{max} eigenvectors.

The value of RS_j is shown in the top panel of Figure 5.3.6 from the real-time NOAA radiance monitoring web-page: (http://www.orbit.nesdis.noaa.gov/smcd/spb/airs/xindex.html).

In this case an eigenvector set trained on 1688 channels was used of which 8 have been permanently removed in the eigenvector training discussed in this ATBD. On the bottom panel the number of channels marked bad is also shown. In Figure 5.3.7 the reconstruction score is shown for a single day. Notice that the ascending (daytime) orbits show some high scores over desert regions.

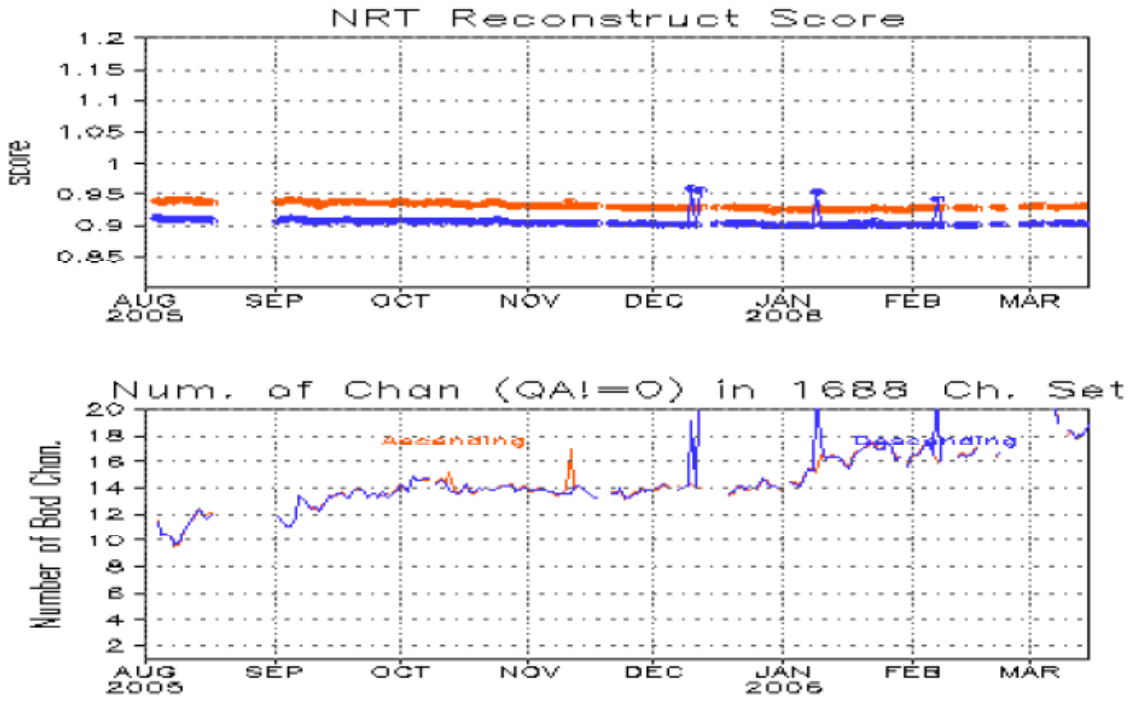

Figure 5.3.6. Upper Panel: Value of RS_j versus Time. Lower Panel: Number of Channels Marked Bad by the L1 QA. Ascending observations shown in gold color and descending shown in blue. From NOAA real-time web site:

http://www.orbit.nesdis.noaa.gov/smcd/spb/airs/xindex.html

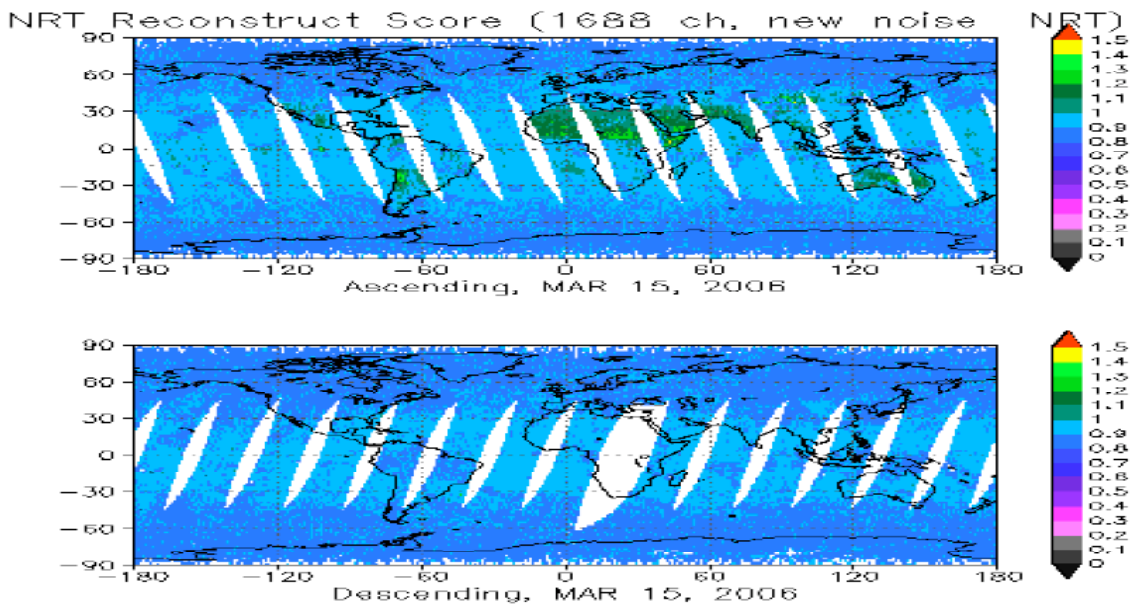

Figure 5.3.7. The Value of RS_j as a Function of Geography for Ascending (Top) and Descending (Bottom) Observations. From NOAA real-time web site:

http://www.orbit.nesdis.noaa.gov/smcd/spb/airs/xindex.html

5.3.7 Computing Temperature and Skin Temperature from Principal Component Scores

The temperature profile is derived from PCSs computed in Eqn. 5.3.23 as follows

$$T(L) = \overline{A^v}_i + A^v_{i,k} \cdot P_{k,j} \qquad i = 1 + 4 \cdot (L-1) \tag{5.3.27}$$

and T_{surf} is computed as

$$T_{surf} = \overline{A^v}_i + A^v_{i,k} \cdot P_{k,j} \qquad i = 397 \tag{5.3.28}$$

Note that the regression coefficients can be related to empirical kernel functions,

$$\tilde{K}_n(L)$$

for channel n and pressure layer L. In the eigenvector regression the empirical kernel functions can be computed for each view angle regime, v, by

$$\tilde{K}_{n(m)}(L,\Theta) = A^{v(\alpha)}_{i(L),k} \cdot E_{k,m} \quad + \quad A^{v(\alpha)}_{i(L),K_{\max+2}} \cdot \left(1 - \cos\left(\frac{\pi \cdot \Theta}{180}\right)\right) \tag{5.3.29}$$

where, we assumes positive view angles (to eliminate need for scan side predictor) and $i(L)$, is the subset of indices for the selection of the geophysical parameter group (*e.g.*, T(L), is given for $L = 1, 2, 3, \ldots$, which is given by $i = 1, 5, 9, \ldots$ in Table 5.3.2)

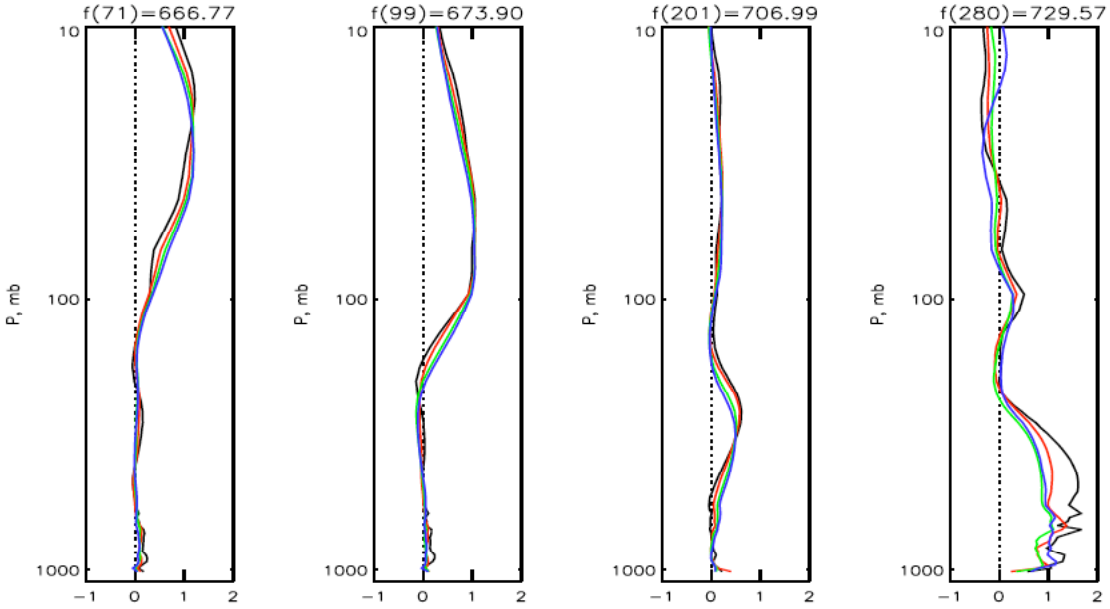

Figure 5.3.8. Example of Empirical Kernal Functions, using Eqn. 5.3.29, for Four AIRS Channels, using the NOAA V4.0 Regression. Black is at $\alpha = 47^{\circ}$ red is at $\alpha = 35^{\circ}$, green is at $\alpha = 25^{\circ}$, and blue is at $\alpha = 10^{\circ}$.

An estimate of the propagated error in the principal components for case j, $\delta \hat{P}_{k,j}$, can be given by the root-sum-square (RSS) of the linear combination and an estimate of the error in the radiance for case j, $\delta R_{n(m),j}$. This results in an error in the argument of $\delta\tilde{\Theta}_{n(m),j} \equiv \delta R_{n(m),j}/\mathrm{NE}\Delta\mathrm{N}_{n(m)}$ and

$$\delta\hat{P}_{k,j} = \sqrt{\frac{1}{\sqrt{\lambda_k}}\sum_{m=1}^{M_e}\left(E_{k,m}\cdot\delta\tilde{\Theta}_{n(m),j}\right)^2} = \sqrt{\frac{1}{\sqrt{\lambda_k}}\sum_{m=1}^{M_e}\left(E_{k,m}\cdot\frac{\delta R_{n(m),j}}{\mathrm{NE}\Delta\mathrm{N}_{n(m)}}\right)^2} \qquad 5.3.30)$$

A propagated error estimate can be computed from the linear combination of principal components

$$\delta\hat{X}_{i,j} = \sqrt{\sum_i\left(A^v_{i,k}\cdot\delta P_{k,j}\right)^2} \qquad (5.3.31)$$

5.3.8 Computing Water Vapor Regression from Principal Component Scores

For moisture, the regression is trained on both the $\log_e(r_w(L))$ and $r_w(L)$, where r_w is the mass mixing ratio of water in grams/kilo-gram (g/kg). Both regressions are computed and the total precipitable water is computed from the linear mass mixing ratio regression. For each level, L, the index into the coefficient tables, i_1 for r_w and i_2 for $\log_e(r_w)$ can be computed easily (see Table 5.3.2)

$$r_{w_1}(L) = \overline{A^v}_{i_1} + A^v_{i_1,k} \cdot P_{k,j} \qquad i_1 = 2 + 4 \cdot (L-1) \tag{5.3.32}$$

$$r_{w_2}(L) = \exp\left(\overline{A^v}_{i_2} + A^v_{i_2,k} \cdot P_{k,j}\right) \qquad i_2 = 3 + 4 \cdot (L-1) \tag{5.3.33}$$

For each profile we can compute the Total Precipitable Water (TPW) as follows

$$TPW = \sum_{L=1}^{L} \frac{r_{w_1}(L) \cdot \Delta p(L)}{g} \tag{5.3.34}$$

If the TPW is less than 1 then we use $r_w(L) = r_{w1}(L)$ otherwise the mass mixing ratio used is $r_w(L) = \exp(r_{w2}(L))$. In addition, if TPW is less than 1 and any element of $r_{w1}(L)$ is less than zero then $\exp(r_{w2}(L))$ is substituted for that element (this may be changed for v5.0, since we do see some instances of very thin dry layers induced by this). In addition, the individual elements are never allowed to exceed the saturation mixing ratio, $r_s(L)$, given by

$$e_s = \sum_{i=0}^{8} a_i \cdot (T - 273.15)^i \tag{3.3.35}$$

The choice of coefficients is determined via an ICE flag. Water is valid over the range of $-85 \le T - 273.15 \le 70$ Celsius and the ice coefficients are valid over the range of $-85 \le T - 273.15 \le 70$ Celsius. The coefficients are given in Table 5.3.3.

Table 5.3.3. Vapor Pressure Coefficients (Flatau, Walto, and Cotton (1992)

i	water -85 → +70 C	ice -90 → 0 C
0	6.11583699	6.09868993
1	$4.44606896 \cdot 10^{-1}$	$4.99320233 \cdot 10^{-1}$
2	$1.43177157 \cdot 10^{-2}$	$1.84672631 \cdot 10^{-2}$
3	$2.64224321 \cdot 10^{-4}$	$4.02737184 \cdot 10^{-4}$
4	$2.99291081 \cdot 10^{-6}$	$5.65392987 \cdot 10^{-6}$
5	$2.03154182 \cdot 10^{-8}$	$5.21693933 \cdot 10^{-8}$
6	$7.02620698 \cdot 10^{-11}$	$3.07839583 \cdot 10^{-10}$
7	$3.79534310 \cdot 10^{-14}$	$1.05785160 \cdot 10^{-12}$
8	$-3.21582393 \cdot 10^{-16}$	$1.61444444 \cdot 10^{-15}$

If we assume $\overline{mw_t} \simeq \overline{mw_d}$ and g = 980.64 ≈ 1000 then the mass mixing ratio can be converted to layer column density (molecules/cm2) as follows

$$\Delta C_w(L) = \frac{r_w(L) \cdot N_A}{\overline{\mathrm{mw}}_w \cdot 1000 \cdot \Delta p(L)} \tag{5.3.36}$$

where $\overline{mw_t} \equiv \overline{mw_d} + \overline{mw_w}$

is the molecular weight for air, $\overline{mw_d}$ is the molecular weight of dry air, $\overline{mw_w}$ is the molecular weight of water, $\overline{mw_w}$ = 18.0151 grams/mole, and N_A is Avogadro's number = $6.02214199 \cdot 10_{23}$ molecules/mole. The conversion to layer column density is done by the routine colden.F. In v5.0 we will remove the approximations above. This should remove a moist bias of approximately 2% in the tropical region.

In a system that has performed a microwave physical retrieval of water vapor we can improve the regression solution over ocean if we adjust the regression water vapor to the total column water vapor from the microwave. This is done by summing the layer column densities from the microwave retrieval,

$$C_w^{MIT} = \sum \Delta C_w^{MIT}(L)$$

which is the total column density in molecules/cm2. The same calculation is done for the regression retrieval resulting in C_w^{REG}. We then multiply the layer column density by the ratio of the total column densities from the regression and microwave retrieval,

$$\Delta C_w^{\mathrm{ADJ}}(L) = \Delta C_w^{\mathrm{REG}}(L) \cdot \left(\frac{\sum_{L=1}^{L_{\mathrm{bot}}} \Delta C_w^{\mathrm{MIT}}(L)}{\sum_{L=1}^{L_{\mathrm{bot}}} \Delta C_w^{\mathrm{REG}}(L)} \right) \tag{5.3.37}$$

This is done in the routine amsu adj.F. Note that in version 5.0 this correction will be removed. With the loss of HSB the total water column derived from the AMSU radiances is not as accurate and this correction is removed.

5.3.9 Computing Ozone Mixing Ratio from Principal Component Scores

For ozone, the regression is trained on the natural logarithm of mass mixing ratio of ozone, $\log_e(r_o(L))$, in grams/kilo-gram (g/kg). For each level L (see Table 5.3.2) the mixing ratio of ozone can be given as

$$r_o(L) = \exp\left(\mathrm{MIN}\left[-3.5, \overline{A^v}_i + A^v_{i,k} \cdot P_{k,j}\right]\right) \qquad i = 4 + 4 \cdot (L-1) \tag{5.3.38}$$

Again, if we assume $\overline{mw}_t \simeq \overline{mw}_d$ and $g = 980.64 \approx 1000$ then the mass mixing ratio can be converted to layer column density (molecules/cm^2) as follows

$$\Delta C_o(L) = \frac{r_o(L) \cdot N_A}{\overline{\mathrm{mw}}_o \cdot 1000 \cdot \Delta p(L)} \tag{5.3.39}$$

where $\overline{mw}_o$ = 47.9982 grams/mole is the molecular weight of ozone and N_A is Avogadro's number = 6.02214199 ·10$_{23}$ molecules/mole.

5.3.10 The Surface Emissivity Regression

In the case of surface emissivity there is no truth datasets that we can utilize to train regressions with real AIRS radiance data. For emissivity we simulated J (l) cases where the infrared radiances were computed from the ECMWF forecast (15 December 2000) and a surface emissivity model (Fishbein, *et al.*, 2003) was used for l different kinds of surface conditions (in v4.0 we performed separate regressions for land, ocean, ice,

and snow, see Table 5.3.6). The eigenvector approach was not used. We used a subset of AIRS radiances for M window channels, $R_{(n(m),j)}$ to regress against the emissivities used to product those radiances, (i, j). The M frequencies, $n(m)$ are given in Table 5.5. The 39 frequencies where emissivity, (i, j), was specified is given in Table 5.3.4. Notice that short-wave observations are not used to predict short-wave emissivity. This regression relies on statistical correlations between the short-wave and long-wave to solve for these parameters.

The predictors consisted of the M radiances, written as signal-to-noise (see Eqn. 5.3.1), and two predictor to account for atmospheric transmittance as a function of viewing angle; one for which side of nadir the observation was made and the other is the cosine of the view angle. Since all $J(l)$ cases in the training ensemble see the surface, there is no subset for topography. Also, window channels require only a minor adjustment for view angle, so the complete ensemble was used rather than making separate regression for each view angle regime, as was done for the atmospheric parameters. The ocean emissivity is a well modeled function (*i.e.,* the AIRS science team uses the Masuda, *et al.,* (1988) model as modified by Wu and Smith (1997). The regression was performed on land, ocean, ice, and snow emissivity models. Figure 5.3.9 and Figure 5.3.10 are the average and standard deviation of surface emissivity for the four different types of land from the emissivity training used in the AIRS v4.0 regression. The complete predictor vector can be written as

$$P_{k,j} = \begin{pmatrix} R_{1,j} \\ R_{2,j} \\ \cdots \\ R_{M_\epsilon,j)} \\ \frac{1-\mathrm{sign}(\alpha_j)}{2} \\ 1-\cos(\frac{\pi \cdot \alpha_j}{180}) \end{pmatrix} \qquad i = 1, M+2 \tag{5.3.40}$$

where we can write,

$$\Delta X_{i,j} = X_{i,j} - < X_j >_{J_\epsilon(l)} \tag{5.3.41}$$

with the X_i's defined in Table 5.3.5 and the least square solution is given by

$$A^{l}_{i,k} = \Delta X_{i,j} \cdot \Delta P^{T}_{j,k} \cdot \left[\Delta P_{k,j} \cdot \Delta P^{T}_{j,k}\right]^{-1} \quad \text{for the } J_{\epsilon}(l) \text{ cases} \tag{5.3.42}$$

Again, once $A^{l}_{i,k}$ is determined we can combine the average of the geophysical emissivity parameter and the average of the predictor into a single value, called $\overline{A}_i$, so that our regression equation becomes

$$X_{j(v,L)} = \overline{A^{l}}_{i} + A^{l}_{i,k} \cdot P_{k,j} \tag{5.3.43}$$

where $\overline{A}^{l}_{i}$ is defined as

$$\overline{A^{l}}_{i} \equiv A^{l}_{i,k} \cdot < P_{k,j} >_{J_{\epsilon}(l)} \tag{5.3.44}$$

These regression coefficients have the same format as the ones described in sub-section 5.3.3 with geophysical index number given in Table 5.3.2.

We use the land fraction and microwave surface class (defined in Table 5.3.7 to determine which surface regression coefficients to utilize. In Table 5.3.6 the logic used in both training and application of the coefficients is shown.

Table 5.3.4. Frequencies for the 39-Point Model for Emissivity Regression

649.35	666.67	684.93	704.22	724.64
746.27	769.23	793.65	819.67	847.46
877.19	909.09	943.40	980.39	1020.4
1063.8	1111.1	1162.8	1204.8	1234.6
1265.8	1298.7	1333.3	1369.9	1408.4
1449.3	1492.5	1538.5	1587.3	1639.3
2173.9	2222.2	2272.7	2325.6	2380.9
2439.0	2500.0	2564.1	2631.6	

Table 5.3.5. AIRS Channels used in Surface EmissivityRegression

v3.0, v3.18			v4.0, (after 4/10/04)	
n	f(n), cm^{-1}		n	f(n), cm^{-1}
475	801.00		475	801.0990
484	804.29		484	804.3860
497	809.08		497	809.1800
528	820.73		528	820.8340
587	843.81		587	843.9130
787	917.21		787	917.3060
791	918.65		791	918.7470
843	937.81		843	937.9080
914	965.32		870	948.1840
950	979.02		914	965.4310
1138	1072.38		950	979.1280
1178	1092.31		1119	1063.285
1199	1103.06		1123	1065.216
1221	1114.53		1178	1092.451
1237	1123.02		1199	1103.199
1252	1131.08		1221	1114.675
1263	1216.84		1237	1123.162
1285	1228.09		1252	1131.229
			1263	1216.974
			1285	1228.225

Table 5.3.6. NOAA Regression Surface Classification Determination from % Land Cover (p) and Microwave Surface Classification (m)

l	surface class	logic
1	non-frozen land	((m=0) or (m=1)) and $p > 1\%$
2	non-frozen water	(m=2) or (p $\leq 1\%$ and ((m=0) or (m=1)))
3	ice	(m=3) or (m=4) or (m=5)
4	snow	(m=5) or (m=7)

Table 5.3.7. Microwave Surface Class Definitions

m	microwave surface classification
0	coastline
1	land (land cover > 50%)
2	ocean
3	high microwave emissivity sea ice
4	low microwave emissivity sea ice
5	snow (higher frequency scattering)
6	glacier/snow (very low frequency scattering)
7	snow (lower frequency scattering)

Figure 5.3.9. Mean Value of the Emissivity Training Database for the 4 Surface Types used in the V4.0 Regression

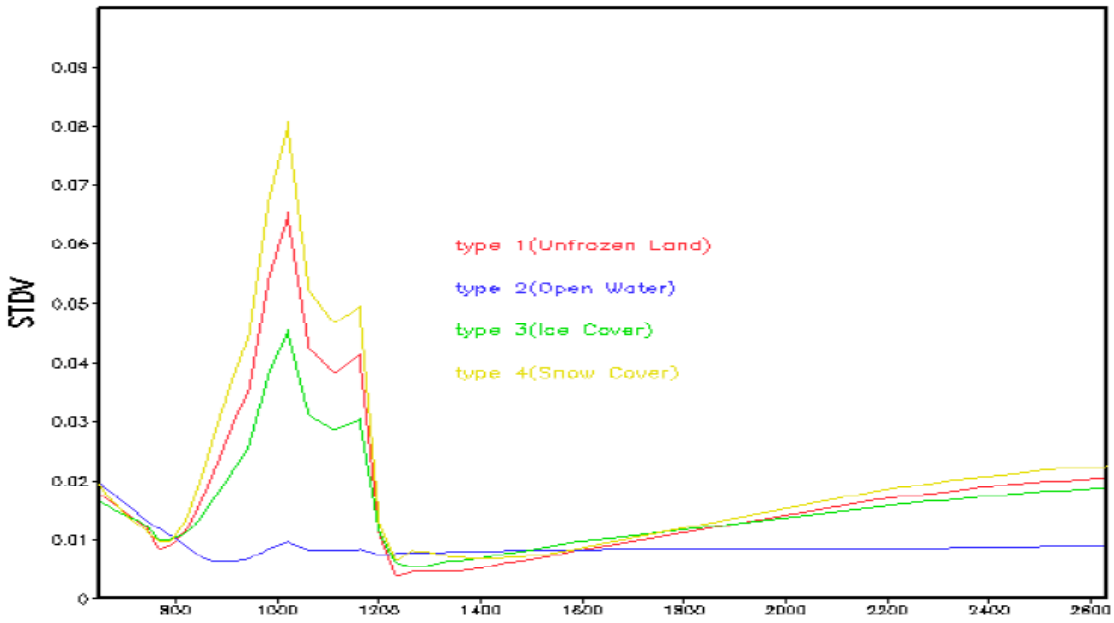

Figure 5.3.10. Standard Deviation of the Emissivity Training Databasefor the 4 Surface Types used in the V4.0 Regression

Table 5.3.8. AIRS Channels used in Eigenvector Computation

1	2	3	4	5	6	7	8	9	10	11	14	15	16	17
18	19	20	21	22	23	24	25	26	27	28	29	30	31	32
33	34	35	36	37	38	39	40	41	42	43	44	45	46	47
50	51	52	53	54	55	56	57	58	59	60	61	62	63	64
65	66	67	68	69	70	71	72	73	74	75	76	77	78	79
80	81	82	83	84	85	86	87	88	89	90	91	92	93	94
95	96	97	98	99	100	101	102	103	104	105	106	107	108	109
110	111	112	113	114	115	116	117	118	119	120	123	124	125	126
127	128	129	130	131	135	136	137	138	139	140	141	142	143	144
145	146	147	148	149	150	151	152	153	154	155	156	157	158	159
160	161	162	163	164	165	166	167	168	169	170	171	172	173	174
175	176	177	178	179	180	181	182	183	184	185	186	187	188	189
190	191	192	193	194	195	196	197	198	199	200	201	202	203	204
205	206	207	208	209	210	211	212	213	214	215	216	217	218	219
220	221	222	223	224	225	226	227	228	229	230	231	232	233	234
235	236	237	239	240	241	242	243	244	245	246	247	248	249	250
251	252	253	254	255	256	257	258	259	260	261	262	263	264	265
266	267	268	269	270	271	272	273	274	275	278	279	280	281	282
283	284	285	286	287	289	290	293	294	295	296	297	298	299	300
301	302	303	304	306	307	308	309	310	311	314	315	316	317	319
320	322	323	325	327	329	330	332	333	334	336	337	338	339	340
343	344	345	347	348	349	351	352	354	355	356	357	358	359	360
362	364	366	368	369	371	375	376	378	380	383	385	387	389	390
392	393	394	395	397	399	400	403	406	407	408	409	410	411	414
416	417	418	419	421	422	423	424	425	426	427	429	430	433	435
436	437	438	439	441	443	444	445	449	450	452	453	455	456	459
462	465	469	471	473	475	476	478	479	480	482	483	484	485	486
493	496	497	501	503	504	505	509	513	516	518	519	521	522	523
524	526	527	528	529	530	532	533	536	538	539	540	541	544	546
547	548	550	551	552	555	556	559	560	562	563	564	565	566	567
570	572	575	576	577	579	580	584	587	592	593	594	597	600	606
607	609	613	614	616	617	618	619	621	626	627	628	632	633	634
635	637	638	639	640	641	642	643	644	645	646	647	648	649	650
651	652	653	654	656	657	658	659	660	661	662	663	665	666	667
668	669	671	672	673	674	675	676	677	679	680	683	684	685	687
689	690	691	692	693	694	695	696	697	698	699	700	701	702	704
705	707	708	709	710	711	712	713	714	718	719	720	721	722	724
725	726	727	728	729	730	731	732	735	737	738	739	740	741	744
745	746	748	752	754	757	758	759	761	763	764	766	767	769	771
772	774	775	776	777	778	779	780	781	782	785	786	787	788	791
792	793	794	796	797	798	799	804	805	807	808	809	810	811	812
813	814	816	818	819	820	821	822	823	824	825	829	833	838	839
840	843	844	845	846	847	848	851	852	853	854	856	857	858	861
862	863	869	870	872	873	874	877	881	882	888	893	895	896	897
898	902	903	904	905	908	909	914	916	921	924	929	932	933	935
936	944	946	948	950	951	953	955	958	959	960	963	964	967	968
969	971	972	973	976	977	978	982	984	985	986	987	988	989	992
993	996	997	998	999	1000	1002	1003	1004	1005	1006	1008	1010	1011	1012
1015	1016	1017	1019	1020	1022	1024	1025	1026	1027	1028	1029	1030	1031	1032

Table 5.3.8. AIRS Channels (Continued)

1033	1034	1038	1039	1042	1043	1044	1045	1046	1047	1048	1050	1051	1052	1055
1057	1058	1060	1061	1062	1064	1065	1067	1069	1070	1071	1072	1074	1075	1077
1078	1079	1080	1081	1082	1083	1084	1085	1086	1088	1089	1090	1097	1098	1099
1100	1101	1103	1104	1106	1107	1108	1110	1111	1113	1114	1115	1116	1117	1118
1119	1121	1122	1123	1130	1131	1134	1136	1137	1139	1140	1141	1142	1143	1144
1145	1146	1147	1150	1151	1152	1153	1154	1155	1156	1157	1158	1159	1160	1161
1162	1163	1164	1168	1169	1170	1171	1172	1174	1175	1176	1177	1178	1179	1180
1181	1182	1183	1184	1186	1187	1188	1189	1194	1195	1196	1199	1200	1201	1202
1204	1205	1206	1207	1209	1211	1212	1213	1214	1215	1218	1219	1220	1221	1223
1226	1227	1228	1229	1231	1232	1233	1234	1235	1236	1237	1238	1241	1245	1247
1248	1249	1250	1252	1253	1254	1257	1258	1259	1260	1261	1262	1263	1264	1265
1266	1267	1268	1269	1270	1271	1272	1273	1274	1275	1276	1277	1278	1279	1284
1285	1286	1300	1301	1302	1303	1304	1305	1306	1307	1308	1309	1310	1311	1312
1313	1314	1315	1316	1317	1318	1319	1320	1321	1322	1323	1324	1325	1326	1327
1329	1330	1331	1332	1334	1335	1336	1337	1338	1339	1340	1341	1342	1343	1344
1345	1346	1347	1348	1350	1352	1353	1356	1357	1358	1359	1360	1361	1362	1363
1364	1365	1366	1367	1368	1369	1370	1371	1372	1373	1374	1375	1376	1377	1378
1379	1381	1382	1383	1384	1385	1386	1387	1388	1389	1390	1391	1392	1393	1394
1395	1396	1398	1400	1401	1402	1403	1404	1405	1406	1407	1408	1409	1410	1411
1412	1413	1414	1415	1416	1417	1418	1419	1420	1421	1422	1423	1424	1425	1426
1427	1428	1429	1430	1431	1432	1433	1434	1435	1436	1437	1438	1439	1440	1441
1442	1443	1444	1445	1446	1447	1448	1449	1450	1451	1452	1453	1454	1455	1456
1457	1458	1459	1460	1461	1462	1463	1464	1465	1466	1467	1468	1469	1470	1471
1472	1473	1474	1475	1477	1478	1480	1481	1482	1494	1495	1496	1497	1498	1499
1500	1501	1502	1503	1504	1505	1506	1508	1509	1510	1511	1513	1514	1516	1517
1518	1519	1520	1521	1522	1523	1524	1525	1526	1527	1528	1529	1530	1531	1532
1533	1534	1535	1536	1537	1539	1540	1541	1542	1544	1545	1546	1547	1548	1549
1550	1551	1552	1553	1554	1555	1556	1557	1558	1559	1560	1561	1562	1563	1564
1565	1566	1567	1568	1569	1570	1571	1572	1573	1574	1575	1576	1577	1578	1580
1581	1582	1583	1584	1585	1586	1587	1588	1589	1590	1591	1592	1593	1594	1595
1596	1597	1598	1599	1600	1601	1602	1604	1605	1606	1607	1608	1609	1610	1611
1612	1613	1614	1615	1616	1618	1619	1620	1621	1622	1623	1624	1625	1626	1627
1628	1629	1630	1631	1632	1633	1634	1635	1636	1637	1638	1639	1640	1641	1642
1643	1644	1645	1646	1647	1648	1649	1650	1651	1652	1653	1654	1655	1656	1657
1658	1659	1660	1661	1662	1663	1664	1665	1666	1667	1668	1669	1670	1671	1673
1674	1675	1676	1677	1678	1679	1680	1681	1682	1683	1684	1685	1686	1687	1688
1692	1693	1694	1695	1696	1697	1698	1699	1700	1701	1702	1703	1704	1705	1706
1707	1708	1709	1710	1711	1714	1715	1716	1717	1718	1719	1720	1721	1722	1723
1724	1737	1738	1739	1740	1742	1743	1744	1745	1747	1748	1749	1750	1751	1752
1753	1754	1755	1756	1757	1758	1760	1761	1762	1763	1764	1765	1766	1767	1768
1769	1770	1771	1772	1773	1775	1776	1777	1778	1779	1780	1783	1785	1789	1790
1793	1794	1795	1796	1797	1798	1799	1800	1801	1803	1804	1805	1806	1807	1808
1809	1810	1811	1813	1814	1815	1816	1817	1818	1819	1821	1822	1823	1824	1825
1826	1827	1828	1829	1830	1831	1832	1833	1834	1835	1838	1839	1840	1841	1843
1844	1845	1846	1847	1848	1849	1850	1851	1852	1853	1854	1855	1856	1857	1858
1859	1860	1861	1862	1863	1864	1865	1866	1867	1868	1869	1870	1871	1872	1873
1874	1875	1876	1877	1878	1879	1880	1881	1882	1883	1884	1885	2109	2110	2111
2112	2113	2114	2115	2116	2117	2118	2119	2120	2121	2122	2123	2124	2125	2126
2127	2128	2129	2130	2131	2132	2133	2134	2135	2136	2137	2138	2139	2140	2141

Table 5.3.8. AIRS Channels (Continued)

2142	2143	2144	2145	2146	2147	2148	2149	2150	2152	2154	2155	2156	2157	2158
2159	2160	2161	2162	2163	2164	2165	2166	2167	2168	2169	2170	2171	2172	2173
2174	2175	2176	2177	2178	2179	2180	2181	2182	2183	2184	2185	2186	2187	2188
2189	2190	2191	2192	2193	2194	2195	2196	2197	2198	2199	2200	2201	2202	2203
2204	2205	2206	2207	2208	2209	2210	2211	2212	2213	2214	2215	2216	2217	2218
2219	2220	2221	2222	2223	2224	2225	2226	2227	2228	2229	2230	2231	2232	2233
2234	2235	2236	2237	2239	2240	2241	2242	2244	2245	2246	2247	2248	2249	2250
2251	2252	2253	2273	2274	2275	2276	2277	2278	2279	2280	2281	2282	2283	2284
2285	2286	2287	2289	2290	2291	2292	2293	2294	2295	2296	2297	2298	2299	2300
2301	2302	2303	2304	2305	2306	2307	2308	2309	2310	2311	2312	2313	2314	2315
2316	2317	2318	2319	2320	2321	2322	2323	2324	2325	2326	2327	2328	2329	2330
2331	2332	2333	2334	2335	2336	2337	2338	2339	2340	2341	2342	2343	2344	2345
2346	2347	2348	2349	2350	2351	2352	2353	2354	2355	2356	2358	2360	2361	2362
2363	2364	2365	2366	2367	2368	2369	2370	2371	2372	2373	2374	2376	2377	2378

5.3.11 References for Statistical Regression

Goldberg, M. D., Y. Qu, L. M. McMillin, W. Wolf, L. Zhou and M. Divakarla 2003. AIRS near-real-time products and algorithms in support of operational weather prediction. *IEEE Trans. Geosci. Remote Sens.***41** p.379-389.

Fishbein, E., C. B. Farmer, S. L. Granger, D. T. Gregorich, M. R. Gunson, S. E. Hannon, M. D. Hofstadter, S. Y. Lee, S. S. Leroy and L. L. Strow 2003. Formulation and validation of simulated data for the atmospheric infrared sounder (AIRS). *IEEE Trans. Geosci. Remote Sens.* **41** p. 314-329.

Flatau, P. J., R. L. Walko and W. R. Cotton 1992. Polynomial fits to saturation vapor pressure. *J. Appl. Meteor.* **31** p.1507-1513.

Masuda, K., T. Takashima and Y. Takayama 1988. Emissivity of pure and sea waters for the model sea surface in the infrared window regions. *Remote Sens. Envir.* **24** p.313-329.

Press, W. H., B. P. Flannery, S. A. Teukolsky, and W. T. Vettering 1986. **Numerical Recipes in FORTRAN: the art of scientific computing**, *Cambridge Univ. Press*, 818 pgs.

Smith, W. L. and H. M. Woolf 1976. The use of eigenvectors of statistical covariance matrices for interpreting satellite sounding radiometer observations. *J. Atmos. Sci.* **33** p.1127-1140.

Wu, X. and W. L. Smith 1997. Emissivity of rough sea surface for 8-13 um: modeling and verification. *Applied Optics* **36** p.2609-2619.

5.4 Final Product

5.4.1 Introduction

To satisfy the science requirements of NASA's Earth Science Enterprise, a final adjustment is made to the first product based on the difference between calculated and cloud-cleared radiances, producing more accurate results. In addition, final product steps calculate cloud parameters and research products not generated by the first product steps.

When solving for a set of geophysical parameters, it is desirable to be able to choose an appropriate set of parameters to solve for and select channels that are both sensitive to those parameters and relatively insensitive to other parameters. In general, channels will be affected by more than one type of parameter. For example, channels with radiances sensitive to the water vapor or ozone distribution are also sensitive to the temperature profile and often to the surface skin temperature. Our approach is to solve sequentially for the surface parameters, temperature profile, water vapor profile, and ozone profile in that order. In this approach, variables already solved for, used in conjunction with first guess variables, are kept fixed when solving for the next set of variables. Table 5.4.1 lists the variables solved for and the number of channels used in each step. The above order is chosen because channels can be selected for a given step that is relatively insensitive to variables to be solved for subsequently. The general methodology described in Section 5.4 is identical to that shown in Susskind, *et al.*, (2003). Some details have changed however, based on experience using observed, rather than simulated, AIRS data. The areas where modifications to Susskind, *et al.*, (2003) have been made are indicated.

The iterative solution to the problem contains equations that are of the form of equation 5.3.13. However, the final product methodology solves for updates to coefficients of functions of temperature, moisture, etc., rather than updates to the geophysical parameters themselves. Therefore, the terms in the equation have a very different meaning. For this reason, a different notation is used so as not to confuse the reader. For example, in place of A in the analog of equation 5.3.13, which refers to the derivative of

the radiance with respect to changes in a geophysical parameter, the sensitivity of the radiances to changes in the coefficients of the expansion functions, S, is used.

Table 5.4.1. Variables and Channels

Variables	Channels	Frequency Ranges
	Ground Temperature Retrieval	
T_s, 2 IR spectral emissivity	15	759 - 1228 cm^{-1}
functions, 1 IR spectral bi-directional	10	2456 - 2659 cm^{-1}
reflectance function; 1 MW spectral	5	23.8 - 89 GHz
emissivity function	1	150 GHz
	Temperature Profile Retrieval	
23 layer temperature-	50	664 - 760 cm^{-1}
functions (trapezoids)	6	1238 - 1382 cm^{-1}
	9	2387 - 2396 cm^{-1}
	11	50.3 - 57.29 GHz
	Water Vapor Profile Retrieval	
10 layer column density functions	1	938 cm^{-1}
	33	1310 - 1606 cm^{-1}
	8	2607 - 2657 cm^{-1}
	4	23.8 - 89 GHz
	3	150 – 189.31 GHz
	Ozone Profile Retrieval	
7 layer column density functions	26	997 - 1069 cm^{-1}
	CO Profile Retrieval	
4 layer column density functions	20	2183 - 2193 cm^{-1}
	Cloud Clearing	
4 unknown extrapolation parameters	33	672 - 755 cm^{-1}
	5	790 - 1133 cm^{-1}
	6	2420 - 2658 cm^{-1}
	Cloud Parameters	
2 cloud top pressures	33	672 - 755 cm^{-1}
2 effective cloud fractions per FOV	5	790 - 1133 cm^{-1}

Total: 57 variables 214 channels (AIRS + AMSU-A + HSB)

A total of 195 AIRS channels, 15 AMSU-A channels, and 4 HSB channels are selected for use in the AIRS/AMSU-A/HSB retrieval algorithm. Some of the surface parameter sounding channels are also used in the water vapor or temperature profile retrievals. Therefore, the total number of channels is less than the sum of the channels in column 2. The 214 channels are used to solve for 42 variables. HSB failed early in the mission. The HSB channels are not included in my processing step when AIRS is run in the AIRS/AMSU-A only mode. Time periods before HSB failed were analyzed in both the AIRS/AMSU-A/HSB processing mode and the AIRS/AMSU-A processing mode so as to allow for consistency of products generated after HSB failed.

The general AIRS/AMSU-A/HSB retrieval algorithm does not require any field of view to be cloud free (Susskind, *et al.*, 1996). The algorithm used in the final product retrieval consists of a number of steps. Before the full physical retrieval procedure begins, there are a number of startup steps: (S1) Use the state resulting from the AIRS regression, $X^{(R)}$, as an initial guess for the temperature, moisture, and ozone profiles. $X^{(R)}$ was computed using $\hat{R}_i^{(1)}$, derived based on the microwave state $X^{(M)}$. (S2) Derive an estimate of the cloud-cleared radiances and clear-column-radiance noise covariance matrix, $\hat{R}_i^{(2)}$ and $\hat{M}_{ij}^{(2)}$, based on the geophysical state $X^{(R)}$. (S3) $X^{(R)}$ is now improved to give the initial guess used in the physical retrieval process $X^{(0)}$, and is also used to generate $\hat{R}_i^{(3)}$ and $\hat{M}_{ij}^{(3)}$. This loop ends the basic startup procedure, that precedes the physical retrieval process. The physical retrieval process sequentially determines: (1) surface parameters; (2) temperature profile; (3) water vapor profile; and (4) ozone profile. This improved state is used to derive the final cloud -cleared radiances $\hat{R}_i^{(4)}$ and channel noise covariance matrix $\hat{M}_{ij}^{(4)}$. Cloud parameters as well as OLR and clear-sky OLR are derived based on retrieved geophysical state $X^{(1)}$, or the microwave state $X^{(M)}$, depending on quality control. A second pass physical retrieval is now performed using $\hat{R}_i^{(4)}$ and $\hat{M}_{ij}^{(4)}$ to improve the surface parameters and temperature

profile. A CO profile is then derived using the final state $X^{(2)}$ and $\hat{R}_i^{(4)}$ and $\hat{M}_{ij}^{(4)}$. A flow diagram of the steps in the physical retrieval algorithm is given in Figure 5.4.1.

The general approach used in the physical retrieval algorithm to solve for all the geophysical parameters is in the form of iterative, constrained least-squares solutions, one for each set of variables to be solved for. The form of the equations to be solved is identical for each of the four steps. The following sections described the details of all the steps in the physical retrieval algorithm.

5.4.2 Overview of the AIRS Physical Retrieval Algorithm

AIRS has 2386 spectral channels. Different channels are used in different steps of the AIRS physical retrieval process. Figure 5.4.2 shows an example of an AIRS spectrum. All AIRS channels used in any physical retrieval step or in the cloud clearing step are marked in Figure 5.4.2. Figure 5.4.2 includes channels sensitive to CH_4 profile, but this retrieval step is not performed in Version 4.0 of the Science Team retrieval algorithm. Table 5.4.2, lists all the AIRS channels along with AMSU-A and HSB channels, used in cloud clearing or physical retrieval steps. AMSU-A channels 8-14 are all in the vicinity of 57.29 GHz and all listed as such in Table 5.4.2. Also indicated in Table 5.4.2 are the steps in which all channels are used.

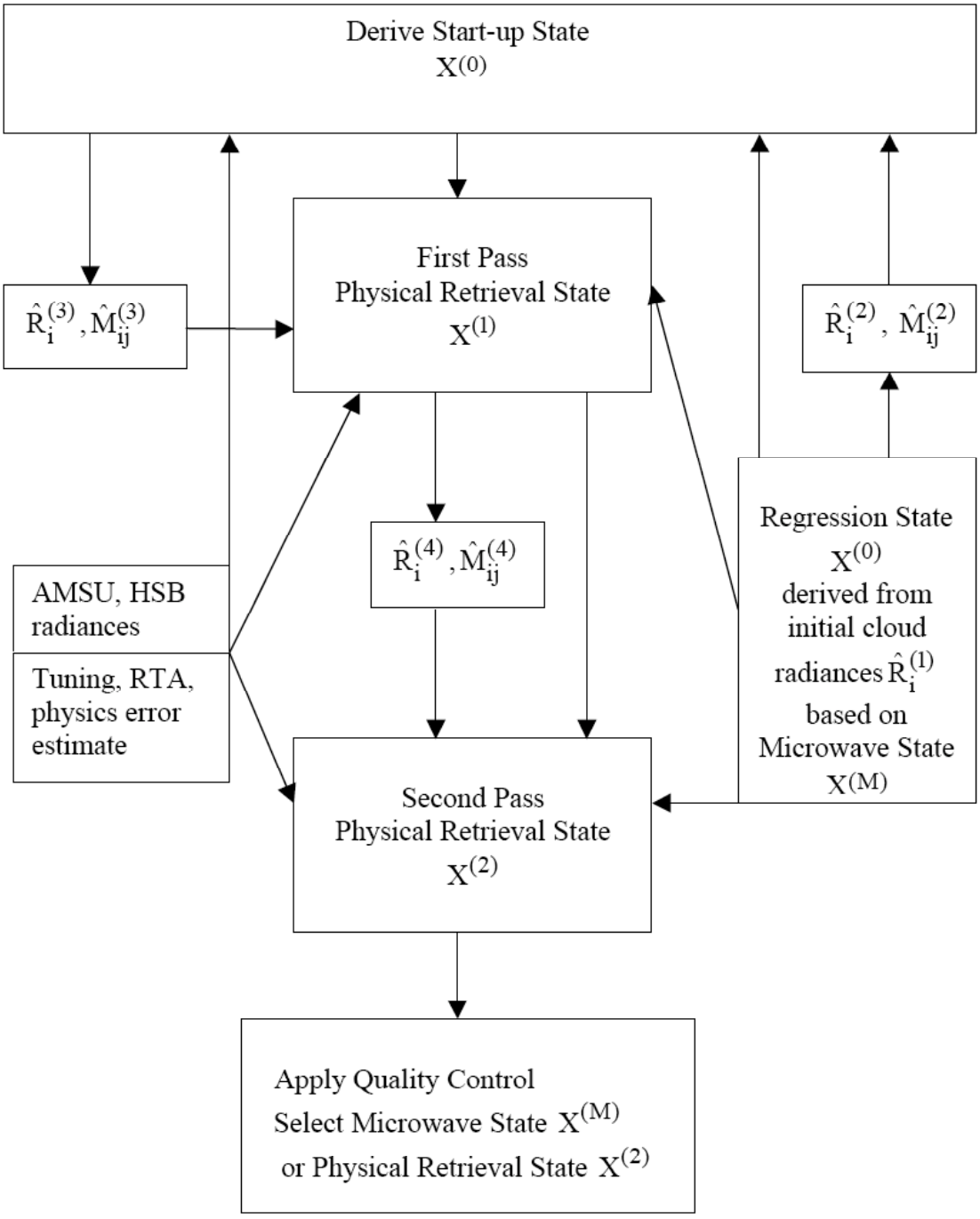

Figure 5.4.1. Physical Retrieval Flowchart

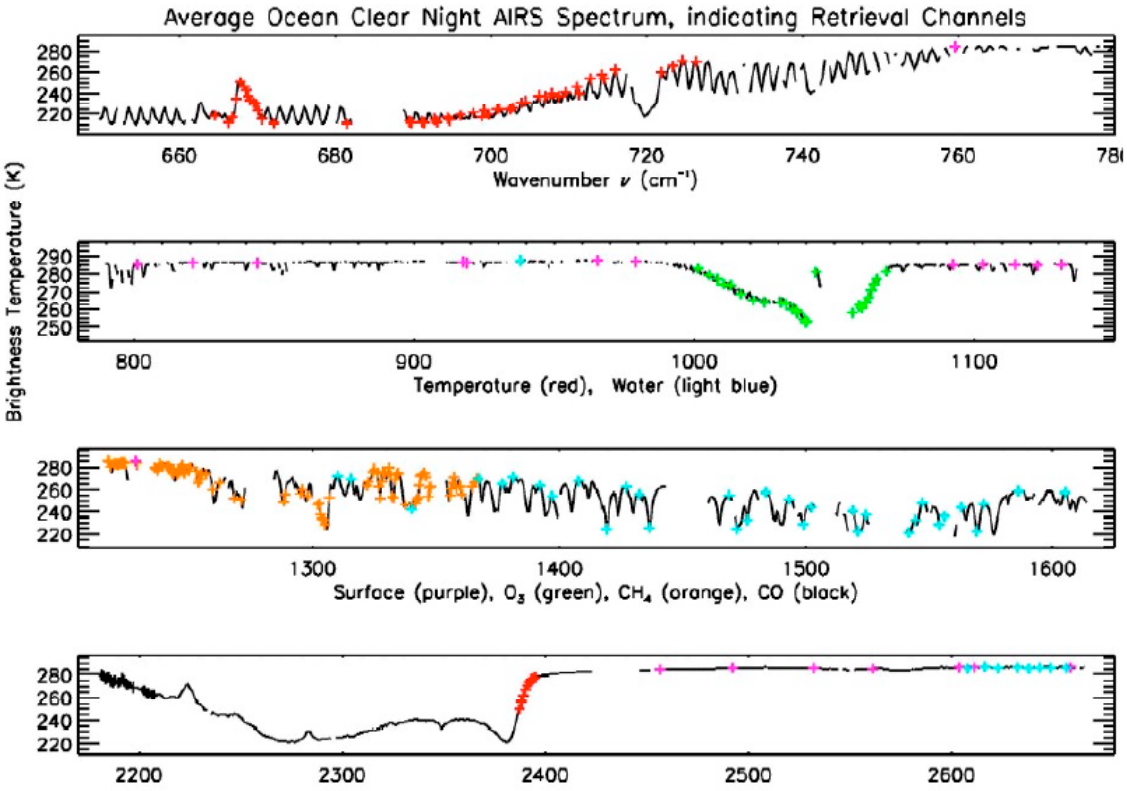

Figure 5.4.2. AIRS Channels, Physical Retrieval or Cloud Clearing

Table 5.4.2. AIRS, AMSU-A, and HSB Channels, Physical Retrieval and Cloud Clearing

$\nu(cm^{-1}$ or GHz)	Temp1	Temp2	Strat	Surf	H_2O	O_3	CC	HGT	CO
650.33			X						
650.81			X						
652.01			X						
653.45			X						
654.90			X						
656.36			X						
658.07			X						
659.54			X						
662.51			X						
662.76			X						
663.01			X						
664.51	X	X							
666.26	X	X							
666.77	X	X							
667.27	X	X	X						
667.52			X						
667.77	X	X	X						
668.03			X						
668.28	X	X	X						
668.53	X	X	X						
668.79	X	X	X						
669.04	X	X	X						
669.55	X	X	X						
669.80	X	X	X						
670.06	X	X	X						
670.57	X	X							
672.10	X	X					X	X	
677.53			X						
681.46	X	X					X	X	
689.49	X	X							
689.76	X	X							
691.12	X	X							
691.39	X	X							
692.76	X	X					X	X	
693.03	X	X					X	X	
694.40	X	X							
694.67	X	X							
696.05	X	X					X	X	
697.71	X	X							

$\nu(cm^{-1}$ or GHz)	Temp1	Temp2	Strat	Surf	H_2O	O_3	CC	HGT	CO
698.82	X	X							
699.10	X	X							
699.66	X	X							
700.78	X	X					X	X	
701.06	X	X					X	X	
702.46	X	X							
702.74	X	X					X	X	
703.87	X	X					X	X	
704.44	X	X					X	X	
706.14	X	X					X	X	
706.99	X	X					X	X	
707.85	X	X					X	X	
708.71	X	X					X	X	
709.57	X	X					X	X	
711.00	X	X					X	X	
711.29	X	X					X	X	
712.74	X	X					X	X	
714.19	X	X					X	X	
714.48	X	X					X	X	
715.94	X	X					X	X	
721.84	X	X					X	X	
723.03							X	X	
723.33	X	X					X	X	
724.52	X	X					X	X	
726.33	X	X					X	X	
738.48							X	X	
746.01							X	X	
747.60							X	X	
749.20							X	X	
750.48							X	X	
753.06							X	X	
755.33							X	X	
759.57		X		X					
790.32							X	X	
801.10				X					
820.83				X					
843.91				X			X	X	
917.31				X					
918.75				X					
937.91				X	X		X	X	
965.43				X					
979.13				X					
997.11						X			

$\nu(cm^{-1}$ or GHz)	Temp1	Temp2	Strat	Surf	H_2O	O_3	CC	HGT	CO
998.39						X			
999.67						X			
1001.38						X			
1003.54						X			
1005.26						X			
1006.56						X			
1008.30						X			
1010.48						X			
1011.79						X			
1013.11						X			
1014.87						X			
1016.64						X			
1018.41						X			
1020.63						X			
1021.97						X			
1023.31						X			
1061.33						X			
1061.81						X			
1062.29						X			
1063.26						X			
1064.22						X			
1064.70						X			
1065.19						X			
1068.58						X			
1069.07						X			
1092.42				X			X	X	
1103.17				X					
1114.64				X					
1122.60				X					
1131.20				X					
1133.91							X	X	
1228.23				X					
1238.11		X							
1251.36		X							
1285.48		X							
1310.18					X				
1315.47					X				
1330.98		X							
1334.61		X							
1340.20					X				
1367.25					X				
1376.89					X				
1381.21		X			X				

$\nu(cm^{-1}$ or GHz)	Temp1	Temp2	Strat	Surf	H_2O	O_3	CC	HGT	CO
1392.15					X				
1397.13					X				
1407.77					X				
1419.15					X				
1427.23					X				
1432.47					X				
1436.58					X				
1468.83					X				
1471.91					X				
1476.25					X				
1483.74					X				
1493.22					X				
1498.96					X				
1502.17					X				
1519.07					X				
1521.05					X				
1524.35					X				
1541.77					X				
1544.48					X				
1547.20					X				
1554.04					X				
1556.10					X				
1563.01					X				
1569.29					X				
1572.09					X				
1586.26					X				
1605.05					X				
2181.49									X
2182.40									X
2183.31									X
2184.21									X
2185.12									X
2186.03									X
2186.94									X
2187.85									X
2189.67									X
2190.58									X
2191.50									X
2192.41									X
2193.33									X
2194.24									X
2196.99									X
2202.51									X

$\nu(cm^{-1}$ or GHz)	Temp1	Temp2	Strat	Surf	H_2O	O_3	CC	HGT	CO
2203.44									X
2204.36									X
2206.21									X
2207.14									X
2387.18	X	X							
2388.15	X	X							
2389.13	X	X							
2390.11	X	X							
2391.09	X	X							
2392.07	X	X							
2393.05	X	X							
2394.03	X	X							
2395.01	X	X							
2419.83							X		
2456.48				X					
2492.08				X			X		
2531.98				X					
2561.13				X			X		
2603.66				X					
2607.89					X				
2611.07							X		
2616.38				X	X				
2622.79				X	X				
2632.47					X		X		
2637.87				X	X				
2643.30				X	X				
2648.75					X				
2656.42					X				
2658.62				X			X		
23.80				X	X				
31.40				X	X				
50.30	X	X	X	X					
52.80	X	X	X	X					
53.59	X	X	X						
54.40	X	X	X						
55.50	X	X	X						
57.29	X	X	X						
57.29	X	X	X						
57.29	X	X	X						
57.29	X	X	X						
57.29	X	X	X						
57.29	X	X	X						

$\nu(cm^{-1}$ or GHz)	Temp1	Temp2	Strat	Surf	H_2O	O_3	CC	HGT	CO
89.00				X	X				
150.00				X	X				
183.31					X				
183.31					X				
183.31					X				

5.4.2.1 Steps in the AIRS Final Product Algorithm

The AIRS final product algorithm is comprised of a number of sequential steps listed below. All steps start from the conditions found in the previous step, with appropriate computed uncertainty estimates, δX^0 (see Section 5.4.9), unless otherwise noted.

1. Use as a starting point the microwave product which agrees with the AMSU-A and HSB radiances (Rosenkranz, 2000). This provides initial values of temperature and moisture profiles, surface skin temperature, microwave spectral emissivity, and liquid water, W_{liq}. The initial value of W_{liq} is held fixed in all subsequent retrieval steps. This is followed by a temperature profile retrieval using AMSU-A radiances as well as AIRS radiances for stratospheric sounding channels that never see clouds to update the temperature profile. As part of this temperature profile retrieval, the surface skin temperature and microwave spectral emissivity is also updated. The geophysical parameters retrieved in this step are called the MW/strat IR retrieval. To the extent that HSB channels are present, the option exists to then perform a moisture profile retrieval using HSB channels.

2. Determine initial cloud cleared radiances $\hat{R}_i^1$ (as in Section 5.2) using the atmospheric and surface parameters obtained in Step 1. A cloud parameter retrieval is also performed to help determine which IR channels are not affected by clouds. These cloud parameters are also taken as the final cloud parameters if the combined IR/MW retrieval is not used (see Step 16). The AIRS channels used in the cloud clearing and cloud parameter retrieval steps are shown in Table 5.4.2. Short wave window channels aid in cloud clearing during the day because clouds appear warm in shortwave window channel as a result of solar indication reflected by the clouds. Clouds generally appear cold in the longwave window channels however. Thus, cloudier cases can be more easily distinguished from colder cases. For the same reason, the shortwave window channels are not used in the cloud parameter retrieval step because of the difficulty in the physical modeling of the effects of sunlight reflected by clouds.

3. Determine the first guess IR surface parameters and temperature-moisture-ozone profile using $\hat{R}_i^1$ based on a regression step using 1524 AIRS channels (as in Section 5.3).

4. Produce an improved temperature profile and microwave spectral emissivity, starting from the surface and atmospheric parameters determined in step 3, using the AMSU-A channel radiances and AIRS channel radiances which do not see clouds. The AIRS channels used in this step are listed in Table 5.4.2 under the column marked Strat. The surface skin temperature is not updated as it is estimated better from AIRS radiances than can be determined from AMSU radiances. This retrieval step is referred to as AMSU/strat IR.

5. Determine updated cloud-cleared radiances, $\hat{R}_i^2$, taking advantage of the geophysical parameters determined in Step 3. $\hat{R}_i^2$ is considerably more accurate than $\hat{R}_i^1$ because the surface and atmospheric parameters obtained from the AIRS regression step are more accurate than those from the microwave first product, especially the infra-red surface spectral properties which are not determined from the microwave retrieval.

6. Perform a surface parameter retrieval using AIRS surface-sounding channels shown in Figure 1 along with AMSU channels 1, 2 and 15. This produces a new skin temperature, IR and microwave spectral emissivity, and IR spectral bi-directional reflectance.

7. Determine $\hat{R}_i^3$ and new cloud parameters using the geophysical parameters determined in Step 6.

8.-11. Use $\hat{R}_i^3$ to sequentially determine surface parameters, temperature profile, humidity profile, and ozone profile using the appropriate channels shown in Figure 1. AMSU-A temperature sounding channels 3-6 and 8-14 are also included in the determination of the temperature profile. AIRS and AMSU channels used in the first pass temperature retrieval are listed in Table 5.4.2 in the column Temp1. The results of these steps are called the first pass retrieved products.

12. Update the temperature profile, using only AMSU-A radiances and AIRS channel radiances insensitive to clouds. This profile is also used in the application of quality flags and is referred to as the test microwave only retrieval.

13. Using the first pass retrieved products and updated temperature profile, determine $\hat{R}_i^4$, and the final cloud parameters.

14. Repeat steps 8 and 9 using $\hat{R}_i^4$ to obtain the final product surface parameters and temperature profile. The initial guess used in the second pass surface parameter and temperature profile retrievals is identical to that of the first pass but all other parameters are updated, such as the clear column radiances, moisture profile, etc. The channel noise covariance matrix is also updated to account for better estimates of the other parameters. In addition, channels in the water vapor band which are highly sensitive to lower tropospheric water vapor are included in the final temperature profile step (but not the first pass) because an accurate moisture profile has now been retrieved. These channels are indicated in the AIRS channels used in the second pass temperature

retrieval under the column Temp2. The moisture profile and ozone profile retrieval steps are not repeated, as no appreciable improvement in parameters resulted from further retrieval steps. The geophysical parameters retrieved from this step and the following steps are called the combined IR/MW retrieval.

15. Determine the CO profile using channels listed under CO in Table 5.4.2.

16. Determine whether products derived in Steps 1 and 2 (MW/strat IR retrieval) or 13 and 14 (IR/MW retrieval) should be reported. Apply quality control flags to all retrieved parameters.

17. Compute OLR and clear sky OLR using the appropriate state, either from Step 14 geophysical parameters and Step 13 cloud parameters, or Step 1 geophysical parameters and Step 2 cloud parameters.

5.4.3 General Iterative Least Squares Solution

An iterative approach is used to linearize the radiative transfer equation about the n^{th} iterative parameters X_ℓ^{n+1}. The iterative retrieval process described here is different from the use of different passes in the determination of η. The values of $\hat{R}_i$ used in the iterative retrieval loop are held fixed in a given pass. The $n+1^{th}$ iterative estimate of X_ℓ is expanded according to

$$X_\ell^{n+1} = X_\ell^n + \sum_{j=1}^{J} F_{\ell j} \Delta A_n^j = X_\ell^0 + \sum_{j=1}^{J} F_{\ell j} A_j^n \qquad 5.4.1$$

where the columns of F represent a set of functions, X_ℓ^0 is the initial guess, and A_j^n are corresponding coefficients given by

$$A_j^n = A_j^{n-1} + \Delta A_j^n \qquad 5.4.2$$

which together with X_ℓ^0 determine the solution. A solution is found that attempts to minimize the residuals $\Delta\Theta_i^n$ weighted inversely with respect to expected noise levels for

the channels used to determine A_j. The residual for channel i is defined by

$$\Delta\Theta_i^n = \left(\hat{R}_i - R_i^n\right)\left(\frac{dB}{dT}\right)^{-1}_{\Theta_i^n} \qquad 5.4.3$$

where $\hat{R}_i$ is the reconstructed clear column radiance, R_i^n is the radiance computed from the n^{th} iterative parameters, and Θ_i^n is the brightness temperature computed from the n^{th} iterative parameters. The nth iteration residual for channel i is attributed to errors in the coefficients, δA_j^n, and to noise effects, i.e.,

$$\Delta\Theta_i^n = \sum_j S_{ij}^n \, \delta A_j^n + \tilde{\Theta}_i \qquad 5.4.4$$

where S_{ij} is an element of the sensitivity matrix or Jacobian given by

$$S_{ij}^n = \frac{\partial R_i^n}{\partial A_j^n}\left(\frac{dB}{dT}\right)^{-1}_{\Theta_i^n} \qquad 5.4.5$$

The noise factor $\tilde{\Theta}_i$ for a given case has two parts: errors in observed cloud-cleared radiances $\delta\hat{\Theta}_i$, which are affected by instrumental noise and cloud clearing errors, and computational noise $\delta\Theta_i^c$.

In Susskind, *et al.*, (2003), dealing with simulated data, a perfect knowledge of physics is assumed, i.e., if all the variables were known exactly, the exact noise free radiances are computed. Nevertheless, the transmittances depend on the variables to be solved for. Therefore, computational noise exists. Computational noise, arising from errors such as too low (high) an estimate of atmospheric water vapor, produce noise that is correlated between channels. Instrumental noise is uncorrelated from channel-to-channel but cloud-

clearing errors are correlated from channel-to-channel. Therefore, the channel noise covariance matrix has both diagonal and off-diagonal matrix elements.

Each retrieval step uses an appropriate channel noise covariance matrix

$$M_{ij} = \left(\hat{M}_{ij} + \tilde{M}_{ij}\right)\left(\frac{dB_i}{dT}\right)^{-1}_{\Theta_i}\left(\frac{dB_j}{dT}\right)^{-1}_{\Theta_j} \qquad 5.4.6$$

where $\hat{M}$ is defined in Equation 5.2.25 and $\tilde{M}$ is discussed later. The values of M_{ij} depend on the pass. A general form of the solution to this problem is given by

$$\Delta A^n = \left[S'^n\, W\, S^n + H^n\right]^{-1} S'^n\, W \Delta\Theta^n = \bar{M}^n \Delta\Theta^n \qquad 5.4.7$$

where ΔA^n is the vector of updates to the expansion coefficients, $\Delta\Theta^n$ is the vector of channel residuals, W is a shorthand for M^{-1}, and H^n is a stabilizing or damping matrix used to constrain the otherwise ill-conditioned inverse problem.

Hanel, *et al.,* (1992) and Rodgers (1976) have reviewed several methods of constraining the ill-conditioned inverse problem. In the minimum variance approach (Rodgers, 1976), H is taken to be the inverse of the *a priori* error covariance. If the statistics of both the measurement and *a priori* are Gaussian, the maximum likelihood solution is obtained. If the *a priori* covariance is taken to be $H = \gamma I$, the maximum entropy solution is obtained. Other forms of H include the first or second derivative formulations (Twomey, 1963) that force a smoothness constraint on the solution. These formulations all weight the *a-priori* information into the final retrieved state to some extent. The solution can also be constrained by the relaxation method (Chahine, 1968) and by the Backus and Gilbert (1970) method.

The minimum variance and maximum likelihood solutions are often considered to be "optimal." However, if the *a priori* error covariance is not known or estimated incorrectly, the solution is sub-optimal. If the *a priori* errors are underestimated, the solution is over constrained. Potentially, this creates biases in the retrievals. The biases

mask small trends in the retrieved data that scientifically important. The approach described here attempts to keep the effects of instrument noise at a tolerable level without assumptions regarding the *a priori* data error covariance.

5.4.4 Transformation of Variables

As a consequence of stabilizing the ill-conditioned solution, the addition of H also has the effect of damping the potential information content of the radiances, reducing the values of ΔA. The variables are transformed to apply a constraint such that the well-determined components of the variables are solved for without appreciable damping.

If a different set of functions were chosen which are linear combinations of original functions, i.e.,

$$G = FU \tag{5.4.8}$$

where U is a unitary transformation $(UU' = 1)$, and the solution was expanded in the same way as in Equation 5.4.1 with unknowns ΔB^n, one obtains the equation

$$X^{n+1} = X^n + G\Delta B^n = X^n + FU\Delta B^n = X^n + F\Delta A^n \tag{5.4.9}$$

In the new basis set, the transformed Jacobian is given by

$$T^n = \frac{\partial R}{\partial B^n}\left(\frac{dB}{dT}\right)^{-1}_{\Theta} = S^n U \tag{5.4.10}$$

The constrained solution, as given by Equation 5.4.7, in terms of this new set of functions, is given by

$$\Delta B^n = \left(T'^n W T^n + H\right)^{-1} T'^n W\left(\Delta\Theta^n - \delta\Theta^{n-1}\right) = U'\Delta A^n \tag{5.4.11}$$

An additional term $\delta\Theta^{n-1}$ has been included in Equation 5.4.11, and represents an iterative background correction term that is zero in the first iteration (it is discussed further below).

U^n is selected such that $T'^n W^n T^n = U'S'WSU$ is diagonal with real non-negative eigenvalues λ_j^n. The inverse of each eigenvalue is the variance in that eigenmode. The total variance is the trace of $\left(US'WSU\right)^{-1}$. The unconstrained solution (H=0), with no background correction $\left(\delta\Theta^{n-1} = 0\right)$, is then given by

$$\Delta B_j^n(0) = \left(\lambda_j^n\right)^{-1} \sum_{k,i} T_{kj}^n W_{k,i} \Delta\Theta_i^n = \left(\lambda^n\right)_j^{-1} \bar{m}_j^n \Delta\Theta^n \qquad 5.4.12$$

where $\bar{m}_j^n$ is the vector corresponding to the jth row of $T'W$.

In general, the ill-conditioned cases arise from those components of G having low information content and small eigenvalues (high variance), indicating that those components are not well determined from the observations alone and need damping. Components with large eigenvalues are quite well determined and require little or no damping to achieve a stable solution. If H is chosen to be a diagonal matrix with values $\Delta\lambda$, the constrained solution with no background correction term is given by

$$\Delta B_j^n\left(\Delta\lambda^n\right) = \left(\lambda_j^n + \Delta\lambda_j^n\right)^{-1} \bar{m}_j^n \Delta\Theta^n \qquad 5.4.13$$

The coefficients $\Delta B_j^n\left(\Delta\lambda_j^n\right)$ are therefore damped from the unconstrained coefficients $\Delta B_j^n(0)$ by

$$\Delta B_j^n\left(\Delta\lambda_j^n\right) = \frac{\lambda_j^n}{\lambda_j^n + \Delta\lambda_j^n} \Delta B_j^n(0) = \Phi_j^n \Delta B_j^n(0) \qquad 5.4.14$$

where Φ_j can be thought of as a filter or damping function. This formulation is the same as the maximum entropy solution, applied in transformed space, if $\Delta\lambda$ is set equal to a constant. However, instead of using a single constant $\Delta\lambda$ for all eigen functions, a different value is computed for each eigenfunction. For well-determined eigenmodes,

$\Delta\lambda$ is set equal to 0. This has the consequences of giving no weight to the *a priori*. For modes that are not well determined by the measurements, $\Delta\lambda$ is determined in such a way as to limit the propagation of instrument noise to a pre-specified amount. The determination of $\Delta\lambda_j^n$ is discussed in detail in the next section.

5.4.5 Application of Constraint

The residual $\Delta\Theta_i^n$ can be thought of as having both a signal and a noise component, i.e.,

$$\Delta\Theta_i^n = \Delta\Theta_i^{signal} + \tilde{\Theta}_i \qquad 5.4.15$$

The component of ΔB_j that arises from the propagation of channel noises, $\tilde{\Theta}_i$, is given by

$$\delta\tilde{B}_j^n\left(\lambda_j^n\right) = \left(\lambda_j^n + \Delta\lambda_j^n\right)^{-1}\left[T'^n\, W\right]\tilde{\Theta}. \qquad 5.4.16$$

A statistical estimate of $\delta\tilde{B}_j^n$ over an ensemble of profiles can be obtained by

$$\begin{aligned}\delta\tilde{B}_j^n &= \left[\delta\tilde{B}^n\delta\tilde{B}^{n'}\right]_{jj}^{1/2} = \left(\lambda_j^n + \Delta\lambda_j^n\right)^{-1}\left[T' W\,\tilde{\Theta}\tilde{\Theta}' W' T\right]_{jj}^{1/2} \\ &= \frac{\left(\lambda_j^n\right)^{1/2}}{\lambda_j^n + \Delta\lambda_j^n} = \Phi_j^n\left(\lambda_j^n\right)^{-1/2}\end{aligned} \qquad 5.4.17$$

because $\tilde{\Theta}\tilde{\Theta}' = M = W^{-1}$. This formulation of $\delta\tilde{\Delta}$ is similar to that given by Rodgers (1990). If $\Delta\lambda_j^n$ were zero, $\delta\tilde{B}_j^n$ becomes large if λ_j^n is small. $\Delta\lambda_j^n$ is selected such that $\delta\tilde{B}_j^n$ is less than or equal to a threshold value. If $\delta\tilde{B}_j^n$ is allowed to be no more than δB_{MAX}, then $\Delta\lambda_j$ is set to zero if $\lambda_j \geq \delta B_{MAX}^{-2}$ and $\Delta\lambda_j = \dfrac{\lambda_j^{1/2} - \delta B_{MAX}\lambda_j}{\delta B_{MAX}}$ otherwise. For example, if $\delta B_{MAX} = 0.5$, the resultant value of $\Delta\lambda_j$ is set equal to 0 for $\lambda_j \geq 4$,

and if $\delta B_{MAX} = 1$, $\Delta\lambda_j$ is set equal to 0 for $\lambda_j \geq 1$, corresponding to damping (non-zero values of $\Delta\lambda_j$) for fewer eigen values.

Constraints are only applied to those eigenfunctions with lower information content than the critical value corresponding to δB_{MAX}. The value of δB_{MAX} has been determined empirically for each type of retrieval. In Version 4.0, δB_{MAX} = 1 in the AMSU-A temperature retrieval step, $\delta B_{MAX} = 0.35$ in the AIRS surface temperature retrieval step, $\delta B_{MAX} = 1.2$ and 1.0 in the AIRS temperature and moisture profile retrieval steps respectively, and $\delta B_{MAX} = 4$ in the ozone profile retrieval step. The computation of all matrix elements shown above, including λ and $\Delta\lambda$, is done in each iteration.

5.4.6 Formulation of the Background Term

The need for an iterative process arises because the radiative transfer equation is not linear. In every iteration, Θ_i^n, S^n, U^n and λ^n are each recomputed. If the solutions were completely linear, and no damping was applied, then

$$\Delta\Theta^{n+1}(0) \cong \Delta\Theta^n - S^n U^n \Delta B^n(0) \qquad 5.4.18$$

Under these conditions, $\Delta B^{n+1}(0)$ would be zero because $\Delta B^n(0)$ already matched the residuals and $\Delta\Theta^{n+1}$ would be zero.

Equation (5.4.18) is not exact, because on the one hand, $\Theta^{n+1}(0)$ is not given exactly by $\Theta^n + S^n U^n \Delta B^n$, and also because $\Delta B_j^n \neq \Delta B_j^n(0)$. As a result of applying ΔB_j^n rather than $\Delta B_j^n(0)$, which would have minimized the radiance residuals,

$$\Delta\Theta^{n+1} \approx \Delta\Theta^{n+1}(0) + S^n U^n \left[\Delta B^n(0) - \Delta B^n \right] = \Delta\Theta^{n+1}(0) + \delta\Theta^n \qquad 5.4.19$$

In Equation (5.4.19), $\Delta\Theta^{n+1}(0)$ represents the portion of $\Delta\Theta^{n+1}$ that is due to effects of non-linearity on the solution, while $\delta\Theta^n$ represents the residual portion of $\Delta\Theta^{n+1}$ due to

the effects of damping in iteration n. The second term is zero for undamped modes and increases in significance with increased damping. This term is also zero for all modes in the first iteration.

It is desirable to include the effects of non-linearity in the iterative procedure used in the determination of ΔB^n. Therefore, the background term to be used in Equation 5.4.12 is given by

$$\delta\Theta^n = S^n U^n \left[\Delta B^n(0) - \Delta B^n \right]$$

and we solve for ΔB_j^{n+1} according to

$$\Delta B_j^{n+1} = \left(\lambda_j^{n+1} + \Delta\lambda_j^{n+1} \right)^{-1} U'^{n+1} S'^{n+1} W^{n+1} \left[\Delta\Theta^{n+1} - \delta\Theta^n \right]$$

$$= \Phi^{n+1} \Delta B_j^{n+1}(0) - \left(\lambda_j^{n+1} + \Delta\lambda_j^{n+1} \right)^{-1} \qquad 5.4.20$$

$$\cdot \left[U'^{n+1} S'^{n+1} W^{n+1} S^n U^n \left(\Delta B_j^n(0) - \Delta B_j^n \right) \right]$$

where ΔB_j^n is the value of ΔB_j which was applied in iteration n. Inclusion of the background term in Equation 5.4.20 ensures second order convergence along the lines discussed by Rodgers (1976) with regard to treatment of the *a priori* term.

5.4.7 Convergence Criteria

Solving Equation 5.4.20 finds solutions to the radiative transfer equations which minimize weighted residuals of observed and computed brightness temperatures, corrected for the background term. To test convergence of the solution, the weighted residual is monitored

$$R = \left[(\Delta\Theta - \delta\Theta)' V' V (\Delta\Theta - \delta\Theta) \right]^{1/2} \qquad 5.4.21$$

where the weight matrix V accounts for noise effects on the channel residuals, as well as the relative information content of the channels with regard to the variables being solved for. For example, if a channel (or linear combination of channels) carries little information content in terms of signal-to-noise, it is given little weight in the estimation of the residual in Equation 5.4.21. An appropriate choice of V, expressing the information content of the channels is

$$V = \left(\lambda_j + \Delta\lambda_j\right)^{-1} \left(T' W\right) \qquad 5.4.22$$

in which case we obtain

$$R = \left[\Delta B' \Delta B\right]^{1/2} \qquad 5.4.23$$

As shown in Equation 5.4.23, a reasonable way to determine if the solution has converged, in terms of weighted residuals, is to see if the solution converges in terms of the iterative changes in the solution itself. Initially, we set $\Delta B_j = 0$ if $\Phi_j^1 < 0.05$, that is, coefficients of very heavily damped components with little information content are given no weight. The solution is said to have converged when the RMS value of ΔB_j^n is less than 10% of the RMS value of $\delta\tilde{B}^n$ for all components not set equal to zero. The iterative procedure is also terminated if the RMS value of ΔB_j^n is not less than 75% of ΔB_j^{n+1} for the non-zero components. This indicates the solution is not converging rapidly enough and is responding primarily to unmodeled noise. The iterative procedure, which usually converges in 3 iterations, is carried out analogously for all retrieval steps.

5.4.8 Retrieval Noise Covariance Matrix

The matrix W used in Equation 5.4.11 is the inverse of the retrieval noise covariance matrix, $M\left(W \equiv M^{-1}\right)$. The matrix M is given by a sum of two terms

$$M_{ij} = \left(\hat{M}_{ij} + \tilde{M}_{ij}\right)\left(\frac{dB_i}{dT}\right)_{\Theta_i}^{-1}\left(\frac{dB_j}{dT}\right)_{\Theta_j}^{-1} \qquad 5.4.24$$

where $\hat{M}$ represents the error covariance in the reconstructed cloud-cleared radiances and $\tilde{M}$ represents the error covariance in the radiances computed from the estimated profile, as a result of errors in parameters assumed known (being held fixed) in a retrieval step. $\hat{M}$ is given in Equation 5.2.35.

The computational noise covariance matrix $\tilde{M}$ is designed to account for errors in the computed cloud free radiance expected for a given state, R_i^n, resulting from errors in the geophysical parameters held fixed in the retrieval step. $\tilde{M}$ is modeled according to

$$\tilde{M}_{ii} = \sum_j \left[\frac{\partial R_i}{\partial X_j} \delta X_j^n \right]^2 + (0.1)^2 \left(\frac{dB_i}{dT} \right)^2_{\Theta_i} + \left(M_{ii}^{phys} \right)^2 \left(\frac{dB_i}{dT} \right)^2_{\Theta_i} \qquad 5.4.25$$

and

$$\tilde{M}_{ii'} = \sum_j \frac{\partial R_i}{\partial X_j} \frac{\partial R_{i'}}{\partial X_j} \delta X_j^{n\,2} \qquad 5.4.26$$

where $\frac{\partial R_i}{\partial X_j}$ represents the derivative of R_i^n with respect to parameter X_j and δX_j^n is the estimated uncertainty in parameter X_j in iteration n. The parameters used for X_j in modeling $\tilde{M}$ represent uncertainties in surface skin temperature, surface emissivity, surface reflectance, temperature profile, and water vapor and ozone profiles. The derivatives $\frac{\partial R_i}{\partial X_j}$ are computed empirically for those variables held fixed in a given retrieval step. The term 0.1 in Equation 5.4.25 is taken to represent additional unmodeled errors. Details of how these uncertainties are computed for each pass are given later.

5.4.9 Variable Channel Selection

5.4.9.1 Surface Parameter Retrieval

Channel radiances depend on several unknown surface parameters: the surface skin temperature (T_s); the spectral emissivity, $\varepsilon(\nu)$, and spectral bi-directional reflectance $\rho(\nu)$; and the microwave spectral emissivity $\varepsilon_m(\nu)$. The surface parameter retrieval step uses 25 infrared window channels, 5 AMSU-A window channels, and 1 HSB window channel included in the spectral ranges shown in Table 5.4.1 and listed in the column marked surf in Table 5.4.2. The AIRS channels used in the surface parameter retrieval step are indicated by the orange stars in Figure 5.4.1. Inclusion of the microwave window channels stabilizes the surface parameter retrieval and also provides one piece of information about modifying the microwave spectral emissivity provided by the microwave product (generated in step 1).

In the surface parameter retrieval, infrared window channels are selected from both long-wave and short-wave infrared window regions, generally avoiding even weak absorption lines. For window channels, the transmittance at the surface, $\tau(p_s)$, is generally close to unity. Although the opacity of infrared window channels is small, there is absorption and emission due to the water vapor continuum and the nitrogen continuum, both absorbing primarily in the lowest portions of the atmosphere. Therefore, the radiance in window regions depends not only on T_s, $\varepsilon(\nu)$, and $\rho(\nu)$, but also on the temperature and moisture in the boundary layer. The radiances of window channels do not depend appreciably on temperature and moisture above the boundary layer. To account for the additional dependencies in the surface parameter retrieval, two additional variables can in principle be solved for by scaling the total precipitable water ($\Delta\ell$n W) and shifting the air temperature (ΔT_{AIR}). We do not do this however because it is felt that the regression step produces accurate enough boundary layer temperature and moisture profiles for use without further modification. A few channels centered on weak water vapor absorption lines are included in the surface parameter retrieved in the 3.7 μm window which are sensitive to water vapor absorption as well as reflected solar radiation. The reflected solar radiation causes the surface to appear hotter than in other window regions not affected by

reflected solar radiation. Inclusion of these channels helps distinguish between changes in $T_s, \varepsilon,$ and ρ during the day. Several of the shortwave window channels in the surface parameter retrieval are also used later in the moisture profile retrieval. They are particularly sensitive to boundary layer water vapor during the day, and improve retrieved boundary layer water vapor given an accurate value of ρ.

A total of five variables are solved for in the surface parameter retrieval for daytime cases and four for nighttime cases. The perturbation functions include a perturbation to T_s, a perturbation to each of 2 infrared spectral emissivity functions, 1 spectral bi-directional reflectance functions (during the day), and 1 piece of information about a perturbation to the microwave spectral emissivity. The values of the perturbations are selected to give comparable values of the S matrix for a typical case. If all perturbation functions F_j were half as large, S_{ij} would be half as large for each mode, and the solution vector ΔA_j would be twice as large. The perturbations are large enough to produce significant S matrix elements, but not so large as to produce an appreciable non-linear response.

The Jacobian or sensitivity matrix S^n is computed every iteration. The partial derivative of channel radiance with respect to the coefficients of each of the above functions are computed empirically as follows: (1) Compute the i^{th} channel radiance

using the n^{th} iteration parameters (i.e., T_s^n, $\varepsilon^n(\nu), \rho^n(\nu)$, etc.) (2) Compute the i^{th} channel transmittance (if necessary) and radiance using the n^{th} iteration parameters but setting the coefficient (ΔA_{ij}) of perturbation function F_j to unity. (3) The sensitivity S_{ij}, related to the change in channel radiance per unit change in coefficient ΔA_j, is given by the difference in radiances computed in steps (1) and (2), divided by $(dB/dT)_{\Theta_i^n}$. The sensitivity or partial derivative of radiance with respect to surface temperature, spectral emissivity, and surface bi-directional reflectance can be computed theoretically by differentiating the clear column radiative transfer equation because the transmittance functions do not depend on these parameters.

After the sensitivity matrix is computed, the inversion procedure described earlier proceeds. In the surface temperature retrieval, as well as in all other retrieval steps, an empirical term, M_{ij}^{phys}, which is of unmodelled component noise, is included in Equation 5.4.26. M_{ij}^{phys} will be discussed in detail later. The retrieved values of T_s, $\varepsilon(\nu)$, and $\rho(\nu)$ are held constant and used in the subsequent iterative steps for temperature, moisture, and ozone profile retrievals.

5.4.9.2 Temperature Profile Retrieval

The temperature profile retrieval problem is set up and solved in a manner completely analogous to the surface parameter retrieval. The solution for the retrieved temperature profile is written in the form

$$T^n(p_\ell) = T^0(p_\ell) + \sum_{j=1}^{J} F_j(p_\ell) A_j^n = T^0(p_\ell) + FA \qquad 5.4.27$$

where ℓ ranges over the number of levels used to compute channel transmittances and radiances, and j ranges over the number of functions that are solved for, currently set to 23. The functions in the surface parameter retrieval are taken as discrete changes in different surface or atmospheric parameters. Following the approach of the surface parameter retrieval, the functions F_j are selected as localized functions of pressure, corresponding to changes in temperature primarily in a layer from p_j to p_{j-1}. Use of localized functions is convenient for computing the S matrix and makes the problem more nearly linear. The methodology discussed previously does not require the functions to be orthogonal. In order for the solution to be continuous, the functions chosen are trapezoids, with a value of 0.5K between p_j and p_{j-1} and falling linearly in log p to 0K at p_{j+1} and p_{j-2}. The highest and lowest functions in the atmosphere are special cases, with values of 1K at the upper or lower limit of the atmosphere (0.016 mb or the surface), 0.5K at the adjacent pressure, and followed by 0 K at the next pressure level.

The Jacobian matrix is computed exactly as in the surface parameter retrieval. In any iteration, transmittances and radiances are computed for the temperature sounding

channels using $T^n(p)$ and $T^n(p)+F_j(p)$, where $F_j(p)$ is one of the trapezoids, and the Jacobian is obtained empirically according to

$$S_{ij}^n = \left[R_i\left(T^n(p)+F_j(p)\right) - R_i\left(T^n(p)\right)\right]\left(\frac{dB_i}{dT}\right)_{\Theta_i}^{-1} \qquad 5.4.28$$

It can be shown that for an opaque temperature sounding channel, a shift of the entire atmospheric temperature profile by 1K will cause roughly a 1K change in brightness temperature (Susskind, *et al.*, 1984). Moreover, a localized change of 1K in an atmospheric layer containing the non-zero part of the channel's weighting function likewise results in a 1 K change in brightness temperature. This brightness temperature change decreases as the layer becomes thinner than the weighting function. To insure sensitivity of at least one sounding channel to changes in the layer (or trapezoid) temperatures, layers are selected to be sufficiently coarse as to have an element of the S matrix of at least 0.2 for the layer. While the Jacobian is profile dependent, the layer structure used to define the trapezoid functions is held fixed for all soundings. They are selected so as to be neither too thin, resulting in lack of sensitivity, nor too coarse, resulting in lack of resolution. The pressure boundaries for the 23 functions used are shown in Table 5.4.3. According to Equation 5.4.28, the only structure in the solution with finer spacing than these pressure boundary levels must come from the initial guess. The procedure of transformation of variables and use of damping functions designed to stabilize the solution, as discussed earlier, further decreases the ability of the solution to discern fine structure not contained in the information content matrix $S'WS$. This damping is profile dependent.

In the first pass temperature profile retrieval, channels are selected which are relatively insensitive to the ozone and water vapor distribution. An estimate of these variables is given by regression, but this is not considered to be of high enough accuracy to allow for use of channels highly sensitive to these parameters in the first pass physical temperature profile retrieval step. The temperature-sounding channels used are generally selected between absorption lines to optimize the channel weighting functions (Kaplan, *et al.*, 1977). Along the lines of Kaplan, *et al.,* (1977) and outlined in Table 5.4.1, the retrieval

uses 50 channels in the 15 μm CO_2 band. These include the Q-branch near 666 cm^{-1} to sound the mid to upper stratosphere and channels between CO_2 absorption lines to sound through the upper troposphere. In addition, 9 channels in the CO_2 4.2 μm band R branch in the vicinity of 2388 cm^{-1} are used to sound the mid- to lower troposphere. It was found that the R branch channels at frequencies less than 2386 cm^{-1} were affected significantly by non-LTE during the day and they are currently not used in the retrieval process. There are also 11 AMSU-A channels included (AMSU A channels 3-6 and 8-14 from Table 2.3) in the temperature profile retrieval. AMSU A channel 7 contains excessive noise and is not used in any retrieval step. All channels used in the first pass temperature profile retrieval step are indicated in Table 5.4.2 in the column Temp 1. The AIRS channels are marked by red stars in Figure 5.4.1.

Table 5.4.3. Trapezoid or Layer Endpoints

Temperature Retrieval	Moisture Retrieval	Ozone Retrieval	CO Retrieval
0.016	0.016	0.016	0.016
0.714	170.1	20.92	300.0
1.297	272.9	51.53	407.5
2.701	314.1	71.54	575.7
4.077	343.6	103.0	surface
8.165	407.5	142.2	
16.43	515.7	300.0	
23.45	617.5	surface	
39.26	706.6		
56.13	852.8		
71.54	surface		
96.11			
125.6			
160.5			
212.0			
272.9			
343.6			
424.5			
490.6			
596.3			
661.2			
729.9			
878.6			
surface			

*If the lowest layer is less than 50 mb thick in any step, it is combined with the layer above.

Errors in the estimate of the water vapor profile, ozone profile, and surface parameters used to compute expected radiances in the temperature profile retrieval step produce errors in the computed brightness temperature for a given channel, as well as correlated brightness temperatures errors in radiances computed in other temperature sounding channels. These errors are accounted for in the noise covariance matrix $\tilde{M}_i$ given in Equations 5.4.25 and 5.4.26.

Incorporation of these terms into the noise covariance matrix has the effect of making channels sensitive to water vapor absorption, ozone absorption, and/or the surface temperature appear noisier than the value given by their instrumental noise. It should be noted that in general, the mid-tropospheric sounding 15 μm channels, which are sensitive to water vapor absorption, will be "noisier" for humid cases than for very dry ones, while uncertainty in water vapor profile will have a smaller effect on the 4.2-μm radiances. Conversely, 4.2-μm channels are “noisier” during the day than at night due to effects of uncertainty in the surface bi-directional reflectance.

The estimated errors in surface parameters and temperature profile are included in the noise covariance matrix in the subsequent steps of water vapor profile retrieval and ozone profile retrieval, and the estimated error in water vapor profile is also included in the ozone profile retrieval, but not in the water vapor retrieval because water vapor is the variable being solved for. Effects of estimated errors in the temperature profile are also included in these subsequent steps.

The temperature profile retrieval step described above (step 9) is done after the AMSU/strat IR temperature profile retrieval (step 5) subsequent to the regression (step 4) has been completed. That AMSU/strat IR temperature retrieval step is analogous to the temperature retrieval step described above, but uses only AMSU-A channels and stratospheric AIRS temperature sounding channels which do not see clouds. The AMSU/strat IR temperature profile retrieval step solves for one piece of information about the microwave spectral emissivity as well as coefficients of 13 temperature perturbation functions. Less functions are used in the AMSU-A temperature retrieval step because there is considerably less inherent vertical resolution in the troposphere

when only AMSU-A channels are used with the stratospheric sounding AIRS channels, as compared to using tropospheric AIRS temperature sounding channels as well.

5.4.9.3 Water Vapor Profile Retrieval

Unlike surface parameter and temperature profile retrievals, the water vapor profile retrieval problem is highly non-linear. A change in water vapor abundance in a given level affects the transmittance in that layer as well as the atmospheric emission and absorption at all lower levels in a complex manner. The solution for the retrieved moisture profile is expressed as

$$q^n(p_\ell) = q^0(p_\ell)\left[1 + \sum_{j=1}^{J} F_j(p_\ell) A_j^n\right], \qquad 5.4.29$$

where ℓ ranges over the 100 levels used to compute transmittances and radiances, and j ranges over J solution functions. The functions $F_j(p_\ell)$ are expressed as trapezoids with a value of 0.05 in coarse atmospheric layers, in a manner analogous to that described above for the temperature profile retrieval. The endpoints of the 10 trapezoids used in the moisture profile retrieval are included in Table 5.4.3. The highest trapezoid has a value of 0.05 at 170.1 mb and 272.9 mb and 0 at .016 mb and 314.1 mb. The lowest function is comprised of two straight lines, with a value at the surface and 852.8 mb of 0.05, and a value of 0 at 706.6 mb.

In the moisture retrieval, we primarily use channels between absorption lines in the 6.3 μm water vapor band that are sensitive to humidity throughout the troposphere. These channels provide sharper weighting functions (more localized absorption) than centers of strong lines and make the problem more linear. In addition, some channels are used on the peaks of the strongest absorption features in the 6.7-μm band, which are sensitive to stratospheric water vapor. One channel is also included in the 11-μm window which is sensitive to the water vapor continuum and improves the sounding capability for lower tropospheric humidity. Channels in the 3.7-μm window provide improved sensitivity to low level moisture during the day as discussed previously. The AIRS channels used in the water vapor retrieval step are shown by green stars in Figure 5.4.1 and indicated

under H_2O in Table 5.4.2. The S matrix is computed empirically exactly as in the temperature profile retrieval. The parameters determined from the surface and temperature profile retrievals are kept fixed in the calculations.

In constructing the noise covariance matrix, terms for uncertainties in surface properties are included, as in the temperature profile retrieval, as well as a term representing radiance uncertainties due to a perturbation of the entire temperature profile, as done in the noise covariance matrix used in the determination of η (Equation 5.2.9). These terms will be discussed in Section 5.5.

5.4.9.4 Ozone Profile Retrieval

The solution for the ozone profile retrieval has the same form as that for the moisture profile retrieval. The ozone profile retrieval uses 7 trapezoid functions with values of 0.05, as in the water vapor retrieval. The end points of the trapezoids are included in Table 5.4.3. The same steps outlined in the previous section are used to compute the Jacobian. It is critical to solve for water vapor before ozone because ozone channels are sensitive to absorption by boundary layer water vapor. There are 26 channels in the 9.6 μm ozone band selected for the ozone retrieval. These channels are shown by the blue stars in Figure 5.4.1 and indicated in Table 5.4.2 in the column marked O_3. Uncertainties in surface parameters, temperature profile, and water vapor profile are included in the ozone noise covariance matrix.

5.4.9.5 CO Profile Retrieval

The retrieval of CO profile is totally analogous to that of the other constituents. 20 CO sounding channels are used in the retrieval process, 4 perturbation functions are used, and ΔB_{max} is set equal to 1.7. The channels used are indicated in Table 5.4.2 under the column CO and the endpoints of the trapezoids are shown in Table 5.4.3. The regression step does not generate an initial guess CO profile. A fixed zonally dependent mixing ratio is used as the CO initial guess.

5.4.10 Estimation of State Errors and their Effect on the Channel Noise Covariance Matrix

Equations 5.2.9 and 5.4.26 contain terms such as $\frac{\partial R_i}{\partial T(p)}\delta T(p)$, representing the contribution of errors in computed radiances resulting from expected errors in state parameters used in a given pass and step. These errors are case dependent and can be estimated by propagating expected errors through the retrieval system. In addition to being used in the generation of the channel noise covariance matrix, the expected state errors are useful in their own right and are reported along with the retrieved state. The following sections show how the expected state errors and their contributions to Equations 5.2.9 and 5.4.26 are computed.

5.4.10.1 Propagation of Errors

In any iteration, the estimate of a parameter, such as $T(p)^m$, is given by

$$\begin{aligned} T(p)_j^m &= T(p)_j^0 + \sum_{\ell=1}^{L} F_{j\ell} A_\ell^m \\ &= T(p)_j^0 + (FU\,B^m)_{j,1} \end{aligned} \qquad 5.4.30$$

where j is a discrete pressure level. There are three contributions to the expected error $\delta T(p)_j^m$. The first contribution comes from the null space error, arising from the error of the first guess in the space outside that of the L functions used to expand the solution. The second component arises from errors in the coefficients B^m. The last contribution arises from the damping of the solution in which $(1-\Phi)$ of the first guess (or previous iteration) is believed for each eigen function, G=FU.

Equations 5.2.9 and 5.4.26 contain radiance uncertainties resulting from the square of the expected error in state parameter X_j^m, $\delta X_j^{m\,2}$, which can be expressed in terms of errors in the expansion coefficients A according to

$$\delta X_j^{m\,2} = \delta X_j^{N\,2} + \sum_k F_{jk}^2 \delta A_k^{m\,2} \qquad 5.4.31$$

where δX_j^N is the null space error and δA^m is the error in the coefficients A^m used to represent X^m. Errors in A arise both from errors in the B coefficients and errors in the damped portion of the m-1 iterative guess. In every step in the retrieval process, we begin with parameters X^0 having an uncertainty δX_j^0. The uncertainty of the microwave product first guess is specified based on expected errors, as is the null space error. Given δX^0, δA^0 can be solved for according to

$$\begin{aligned} \delta A_k{}^0 &= \left[(F'^2\, F^2)^{-1} F'^2 \left(\delta X^0 - \delta X^N\right)^2 \right]^{1/2} \\ &= \left[\left(F'^2\, F^2\right)^{-1} F'^2 \left(\delta \tilde{X}^0\right)^2 \right]^{1/2} \end{aligned} \qquad 5.4.32$$

In a given iteration, we can express δA_k^m according to

$$\delta A_k^m = \left[\Sigma_\ell \left(U_{k\ell} \cdot \frac{\Phi_\ell^m}{\sqrt{\lambda_\ell^n}} \right)^2 + \Sigma_\ell \left(U_{k\ell} (1 - \Phi_\ell{}^m) \sum_j U_{j\ell}\, \delta A_j^{m-1} \right)^2 + \delta A_k^{N\,2} \right]^{1/2} \qquad 5.4.33$$

where $\dfrac{\Phi_\ell^m}{\sqrt{\lambda_\ell^m}}$ represents the predicted error in B_ℓ^m due to noise propagation, and the second term represents the portions of the errors δB_ℓ^{m-1} of the previous iterative profile which are believed in the current iteration. Given δA_k^m from Equation 5.4.33 for the final iterative step, we compute the square of the corresponding profile error to be used in Equations 5.2.9 and 5.4.26 according to Equation 5.4.31. This term is carried to the next retrieval step and used in Equation 5.4.32 to give $\delta A_k{}^0$ which is in turn used in Equation 5.4.33 to generate the uncertainty in parameter X for use in subsequent steps.

For moisture and ozone profile, the form of the expansion is slightly different (see Equation 5.4.29) and we write

$$\left(\frac{\delta q^{N}(p)}{q}\right)^2 = \left(\frac{\delta q^{m}(p)}{q}\right)^2 + \sum_k F_k{}^2(P)\,\delta A_k^{m2} \qquad 5.4.34$$

Surface spectral emissivity and bi-directional reflectance are analogous to temperature profile, as is skin temperature, in which case F is a number. The liquid water profile comes from the microwave product and is not iterated. We assume an error estimate of 10% of the liquid water profile. In addition, if the total liquid water is less than 0.01 g/cm^2, we consider the possibility that liquid water may have been missed due to an error in the water vapor microwave solution. For these low liquid water solutions, an alternative error estimate of (2*RH-1)*0.05*q, where RH is the relative humidity and q is the layer water vapor in mg/cm^2, is considered and used if it is larger than 20% of the liquid water. The null space temperature error is taken as 0.1K above 40 mb and below 200 mb, increasing linearly in log p to 0.2K at 100 mb. The null space error in percent is taken as 5% for water vapor and ozone above 40 mb and beneath 200 mb, with values of 10% and 50% at 100 mb for water vapor and ozone respectively.

Equation 5.4.33 is case dependent through the parameters Φ_ℓ and λ_ℓ which depend both on the S matrix, and more significantly on the M matrix. M contains contributions from clouds, $\hat{M}$, and parameter uncertainty $\tilde{M}$. The uncertainties in parameters determined from Equations 5.4.33, 5.4.31, and 5.4.34 in turn are used in the computation of the matrices $\tilde{M}$ (Equation 5.4.29) and N (Equation 5.2.9).

5.4.10.2 Contribution of State Errors to the Channel Noise Covariance Matrix

Equations 5.4.31 and 5.4.34 give the magnitude of the estimated error in each parameter but contain no information about sign. If we assume all $\delta X(p)$ are of the same sign, we would overestimate the effect of the uncertainty on that parameter on the computed radiances, because retrieval process errors are negatively correlated over some layers of

the atmosphere. Bearing this in mind, when the derivatives in Equations 5.2.9 and 5.4.29 are computed numerically, we write

$$\frac{\delta R}{\delta X(p)}\delta X(p) = R\left(X(p) + \Delta X(p)\right) - R(X(p)) \qquad 5.4.35$$

where $\Delta X(p)$ is related to, but not equal to $\delta X(p)$. To allow for some negative correlation in expected profile errors, $\Delta X(p)$ is constructed by multiplying $\delta X(p)$ by a sine wave with a full period of six temperature profile functions in the case of uncertainty of temperature profile to be used in the humidity and ozone profile retrievals, and six humidity profile functions in the case of water vapor uncertainty to be used in the temperature and ozone profile retrievals. In the case of ozone profile, with only seven functions, we simply multiply the predicted uncertainty by 0.5. We have also found that in constructing the noise covariance terms in Equation 5.2.9 used for cloud clearing and cloud property retrievals, it was more advantageous to instead set $\Delta X = 0.5\ \delta(X)$ for all profile terms. For surface parameters we take $\Delta X = \delta X$, as for the liquid water profile.

5.4.11 Retrieval of Cloud Parameters

Retrieval of cloud parameters is a fundamentally different process from, and should not be confused with, the process of cloud clearing. Both applications use observed radiances in the 9 AIRS FOVs within an AMSU A FOR. Cloud clearing (Section 5.2) extrapolates AIRS observations in the 9 potentially cloudy FOVs to obtain the cloud-cleared radiances, $\hat{R}_i$, which represent what the observations would have been if everything else were the same, but no clouds were present. These cloud-cleared radiances are then used to determine the surface and atmospheric properties within the AMSU FOR. There is no need to know anything about the properties of the clouds in the FOR to do this, nor is there any need to compute expected radiances in the cloudy portion of the scene.

In order to determine cloud parameters from the observed AIRS radiances, one does essentially the reverse procedure. Surface and atmospheric conditions are first determined consistent with the cloud cleared radiances, and then cloud parameters are

obtained such that radiances computed using the surface, atmospheric, and cloud parameters best match the observed radiances in the different fields of view for an ensemble of channels. This process involves the computation of expected radiances for cloudy scenes, which was not required for cloud clearing.

Retrieved cloud parameters are important geophysical parameters in their own right and are useful for process and climate studies. They are also used to compute OLR, which has been used extensively in the study of climate process. In addition, the retrieved cloud top pressure is used in the procedure to determine whether a channel "sees" or "does not see" clouds, which in turn affects the derived clear column radiance $\hat{R}_i$ for that channel as well as its channel noise amplification factor (see Section 5.2). For this reason, cloud parameter retrievals are performed each time clear column radiances are determined (steps 2, 5, 7, and 13 in the processing systems).

5.4.11.1 Computation of Radiances in the Presence of Clouds

The observed radiance for the i^{th} channel, R_i, in a scene with j cloud types, can be expressed by

$$R_i = (1 - \sum_j \alpha_j) R_{i,CLR} + \sum_j \alpha_j R_{i,CLD,j} \qquad 5.4.36$$

where α_j is the fraction of the scene covered by cloud type j, $R_{i,CLR}$ is the clear sky radiance for channel i (i.e., the radiance emerging from the clear portion of the scene), and $R_{i,CLD,j}$ is the i^{th} channel radiance emerging from the cloudy portion of the scene covered by cloud type j (Chahine, 1982).

The computation of $R_{i,CLD,j}$ for a given scene is complex as a result of to the detailed spectral absorption and reflection properties of clouds, cloud morphology within the field-of-view, and geometric shadowing factors. Assuming plane parallel cloud formations, $R_{i,CLD,j}$ can be computed according to

$$R_{i,CLD,j} = \varepsilon_{ic_j} B_i(T_{c_j})\tau_i(p_{c_j}) + \int_{p_{c_j}}^{0} B_i\left[T(p)\right]\left(\frac{d\tau_i}{d\ell np}\right)d\ell np +$$

$$\tau_{ic_j}\left[R_{i,CLR} - \int_{p_{c_j}}^{0} B_i T(p)\frac{d\tau}{d\ell np}d\ell p\right] + \rho_{ic_j} H_i \tau_i'(p_{c_j})\cos\theta_0$$

5.4.37

where τ_{ic_j} and ε_{ic_j} are respectively the transmissivity and emissivity of cloud type j at channel frequency ν_i and cloud top temperature T_{c_j}; ρ_{ic_j} is the cloud bi-directional reflectance of solar radiation incoming at solar zenith angle θ_o and outgoing in the direction of the satellite; $\tau_i'(p_{c_j})$ is the two path atmospheric transmittance from the top of the atmosphere to the cloud top pressure p_{c_j}; and H_i is the solar irradiance. In Equation (5.4.37), the first term represents radiation emitted by the cloud that is transmitted by the atmosphere to the satellite; the second term represents the portion of the radiation absorbed and emitted by the atmosphere above the cloud; the third term represents the additional contribution to the radiance of upwelling radiation from below the cloud that passes through the cloud, and the fourth term represents solar radiation reflected by the cloud in the direction of the satellite. Equation 5.4.37 neglects a small term due to downwelling thermal radiation reflected off the cloud in the direction of the satellite.

When retrieving cloud properties, the channels used are limited (see Table 5.4.1) to those at frequencies less than 1250 cm^{-1}, for which the last term in Equation 5.4.37 is not significant. The cloud property retrieval step uses the 38 AIRS channels which are indicated in Table 5.4.2 in the column marked HGT.

If there is only one cloud type in the scene, then the radiance emanating from that cloud for the channels used in the cloud parameter retrieval step can be expressed as

$$R_{i,CLD,1} = \tau_{ic_1} R_{i,CLR} + \varepsilon_{ic_1} B_i(T_{c_1})\tau_i(p_{c_1}) + (1-\tau_{ic_1}) \int_{p_{c_1}}^{0} B_i\left[T(p)\right]\left(\frac{d\tau_i}{d\ell np}\right) d\ell np. \qquad 5.4.38$$

Making the approximation that $\tau_{ic_1} = (1-\varepsilon_{ic_1})$, then Equations 5.4.36 and 5.4.38 combine to give

$$R_i = \left(1-\alpha_1\varepsilon_{ic_1}\right)R_{i,CLR} + \left(\alpha_1\varepsilon_{ic_1}\right)R^B_{i,CLD}\left(p_{c_1}\right) \qquad 5.4.39$$

where $R^B_{i,CLD}\left(p_{c_1}\right)$ is the radiance computed for a black cloud $(\tau_{ic}=0,\ \varepsilon_{ic}=1)$ with cloud top pressure p_{c_1}. It is apparent that the term $\alpha_1\varepsilon_{ic_1}$ appears only as a product in Equation 5.4.39. Therefore α and ε_{ic} cannot determined independently, but only as a product, which can be thought of as a radiatively effective cloud fraction that may be a function of frequency. To the extent that ε_{ic} is a function of frequency, the frequency dependent term $\alpha_1\varepsilon_{ic_1}$ can be expressed as $(\alpha\varepsilon_{c\bar{\nu}})_1 F_1(\nu)$ where $(\alpha\varepsilon_{c\bar{\nu}})_1$ is a representative value of the effective cloud fraction $\alpha_1\varepsilon_{ic_1}$ at a given frequency $\bar{\nu}$, and $F_1(\nu)$ expresses the frequency dependence of $\frac{\varepsilon_{c\nu}}{\varepsilon_{c\bar{\nu}}}$.

If there were two cloud types, and $\tau_{ic_2} = \left(1-\varepsilon_{ic_2}\right)$, then the observed radiances can be expressed as

$$R_i = \left(1-(\alpha\varepsilon_{i,1})-(\alpha\varepsilon_{i,2})\right)R_{i,CLR} + (\alpha\varepsilon_{i,1})R^B_i\left(p_{c_1}\right) + (\alpha\varepsilon_{i,2})R^B_i\left(p_{c_2}\right) \qquad 5.4.40$$

where $(\alpha\varepsilon_{i,1})$ and $(\alpha\varepsilon_{i,2})$ are the radiatively effective cloud fractions for the clouds at p_{c_1} and p_{c_2}. For the higher cloud at p_{c_1}, $(\alpha\varepsilon_{i,1}) = \alpha_1\varepsilon_{ic_1}$ as before. On the other hand, for the lower cloud, the effective cloud fraction $(\alpha\varepsilon_{i,2})$ is given by

$$(\alpha\varepsilon_{i,2}) = \varepsilon_{ic_2}\left[\alpha_2 + \left(1-\varepsilon_{ic_1}\right)\alpha_1\alpha_{12}\right] \qquad 5.4.41$$

where α_{12} is the fraction of the area covered by cloud type 1 which is undercovered by cloud type 2. To the extent that $\left(1-\varepsilon_{ic_1}\right)$ is frequency dependent and α_{12} depends on field-of-view, this situation actually contains three cloud formations, because the spectral dependence of radiances in areas covered by clouds at both levels is different from that of clouds at either of the two levels, in a manner that is field-of-view dependent. In principle, this should not by itself degrade the ability to derive cloud cleared radiances, which allows for up to four cloud formations. On the other hand, the cloud parameter retrieval algorithm described in the next section allows for only two layers of grey clouds. Such a situation would give effective values of cloud top pressure as well as

cloud fraction, as would the presence of three or more distinct cloud types in the FOR.

5.4.11.2 Cloud Parameter Retrieval Methodology

The cloud parameter retrieval is performed in an exactly analogous manner to that of all other retrieval steps. Observations in each of the nine fields of view k=1,9 are used to determine cloud parameters, assuming there are clouds with two distinct cloud top pressures, with varying frequency independent effective cloud fractions, $(\alpha\varepsilon)_{1k}$ and $(\alpha\varepsilon)_{2k}$ within the 9 fields of view k. Using this assumption, the computed channel radiances R_{ik}^{n} are expressed in terms of the n^{th} iterative estimate of the relevant cloud parameters according to

$$R_{ik}^{n} = \left(1-(\alpha\varepsilon)_{1k}^{n}-(\alpha\varepsilon)^{n}{}_{2k}\right)R_{i,CLR} + (\varepsilon)^{n}{}_{1k}\,R_i^B\left(p_{c_1}\right)^n + (\alpha\varepsilon)_{2k}\,R_i^B\left(p_{c_2}\right)^n. \qquad 5.4.42$$

In computing R_{1k}^{n}, the previously retrieved values of surface skin temperature, surface spectral emissivity, and atmospheric temperature, moisture, and ozone profiles are used to compute $R_{i,CLR}$ and $R_i^B\left(p_{c_j}\right)$. The only unknowns in Equation 5.4.42 are $\left(\alpha\varepsilon\right)_{jk}$ (j = 1, 2; k = 1, 9), and p_{c_1} and p_{c_2}. The observed radiances $R_{i,k}$ in each of the 9 fields-

of-view for each of the 38 cloud parameter retrieval channels (a total of 342 observations) are used to solve for these 20 variables (18 cloud fractions and 2 cloud top pressures). The noise covariance matrix N used to retrieve cloud parameters, which represents both noise in the observations and uncertainties in the computed values of $R_{i,CLR}$, is taken to be identical to that used in the determination of η (Equation 5.2.9) for the appropriate subset of channels.

The 20 unknown cloud parameters are solved for in an iterative manner. We define Y_{ik}^n as the difference between the observed channel radiances in field of view k, $R_{i,k}$, and that computed from the n^{th} estimate of the cloud parameters, R_{ik}^n. The goal is to find nth iterative parameters so as to minimize Y_{ik}^n. Y_{ik}^n can be expressed according to

$$Y_{ik}^n \equiv R_{i,k} - R_{ik}^n = \left(R_{i,k} - R_{i,CLR}\right) + \sum_{j=1,2} \alpha\varepsilon_{jk}^n \left(R_{i,CLR} - R_i(p_{c_j}^n)\right). \qquad 5.4.43$$

This gives rise to the iterative equation

$$Y_{ik}^{n+1} - Y_{ik}^n = \sum_{j=1,2}\left[\left(R_{i,CLR} - R_i(p_{c_j}^n)\right)\right]\Delta(\alpha\varepsilon)_{jk}^n + \sum_{j=1,2}\left[(\alpha\varepsilon)_{jk}^n\left(\frac{-\delta R_i(\delta p_{c_j})}{\delta p_{c_j}}\right)\right]\Delta p_{c_j}^m$$

$$= \sum_{j=1,2}\left[S_{ik,\Delta\alpha\varepsilon_{jk}}^n\right]\Delta(\alpha\varepsilon)_{jk}^n + \sum_{j=1,2}\left[S_{ik,\Delta p_{c_j}}^n\right]\Delta p_{c_j}^n \qquad 5.4.44$$

in which the terms in brackets are the appropriate Jacobians, computed empirically as are all other Jacobians. Note that if $(\alpha\varepsilon)_{jk}$ (for all k) and/or $\delta R_i / \delta p_{c_j}$ (for all i) are small for a given p_{c_j}, the Jacobian for that cloud top pressure is small and the cloud top pressure is contained primarily in a heavily damped mode and is not changed significantly from the initial guess.

As stated previously, the cloud parameter retrieval step is performed four times, occurring each time new cloud cleared radiances $\hat{R}_i$ are derived. This is done primarily because the retrieved pressure of the highest cloud is used to decide which channels "see" clouds. In the methodology described above, only 2 cloud top pressures are derived to be representative of clouds in the entire AMSU FOR comprised of 9 AIRS FOV's. Because the primary purpose of the cloud parameter retrieval step, the first three times it is performed, is to determine cloud top pressure, the process is simplified the first three times it is done to derive only 2 cloud top pressures and 2 effective cloud fractions. This saves a considerably amount of processing time. The retrieval methodology is analogous to that described in Equations 5.4.43 and 5.4.44, with the exception that $R_{i,k}$ is replaced by $\bar{R}_i$, $(\alpha\varepsilon)^n_{jk}$ is replaced by $(\bar{\alpha}\bar{\varepsilon})^n_j$, Y^n_{ik} is replaced by $\bar{Y}^n_i$, and S_{ik} is replaced by $\bar{S}_i$, where in each case, the bar superscript refers to the average of the appropriate value over all 9 FOV's k. The first three cloud parameter retrievals then use 38 observations $(\bar{R}_i)$ to determine 2 cloud top pressures and two effective cloud fractions, representative of the average effective cloud fraction over the whole FOR corresponding to each cloud top pressure. The 9 individual cloud fractions are only derived in the last cloud parameter retrieval step.

For our retrievals, the first guess cloud top pressures are taken as 350 mb and 850 mb (or 100 mb above the surface, whichever is less), and the first guess effective cloud fractions taken as 1/6 for the upper cloud and 1/3 for the lower cloud. ΔB_{max} is set equal to 5 when two pairs of cloud fractions are determined, and ΔB_{max} is set equal to 20 when 9 pairs of cloud fractions are determined. The solution is constrained such that $p_{c_1} \geq 100\,\text{mb}$ and $p_{c_2} \leq p_s - 50\,\text{mb}$ where p_s is the surface air pressure. In addition, $(\alpha\varepsilon)_{1,k} + (\alpha\varepsilon)_{2,k}$ are constrained to be $\leq$ 1.0. If the second effective cloud fraction is either set very small in the first guess, or becomes very small in the retrieval, no useful information about the second cloud top pressure can be determined.

In most cases, IR/MW retrieval based cloud parameters and geophysical parameters, derived in Steps 13 and 14, are reported. In such cases, the 2 cloud top pressures and 18

effective cloud fractions will be reported. These are used to derive 9 values of OLR and clear sky OLR, one for each AIRS FOV, which are also reported. Under some conditions, primarily when cloud cleared radiances cannot be generated in an accurate enough manner to produce meaningful results (e.g., if the FOR were overcast), then MR/strat IR based cloud parameters and geophysical parameters, derived in Steps 1 and 2 are reported. In such a case, 2 cloud top pressures and 2 effective cloud parameters are reported, as well as one value each of OLR and clear sky OLR, valid for the whole FOR.

5.4.12 Computation of OLR and Clear Sky OLR

OLR is computed from the AIRS products in a manner analogous to that used to compute OLR from TOVS (Mehta and Susskind, 1999a; 1999b)

$$F = (1-(\alpha\varepsilon)_1-(\alpha\varepsilon)_2)F_{CLR}+(\alpha\varepsilon)_1 F_{CLD}(p_{c_1})+(\alpha\varepsilon)_2 F_{CLD}(p_{c_2}), \qquad 5.4.45$$

where in Equation 5.4.45, F represents the OLR for the entire scene, F_{CLR} represents the OLR emanating from the clear portion of the scene, and $F_{CLD}(p_c)$ represents the OLR that would be observed if the scene were covered by a black cloud with cloud top pressure p_c. All OLR flux terms are computed as the sum of contributions from 14 spectral bands. F_{CLR} is computed according to

$$F_{CLR} = \pi \sum_{i=1}^{14}\left[\varepsilon_i B_{\nu_i}(T_s)\tau_i(p_s)+\int_{\ell np_s}^{\ell n\overline{p}} B_{\nu_i}(\tau)\frac{d\tau_i}{d\ell nP}d\ell np\right] \qquad 5.4.46$$

where ε_i is the average surface emissivity over spectral band i. The band transmittances $\tau_i(p)$ used in Equation 5.4.46 are computed at band dependent effective zenith angles, θ_i. A small term related to downwelling thermal radiation reflected off the surface and transmitted to space is neglected in Equation 5.4.46. $F_{CLD}(p_c)$, the flux emanating from the portion of the scene covered by black cloud at cloud top pressure p_c, is computed in an analogous way

$$F_{CLD}(p_c) = \pi \sum_{i=1}^{14} \left[B_{\nu_i}\left(\tau_{p_c}\right)\tau_i(p_c) + \int_{\ell n p_c}^{\ell n \bar{p}} B_{\nu_i}(\tau) \frac{d\tau_i}{d\ell np} d\ell np \right] \qquad 5.4.47$$

The band transmittances $\tau_i(p)$ are parameterized as a function of temperature, moisture, and ozone profile in an identical manner to those used by Mehta and Susskind (1999a, 1999b).

In all cases, F_{CLR}, F_{CLD}, and $\alpha\varepsilon$ are computed using the appropriate state estimates, IR/MW or MW/strat IR, as described previously. F_{CLR} is also reported as the clear sky OLR, representative of what OLR would be if the scene were otherwise identical but contained no clouds. This is a physically different quantity to that which would have been observed if sampled only under completely clear conditions because of sampling differences.

5.4.13 Differences Between At-Launch Algorithm and Version 4

The at-launch algorithm, described in Susskind, *et al.*, (2003), was developed and optimized based on simulated data. The differences between Version 4, used with real AIRS/AMSU/HSB data, and the at-launch version of the retrieval algorithm are relatively small. The post-launch channel frequencies were somewhat different from those pre-launch, as expected, as were the channel spectral response functions. Consequently, new Radiative Transfer Algorithm (RTA) coefficients were generated (Strow, *et al.*, 2005) to be consistent with the post-launch instrumental conditions. Minor modifications were therefore made to the set of channels used in the retrieval algorithm shown in Table 5.4.2. The most significant of these modifications resulted from the finding that more channels in the 4.3-μm region were affected by non-local thermodynamic equilibrium (non-LTE) than previously thought. Radiances in these channels are perturbed during the day, and these channels are currently not used in the retrieval algorithm day or night. It was also found that observed channel brightness temperatures for AIRS, as well as AMSU, were biased from those computed using the RTA with the best estimate of the truth. These biases, referred to as "tuning coefficients," are subtracted from all terms in the retrieval algorithm involving observed minus computed brightness temperatures. New regression

coefficients were also generated (see Section 5.3) based on clear column radiances for an ensemble of accepted retrievals, using the 3-hour ECMWF forecast at "truth." A few AIRS channels exhibit a radiometric instability characteristic, known as "popping", and these channels are excluded from the list of channels used either in the regression or the physical retrieval steps. It was also found that many of the channels used in the at-launch physical retrieval algorithm were not needed in practice, and are no longer used in the physical retrieval steps so as to make the physical retrieval computationally more efficient with no loss of accuracy. A new concept has also been introduced in terms of quality control, in which different geophysical parameters retrieved from AIRS/AMSU data have different criteria for acceptance. The basic steps in the retrieval algorithm, given in Section 5.4.1, are essentially identical to those shown in Susskind, *et al.*, (2003). The only change is a new step to determine the CO profile done after the retrieval of the final surface skin temperature and temperature profile. This step is done in an analogous manner to what is done in the H_2O and O_3 profile retrieval steps. No change was made to the cloud clearing algorithm other than the AIRS channels used in the cloud clearing step. The major change from the at-launch algorithm is with regard to the new quality flag concept.

5.4.13.1 Minor Differences from the At-Launch Version

There are only minor differences in the details of the different retrieval steps, compared to what was done in the pre-launch algorithm described in Susskind, *et al.*, 2003. These minor differences are detailed in the following sections.

5.4.13.1.1 Temperature Profile Retrieval Step

The number of AIRS channels used in the physical retrieval of temperature profile has been decreased from 147 to 65, the number of functions remains at 23, and ΔB_{max} has been reduced from 0.75 to 0.5 (increasing damping). Information about the mid-lower troposphere comes primarily from the 9 temperature sounding channels between 2387 cm^{-1} and 2395 cm^{-1}.

5.4.13.1.2 Water Vapor Profile Retrieval Step

The number of AIRS channels used has been decreased from 66 to 42, the number of functions remains at 10, and ΔB_{max} remains at 1.0.

5.4.13.1.3 Ozone Profile Retrieval Step

The number of AIRS channels has been increased from 23 to 26, the number of functions remains at 7, and ΔB_{max} remains at 0.75.

5.4.13.1.4 Surface Parameter Retrieval Step

Some significant modification has been made to the surface parameter retrieval step. The surface parameter retrieval step determines surface skin temperature, IR surface spectral emissivity ε_i, and IR effective surface spectral bi-directional reflectance ρ_i. The initial guess for ε_i and ρ_i is generated by the regression step. Over ocean, we replace this by the Masuda model refined by Wu and Smith (1997) as the initial guess for ε_i^0, and set $\rho_i^0 = \left(1-\varepsilon_i^0\right)/\pi$. In addition to determining T_s, Susskind, *et al.*, (2003) determined coefficients of 8 perturbation functions for ε_i and 3 perturbation functions for ρ_i. 53 window channels were used, and ΔB_{max} was set at 0.2.

Detailed analysis of sea surface temperature retrieval accuracy showed that use of 8 perturbation functions over ocean, even with considerable damping resulting from $\Delta B_{max} = 0.2$, was causing spurious oscillations in the retrieved spectral emissivity, and resultant biases in retrieved sea surface temperature. Over ocean, the Masuda spectral emissivity model generates a reasonable shape of the spectral surface emissivity. Therefore, the number of ε perturbation functions was reduced from 8 to 2. One function adds a spectrally constant value to ε_i^0 at frequencies lower than 1614 cm^{-1}, and the second adds a different spectrally constant value to ε_i^0 at frequencies higher than 2181 cm^{-1} (there are no AIRS channels between 1614 and 2181 cm^{-1}). Also, only a single spectrally constant perturbation function, which is added to ρ^0, is used. ΔB_{max} has been increased (less damping) to 0.5. This resulted in a significant improvement in the accuracy of the retrieved sea surface skin temperature.

For simplicity, the same procedure is used over land, sea ice and coasts (henceforth referred to as "land"). Unlike ocean cases, the initial guess for the shape of the surface spectral emissivity, coming from the regression step, is in general very poor, especially over arid land. The Version 4 surface emissivity algorithm, optimized for ocean cases, needs more development for land cases. Consequently, the surface spectral emissivity product over land should not be used by researchers at this time. We are conducting research to produce a better land surface spectral emissivity in the next version of the AIRS retrieval algorithm.

5.4.13.1.5 Cloud Clearing

The cloud-clearing methodology, developed and optimized using simulated cloudy radiances, is essentially unchanged when used with real data. Less channels are used than in the at-launch algorithm because it was found that their elimination served only to speed up the cloud-clearing step with no appreciable loss in accuracy. In particular, channels in the spectral region 2387 – 2392 cm^{-1} are no longer included in the cloud clearing step.

5.4.13.1.6 Cloud Parameter Retrievals

The most significant change to any step in the at-launch retrieval system is in the cloud parameter retrieval. The at-launch cloud parameter retrieval algorithm was optimized based on simulated gray clouds at two levels, with varying cloud fractions in the nine AIRS spots. Real clouds are of course more complex. Since cloud clearing anticipates cloud formations and cloud parameter retrieval anticipates cloud layers, the impact is entirely different. Susskind, *et al.*, (2003) accounts for up to four independent cloud formations within a 3x3 array of AIRS FOVs in deriving the clear column radiances. The identical methodology is used in Version 4, and in most cases, excellent results are obtained. Cases in which the cloud-clearing methodology breaks down are usually identified by the quality control algorithm described in the next section.

For cloud parameter retrieval, however, we found that in many cases, the two-layer assumption does not represent the clouds very well and the rate of convergence to the best radiatively equivalent two-layer solution is slower than found in simulation. To

accommodate this realization, the convergence test, which in simulation specified that each iteration must reduce residuals by at least 25% before the retrieval is terminated, was relaxed to a test which specified a minimum reduction of 5%, and this convergence test was applied only after the third iteration. The damping criterion was also relaxed, increasing ΔB_{max} from a pre-launch value of 7.0 to 20.0, so that the radiances would be believed much more, relative to our arbitrary cloud parameter first guess state with cloud top pressures of 350 and 850 mb. It was discovered that the algorithm is more able to move clouds up in the atmosphere than to move them down. For this reason, the first guess, which was 350 mb and 650 mb in Susskind, *et al.*, (2003), was altered to 350 and 850 mb, subject to being a minimum of 100 mb above the surface. However, there were no adjustments made to the fundamental cloud parameter retrieval methodology described in Susskind, *et al.*, (2003) and in Section 5.4.8.6.

5.4.13.2 Generation of Tuning Coefficients

Steps in the physical retrieval and cloud clearing algorithms involve the difference between observed (or cloud cleared) radiances R_i, and those computed from some geophysical state, R_i^{comp}, using the radiative transfer algorithm (RTA) described in Strow, *et al.*, (2005). If one had a perfectly calibrated instrument and perfect parameterization of the radiative transfer physics, then, given the true surface and atmospheric state, expected radiances, R_i^{true}, could be calculated that match the observed radiances R_i up to instrumental noise. Systematic errors in either the calibration of the observed radiances $R_{i,\ell}$ (channel i, zenith angle ℓ), or in the computation of radiances $R_{i,\ell}^{comp}$, would introduce biases in $\left(R_{i,\ell} - R_{i,\ell}^{comp}\right)$ and propagate errors into the solution. We attempt to identify these biases and remove their effect by subtracting them from all terms of the form $\left(R_i - R_i^{comp}\right)$ whenever they occur in the retrieval and cloud clearing processes, as well as in the cloud parameter retrieval process. This subtraction is done in the brightness temperature domain for both AIRS and AMSU radiances, in a manner analogous to that described in Susskind and Pfaendtner (1989) and used by Susskind, *et al.*, (1997) in the analysis of HIRS2 and MSU radiances:

$$\left(\hat{\Theta}_{i,\ell} - \Theta_{i,\ell}^{comp}\right)' = \left(\hat{\Theta}_{i,\ell} - \Theta_{i,\ell}^{comp}\right) - \delta\Theta_{i,\ell} \qquad 5.4.48$$

where $\left(\hat{\Theta}_{i,\ell} - \Theta_{i,\ell}^{comp}\right)'$ is the tuned value, Θ_i is the brightness temperature corresponding to R_i, and $\delta\Theta_{i,\ell}$ is the tuning correction.

All retrieval steps involve $\hat{R}_i - R_i^{comp}$. For AIRS channels, the tuned value of $\left(\hat{R}_{i,\ell} - R_{i,\ell}^{comp}\right)$, denoted by $\left(\hat{R}_{i,\ell} - R_{i,\ell}^{comp}\right)'$, is computed according to

$$\left(\hat{R}_{i,\ell} - R_{i,\ell}^{comp}\right)' = \left(\hat{\Theta}_{i,\ell} - \Theta_{i,\ell}^{comp}\right)' \left(\frac{dB}{dT}\right)_{\hat{\Theta}_{i,\ell}}, \qquad 5.4.49$$

and is used in place of $\left(\hat{R}_{i,\ell} - R_{i,\ell}^{comp}\right)$ in all retrieval steps. An analogous procedure is used to adjust observed minus computed radiances in the cloud clearing and cloud parameter retrieval steps.

5.4.13.2.1 Generation of AIRS Tuning Coefficients

In order to generate AIRS channel tuning coefficients, cases were selected thought to be unaffected by clouds so as not to have to account for cloud effects on the observed radiances. The 3-hour ECMWF forecast, collocated to the satellite observations, is used as truth, and observations were limited to nighttime non-frozen ocean (henceforth referred to as "ocean") so as to avoid effects of solar radiation reflected by the surface as well as effects of non-LTE. Ocean cases were selected because we have the best estimate of both sea-surface temperature and surface emissivity over oceans, compared to land, to be used in the computation of R_i^{true}. Over ocean, the IR surface spectral emissivity is parameterized according to Masuda, *et al.*, (1988), as modified by Wu and Smith (1997), assuming a surface wind speed of 5 m/sec. For the computation of IR biases, cases were selected for which the retrieval was accepted and called essentially clear according to the methodology described in Susskind, *et al.*, (2003). In addition, a cirrus screening test was added, eliminating all scenes in which the absolute difference of the difference of

observed minus computed brightness temperatures for 790 cm^{-1} and for 945 cm^{-1} was greater than 0.3K.

Figure 5.4.3a shows the nighttime biases of observed minus computed brightness temperatures averaged over all zenith angles ℓ for the AIRS channels for the 5138 clear ocean night cases found on 6 September 2002. These biases had very little scene or zenith angle dependence. Therefore, for AIRS channels, the tuning coefficient for channel i is taken as an angle independent constant

$$\delta\Theta_{i,\ell} = A_i \qquad 5.4.50$$

Computed biases in channels affected significantly by radiation emitted from the surface are less meaningful because of effects of uncertainty in the "true" surface skin temperature and surface emissivity on R_i^{true}. Likewise, biases for channels significantly effected by ozone absorption are suspect because of limited accuracy of ozone profiles in the ECMWF forecast, and to a lesser extent, this holds for channels significantly affected by water vapor absorption as well. In general, observed brightness temperatures are somewhat warmer (generally 0.5K-1.5K) than those computed using the RTA in the CO_2 absorption region 650 cm^{-1} – 750 cm^{-1}.

Figure 5.4.3b shows that daytime biases are very similar to nighttime biases, except for the region between 2240 cm^{-1} and 2386 cm^{-1}, and greater than 2400 cm^{-1}. Daytime radiances in the first spectral range are affected to varying degrees by non-LTE. Figure 5.4.3b indicates by stars the channels currently used for temperature sounding in the spectral region 2200 cm^{-1} – 2420 cm^{-1}, which is a smaller set than in the at-launch version. Channels sensitive to non-LTE effects are not used in the physical retrieval step at this time because non-LTE effects are not currently accounted for in the RTA. The negative differences at frequencies greater than 2400 cm^{-1} are indicative of limitations in the treatment of the surface bi-directional reflectance, ρ, when generating the "truth". This is of no consequence because ρ is solved for as part of the retrieval process. Tuning coefficients are applied only for channels in the range 650 cm^{-1} – 756 cm^{-1} (CO_2

absorption), and 2180 cm^{-1} – 2422 cm^{-1} (CO, N_2O and CO_2 absorption). Those spectral regions in which the tuning coefficients are applied are indicated by the horizontal bars in Figure 5.4.3.

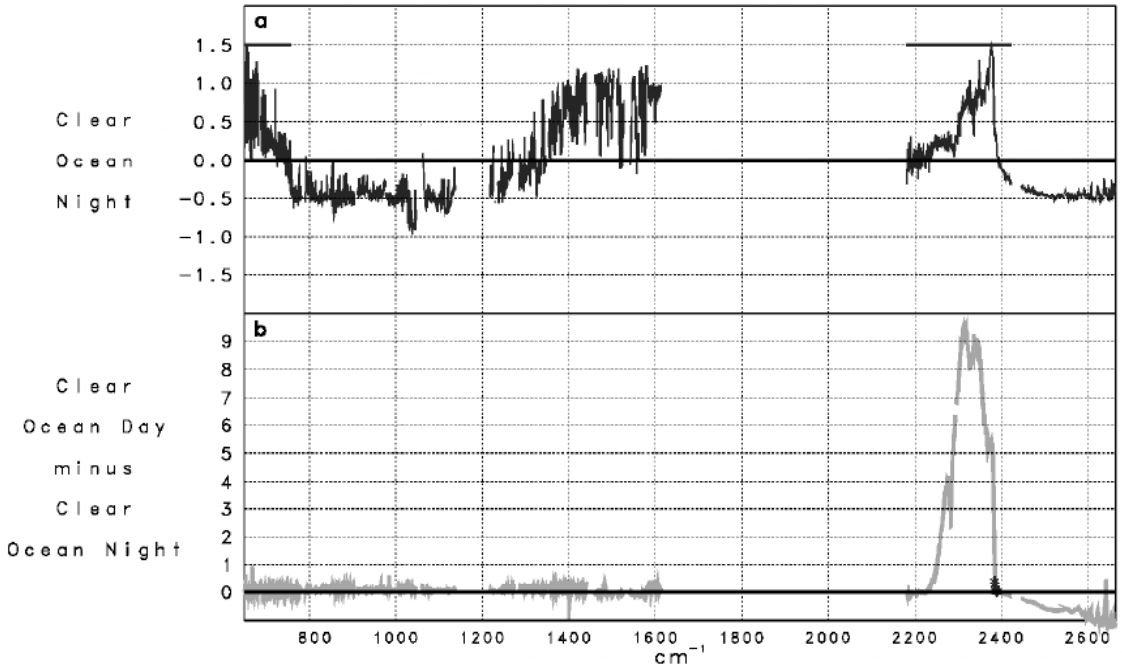

Figure 5.4.3. Brightness Temperature BIAS Observed minus Computed (K)

5.4.13.2.2 Generation of AMSU Tuning Coefficients

The procedure used to generate AMSU tuning coefficients is analogous to that used to generate AIRS tuning coefficients. The coefficients used were generated for ocean cases on 6 September 2002. These cases were screened to eliminate contamination from precipitating clouds. Unlike the biases found for AIRS channels, AMSU channels had a pronounced, and systematic, zenith angle (beam position) dependence. This arises from effects of antenna side-lobes, which were not adequately accounted for in the calibration of the AMSU observations. Figure 5.4.4 shows the beam position biases observed on 6 September 2002, for the AMSU-A channels. The larger the AMSU-A channel number, the higher in the atmosphere the channel is sensitive to, and less of the surface is seen. Also shown are analogous biases determined using data for 25 January 2003. The beam position biases found on 6 September 2002 and 25 January 2003 are very similar to each other, including coarse and fine angle dependent features.

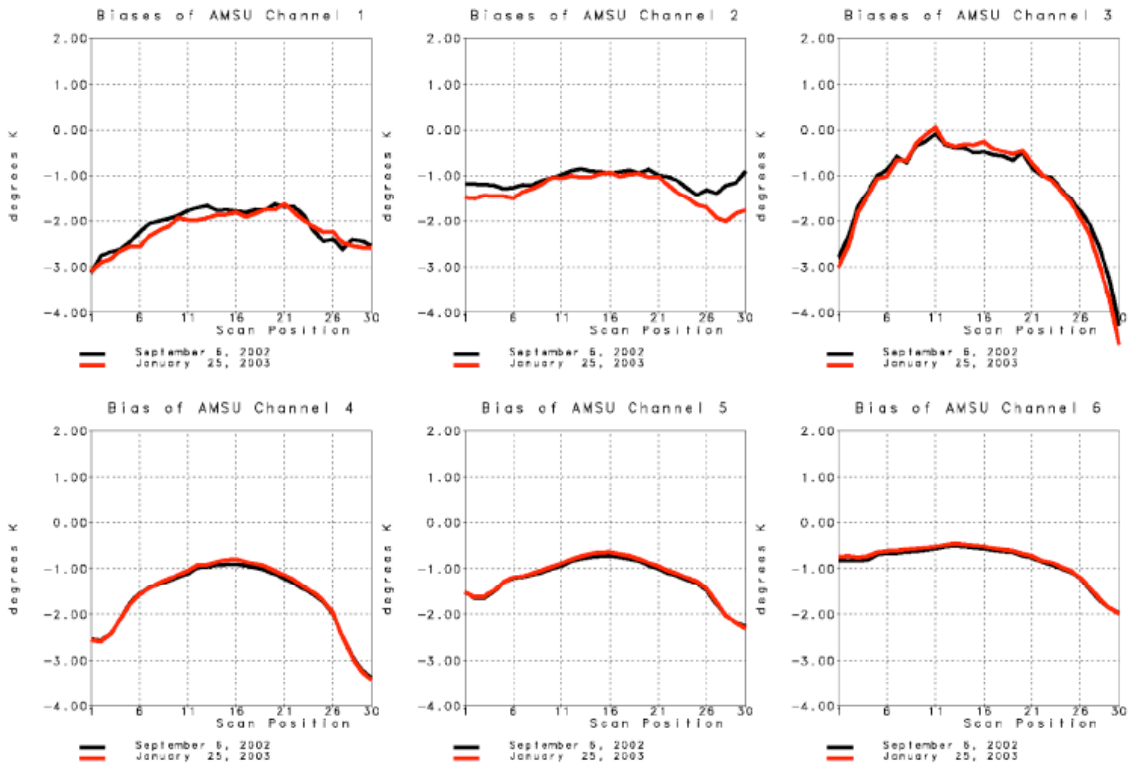

Figure 5.4.4a. Biases of Microwave Channels vs. ECMWF

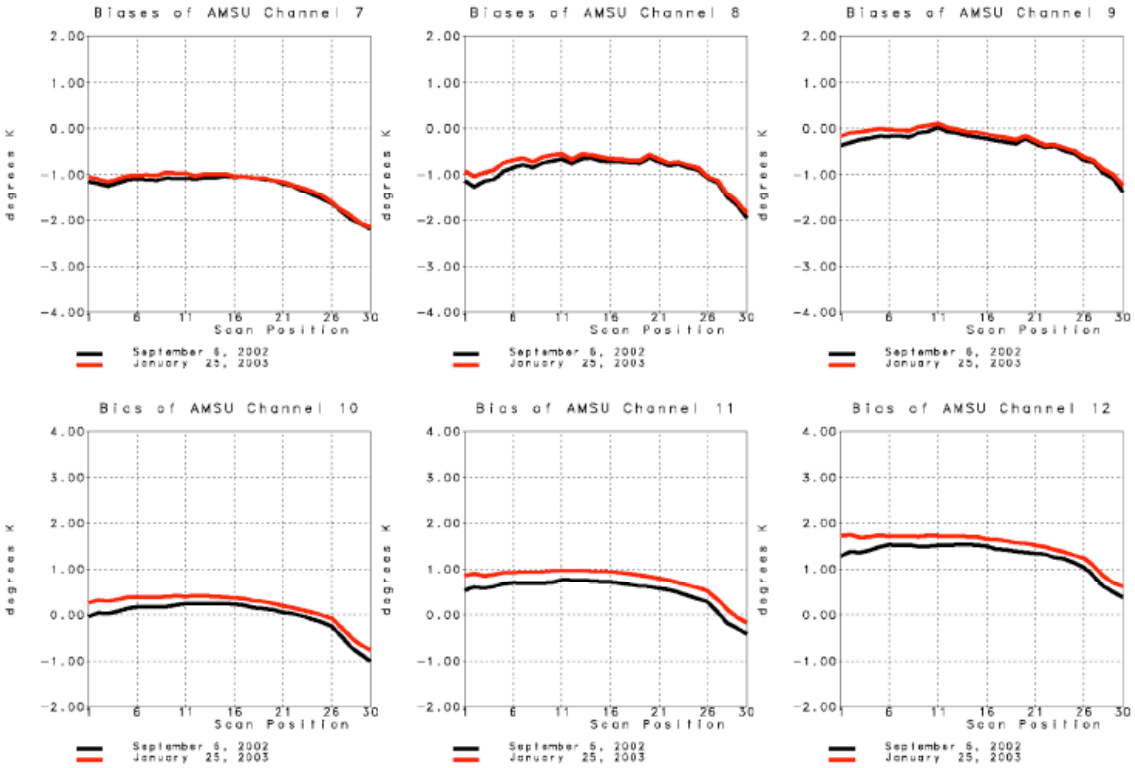

Figure 5.4.4b. Biases of Microwave Channels vs. ECMWF

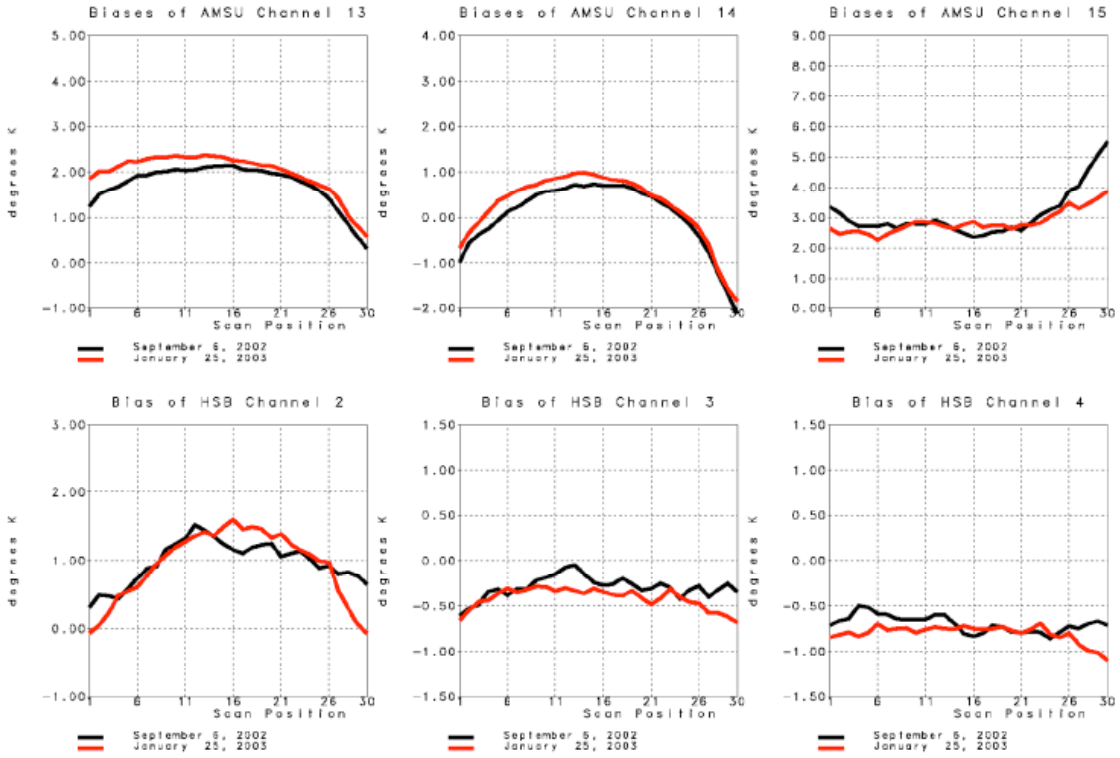

Figure 5.4.4c. Biases of Microwave Channels vs. ECMWF

The standard deviations of the difference between observed and computed brightness temperatures for these channels are shown in Figure 5.4.5. The standard deviations are affected by channel noise, errors in the "truth", and scene dependence of the necessary tuning. For the most part, the beam dependent standard deviations are on the order of the instrumental noise. This indicates that there is only small scene dependence of the required tuning. Standard deviations increase with increasing sensitivity of the channel radiance to surface effects, because of errors in the "truth". Note, for example, the standard deviations in channels 1 and 2, and the central angles of channels 3 and 4, which see less and less of the surface respectively, especially as zenith angles increase from nadir. Figure 5.4.5 also confirms the finding that AMSU channel 7 is very noisy, and for this reason, radiances in AMSU-A channel 7 are not used in the retrieval procedure.

Based on these findings, AMSU channels are tuned according to

$$\delta\Theta_{i,\ell} = A_{i,\ell} \qquad 5.4.51$$

with $A_{i,\ell}$ determined using the September 6, 2002 data, and shown by the fine black curves in Figure 5.4.3a. All AMSU channels are tuned (i.e., the tuning correction is applied) except for channel 15 (89 GHz), because radiances in channel 15 over ocean are highly sensitive to absorption by water vapor, which is not adequately characterized by the ECMWF forecast. For the same reason, HSB channels are not tuned. AMSU-A channels 1 and 2 are tuned, even though they are highly sensitive to surface effects,because of the obvious large angle dependence to the biases. As with AIRS tuning coefficients, these adjustments are used globally and for all time periods.

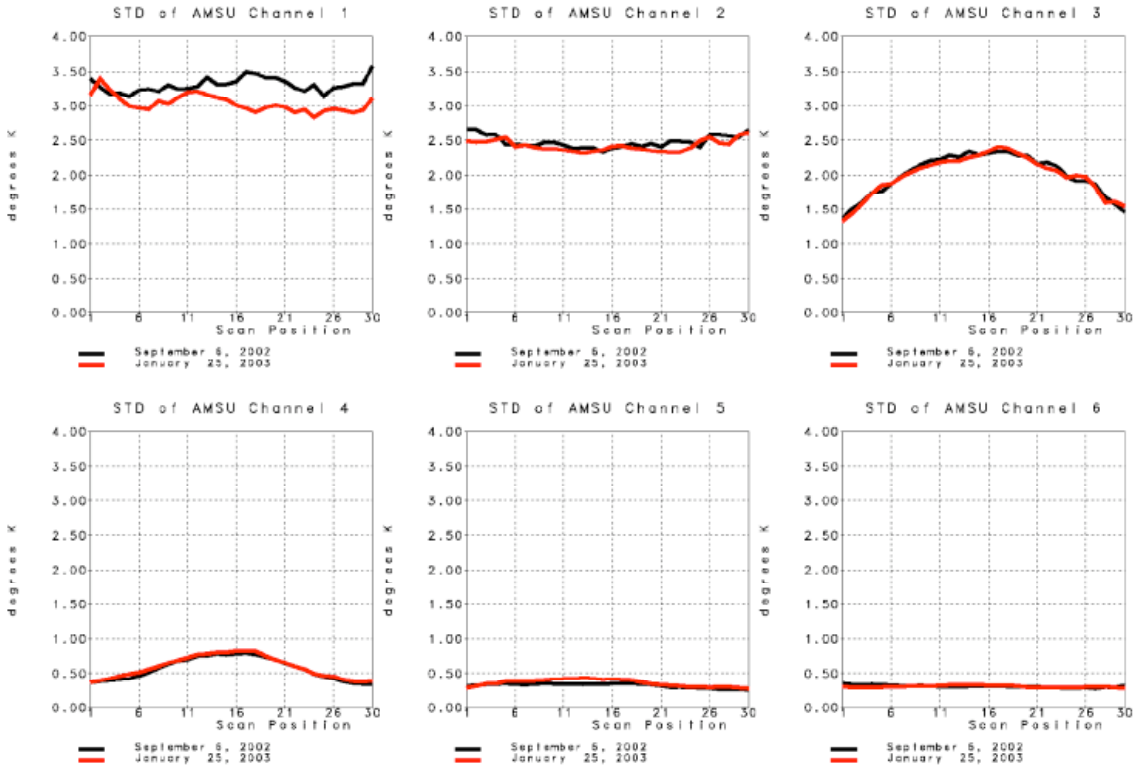

Figure 5.4.5a. STD Microwave Channels vs. ECMWF

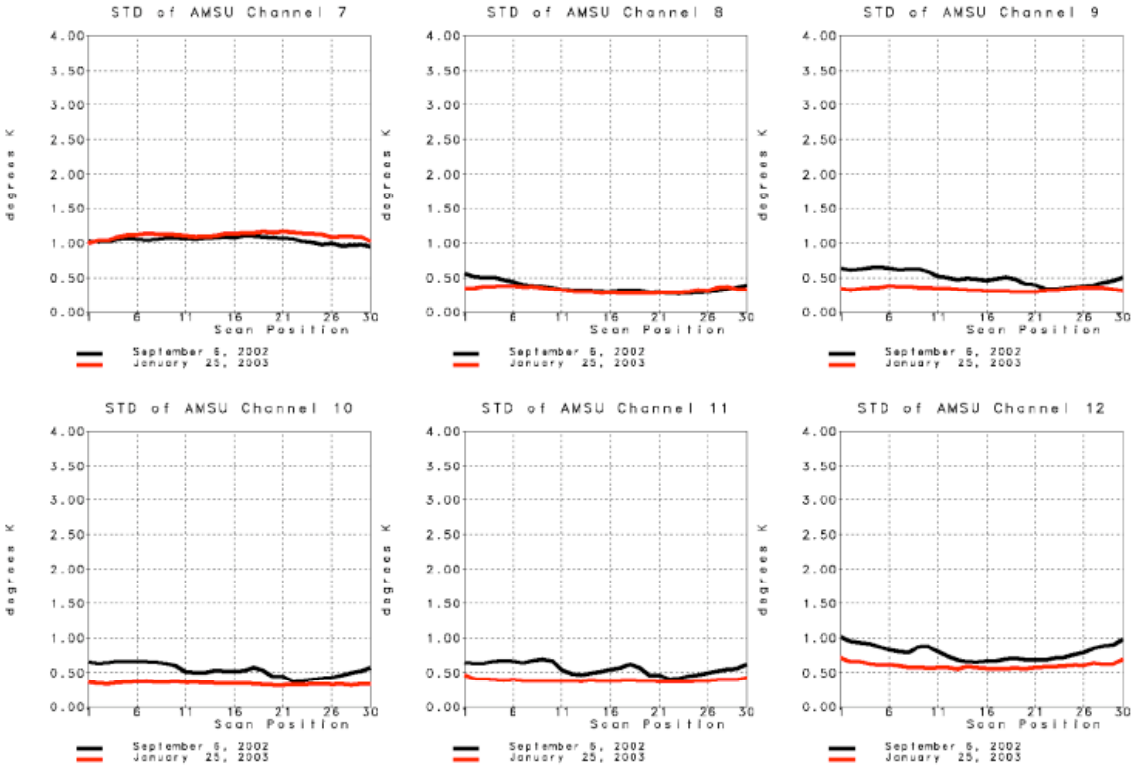

Figure 5.4.5b. STD Microwave Channels vs. ECMWF

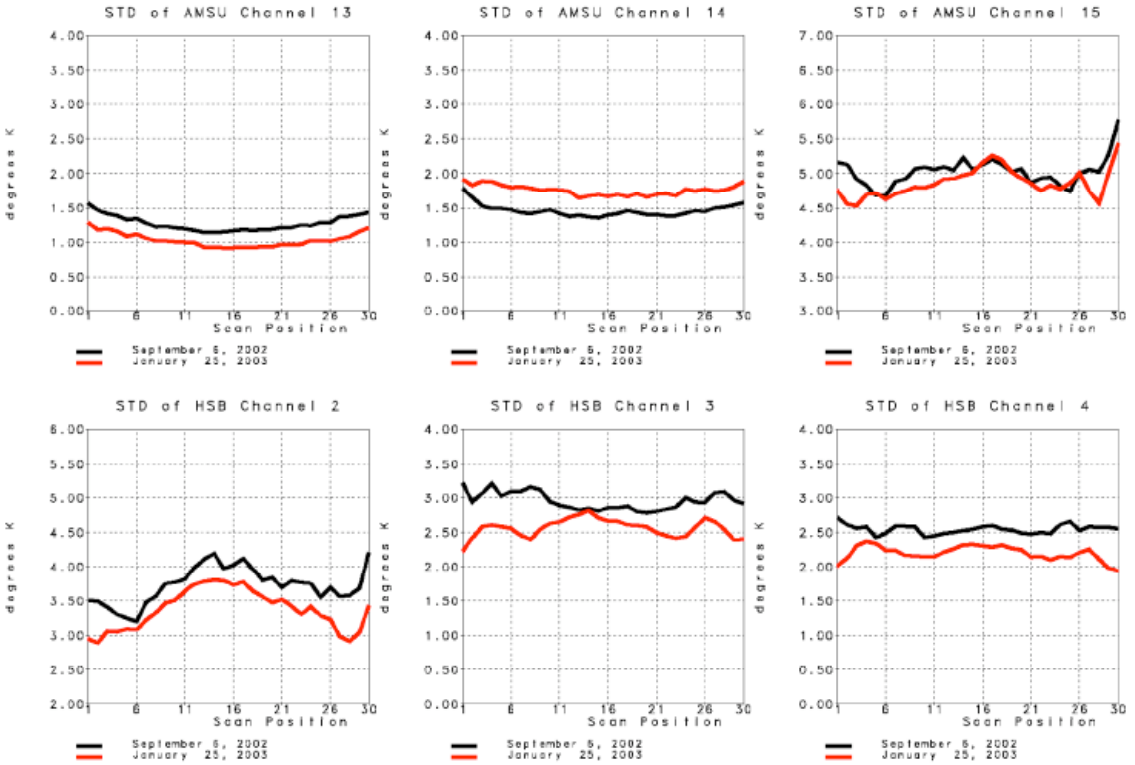

Figure 5.4.5c. STD Microwave Channels vs. ECMWF

5.4.13.3 Modeling of Computational Noise

The physical retrieval algorithm (Susskind, *et al.*, 2003) involves the matrix $\left(S'N^{-1}S\right)$ where S_{ij} is the Jacobian, (the derivative of the computed radiance of channel i with regard to variable j), and $N_{ii'}$ is the channel noise covariance matrix. An analogous equation, involving the matrix N, is used in the cloud clearing process.

In Susskind, *et al.*, (2003), N is written as a sum of two components

$$N = \hat{N} + \tilde{N} \qquad 5.4.52$$

where $\hat{N}$ represents errors in $\hat{R}$ due to instrumental noise, including effects of noise amplification and errors resulting from the cloud clearing process, and $\tilde{N}$ represents uncertainty in R_i^{comp} resulting in errors in variables assumed to be known. An additional term, reflecting errors in $\left(\hat{R}_i - R_i^{comp}\right)$ resulting from a combination of calibration errors and errors in the RTA, was not included in Susskind, *et al.*, (2003). Such a term is included in the channel noise covariance matrix given in Equation 5.4.25, and called M_{ii}^{phys}. In the following discussion, M_{ii}^{phys} will be referred to as $\bar{N}_{ii}$.

In Section 5.4.11.2, the procedure to identify biases in $\left(\hat{R}_i - R_i^{comp}\right)$ was given, as well as the methodology to account for the effects of biases in the retrieval process. There are still residual (possibly case dependent) errors in $\left(\hat{R}_i - R_i^{comp}\right)$. These uncertainties, $\bar{N}_{ii}$, need to be modeled and included in the channel noise covariance matrix

$$N = \hat{N} + \tilde{N} + \bar{N} \qquad 5.4.53$$

Figure 5.4.5b showed standard deviations of $\left(\hat{\Theta}_{i,\ell} - \Theta_{i,\ell}^{true}\right)$ for the AMSU-A channels. The values in Figure 5.4.5b combine the effects of $\hat{N}$ (channel noise), $\tilde{N}$ (effects of errors in the truth) and $\bar{N}$ (residual errors). It is difficult to separate $\bar{N}$ from $\hat{N}$ and

(especially) from $\tilde{N}$. For some channels, $\tilde{N}$ (errors in the "truth") could be the dominant term.

In an attempt to estimate $\overline{N}$, we look at the standard deviation of $\left(\hat{\Theta}_i - \Theta_i^{sol}\right)$, where R_i^{sol} is computed from the retrieved state and Θ_i^{sol} is the brightness temperature corresponding to R_i^{sol}. For AIRS channels, the same set of clear ocean observations on 6 September 2002 that were used to generate the tuning coefficients were used to estimate $\overline{N}_{ii}$. Clear cases were chosen so as to avoid noise amplification and other errors arising from the cloud-clearing process. If $\overline{N}_{ii}$ were set equal to the standard deviation of $\left(\hat{\Theta}_i - \Theta_i^{sol}\right)$, $\overline{N}_{ii}$ could be overestimated on the one hand, because of inclusion of noise effects $\hat{N}_{ii}$ in the residual, and underestimated on the other hand, if an incorrect solution could be found that matched, case by case, the noise in $\hat{R}_i$ as well as the residual physics errors. The latter will not happen in general because radiances in many channels influence the solution. Nevertheless, if a geophysical parameter (say, 1-mb temperature) is determined primarily by the radiance in a single channel i, then a case by case solution would be found such that $\left(\hat{R}_i - R_i^{sol}\right)$ would be very small. This situation occurs in those 15-μm channels primarily sensitive to the upper stratosphere, at frequencies lower than 670 cm^{-1}. Therefore, (somewhat arbitrarily), $\overline{N}_{ii}$ was set equal to twice the standard deviation of $\left(\hat{\Theta}_i - \Theta_i^{sol}\right)$ for AIRS channels with frequencies less than or equal to

670 cm^{-1}. At all higher frequencies, (somewhat arbitrarily) $\overline{N}_{ii}$ was set equal to one half the standard deviation of the residual of $\left(\hat{\Theta}_i - \Theta_i^{sol}\right)$ because of possible inclusion of channel noise effects. A number of options were tested, and the above specification of $\overline{N}_{ii}$ resulted in the best retrieval performance. $\overline{N}_{ii}$ is defined in this manner for all channels, but is only relevant for those channels used in the physical retrieval process. Off diagonal terms $\overline{N}_{ij}$ were set equal to zero for all channels. An analogous procedure was used to generate $\overline{N}_{ii}$ for all microwave channels, in which case $\overline{N}_{ii}$ was set equal to

the RMS residual of $\left(\hat{\Theta}_i - \Theta_i^{sol}\right)$. No appreciable zenith angle dependence was found in the standard deviation of $\left(\hat{\Theta}_i - \Theta_i^{sol}\right)$ for either AIRS or AMSU channels. Figure 5.4.4 shows $\overline{N}_{ii}$ determined in this fashion for all AIRS channels. The residuals were evaluated and shown in the brightness temperature sense. The values of $\overline{N}_{ii}$ are typically on the order of 0.3K in brightness temperature units for AIRS channels at frequencies greater than 668 cm^{-1}. When used in Equations 5.2.9 and 5.4.25, $\overline{N}_{ii}$ is converted into the radiance units. $\overline{N}_{ii}$ for AMSU channels was also on the order of 0.3K.

5.4.13.4 New Quality Flags

The major change to the at-launch algorithm is a new concept with regard to quality flags. Susskind, *et al.*, (2003) discussed a number of threshold tests used to determine whether the combined IR/MW retrieval is of good quality. These tests utilize only the AIRS/AMSU radiance data. No external data, such as GCM forecast fields or MODIS observations are used. If the tests were all passed, the combined IR/MW retrieval state, and associated clear column radiances, were reported, as well as cloud and OLR values consistent with the AIRS radiance observations and the IR/MW retrieval state. If any of the tests were not passed, IR/MW retrieval state was "rejected" and the MW/strat IR retrieval state was reported, as well as associated values of cloud parameters and OLR constant with that state. Rejection usually implied problems with regard to treating effects of clouds in the field of view, and rejected cases produced generally poorer results in the mid-lower troposphere and at the surface.

5.4.13.4.1 At-Launch Rejection Criteria

A number of tests are made in Susskind, *et al.*, (2003) to determine whether the entire retrieval is rejected or accepted. The major cause of rejection is difficulty in dealing with the effects of clouds on the AIRS radiances. These tests are described in the following sections, with threshold values given in Table 5.4.4.

5.4.13.4.1.1 Assessment of the Cloud-Clearing Fit

Equations 5.2.16, 5.2.17, and 5.2.7 give the solution for the vectors ζ and η, and the resultant clear column radiances $\hat{R}_i$. If a successful solution is produced, the ensemble

$\hat{R}_i$ for the cloud-clearing channels should match the incoming estimates of cloud-cleared radiances $R_{i,CLR}$ to a reasonable degree. A poor match is indicative of either a particularly poor first guess or problems in handling the effects of clouds on the radiances. The weighted residuals of the clear-column radiances are computed for the channels used in the computation of η, and corrected to brightness temperature units according to

$$\Delta F = \left(\frac{\sum_i \left(\hat{R}_i - R_{i,CLR} \right)^2 N_{ii}^{-1}}{\sum_i N_{ii}^{-1} \left(\frac{\partial B_i}{\partial T} \right)_{\Theta_i}^2} \right)^{1/2} \qquad 5.4.53$$

The solution is rejected if ΔF computed when determining $\hat{R}_i^1$ is greater than 1.75K.

5.4.13.4.1.2 Difficult Cloud Cases

Cases with extensive cloud cover, resulting in low contrast, are particularly difficult to analyze. The solution is rejected in Susskind, *et al.*, (2003) if the sum of the final retrieved cloud fractions $\alpha\varepsilon$ for all cloud layers is greater than 0.8, the noise amplification factor in the final cloud clearing step, $A^{(4)}$, is greater than 3, or the effective noise amplification factor $A_{eff}^{(4)}$ is greater than 8. The retrieval is also rejected if the total cloud liquid water determined in the microwave product retrieval step, W_{liq}, is greater than 0.03 gm/cm^2.

5.4.13.4.1.3 Large Residuals in Second-Pass Retrievals

The general iterative solution is terminated when either the residual R^n (Equation 5.4.23) is less than 10% of the RSS of the predicted noise for each mode $R^n \delta\tilde{B}_\ell$, Equation 5.4.17 or R^n is more than 75% of R^{n-1}. Slow convergence indicates a poor solution. The solution is rejected if the converged value of R is greater than 1.0 times the root-sum-square of $\delta\tilde{B}_\ell$ in either the surface parameter retrieval (R_{surf}) or the

temperature profile retrieval $\left(R_{temp}\right)$ in the second pass. Poor convergence generally indicates problems with the clear column radiances $\hat{R}_i^4$.

5.4.13.4.1.4 Inconsistency of Test "Microwave-Only" Retrievals and Combined Infrared/Microwave Retrievals

Under some conditions, the cloud-cleared radiance $\hat{R}_i^4$ is poor but all convergence tests are passed. Nevertheless, the test microwave-only retrieval produces low level temperatures which differ significantly from those of the second pass retrieval. This generally indicates poor cloud-cleared radiances. The solution is rejected if the root-mean-square differences between the temperatures in the lowest 3 km of the test microwave-only retrieval $\left(\Delta T(p)\right)$ differs from that of the second pass retrieval by more than 1.25K.

5.4.13.4.2 Geophysical Parameter-Dependent Quality Flags

The basic approach used in Version 4.0 with regard to quality flags is identical to that of Susskind, *et al*., (2003) with one major exception: different quality flags are used for different geophysical parameters. Problems dealing with clouds in the field of regard (3x3 array of AIRS fields of view) may produce a poor temperature profile in the lower troposphere, but should not degrade accuracy of stratospheric temperature or upper tropospheric water vapor. For this reason, a less strict threshold test is applied to accept stratospheric temperatures than lower tropospheric temperatures. Cases are classified 0-6 according to their ability to pass 6 increasingly more stringent threshold tests. The higher the number, the tighter the test which is passed. Class 6 passes the tight sea surface temperature test, Class 5 passes the standard sea surface temperature test, Class 4 passes the lower tropospheric temperature test, Class 3 passes the mid-tropospheric temperature test, Class 2 passes the constituent profile test, Class 1 passes the stratospheric temperature test, and Class 0 fails the stratospheric temperature test. The final IR/MW retrieval state and associated clear column radiances and cloud and OLR fields are provided for all Classes except for 0, in which case the MW/strat IR state and associated cloud and OLR parameters are reported.

The threshold tests used to assign quality flags are for the most part identical to those in Susskind, *et al.*, (2003), with the addition of 4 new tests. As before, all tests involve only AIRS and AMSU radiances. Susskind, *et al.*, (2003) threshold values for all of these tests are shown in the first column of Table 5.4.4. A test is passed if the value of the parameter used in the test is less than or equal to the threshold value. All tests must be passed for the final IR/MW retrieval state to be accepted.

Version 4 threshold values for each of the 6 Classes described above for all of these tests are included in Table 5.4.4. Tests for some classes use separate threshold values for ocean cases and land cases. When the thresholds are different, the land threshold is shown in parenthesis, and is always larger or the test is non-applicable. Non-applicable tests are indicated by X. Four new tests have also been added: $A_{eff}^{(1)}$, which is analogous to $A_{eff}^{(4)}$ but is applied after the initial cloud clearing; $\Delta\Theta_5$, which is the absolute value of the (tuned) difference between the observed brightness temperature of AMSU channel 5 and that computed from the final retrieval state; Δ_{tskin}, which is the absolute value of the difference between the regression surface skin temperature and the final surface skin temperature; and RS (Goldberg, *et al.*, 2003), which represents how well the observed AIRS radiances can be represented by use of 200 principle components. Threshold values for these tests for all classes are included in Table 5.4.4. Bold values indicate the introduction of a new test or tightening of a previous threshold. These thresholds were obtained empirically, varying one threshold at a time, in an attempt to achieve the best accuracy while maintaining reasonable spatial coverage of accepted cases. Examples of the tradeoff between coverage and accuracy are given in the following sections. In each case, all other thresholds are held fixed, with only the value of a single threshold being varied.

Table 5.4.4. Quality Flag Test Thresholds

	Susskind et al. (2003)	Version 4					
Test	Acceptable Profile	1) T(p) good 200mb&up	2) q(p) good O_3(p) good	3) T(p) good 3km&up	4) T(p) good above surface	5) SST good Loose	6) SST good Tight
$\alpha\varepsilon$	80%	**90%**	90%	90%	90%	90%	90%
W_{liq}	.03	X	**.03**	.03	.03	**.01**	.01
$\Delta T(p)$	1.25	X	X	**2.0**	2.0	2.0	2.0
$A^{(4)}$	3	X	**8.0**	**2.0**	2.0	2.0	2.0
$A_{eff}^{(4)}$	8	X	X	X	**15** (X)	**8**	8
ΔF	1.75	X	**8.0**	**2.0 (6.0)**	**1.5 (1.5)**	1.5	1.5
R_{temp}	1.0	X	X	**0.75**	0.75	0.75	0.75
R_{surf}	1.0	X	X	**0.75** (X)	0.75 (X)	0.75	0.75
$A_{eff}^{(1)}$	X	**200**	200	**30** (X)	30 **(30)**	**9**	**5**
$\Delta\Theta_5$	X	X	X	**2.0**	2.0	2.0	2.0
Δ_{tskin}	X	X	X	X	**1.5**	1.5	1.5
RS	X	**10**	10	**4**	4	**1.2**	1.2

$\alpha\varepsilon$	is the effective cloud fraction
W_{liq}	is cloud liquid water
$\Delta T(p)$	represents the difference of retrieved lower tropospheric temperatures between MW only and IR/MW retrievals
$A^{(4)}$	represents the final channel noise amplification factor
$A_{eff}^{(4)}$	represents the final effective channel noise amplification factor
ΔF	represents the quality of the initial cloud clearing fit
R_{temp}	represents the degree to which the final temperature profile retrieval has converged
R_{surf}	represents the degree to which the final surface parameter retrieval has converged
$A_{eff}^{(1)}$	represents the initial effective channel noise amplification factor
$\Delta\Theta_5$	represents the agreement between the observed AMSU channel 5 brightness temperature and that computed from the final solution
Δ_{tskin}	represents the difference between the final surface skin temperature and the regression valve
RS	represents the principle component reconstruction score of the observed AIRS radiances

5.4.13.4.2.1 Stratospheric Temperature Test

This is the most fundamental test and is used to indicate, first and foremost, whether the final combined IR/MW retrieval, including associated clear column radiances and cloud and OLR parameters should be used, or whether the combined IR/MW retrieval should be "rejected" in all its aspects. The IR/MW retrieval is "rejected" if it is thought to be poorer than the MW/strat IR retrieval, which uses no AIRS channels affected by clouds. The combined IR/MW retrieval cannot always be used because cloud clearing cannot be done under overcast conditions. If the final retrieval were used under such conditions, not only would very poor (too cold) tropospheric and surface skin conditions be derived, but using those conditions to determine cloud fields would result in little or no fractional cloud cover being derived, because AIRS channel radiances computed using the retrieved state would match observed radiances, without the need to add clouds to the scene. Products derived from the combined final IR/MW retrieval are rejected if the retrieved effective cloud fraction is 90% or more. Two tests are added to make sure the clear column radiances are acceptable: $A_{eff}^{(1)}$ must be less than 200 and RS must be less than 10. Failure of the first test indicates that the initial cloud clearing step had significant problems (note the $A_{eff}^{(4)}$ threshold was set equal to 8 in Susskind, *et al.*, (2003)) and of the second test indicates a significant problem with the observed AIRS radiances (RS equal to 1 is the expected value for nominal radiance performance). Retrieved temperatures 200 mb and above (lower pressures) are flagged as good if this test is passed.

5.4.13.4.2.2 Constituent Profile Test

This test is designed to insure that constituent profiles (O_3, CO, H_2O) are of sufficient accuracy for research use. Constituent profiles are considerably more variable, and less well predicted by models, than are temperature profiles. In general, the more spatial coverage one has, the better, provided the accuracy is adequate. This is especially true with regard to studying interannual variability of monthly mean differences. This applies particularly to water vapor, for which it is desirable to avoid a clear (dry) bias in the selection of the cases to be included in generation of the monthly mean fields. Most CO and H_2O exists in the troposphere, however, and ability to treat cloud effects on the

radiances accurately is more important than with regard to stratospheric temperatures. Therefore three tests used in Susskind, *et al.*, (2003), designed to indicate potential cloud clearing problems, are included in the constituent profile test as shown in Table 5.4.4. The liquid water test threshold is the same as is Susskind, *et al.*, (2003), and the thresholds for $A^{(4)}$ and ΔF are considerably less stringent.

5.4.13.4.2.3 Mid-Tropospheric Temperature Test

Retrieved mid-tropospheric temperatures are affected more by errors in the treatment of clouds in the field of view than are stratospheric temperatures. Therefore, tighter quality control is employed in the mid-tropospheric temperature test. Susskind and Atlas (2004) showed that assimilation of AIRS temperature profiles retrieved from AIRS data, using an earlier version of the AIRS retrieval system (which employed a single rejection threshold for all geophysical parameters), significantly improved forecast skill. Moreover, the improvement was much larger if all accepted cases were used as opposed to use of the slightly more accurate, but much less frequent, temperature soundings in cases found to be clear. Therefore, from the data assimilation perspective, there is a trade-off between accuracy and spatial coverage, as is also true with regard to the study of interannual variability. The thresholds shown in Table 5.4.4 are designed to maximize spatial coverage, while minimizing loss in accuracy. Four tests used in Susskind, *et al.*, (2003) are now included in the mid-tropospheric temperature test. The first test, $\Delta T(p)$, which contains the difference in the retrieved temperature in the lowest 3 km between the combined IR/MW retrieval and the test MW retrieval, is looser than that in Susskind, *et al.*, (2003). In addition, the threshold for ΔF has been tightened from that of the constituent profile test, but is still less stringent than in Susskind, *et al.*, (2003). Thresholds in the three additional new tests, $A^{(4)}$, R_{temp}, and R_{surf} are all somewhat tighter than in Susskind, *et al.*, (2003). Thresholds for $A_{eff}^{(1)}$ and RS have also been tightened from their values in the constituent test, but are still at moderate values. A new test, $\Delta\Theta_5$ has also been added, requiring that the observed brightness temperature for AMSU channel 5, sensitive to lower tropospheric temperatures, should agree with that computed from the combined IR/MW retrieval to within 2K after tuning is applied. The threshold for ΔF over land is less restrictive than over ocean because ΔF is affected by

uncertainty in surface emissivity, which is greater over land than over ocean. R_{surf} and $A_{eff}^{(1)}$ are also affected significantly by uncertainty in surface emissivity and for this reason, these tests are not utilized over land, so as to maximize spatial coverage. Errors in surface emissivity do not degrade retrieved mid-tropospheric temperatures appreciably. If the mid-tropospheric temperature test is passed, the temperature profile is flagged as good above 3 km of the surface.

Figure 5.4.6 gives examples over global ocean of RMS errors of the 477 mb – 535 mb layer mean temperature and the percent cases classified as mid-troposphere good when ΔF and R_{temp} are varied independently from their Version 4.0 ocean thresholds values of 2.0 and 0.75 respectively. Thresholds for all other tests are set at the appropriate values in column 3 of Table 5.4.4. The RMS error of the 477 mb – 535 mb layer mean temperature, using Version 4.0 thresholds, is 0.888K and the percent of cases classified as mid-troposphere good is 58.3%. If the threshold of R_{temp} were set at 0.4 instead of 0.75, the RMS error or this layer mean temperature would drop to 0.846K, but the percentage of cases classified as mid-troposphere good would drop to an unacceptably low value of 33.8%. At an R_{temp} threshold of 1.0, the RMS error rises to 0.904K, with only a small increase in percent of cases classified as good. Analogous statistics for $A_{eff}^{(1)}$ show a RMS error of 0.815K, with 29.1% classified as good, if the $A_{eff}^{(1)}$ threshold were set at 10, rather than 30, and an RMS error of 0.898K, with 62.2% accepted, if the $A_{eff}^{(1)}$ threshold were set at 40 rather than 30.

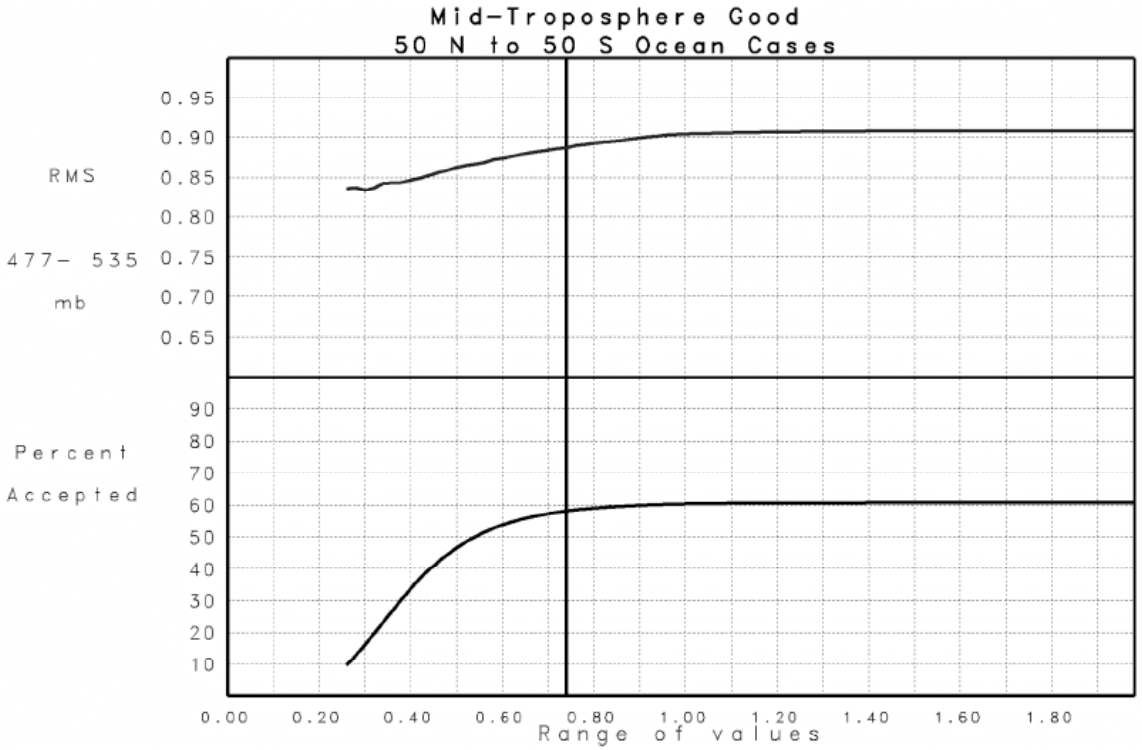

Figure 5.4.6a. R_{temp}: Degree to Which Final Temperature Profile Retrieval has Converged

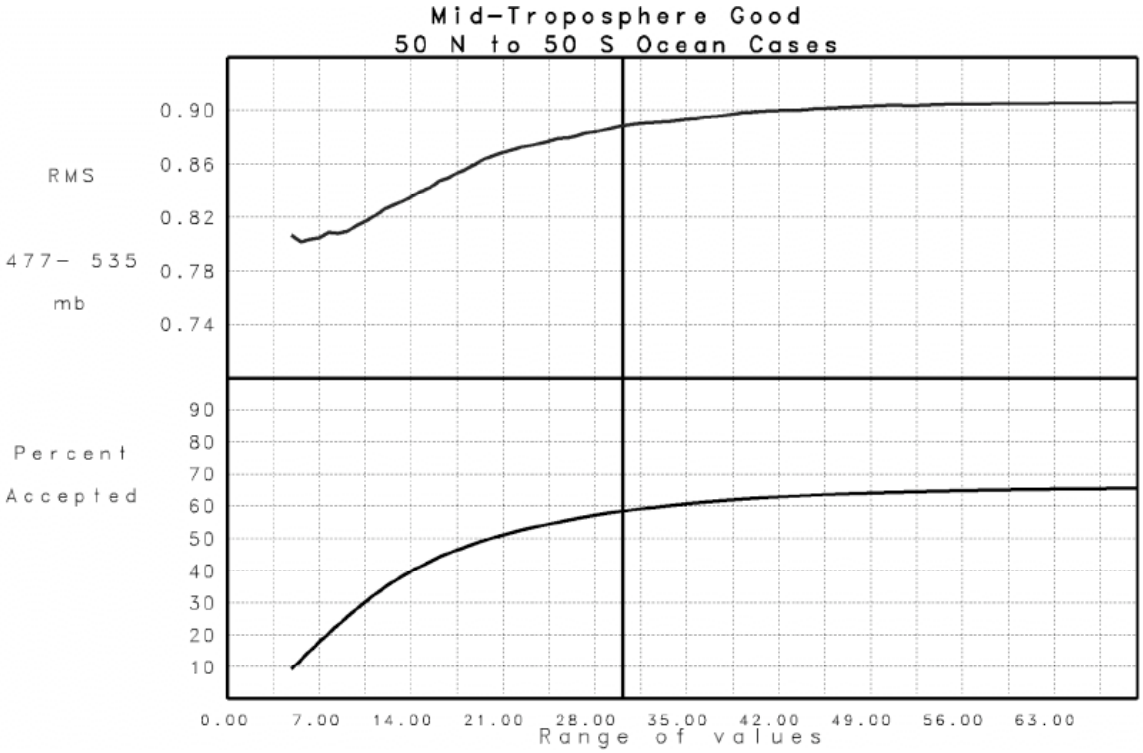

Figure 5.4.6b. $A_{eff}^{(1)}$: Initial Effective Channel Noise Amplification Factor

5.4.13.4.2.4 Lower-Tropospheric Temperature Test

Retrieved temperatures in the lowest 3 km of the atmosphere are most sensitive to cloud clearing errors, as well as errors in surface emissivity. A_{eff} and ΔF are both measures of how well cloud clearing is being done and potential problems with surface emissivity. The threshold for ΔF is now tightened considerably and is tighter than in Susskind et al. (2003), in which it had to be relaxed as a compromise so as not to reject the entire profile too often. $A_{eff}^{(1)}$ is also now used over land, and together with ΔF, flags many cases over arid land (in which retrieved surface emissivity can have large errors) as bad. The test Δ_{tskin} is also introduced which indicates a potential problem with the retrieved surface skin temperature.

Figure 5.4.7 is analogous to Figure 5.4.6, showing RMS errors over global ocean of the 777 mb – 878 mb layer mean temperature and percent cases classified as lower troposphere good as a function of varying Δ_{tskin} and $A_{eff}^{(4)}$. If the Δ_{tskin} threshold is lowered from its Version 4.0 value of 1.5, the percent of cases classified as lower-troposphere good drops significantly with little change in the RMS errors of the remaining cases. On the other hand, raising the threshold increases errors significantly with little change in percent accepted. The introduction of the threshold of 15 for $A_{eff}^{(4)}$ into the lower-tropospheric temperature good test results in a small improvement of RMS error in the 777 – 878 mb temperature over ocean, with little cost in percent of cases accepted.

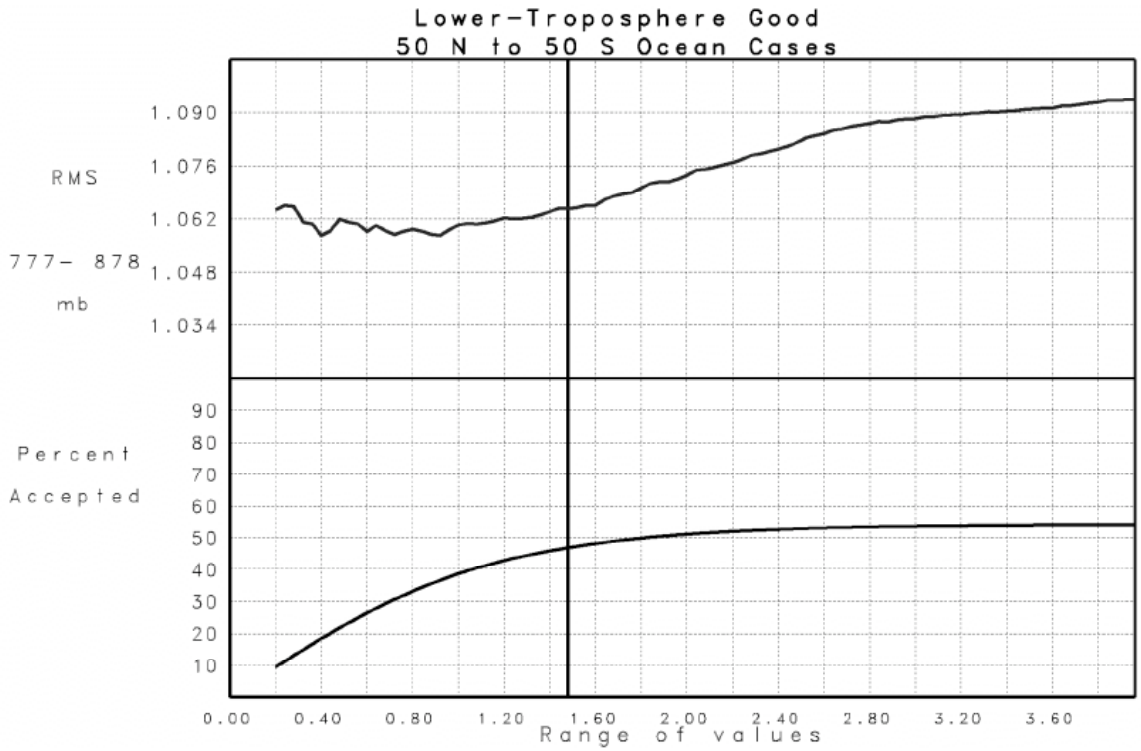

Figure 5.4.7a. ΔTaskin: Difference Between the Final Surface Temperature and the Regression Value

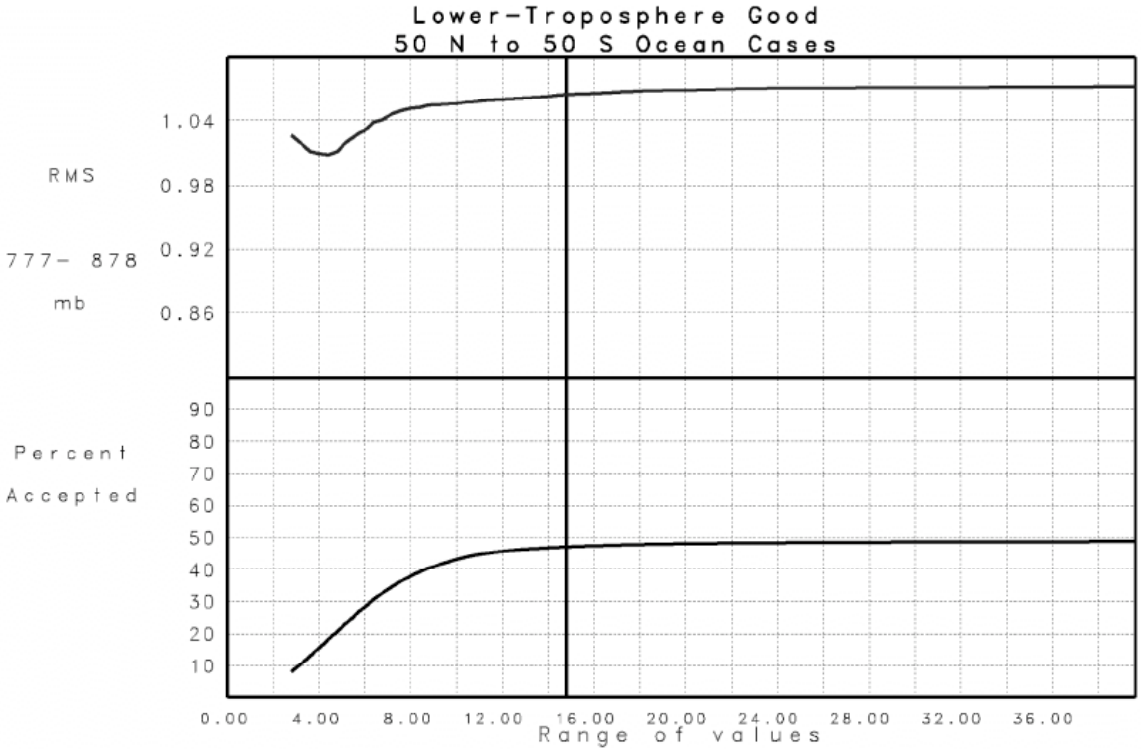

Figure 5.4.7b. $A_{eff}^{(4)}$: Final effective Channel Noise Amplification Factor

5.4.13.4.2.5 Standard and Tight Sea Surface Temperature Tests

Sea surface temperature is determined quite well by other instruments such as MODIS. Therefore, for AIRS to produce a useful sea surface temperature product for climate research, it must have very tight quality control. Surface skin temperature is also the product most affected by errors in the cloud clearing process, especially with regard to very low clouds. In the standard SST Test, thresholds for four tests have been tightened as shown in Table 5.4.4. This test is applied only over ocean, as land temperatures are less well measured by other instruments. The test most correlated with sea-surface temperature accuracy was $A_{eff}^{(1)}$, with lower values indicating more accurate sea-surface temperatures. The percent of accepted sea surface temperatures drops rapidly with decreasing acceptance thresholds however. If $A_{eff}^{(1)}$ is less than a second threshold, shown for Class 6, then the Tight SST Test is passed.

ABBREVIATIONS AND ACRONYMS

AERI	Atmospheric Emitted Radiance Interferometer
AIRS	Atmospheric Infrared Sounder
AIRS-RTA	AIRS Radiative Transfer Algorithm
AMSR-E	Advanced Microwave Scanning Radiometer-EOS
AMSU	Advanced Microwave Sounding Unit
AMSU-A	Advanced Microwave Sounding Unit-A (20-channel MW radiometer)
AMSU-B	Advanced Microwave Sounding Unit-B (5-channel MW radiometer)
ATBD	Algorithm Theoretical Basis Document
AVHRR	Advanced Very High Resolution Radiometer
C	degrees Centigrade
COLR	Clear Sky Outgoing Radiation
DAAC	Distributed Active Archive Center
DB, dB	decibel
EOF	Empirical Orthogonal Functions
EOS	Earth Observing System
ER-2	Earth Research-2 (NASA's civilian version of Lockheed Skunkworks U-2)
ESDIS	Earth Science Distributed Information System
FOR	Field of Regard
FOV	Field of View

FTS	Fourier Transform Spectrometer
FWHH	Full Width Half Height
GHz	Gigahertz (10^9 Hertz, or cycles/second)
GSFC	Goddard Space Flight Center
HITRAN	High Resolution Transmission Molecular Absorption Database
HSB	Humidity Sounder of Brazil
IMG	Infrared Monitor for Greenhouse Gases
IR	infrared
IRIS	Infrared Interferometer Spectrometer
JPL	Jet Propulsion Laboratory
K	degrees Kelvin
kCARTA	kCompressed Atmospheric Radiative Transfer Algorithm
km	kilometer (10^3 meters)
kPa	kilopascal (10^3 pascal, equivalent to 10 bar)
L0-L4	Level 0 through Level 4 (processing)
MHS	Microwave Humidity Sounder
mm	micrometer, micron (10^{-6} meter)
MODIS	Moderate Resolution Imaging Spectroradiometer
MPM87	Millimeter-wave Propagation Model (Liebe and Layton, 1987)
MPM89	Millimeter-wave Propagation Model (Liebe, 1989)

MPM92 Millimeter-wave Propagation Model (Liebe, et al, 1992)

MPM93 Millimeter-wave Propagation Model (Liebe, et al, 1993)

MSU Microwave Sounder Unit

MW microwave

NASA National Aeronautics and Space Administration

NCEP National Center for Environmental Prediction

NEDT Noise Equivalent Temperature Difference

NEDT Noise Equivalent Temperature Difference

NEMS Nimbus-E Microwave Sounder

NESDIS National Environmental Satellite Data and Information Service

NEXRAD Next Generation Radar

NOAA National Oceanic and Atmospheric Administration

OLR Outgoing Longwave Radiation

PCs Principle Components

PCSs Principle Components Scores

PGE Product Generation Executive

QC Quality Control

QA Quality Assessment

OPTRAN Optical Path TRANsmittance

RH Relative Humidity

RMS Root Mean Square

RTA Radiative Transfer Algorithm

SDPS Science Data Processing System

SIRS Satellite Infrared Radiation Spectrometer

SRF Spectral Response Function

SSM/T2 Special Sensor Microwave/Water Vapor Profiler

SST Surface Skin Temperature

SVD Singular Value Decomposition

THz Terahertz (10^{12} Hertz)

TIGR TOVS Initial Guess Retrieval

TIROS Television Infrared Observation Satellite

TLSCF Team Leader Science Computing Facility

TPW Total Precipitable Water

TOVS TIROS Operational Vertical Sounder

VTPR Vertical Temperature Profile Radiometer

APPENDICES

A. GENERATION OF LEVEL 3 PRODUCTS

Level 3 products are quality controlled space-time averages of individual geophysical parameters derived on a Field of Regard (FOR) basis. Level 3 products are produced on a 1° x 1° latitude-longitude spatial grid, with ascending (1:30 PM local time) and descending (1:30 AM local time) orbits gridded separately. Level 3 products are produced on a daily, 8 day, and monthly mean basis. No data is contained in a grid box if no quality controlled soundings were produced.

A.1 Quality Control Used to produce Different level 3 Fields

Different geophysical parameters are included in the generation of Level 3 fields according to the class the sounding belongs to, as described in the previous section. Examples of daily level 3 fields for different geophysical parameters are given in Section C.

A.1.1 Cloud Parameters, OLR, and Clear Sky OLR

Cloud parameters, OLR, and Clear sky OLR are included in the Level 3 product for all cases in which a MW/strat IR retrieval has been produced. This includes classes 1-6 as well as Class 0 (MW/strat IR retrieval only).

A.1.2 Atmospheric Temperature

Atmospheric temperatures 200 mb and above are included in the Level 3 product for all soundings passing the Stratospheric Temperature Test. Atmospheric temperatures beneath 200 mb are included in the Level 3 product for all cases passing the Mid-tropospheric Temperature Test. As is shown in Section C.1, use of this looser test is necessary when producing Level 3 temperatures in the lower troposphere so as to obtain adequate spatial coverage over land.

A.1.3 Constituent Profiles – H_2O, O_3, and CO

Constituent profiles are included in the Level 3 product for all cases passing the constituent profile test.

A.1.4 Surface Skin Temperature and Spectral Emissivity

Non-frozen ocean surface parameters are included in the Level 3 product for all cases passing the Standard Sea Surface Temperature Test. Surface parameters for other than non-frozen ocean cases, referred to as land, are included in the Level 3 product if the Mid-tropospheric Temperature Test is passed. As shown in Section 6, this relatively loose test is used over land to allow for adequate spatial coverage, just as is done for lower tropospheric temperature Level 3 products. Examples of sample monthly mean fields and their interannual differences are given in Section C.2.

B. Expected Improvements in the AIRS Science Team Version 5 Physical Retrieval Algorithm

A number of improvements are being made to the AIRS Science Team algorithm that will be implemented in Version 5.0. A major improvement has been made to the physics of the AIRS RTA, which now accurately accounts for effects of non-LTE on AIRS shortwave stratospheric sounding channels during the day. This allows for potential use of all AIRS shortwave channels in the physical temperature profile retrieval step, both day and night. As a result of other improvements in the physics of the RTA, it was also no longer necessary to add the term $\bar{N}_{ii}$, representing an empirical estimate of uncertainty in computed radiances arising from errors in the RTA physics, to the AIRS channel noise covariance matrix, as done in equation 5.4.33 used in Version 4.0. A new term is included in the channel noise covariance matrix allowing for uncertainty in the CO_2 concentration on computed channel radiances. In addition, the resulting AIRS tuning coefficients based on the new RTA are now significantly smaller than those used in Version 4.0.

Other expected improvements in Version 5.0 result from re-evaluation of the number of steps in the overall retrieval process and the channels, functions, and damping parameters used in all retrieval steps including the possibility of using different channel sets, functions, and damping parameters over land and ocean. The most significant improvement in Version 5.0 results from development of a new methodology to provide accurate error estimates for retrieved geophysical parameters, including clear column radiances, and a new quality control methodology based solely on the error estimates of the retrieval geophysical parameters.

This page intentionally left blank.

C. Results Using Version 4

Chapter 5.0 described the Version 4 methodology used to derive level 2 and level 3 products from the AIRS/AMSU/HSB observations. One of the objectives of the methodology is to be able to derive high quality soundings and clear column radiances from AIRS/AMSU observations in the presence of clouds. The cloud-clearing process does introduce noise in the derived cloud-cleared radiances (Susskind, *et al.*, 2003). Therefore, one would expect a degradation in retrieval accuracy with increasing cloud cover. It is critical that this degradation should not be appreciable if the retrieved parameters are to be useful for weather and climate research purposes. To demonstrate this, the accuracy of global geophysical parameters derived from AIRS/AMSU observations on 29 September 2004 was evaluated by comparison with a co-located ECMWF 3-hour forecast. The ECMWF forecast has errors of its own, and this should be borne in mind when interpreting the results of the comparisons. Instead of an assessment of the absolute accuracy of the retrieved quantities, we concentrate on the degree of degradation in "accuracy," as defined by agreement with ECMWF, occurring with increasing cloud cover. Errors in the ECMWF "truth" may decrease the apparent differences in accuracy between clear and cloudy cases, but only by making the clear cases appear less accurate than they actually are, and not by making the cloudy cases appear more accurate than they are. In all cases, the quality control methodology described in Sections 5.4.11.4.2 (level 2) and 5.4.11.5 (level 3) is used to include (or exclude) data for individual retrieved geophysical parameters in the figures shown.

C.1 Results for a Single Day

Figure C.1 shows in gray the number of cases for each retrieved effective fractional cloud cover, in 0.5 percent bins, for the whole day 29 September 2004. The effective fractional cloud cover is given by the product of the fraction of the field of view covered by clouds and the cloud emissivity at 11 μm. The average global effective cloudiness was determined to be 44.11 percent. There are peaks at 0 percent and 100 percent effective cloud cover, with a very smooth distribution at intermediate effective cloud fractions. The discontinuity at 90 percent cloud cover is an artifact arising from the switch from clouds retrieved primarily using the IR/MW retrieved state to clouds retrieved using the MW/strat IR state. Also shown, in different colors, is the percent of accepted retrievals as a function of retrieved effective cloud cover for all cases passing the Stratospheric Temperature Test, the Constituent Test, the Mid-Tropospheric Temperature Test, and the Lower Tropospheric Temperature Test, as well as for non-frozen ocean cases passing the standard SST Test and the Tight SST Test. Almost all cases with retrieved effective cloud fraction less than 90 percent pass the Stratospheric Temperature Test, with the percent accepted falling slowly with increasing cloud cover, from close to 100 percent at low cloud fractions to about 65 percent at close to 90 percent effective cloud cover. 79.6 percent of the global cases pass the Stratospheric Temperature Test, with an average effective cloud fraction of 33.08 percent. 78.4 percent of the cases pass the slightly more restrictive Constituent Test, with an average effective cloud fraction of 32.74 percent. 48.5 percent of the global cases pass the Mid-Tropospheric Temperature Test, with an acceptance rate of about 80 percent for low effective cloud fraction, falling to about 20 percent at 80 percent effective cloud fraction, and 10 percent at 90 percent effective cloud fraction. The previous acceptance methodology (Susskind, *et al.*, 2003) rejected all cases with effective cloud fraction greater than 80 percent. The mean effective cloud fraction for all cases passing the Mid-Tropospheric Temperature Test is 23.89 percent. Only 26.3 percent of the cases pass the Lower Tropospheric Temperature Test, primarily over ocean, with an acceptance rate near 55 percent for low cloud fractions falling to 5 percent at 80 percent effective cloud fraction and 2 percent at 90 percent effective cloud fraction, and with an average effective cloud fraction of 18.33 percent. The SST acceptance tests are applied only over non-frozen ocean. The standard SST Test accepts 23.3 percent of

the ocean cases, and with an acceptance rate of roughly 50 percent under nearly clear conditions, with an average cloud fraction of 9.18 percent, while the Tight SST Test accepts only 10.6 percent of the cases, with an average effective cloud fraction of 5.96 percent. The Tight SST Test allows for more cases than does the clear test (Susskind, *et al.*, 2003) which includes only 8.2 percent of the non-frozen cases.

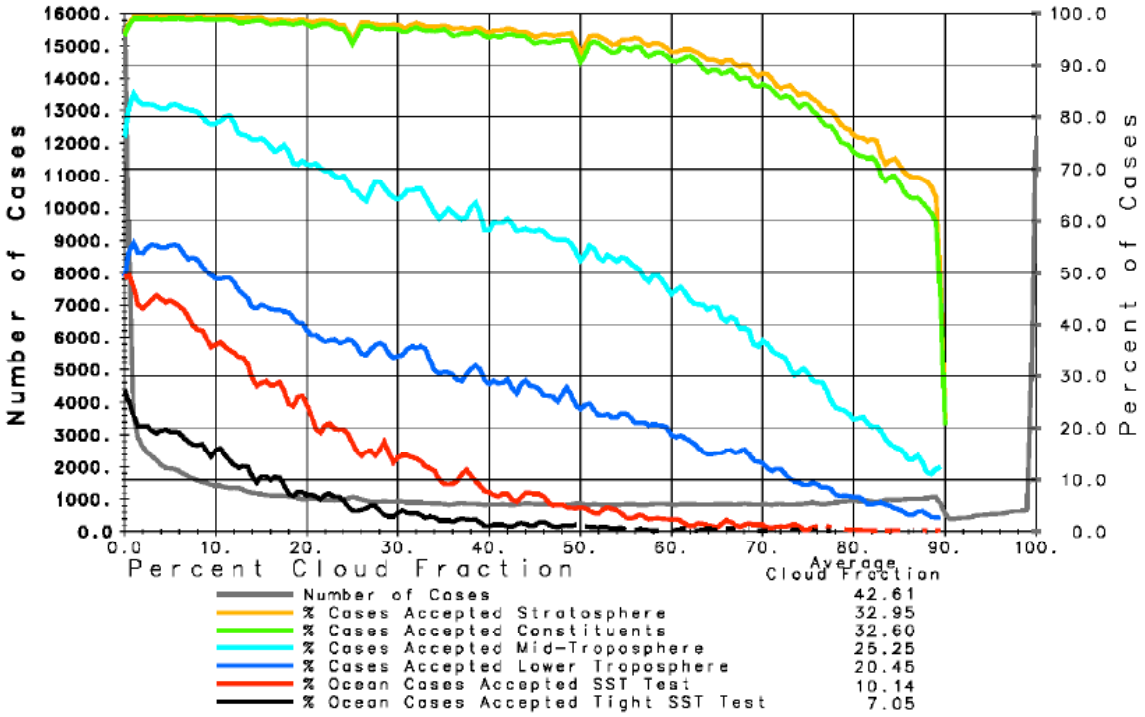

Figure C.1. Percent Accepted vs. Effective Cloud Fraction

Figure C.2a shows the retrieved effective cloud top pressure and effective cloud fraction for ascending orbits on 29 September 2004 in 1°x1° latitude-longitude bins. The area weighted global mean effective cloud fraction and its spatial standard deviation are indicated in the figure. The results are presented in terms of cloud fraction in 5 groups, 0-20 percent, 20-40 percent, etc. with darker colors indicating greater cloud cover. These groups are shown in each of 7 colors, indicative of cloud top pressure. The reds and purples indicate the highest clouds, and the yellows and oranges the lowest clouds. Cloud fields are retrieved for all cases in which valid AIRS/AMSU observations exist. Gray means no data was observed.

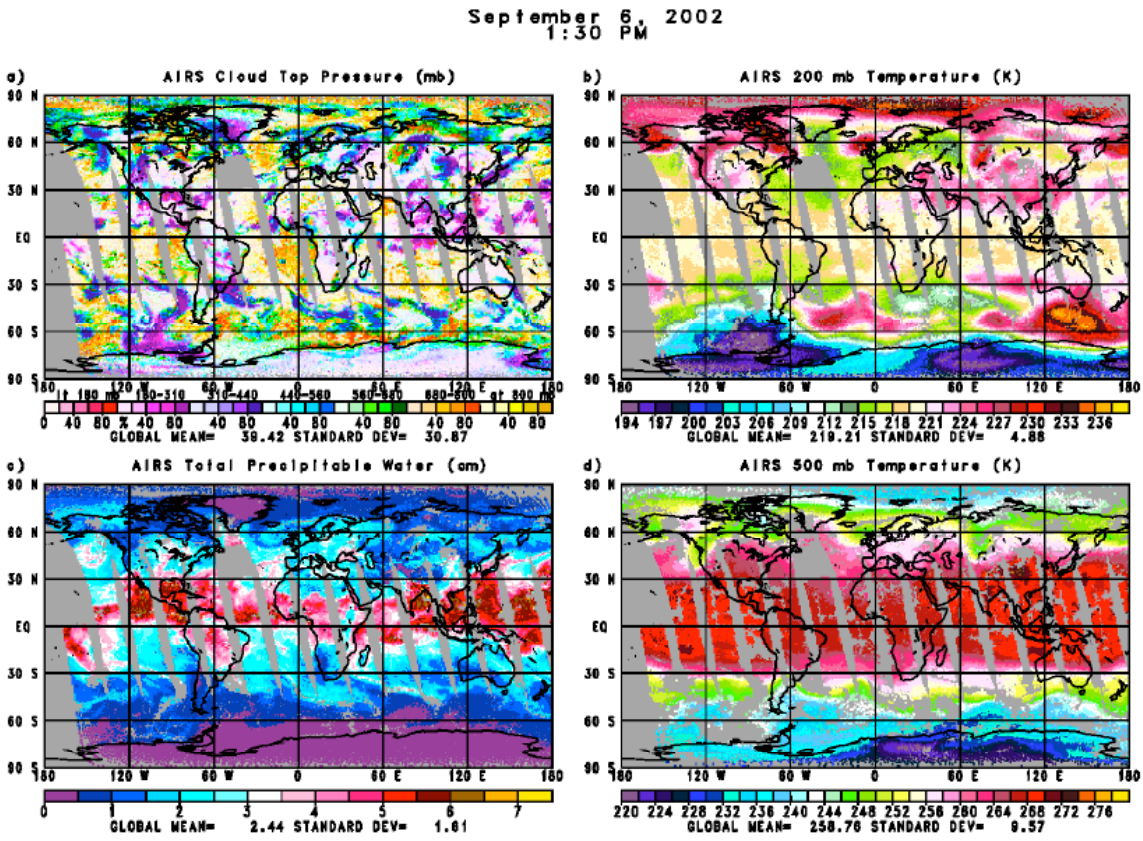

Figure C.2. Retrieved Effective Cloud Top Pressure and Effective Cloud Fraction

Figure C.2b shows the retrieved 200-mb temperature field (K). This demonstrates the coverage of cases where stratospheric temperatures are accepted. Gray indicates regions where either no valid observations existed or the stratospheric temperature retrieval was rejected, generally in regions of cloud cover 90-100 percent. Figure C.2c shows retrieved values of total precipitable water vapor (cm). This demonstrates the coverage of constituent profiles. Figure C.2d shows retrieved values of 500-mb temperature, demonstrating coverage of accepted mid-tropospheric temperatures. Gaps in the data coverage of mid-tropospheric temperature due to extensive cloud cover are larger than for stratospheric temperatures. Retrieved fields are quite coherent, and show no apparent artifacts due to clouds in the field of view. Water vapor has considerably more fine scale structure than temperature and contains some very large spatial gradients. The extent of gaps in water vapor coverage due to areas of rejected retrievals (retrievals which fail the Constituent Test) are considerably less than with regard to the Mid-Tropospheric

Temperature Test, but somewhat larger than with regard to the very loose Stratospheric Temperature Test. As shown in Figure C.2, the percent of cases accepted as a function of increasing cloud cover for these two classes of retrievals is almost identical.

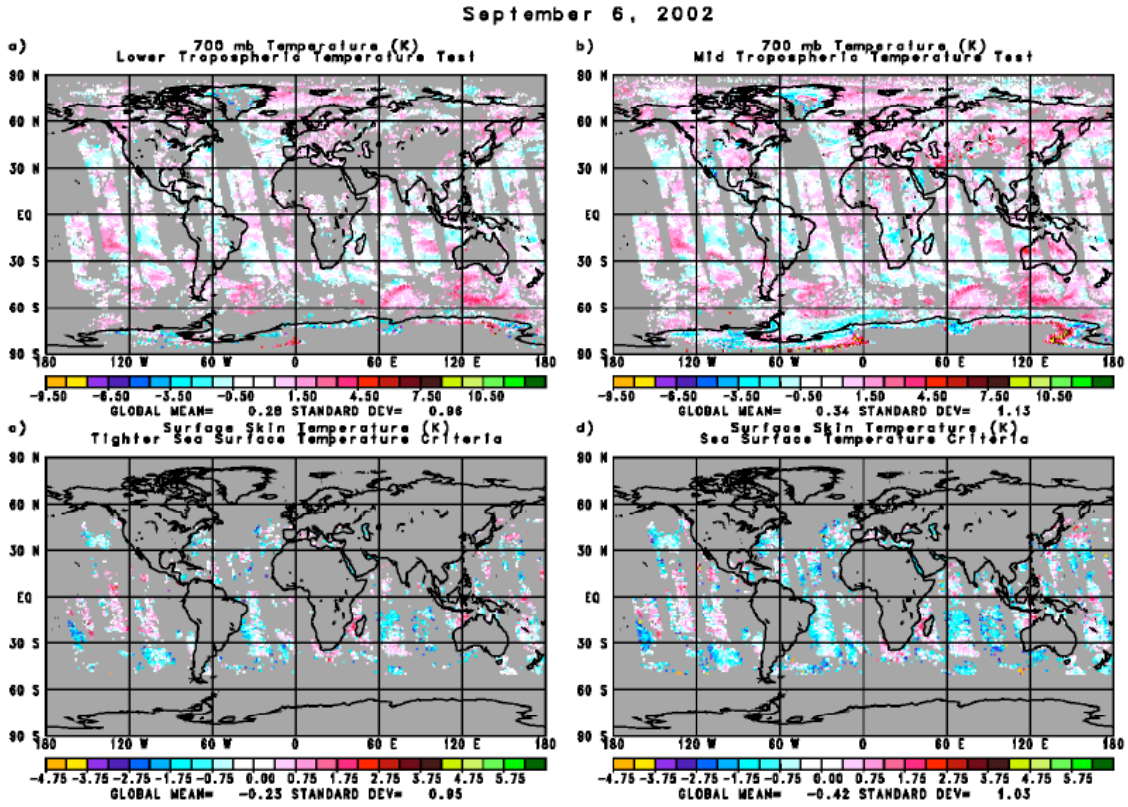

Figure C.3. Temperature Differences, AIRS minus ECMWF

Figure C.3a shows the difference between the retrieved 700-mb temperature and the ECMWF 3-hour forecast field for ascending orbits on 29 September 2004, for those cases passing the Lower Tropospheric Temperature Test, while Figure C.3b shows the same field for all cases passing the looser Mid-Tropospheric Temperature Test. The difference in spatial coverage is significant, particularly over land where 700-mb temperature retrievals appear to be biased warm compared to the ECMWF forecast. Statistics showing the area weighted global mean difference from ECMWF and the spatial standard deviation of the difference are included in the figures. The overall accuracy is somewhat better with the tighter Lower Tropospheric Temperature acceptance criteria, and this difference is significant for data assimilation purposes. When statistics are shown depicting the accuracy of lower tropospheric temperatures (Figures C.6 and C.7), only

cases passing the Lower Tropospheric Temperature Test are included. All data shown in Figure C.3b is included in the generation of lower tropospheric temperature monthly mean fields however, so as to allow for global coverage, especially over arid land regions.

Figures C.3c and C.3d shows the differences of retrieved ocean surface skin temperature (SST) from the ECMWF SST analysis for the ascending orbits of 29 September 2004. Figure C.3c includes only those cases passing the Tight SST Test and Figure C.3d also includes those cases passing the standard SST Test. A considerable increase in yield is obtained using the standard SST Test, with some degradation in accuracy of sea surface temperatures. The biases compared to ECMWF are negative in both cases, with a larger negative bias found in cases passing the standard SST Test. Errors due to cloud clearing are typically negative, resulting from under-correcting for effects of clouds in the field of view. This would imply that the Tight SST Test is eliminating more cases where cloud-clearing errors are resulting in poorer sea surface temperatures. Caution must be taken however because the ECMWF "truth" may have its own biases.

Figure C.4 shows the number of combined daytime and nighttime non-frozen ocean cases between 50°N and 50°S, on 29 September 2004, as a function of the difference of the retrieved SST from the ECMWF analysis in bins of 0.2 K. Results are shown for cases which passed the Tight SST Test, the standard SST Test, and the Lower Tropospheric Temperature Test. Figure C.3c and C.3d showed the spatial distribution differences for the daytime orbits applying each of the SST Tests. The percent of all non-frozen oceanic cases 50°N-50°S passing each test is included in the statistics, as well as the mean difference from ECMWF, the standard deviation of the difference, and the percentage of outliers, defined as cases passing the test that differ from ECMWF by more than 3K from the mean difference. There is a small negative bias of retrieved Sea Surface Temperatures compared to ECMWF, that increases with increasing acceptance rate, from –0.29K for cases within the Tight SST Test, to – 0.72K for cases passing the Lower Tropospheric Temperature Test. The standard deviation of the cases from ECMWF also increases slightly. On the other hand, the number of primarily cold outliers increases significantly, from 0.62 percent to 5.90 percent. Therefore, the Lower Tropospheric

Temperature Test by itself is not adequate for the purpose of producing accurate monthly mean sea surface temperatures. As with all the test thresholds, experiments are being conducted to optimize the trade-off between spatial coverage and accuracy for best use in studying interannual monthly mean sea-surface temperature differences.

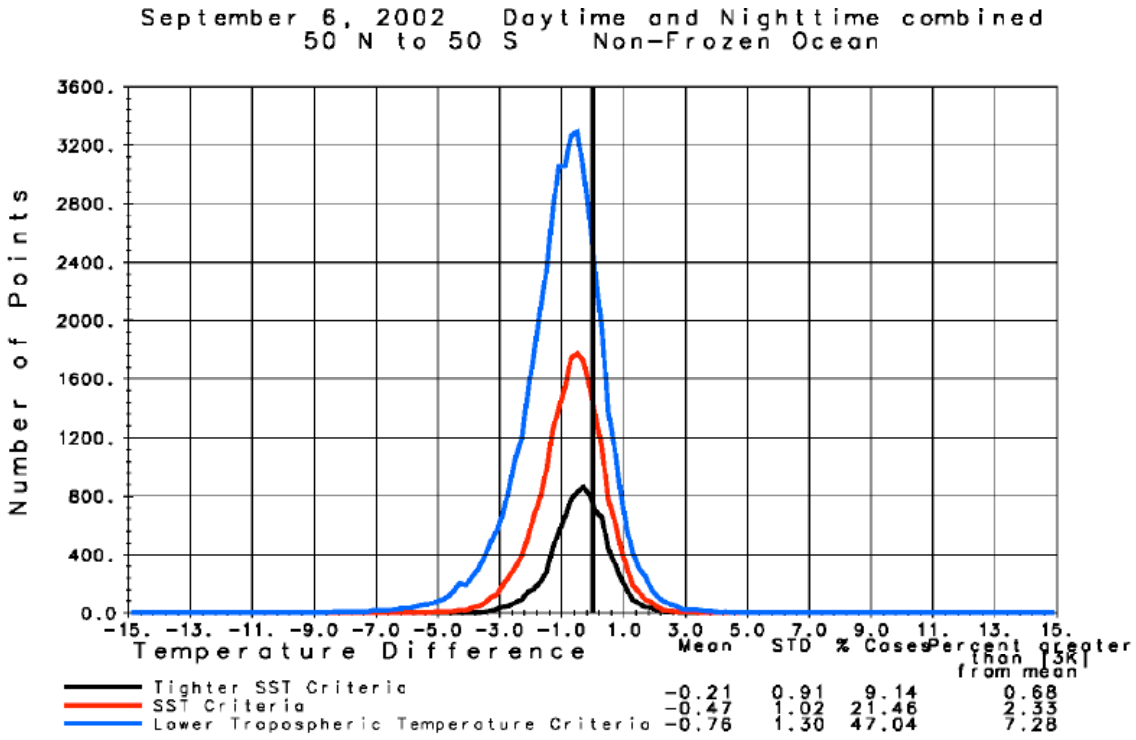

Figure C.4. Surface Skin Temperature Difference from ECMWF

Figure C.5a shows RMS differences from the ECMWF 3-hour forecast of retrieved 1-km layer mean tropospheric temperatures, and 3-km layer mean stratospheric temperatures, for non-frozen ocean cases on 29 September 2004. Results shown are for all cases passing the Stratospheric Temperature Test, the Mid-Tropospheric Temperature Test, the Lower Tropospheric Temperature Test, the standard SST Test, the Tight SST Test. Results for those cases passing an additional clear test, as defined by Susskind, *et al.*, (2003), are also included in the figure. The number of cases and percentage of all cases included in the statistics are indicated for each test.

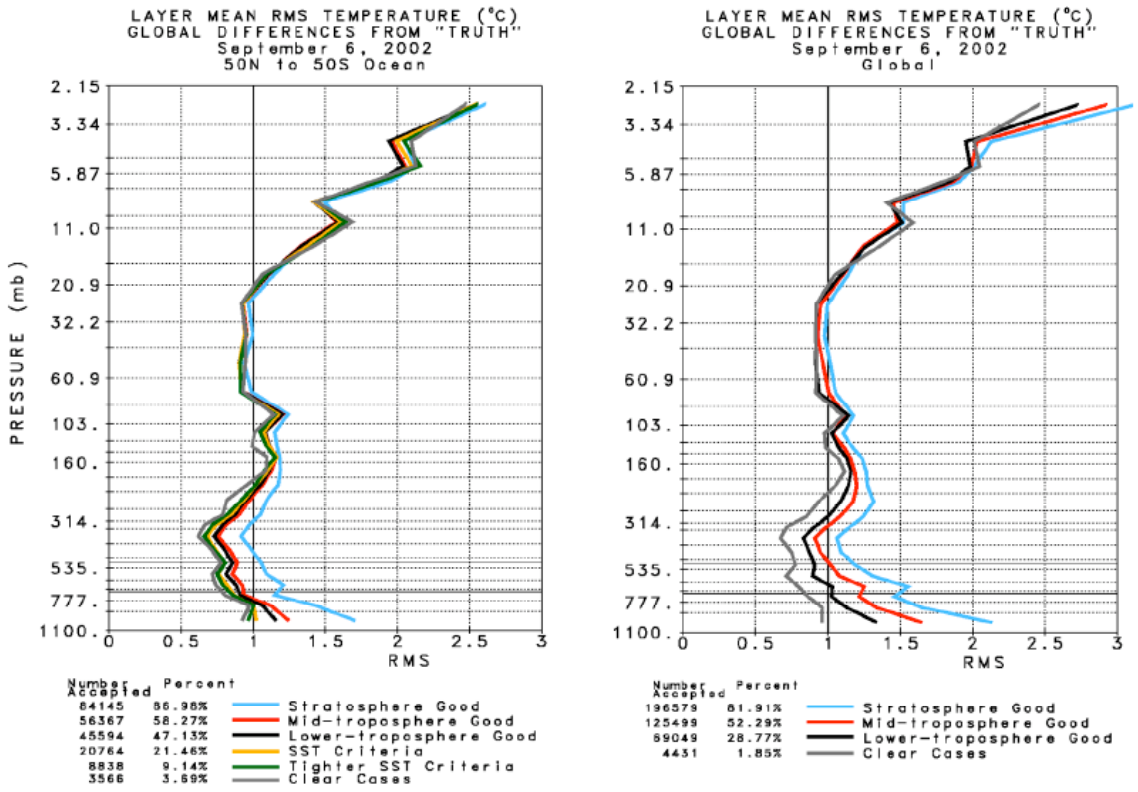

Figure C5. C.5a (left) and C.5b (right)

Accuracies of retrieved stratospheric temperature, as compared to ECMWF "truth," improve slightly with increasing stringency of the tests, but are not appreciably different from one another for cases passing any of the quality tests. The large differences from ECMWF above 15 mb are primarily a result of the lower accuracy of the ECMWF "truth" in the upper stratosphere. Tropospheric soundings passing either of the tropospheric quality control tests agree with the ECMWF forecast on the order of 1K. Part of this difference is due to uncertainty in the ECMWF forecast. It is interesting to note that soundings for the 86 percent of the cases for which the Stratospheric Temperature Test was passed are of relatively high quality throughout the troposphere as well, with an RMS difference from ECMWF on the order of 1.7K in the lowest 1 km of the atmosphere. This shows that the cloud clearing methodology works well in up to 90 percent cloud cover. Nevertheless, the accuracy of all these soundings is not considered high enough for either data assimilation or climate purposes. There is significant further improvement in tropospheric temperature profile accuracy, compared to that for cases passing the tropospheric temperature profile tests, using the smaller subset of cases

passing the standard SST Test (23.3 percent of the ocean cases) but relatively little further improvement in those cases passing the Tight SST Test (10.6 percent of the cases), or the additional clear test (8.2 percent of the cases). For data assimilation purposes, we recommend experiments assimilating temperature profiles passing only the standard SST Test, on the one hand, and passing the test for the appropriate for the level of the temperature on the other hand, to assess the trade-off between coverage and accuracy. One might also consider assimilating lower tropospheric temperatures in cases passing the Mid-Tropospheric Temperature Test over ocean to further increase the spatial coverage of the data being assimilated.

Figure C.5b shows analogous results for global accepted retrievals, including cases passing the Stratospheric Temperature Test, the Mid and Lower-Tropospheric Temperature Tests, and the clear test (which, over land, ice, and coasts, must also pass the Lower Troposphere Temperature Test). Error statistics in the stratosphere degrade somewhat for cases passing the Stratospheric Temperature Test (79.6 percent of all cases) compared to either of the Tropospheric Temperature Tests (48.5 percent and 25.3 percent). The increase in spatial coverage using the Stratospheric Temperature Test is much more significant globally, compared to using either of the tropospheric tests, than over non-frozen ocean. We therefore recommend using the Stratospheric Temperature Test for stratospheric temperatures for both data assimilation and climate purposes. Global agreement with ECMWF is slightly poorer than over ocean. A much larger difference in agreement with ECMWF occurs between all cases passing the Lower Tropospheric Temperature Test and the Mid-Tropospheric Temperature Test than over ocean, especially in the lower troposphere. For data assimilation purposes, we feel lower tropospheric temperatures retrieved over land should not be used when the Lower Tropospheric Temperature Test is not passed. Globally, 3.7 percent of the cases passed the clear test, most of which were over non-frozen ocean. Retrievals in these cases are very accurate, but the global spatial coverage is very poor.

Figures C.6a and C.6b are analogous to Figures C.5a and C.5b but show statistics only for cases at a given pressure level passing the appropriate quality test. Statistics for cases passing the clear test (identical to those shown in Figures C.5a and C.5b) are included for

comparison. Also shown is the accuracy of the regression first guess temperature profiles for all accepted retrievals and under clear conditions. The accuracy of the physical retrieval is higher than the regression, and more so under cloudy conditions than clear conditions. Part of this is due to the increased accuracy of $\hat{R}_i^4$, used to derive the final temperature profile, compared to $\hat{R}_i^1$, used to derive the regression first guess.

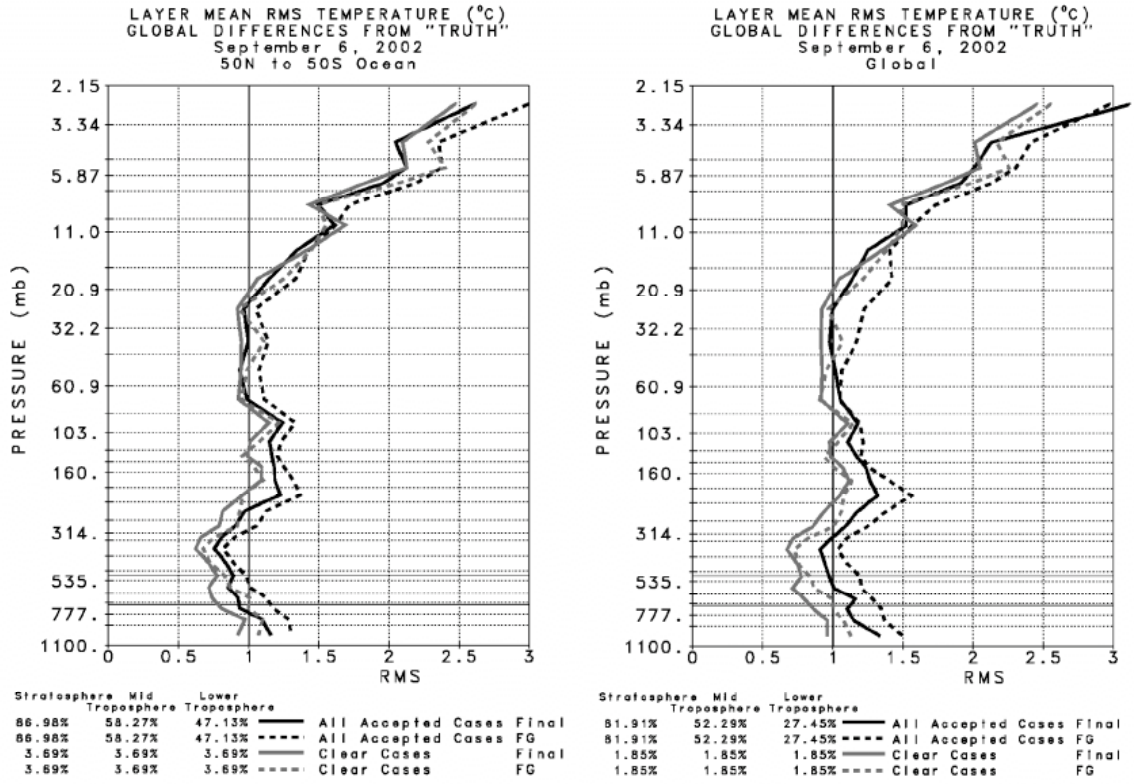

Figure C.6. C.6a (left) and C.6b (right)

Figure C.6b also includes analogous results determined from the global simulation of AIRS performance shown in Susskind, *et al.,* (2003) for all accepted cases (red) and clear cases (pink). In simulation, the truth is known perfectly, while with real data, the 3-hour ECMWF forecast is taken as a proxy for truth. With real data, the degree of degradation for tropospheric accuracy in cloudy retrievals, compared to clear cases, is of the order of a few tenths of a degree, just as it was in simulation. Differences from "truth" are poorer with real data than in simulation however. Two major causes of this degradation are: 1) perfect physics and perfect characterization of the AMSU antenna temperatures were assumed in simulation; and 2) the "truth" has errors of its own in real data. The

degradation of sounding accuracy in the presence of "real clouds," as compared to soundings in clear cases, appears to be similar to that implied by simulation, as does the accuracy of mid tropospheric temperature retrievals for clear cases.

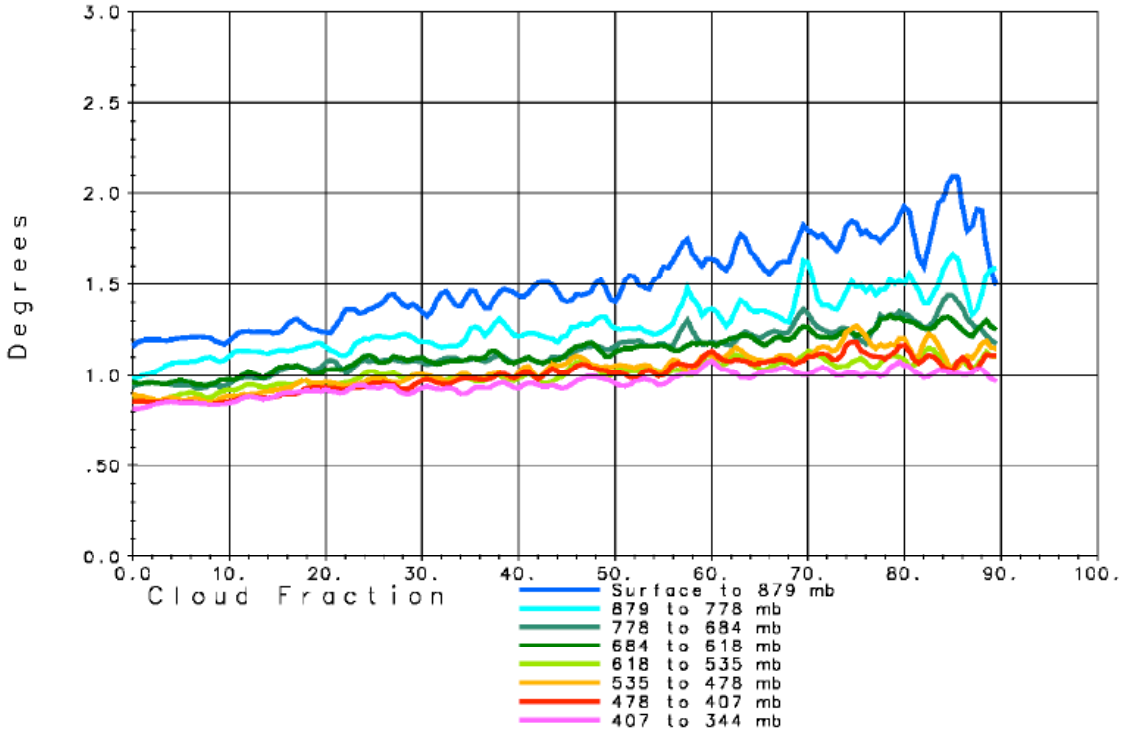

Figure C.7. AIRS RMS Temperature Difference from Truth vs. Effective Cloud Fraction

Figure C.7 shows the RMS difference between retrieved 1-km tropospheric layer mean temperatures and the collocated ECMWF 3-hour forecast for all accepted cases as a function of retrieved effective cloud fraction. Results are shown for each of the 8 lowest 1-km layers of the atmosphere. Only those cases passing the appropriate temperature profile test are included in the statistics. Agreement degrades with increasing cloud cover, but only very slowly. The largest errors are in the 2 lowest layers in the atmosphere, at moderate to high cloud fraction, where the percentage acceptance rate is low. This degradation is similar to that shown in an analogous figure in Susskind, *et al.*, (2003) for simulated retrievals. RMS temperature differences from ECMWF below 600 mb are somewhat larger than the 1-K goal for retrieval accuracy. Part of this difference can be attributed to the fact that the ECMWF forecast is not perfect. It is also possible

that the accuracy of the ECMWF forecast may be somewhat poorer with increasing cloud cover.

Figures C.8a and C.8b are analogous to Figures C.5a and C.5b, but show RMS percent difference of retrieved 1-km layer precipitable water from the ECMWF "truth." In these, and other water vapor statistics, the RMS percent difference weights percent difference in a given case by the "truth," so as not to inflate percent differences for very dry cases, according to

$$\text{RMS percent difference} = 100\,\text{x}\left(\sum_k \left(q_k^{tru}\right)^2 \left(\frac{q_k^{ret} - q_k^{tru}}{q_k^{tru}} \right)^2 / \sum_k \left(q_k^{tru}\right)^2 \right)^{1/2} \qquad \text{C.1}$$

$$= 100\,\text{x}\left[\sum_k \left(q_k^{ret} - q_k^{tru}\right)^2 / \sum_k q_k^{tru\,2} \right]^{1/2} .$$

where q_k^{ret} and q_k^{tru} are the retrieved and true values of water vapor for case k. These statistics should be used with caution, especially in the mid-upper troposphere, where considerable errors could exist in the ECMWF "truth." Nevertheless, over ocean, statistics are not appreciably different for cases passing the different tropospheric and ocean skin temperature thresholds. As with regard to temperature, a larger degradation occurs in agreement of humidity profile with ECMWF in the mid-lower troposphere over land when the looser constituent profile criteria are used. We recommend at this time to use the appropriate temperature test when attempting to assimilate water vapor at a given level of the atmosphere. Soundings passing either tropospheric temperature test also pass the constituent profile test because the temperature profile criteria are equal to, or tighter than, those in the constituent profile test. For climate purposes, we recommend including all cases passing the Constituent Test in the generation of the level 3 product, so as to minimize a dry bias in the sample.

Figures C.9a,b are analogous to Figures C.7a,b and show water vapor percent differences from "truth" for clear cases and cases passing the temperature test for the appropriate level. Figure C.9b includes analogous results found in simulation (Susskind, *et al.*,

2003). There is not a significant difference in water vapor retrieval accuracy occurring between clear cases and all cases passing the appropriate temperature profile test with real data, as in simulation.

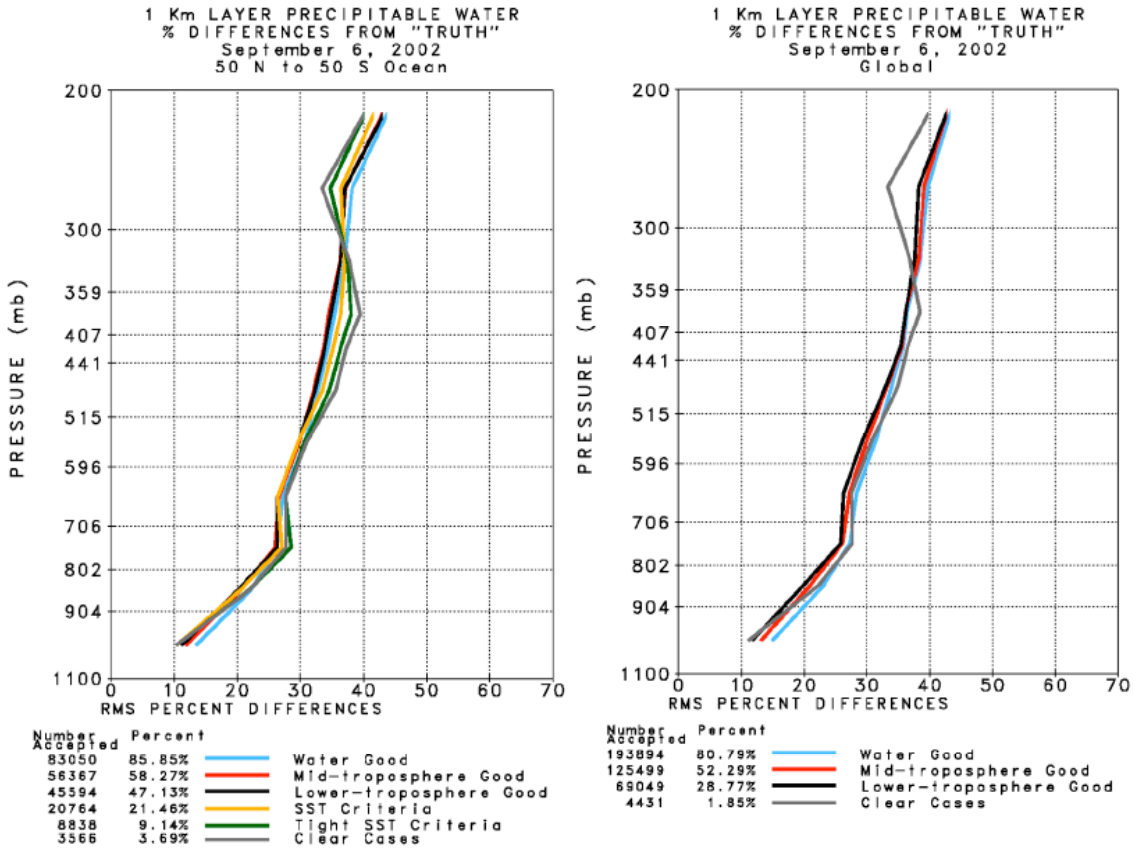

Figure C.8. C.8a (left) and C.8b (right)

Figure C.10 is analogous to Figure C.7, but for percent differences from ECMWF of 1-km layer precipitable water as a function of retrieved effective fractional cloud cover. Only soundings passing the appropriate temperature profile test for a given level of the atmosphere (Mid-Tropospheric Temperature Test or Lower Tropospheric Temperature Test) are included in the statistics, as was done in Figure C.7. Agreement with ECMWF degrades slightly with increasing cloud cover primarily in the lowest 2 km of the atmosphere, but not appreciably. Part of this could be due to sampling differences, because the AIRS retrievals determine water vapor in the clear portions of the partially cloudy scene, while the forecast values are for the whole scene.

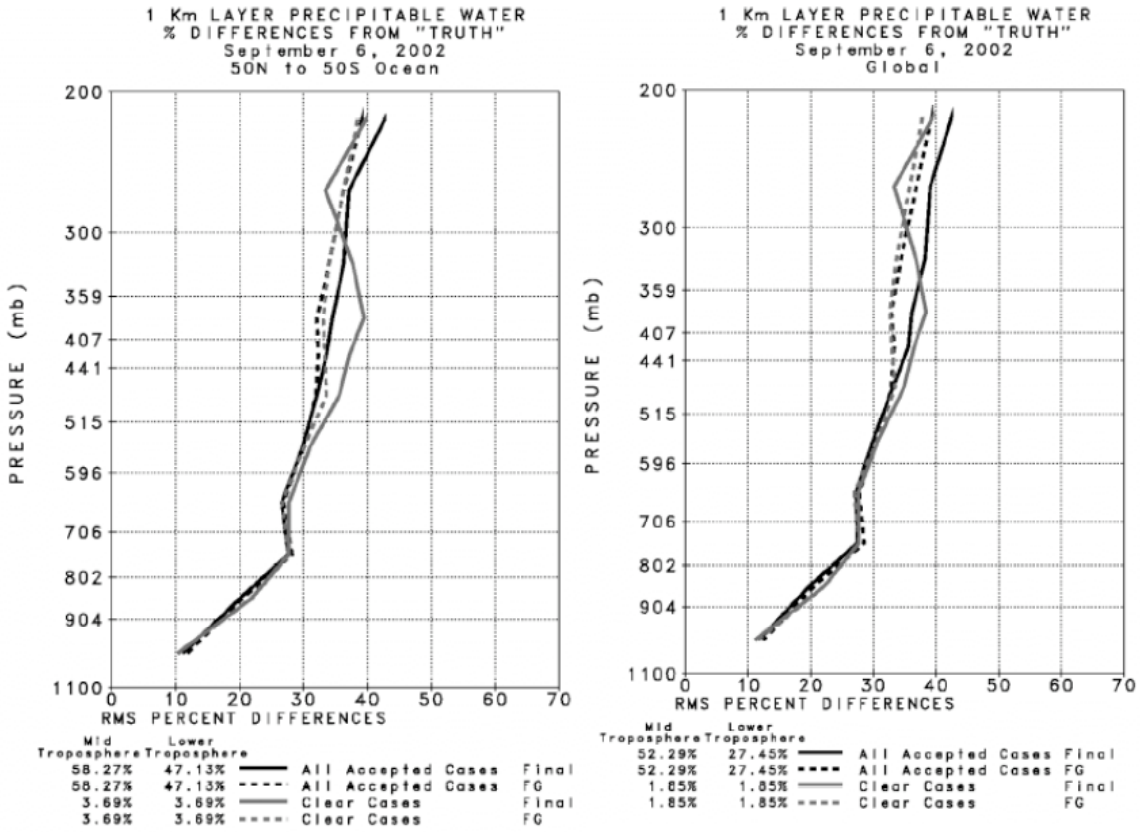

Figure C.9. C.9a (left) and C.9b (right)

The fundamental parameter used in the determination of geophysical parameters from AIRS/AMSU data is the clear column radiance $\hat{R}_i$, which represents the radiance AIRS channel i "would have seen" if no clouds were in the field of view. Geophysical parameters are determined which are consistent with $\hat{R}_i$. Derived geophysical parameters whose accuracy degrades slowly with increasing cloud cover implies that the accuracy of $\hat{R}_i$ also degrades slowly with increasing cloud cover. $\hat{R}_i$ is an important geophysical parameter derived from AIRS in its own right.

Figure C.11a shows the mean value of $\hat{R}_i$ (in brightness temperature units) from 650 cm^{-1} to 756 cm^{-1} for all non-frozen ocean cases 50°N – 50°S on 6 September 2002 passing the Tight SST Test. The most opaque portion of the spectrum is near 667.5 cm^{-1}, and is primarily sensitive to atmospheric temperatures near 1 mb (50 km). Radiances in the surrounding spectral region are also primarily sensitive only to stratospheric temperatures and are not affected by clouds in the field of view. Radiances at frequencies greater than

690 cm^{-1} see increasing amounts of the troposphere, especially between absorption lines (the locally higher brightness temperatures) and are increasingly affected by cloud cover with increasing frequency. Radiances between lines at frequencies higher than 740 cm^{-1} are also increasingly sensitive to contributions from the ocean surface.

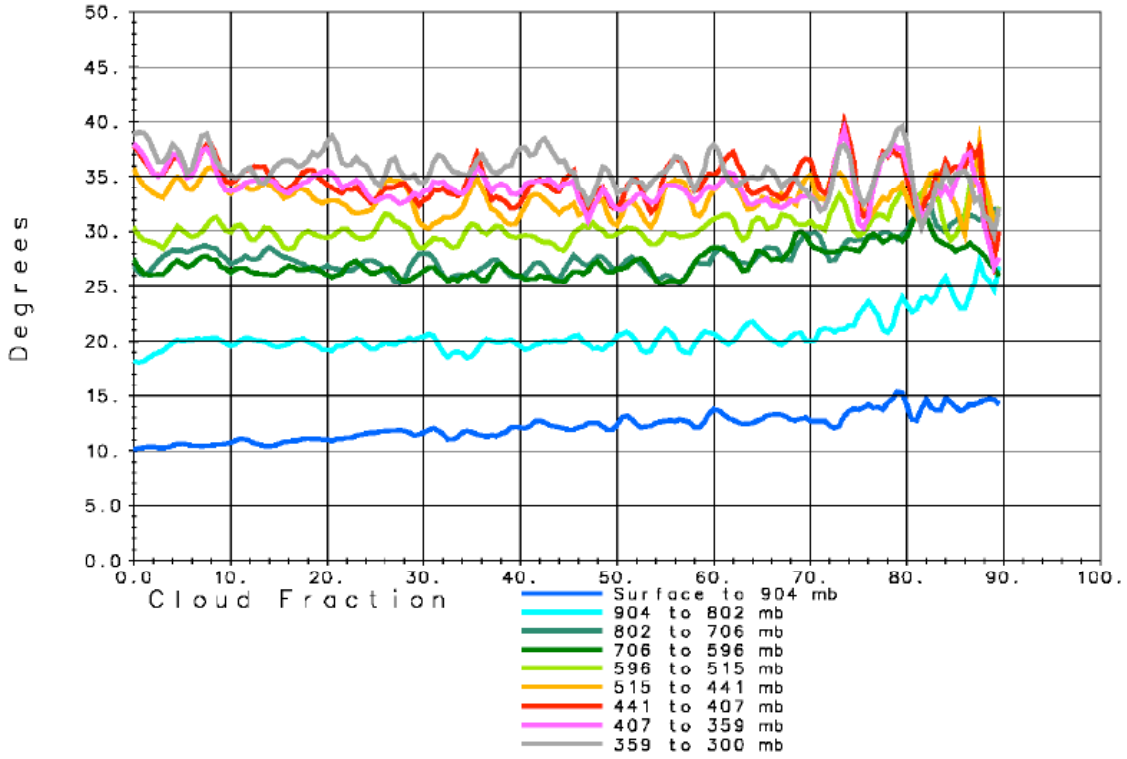

Figure C10. AIRS RMS Precipitable Water Percent Difference from Truth vs. Effective Cloud Fraction

Figures C.11b and C.11c show the mean and standard deviation of the (tuned) differences between $\hat{R}_i$ and R_i computed from the "truth" for all cases in this geographic domain passing the Tight SST Test, the standard SST Test, the Lower Tropospheric Temperature Test, and the Mid-Tropospheric Temperature Test, respectively. Figure C.11c also contains the channel noise spectrum. In this calculation, the "truth" is taken as the ECMWF forecast of temperature-moisture-ozone profile, along with the ECMWF ocean surface skin temperature. The Masuda Ocean surface emissivity model (1988), revised by Wu and Smith (1997), was used to generate the ocean surface emissivities in the calculation of the expected true radiances, assuming a surface wind speed of 5 m/sec. The surface contribution is the biggest uncertainty in the computation of the "truth"

radiances because of errors in both the true ocean skin temperature and in the true surface emissivity.

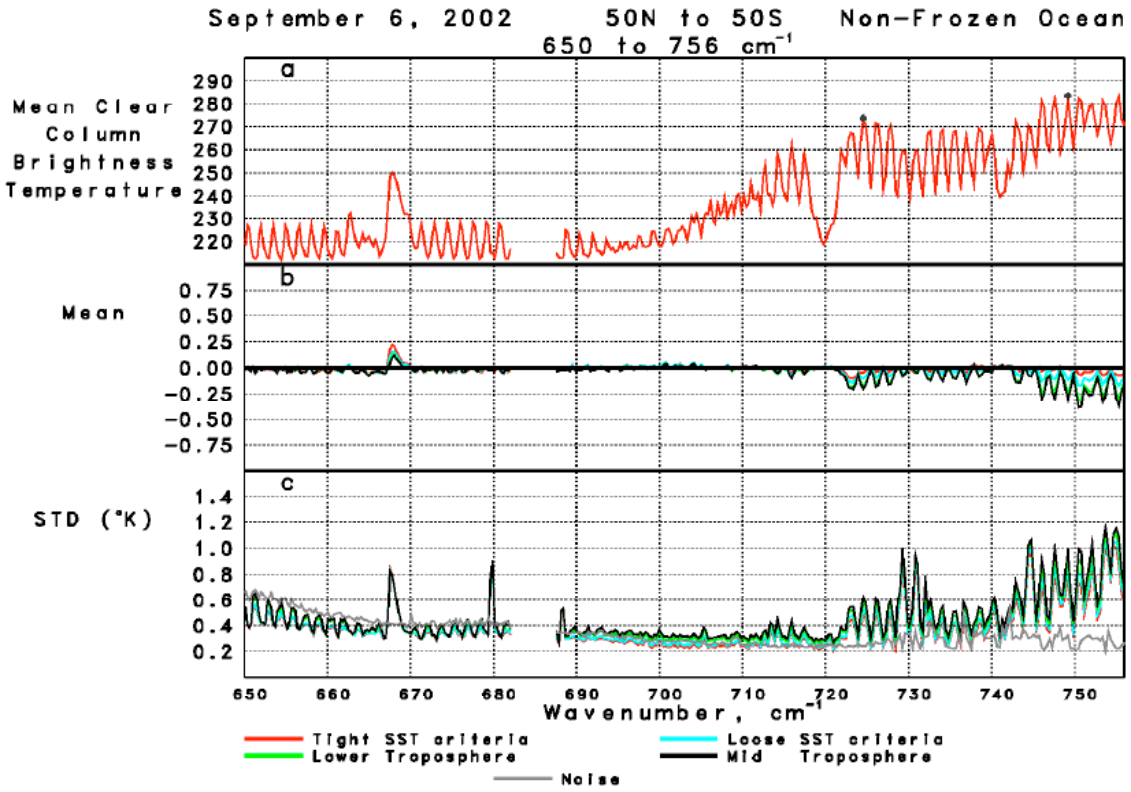

Figure C.11. Tuned Clear Column Brightness Temperature minus "Truth"

It is apparent that the difference of clear column radiances from those computed from the truth increases only slightly in the more difficult cloud cases, and in general matches expected radiances to within the AIRS noise level. Standard deviations of observed minus computed brightness temperatures for stratospheric sounding channels are actually lower than the channel noise, because radiances of a AIRS fields of view are averaged together to produce the cloud cleared radiances. The increasing difference of clear column radiances from those computed from the "truth" between absorption lines above 740 cm^{-1} has a large component arising from errors in the "truth."

It is noteworthy that the biases of observed minus computed brightness temperatures are essentially zero for all cases, with some small negative biases between absorption lines at the frequencies sensitive to the lowest portions of the atmosphere in cases passing the Mid-Tropospheric Temperature Test as a result of small cloud clearing errors in these

cases. First of all, this implies that the tuning coefficients derived from clear ocean night ocean cases on 6 September 2002 are equally well applicable to a much larger ensemble of ocean cases on the same day. Secondly, it demonstrates that clear column radiances for cases passing the Mid-Tropospheric Temperature Test are essentially unbiased at most sounding channel frequencies. The standard deviations of the clear column radiances from "truth" are also only slightly dependent on the degree of cloud contamination. Errors in the "truth" dominate the standard deviations shown in Figure C.11c, especially at 667.5 cm^{-1}, which is primarily sensitive to 1 mb temperature, and at frequencies sensitive to the ocean surface. In addition, the larger standard deviation at 679.31 cm^{-1} is a result of significant absorption by O_3, and those at 729.0 cm^{-1}, 730.8 cm^{-1}, and 745.1 cm^{-1}, and 754.4 cm^{-1} result from significant absorption by H_2O.

Figure C.12 shows histograms of the difference between observed and computed brightness temperatures for the two channels indicated by the black dots in Figure C.11, at 724.52 cm^{-1} and 749.19 cm^{-1} respectively. These frequencies are primarily sensitive to temperatures at 580 mb and 900 mb respectively, with a large surface contribution at 749.19 cm^{-1}. Results are shown for the four most stringent quality tests. The differences between the accuracy of clear column radiances at 724.52 cm^{-1}, for cases passing the different quality tests with spatial coverage ranging from 9.14 percent to 58.27 percent, are miniscule, with essentially no outliers in any category. Differences are somewhat larger at 749.19 cm^{-1}, but increase only slightly for cases passing the Mid-Tropospheric Temperature Test. For this reason, all clear column radiances are flagged as good for those cases passing the Mid-Tropospheric Temperature Test.

It is apparent from Figure C.11 that the tuning coefficients derived for clear ocean night cases on 6 September 2002 are applicable to all ocean night cases on that day. Figures 6.13a-c show analogous results for all (global) cases passing the Mid-Tropospheric Temperature Test on 6 September 2002 and 25 January 2003 corresponding to a different season and year. The biases (necessary tuning) are shown to be globally applicable, and also constant in time. Standard deviations from the truth at channels more sensitive to the surface are somewhat larger than for the non-frozen ocean cases because of larger errors in the "truth" arising from greater uncertainty in both surface skin temperature and

spectral emissivity. The sounding results for September 2004 shown in this paper further demonstrates the stability of the tuning coefficients derived from September 2002 observations.

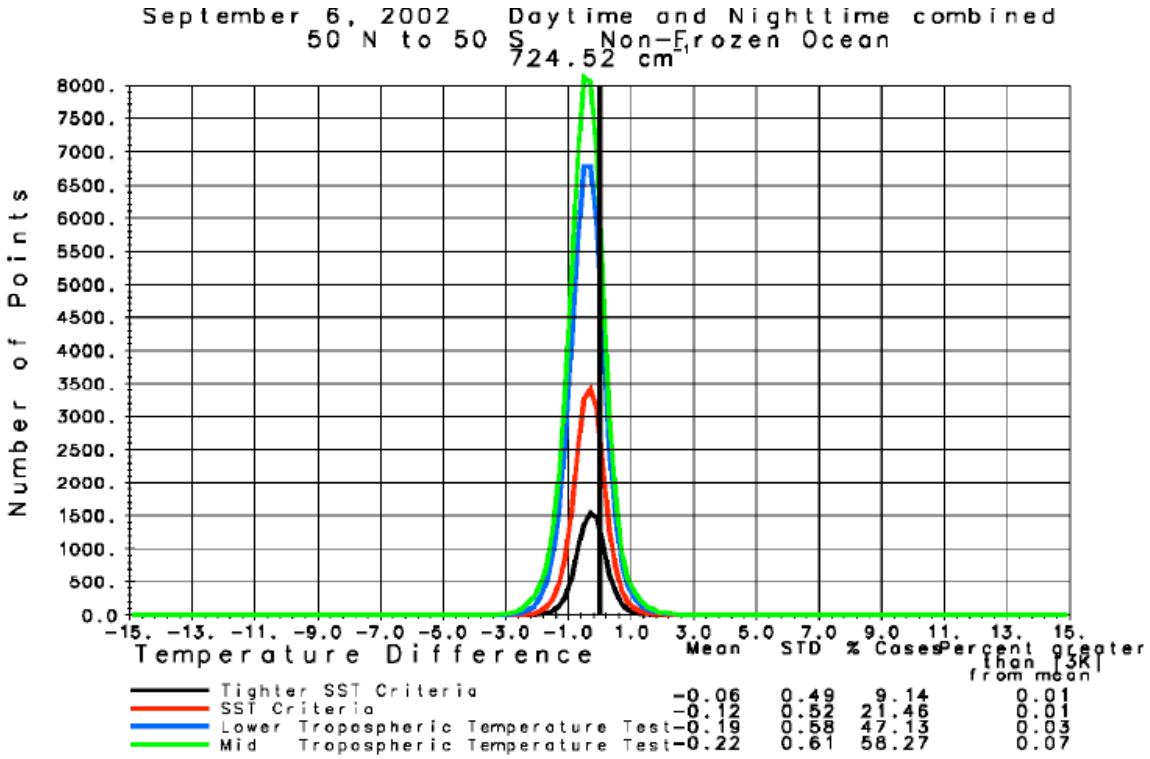

Figure C12a. Brightness Temperature Difference, 724.52 cm^{-1}

Operational numerical weather prediction centers currently assimilate radiance observations from IR sounders only for those cases thought to be unaffected by clouds (McNally, *et al.,* 2000). This criterion severely limits the number of IR channel radiances being used in the assimilation processes, and tends to minimize the potential improvement in forecast skill achievable from optimal use of AIRS radiance observations. We encourage operational centers to attempt to use AIRS derived clear column radiances in their assimilation, applying the same quality control so as to accept only those clear column radiances "thought to be unaffected by clouds."

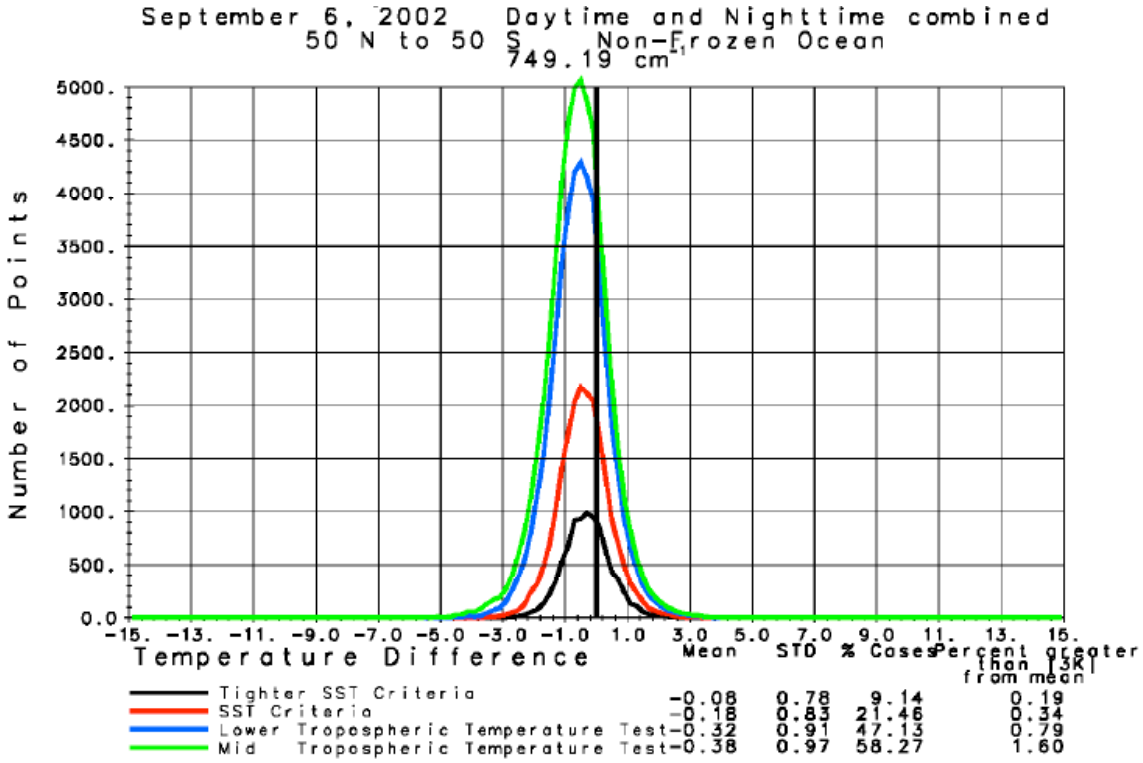

Figure C12b. Brightness Temperature Difference, 749.19 cm^{-1}

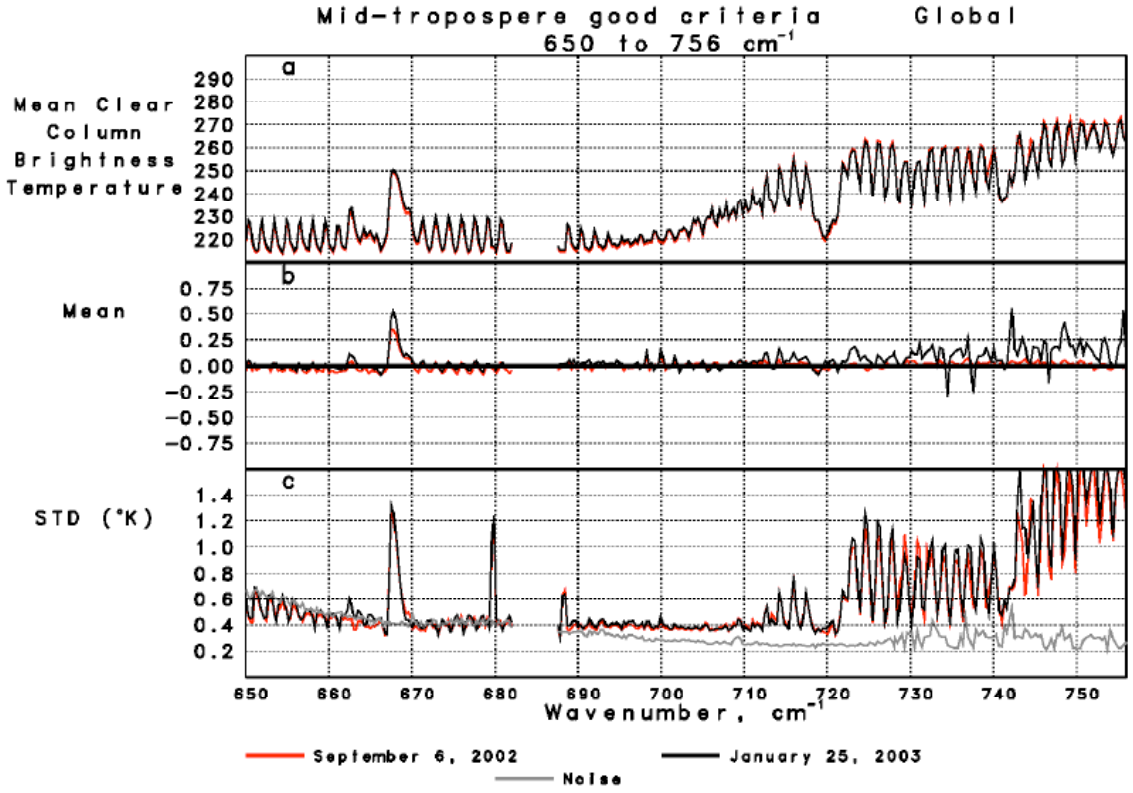

Figure C.13. Tuned Clear Column Brightness Temperature minus "Truth"

This page intentionally left blank.

C.2 Sample Monthly Mean Fields and their Interannual Differences

C.2.1 Atmospheric and Skin Temperatures

In generating monthly mean fields of atmospheric temperatures, the appropriate level dependent quality flags as described in Section 5.4.11.4.2 are used. For temperatures at pressures 200 mb and lower (higher altitude), all soundings passing the Stratospheric Temperature Test are averaged. For atmospheric temperatures at all other levels, all soundings passing the Mid-Tropospheric Temperature Test are averaged.

Figure C.14a shows the monthly mean field for January 2004 of 500-mb temperature derived from accepted AIRS/AMSU retrievals. Monthly mean fields containing only AM and PM overpasses are generated separately and then averaged together with equal weight to produce the monthly mean field. Figure C.15b shows the difference between the AIRS retrievals and the collocated ECMWF 3-hour forecast 500-mb temperatures. All AIRS products are derived and shown on a 1°x1° latitude-longitude grid. White indicates agreement to within 0.5K, with each color interval corresponding to differences increasing by 1K (0.5–1.5, 1.5-2.5, etc.), with shades of red meaning AIRS is warmer. The global mean difference between AIRS and ECMWF 500-mb monthly mean temperature is –0.01K and the spatial standard deviation is 0.45K. This is a positive and expected result, as the ECMWF forecast is very accurate at 500 mb. The largest differences occur at the highest latitudes, where AIRS retrievals are 0.5 to 1.5K cooler than ECMWF.

Figures C.14c and C.14d show analogous results for the difference of monthly mean 500-mb temperature between January 2004 and January 2003. Figure C.14c shows significant interannual differences in monthly mean 500-mb temperatures, with a spatial standard deviation of 1.54K between the 2 months, and a global cooling of 0.36K in January 2004 compared to January 2003. Virtually identical features appear in the ECMWF forecast (not shown). Particular attention should be given to the areas near 45°N,150°W; 50°S,160°W; 50°S,40°W; 50°S,20°E; and 50°S,100°E; in which January 2004 was substantially warmer than January 2003.

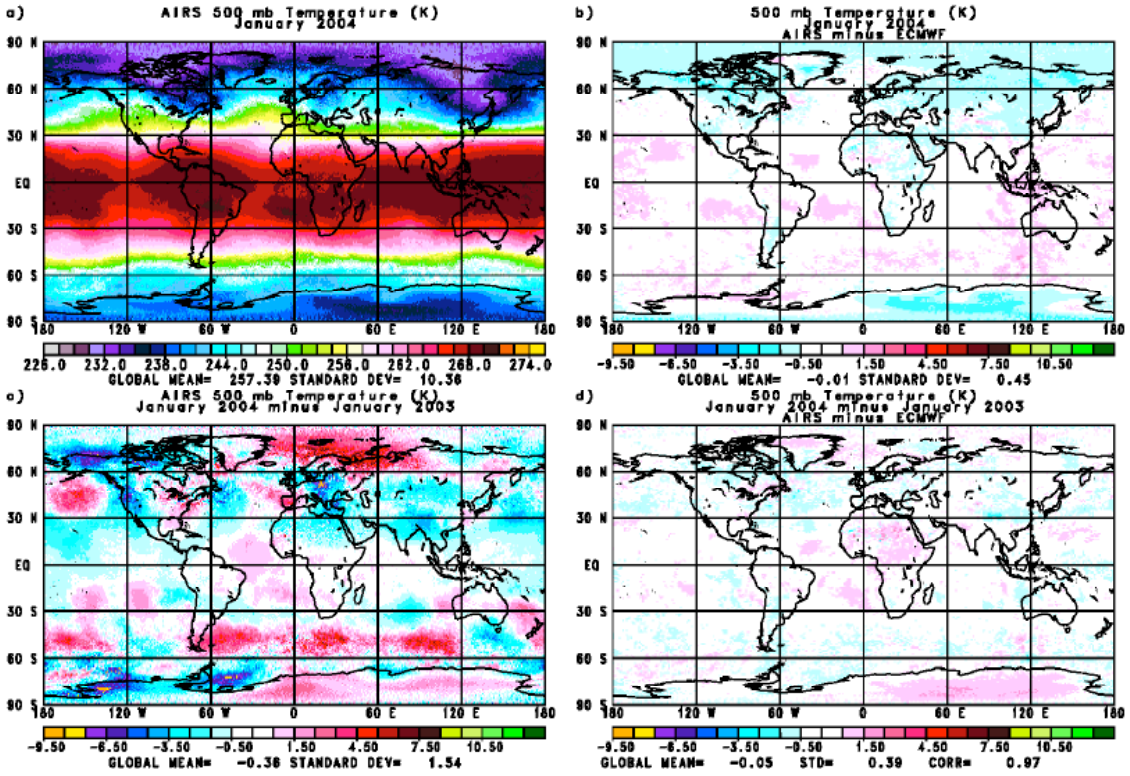

Figure C.14. Monthly Mean, 500 mb Temperature (K)

The difference between the two interannual difference fields, shown in Figure C.14d, indicates excellent agreement in global mean cooling (AIRS has larger cooling than ECMWF by 0.05K), spatial standard deviation (0.39K), and spatial correlation 0.97. The small spatially coherent differences in 500-mb temperature between AIRS and ECMWF in Figure C.15b cancel out for the most part in the interannual difference field. This is reflected in the fact that the spatial standard deviation of the difference of interannual difference field is less than of the monthly mean field. We are investigating the cause of these small regional biases, which do not appear to be very significant in the interannual difference sense.

Figures C.15a-C.15d show analogous results for 1-mb temperature, a level of the atmosphere at which ECMWF should be somewhat less accurate. AIRS is biased warm globally compared to ECMWF at 1 mb by 1.16K, and the spatial standard deviation between the two fields (2.62K) is significantly larger than it is at 500 mb. The monthly

mean temperature differences between January 2004 and January 2003 are much larger at 1 mb than 500 mb, especially north of 60°N, with considerable cooling of more than 20K near the North pole. AIRS data shows a global cooling of 1.47K at 1 mb, with a spatial standard deviation of 4.13K. AIRS agrees reasonably well with ECMWF in terms of global mean, standard deviation, and correlation, but the difference in the spatial standard deviation of the difference of AIRS from ECMWF is considerably larger than at 500 mb, at which ECMWF is globally more accurate. AIRS is most likely adding information at this level from the climate perspective. It should be noted that, as at 500 mb, the spatial standard deviation of the difference of the interannual difference fields is considerably less than of the difference of the monthly mean fields.

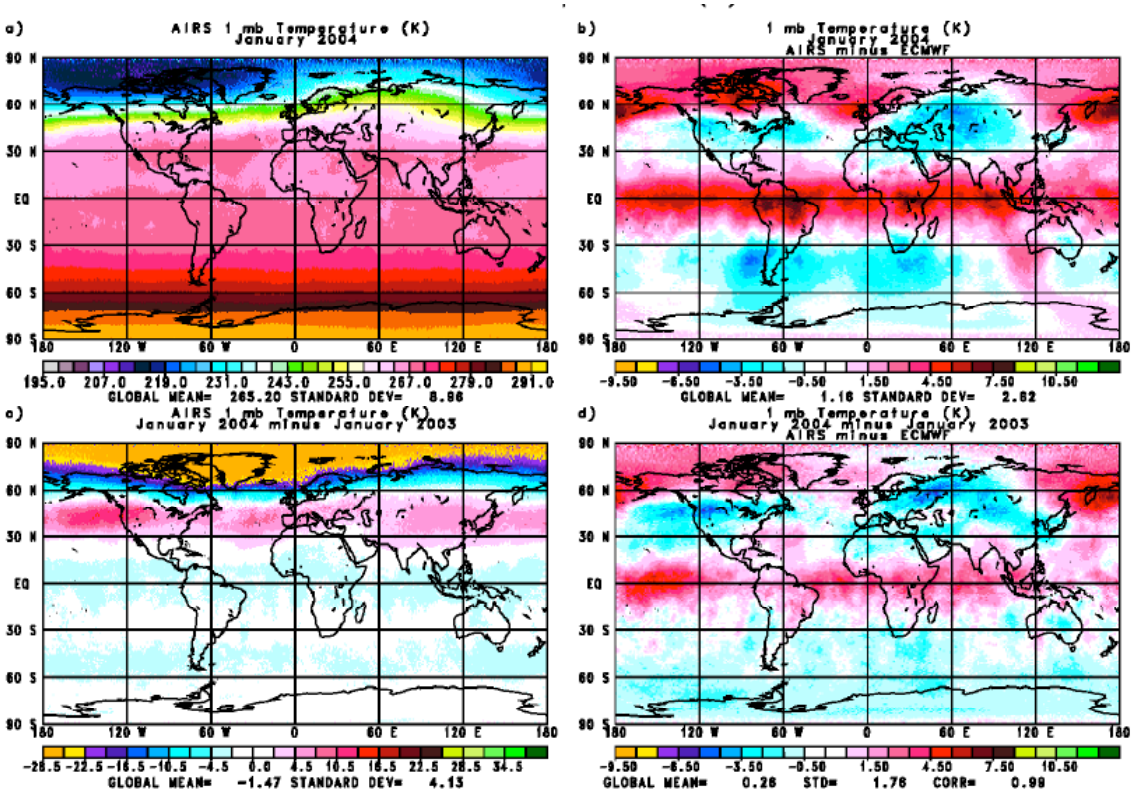

Figure C.15. Monthly Mean, 1 mb Temperature (K)

Table C.1 shows analogous statistics for AIRS January 2004 global mean temperatures and differences of global mean temperatures between January 2004 and January 2003, as well as the difference between AIRS and ECMWF of the global mean interannual differences, the spatial standard deviation of the two interannual difference fields, and their correlation.

Table C.1. Monthly Mean Temperatures (K)

	January 2004				January 2004 – January 2003				
	AIRS		AIRS-ECMWF		AIRS		AIRS-ECMWF		
Pressure	mean	STD	mean	STD	mean	STD	mean	STD	corr
1000 mb	287.42	11.06	0.53	1.15	-0.05	1.44	0.14	0.90	0.82
850 mb	280.32	10.79	0.08	0.86	-0.09	1.69	0.04	0.71	0.93
700 mb	273.23	9.95	0.31	0.51	-0.28	1.54	-0.05	0.45	0.97
600 mb	266.27	10.00	0.40	0.43	-0.15	1.55	0.07	0.42	0.98
500 mb	257.39	10.36	-0.01	0.45	-0.36	1.54	-0.05	0.39	0.97
400 mb	246.02	9.99	-0.40	0.39	-0.45	1.50	-0.15	0.39	0.95
300 mb	232.58	8.35	-0.35	0.43	-0.10	1.33	0.03	0.46	0.94
200 mb	220.16	2.99	0.35	0.56	-0.06	1.99	-0.13	0.53	0.99
150 mb	212.85	6.99	0.14	0.60	0.23	2.07	0.06	0.53	0.99
100 mb	203.85	12.36	-0.46	0.64	-0.10	2.57	0.16	0.84	0.99
70 mb	204.96	11.04	0.26	0.80	-1.01	2.35	-0.21	0.81	0.99
50 mb	209.95	7.71	0.22	0.79	-0.53	2.37	0.04	1.03	0.99
30 mb	216.08	5.64	-0.17	0.67	0.10	3.05	0.09	0.91	0.99
10 mb	228.33	6.05	0.09	0.91	-0.06	2.74	0.02	0.72	0.99
1 mb	265.20	8.96	1.16	2.62	-1.47	4.13	0.26	1.76	0.99

Global mean interannual monthly mean temperature differences between January 2004 and January 2003 as retrieved from AIRS vary somewhat regularly as a function of height. There is cooling up to 200 mb, having a peak value in the region 400-500 mb, but being near 0.0K at 1000 mb and 200 mb. In the stratosphere, January 2004 is again cooler than January 2003, primarily in the region 70 mb to 50 mb and also at 1 mb. The magnitude of the biases in interannual global mean temperature differences determined from AIRS, and contained in the ECMWF 3-hour forecast, are generally less than 0.1K and are considerably smaller than those of monthly mean temperatures themselves. This shows that the small regional dependent biases in monthly mean temperatures tend to cancel in the interannual difference sense at all levels of the atmosphere. The spatial standard deviations of the difference of interannual mean differences are also smaller

than those of the monthly mean temperatures. Spatial correlations of the interannual mean differences found in each data set are very high, especially in the stratosphere, where the spatial standard deviation of the interannual mean differences are considerably larger than in the troposphere.

Figure C.16a shows the interannual monthly mean difference of surface skin temperature derived from AIRS soundings. This field is constructed in a manner analogous to those shown in Figures C.14c and C.16c, except that over non-frozen ocean (referred to henceforth as "ocean"), only those cases passing the standard Sea Surface Temperature Test were used in generating the AM and PM monthly mean fields, while over land, sea-ice, and coasts (referred to henceforth as "land"), all cases passing the Mid-Tropospheric Temperature Test were used. To generate the monthly mean fields, monthly mean AM and PM fields were averaged together with equal weight, provided at least 5 observations during the course of the month were in each the AM and PM monthly mean fields. In the event that this requirement is not met over land, those grid boxes are not included in either the monthly mean or interannual difference fields. Over ocean, AM and PM monthly mean temperatures are weighted together equally unless no observations are included in one of the cases. In this situation, the monthly mean value for the other time period is used. If no observations are found for either time of day, that grid point is not included in the monthly mean or interannual difference fields (note the data void in the area of preferential stratus cloud cover near 20°S, 10°E).

The spatial patterns of Figure C.16a show some similarity to those of Figure C.14c. Over ocean, the areas of warm anomaly for January 2004, mentioned above, also appear, though considerably weaker, in the surface skin temperature interannual difference field. The strong negative sea surface temperature differences near 30°S,130°W and 30°S,10°W are not well reflected in the 500-mb temperature difference field however.

Figure C.16b shows the interannual difference of colocated surface skin temperature as included in the ECMWF 3-hour forecast field. The basic patterns in sea surface temperature interannual differences agree well, including the relative cooling of January

2004 compared to January 2003 at the equator between 120°W and 180°W. ECMWF land temperatures are less reliable for use as "truth."

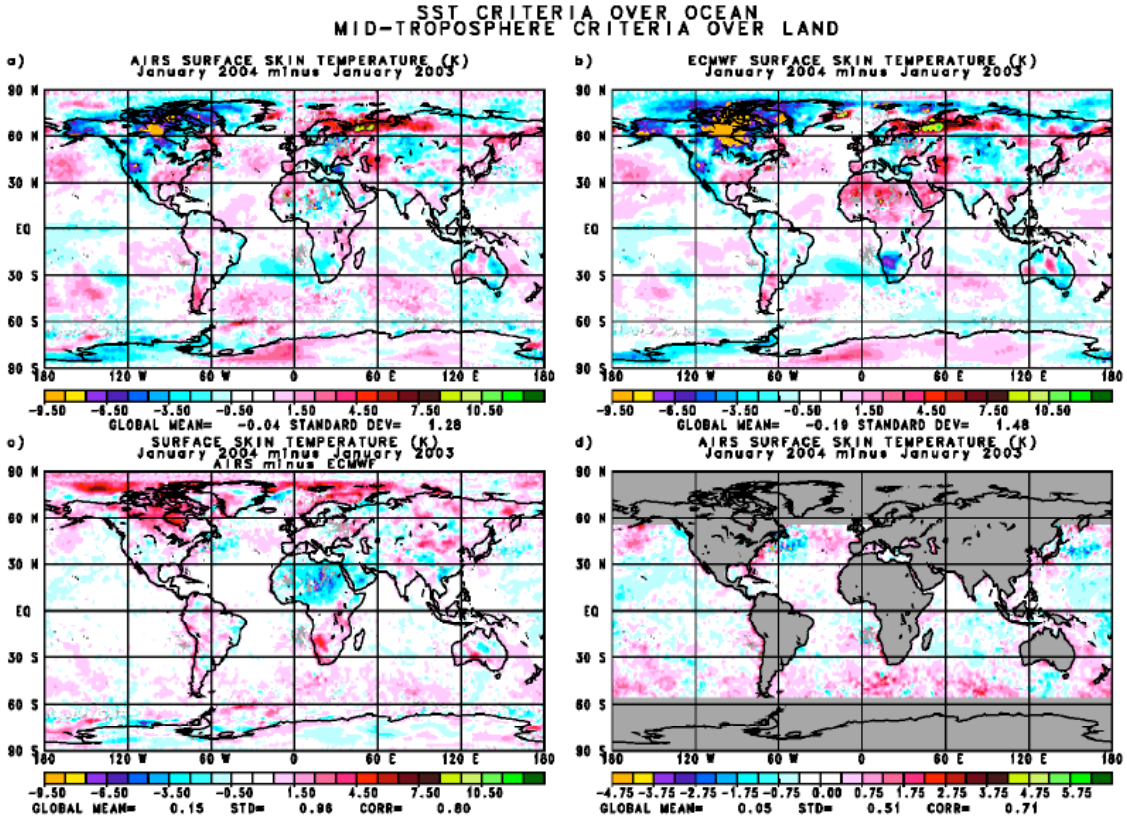

Figure C.16. Surface Skin Temperature

Figures C.16c and C.16d show the difference of the AIRS and ECMWF interannual difference field. Figure C.16c shows that agreement over ocean is much better than over land. Figure C.16d shows the difference of the interannual difference fields only over ocean 50°N-50°S. The color scale is twice as fine as previous scales, in that white represents ± 0.25K and every color is an additional 0.5K. The spatial standard deviation is 0.51K and the correlation is 0.71. Some of the largest differences occur south of 40°S, where ECMWF may be less accurate. It is interesting to note that while the warming in January 2005 near 50°S described previously shows up in the ECMWF interannual difference field, it is weaker than that found in the AIRS field. Significant negative differences are shown in Figure 3d near 45°N,50°W and 40°N,150°E that appear to be artifacts in the AIRS interannual difference field, as ECMWF should be accurate in these areas.

C.2.2 Constituent Profiles

Version 4 of the AIRS Science Team algorithm generates vertical profiles of water vapor, ozone, and carbon monoxide in terms of layer column densities (mol/cm^2) in 100 atmospheric layers. In generating monthly mean fields, the entire profile is accepted if the Constituent Test is passed. CO monthly mean fields are not shown as we do not have another measure of this quantity to compare with.

C.2.2.1 Water Vapor Profiles

Water vapor fields are presented in terms of total integrated water vapor column density above the surface, as well as above different atmospheric pressures. As with all derived products, water vapor profiles represent atmospheric water vapor in the clear portion of the partially cloudy scenes. It does not include water vapor above, within, or below clouds in the scene. Thus, there could be a sampling difference between derived water vapor fields and water vapor as predicted by forecast models, or as measured by microwave based observations, both of which would include water vapor in the cloudy portion of the scene.

Figures C.17a and C.17b show monthly mean total precipitable above the surface (cm) derived from AIRS/AMSU observations for January 2004, and the difference of AIRS monthly mean total precipitable water contained in the collocated ECMWF 3 hour forecast fields. The global mean AIRS total precipitable water for all cases passing the Constituent Test (roughly 85% of all observations) is 2.42 cm. If tighter tests were used (see Susskind, *et al.*, 2005), sampling would eliminate most of the cloudiest cases, and less water vapor would result. We have tried to minimize a clear sky bias in monthly mean fields by including as many cases as possible. In a global mean sense, AIRS is moister than ECMWF by 0.17 cm (7.0%) with a spatial standard deviation of 0.16 cm (7.4%).

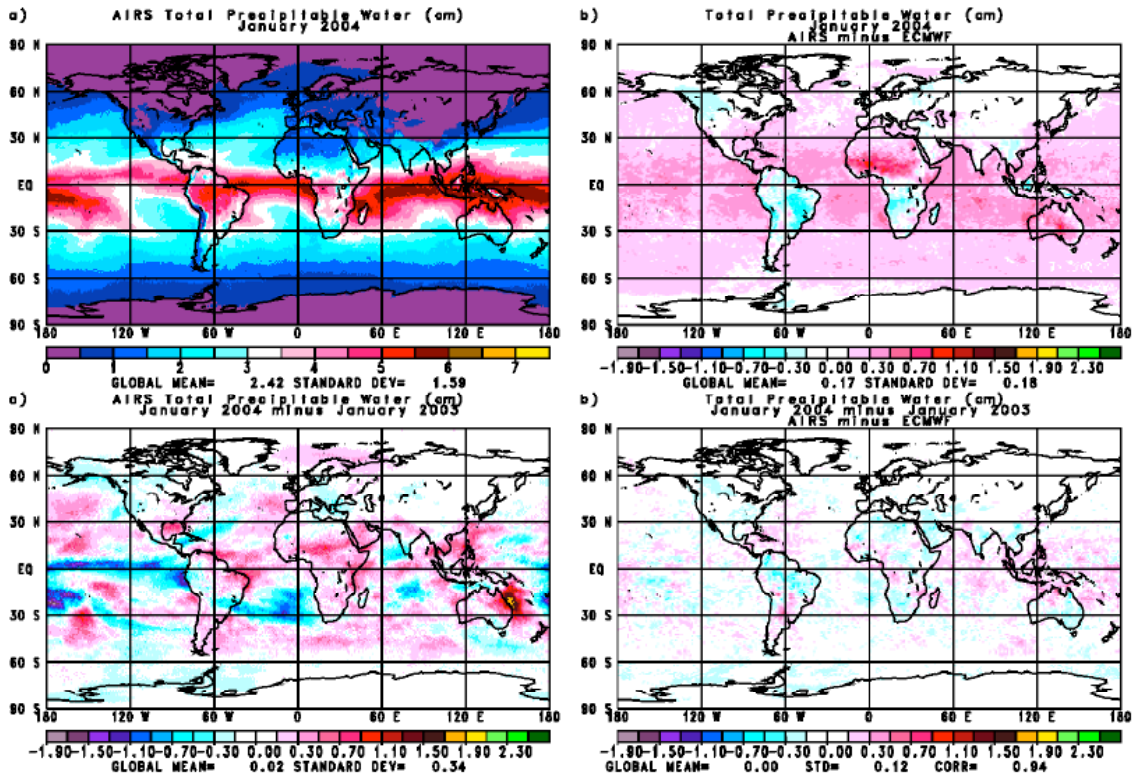

Figure C.17. Total Precipitable Water (cm)

Figures C.17c and C.17d show analogous results for the interannual difference of total precipitable water between January 2004 and January 2003. Globally, AIRS shows 0.02 cm of precipitable water more in January 2004 than January 2003, or roughly 1% of the global mean value of 2.42 cm. This apparent "moistening" is probably within the noise of the measurement. The spatial standard deviation of the difference is 0.34 cm and is almost 15% of the global mean. Large spatially coherent differences exist, with considerable drying along the equatorial Pacific Ocean, and moistening in the tropical Atlantic and Indian Oceans and in the extratropical oceans. These features are in general correlated with interannual sea surface temperature differences. The relatively small negative sea surface temperature difference near the equator between 180°W and 120°W is accompanied by an extremely large drying in this and adjacent areas.

Figure C.17d shows very good agreement with the ECMWF interannual difference of total precipitable water, with a spatial correlation of 0.94. The global standard deviation of the interannual difference of total precipitable water between AIRS and ECMWF is

smaller than that of the monthly mean fields. This also indicates the existence of regional biases that tend to cancel when interannual differences are taken.

Figures C.18a-d show analogous results for total precipitable water vapor above 500 mb (mm*10). ECMWF values of water vapor in the upper troposphere are essentially model driven and should be highly suspect. AIRS has a dry global bias of 0.053 mm compared to ECMWF (roughly 5% of the global mean) and the spatial standard deviation of the difference is 0.117 mm (≈10%). AIRS data indicates a drying of .015 mm above 500 mb (compared to a global mean of 0.996 mm) in January 2004, compared to January 2003 corresponding to 1.5% of the total. This result may be in the noise level of accuracy at this height of the atmosphere. The spatial standard deviation of the interannual difference is 40% of the global total, indicating a considerable redistribution of upper tropospheric water vapor between the two Januaries. The spatial pattern of interannual differences of upper tropospheric water vapor is similar to that of total precipitable water in some areas, but quite different in others. Note, for example, the region 120°E–180°E, 20°N-20°S. AIRS and ECMWF interannual differences agree closely, with a correlation of 0.95. These statistics, as well as analogous statistics for precipitable water above 850 mb, 700 mb, and 300 mb, are shown in Table C.2.

Table C.2. Monthly Mean Precipitable Water

	January 2004				January 2004 – January 2003				
		AIRS	AIRS-ECMWF		AIRS		AIRS-ECMWF		
Pressure mb	mean	STD	mean	STD	mean	STD	mean	STD	corr
surf	24.18	15.88	1.75	1.83	0.21	3.44	0.01	1.19	0.94
850	11.94	8.39	0.95	1.17	0.05	2.51	-0.05	0.98	0.93
700	4.73	3.83	0.07	0.42	-0.08	1.45	-0.03	0.51	0.95
500	0.996	0.877	-0.053	0.117	-0.015	0.403	-0.014	0.132	0.95
300	0.0746	0.0551	-0.0074	0.0148	-0.0018	0.0239	-0.0037	0.0116	0.91

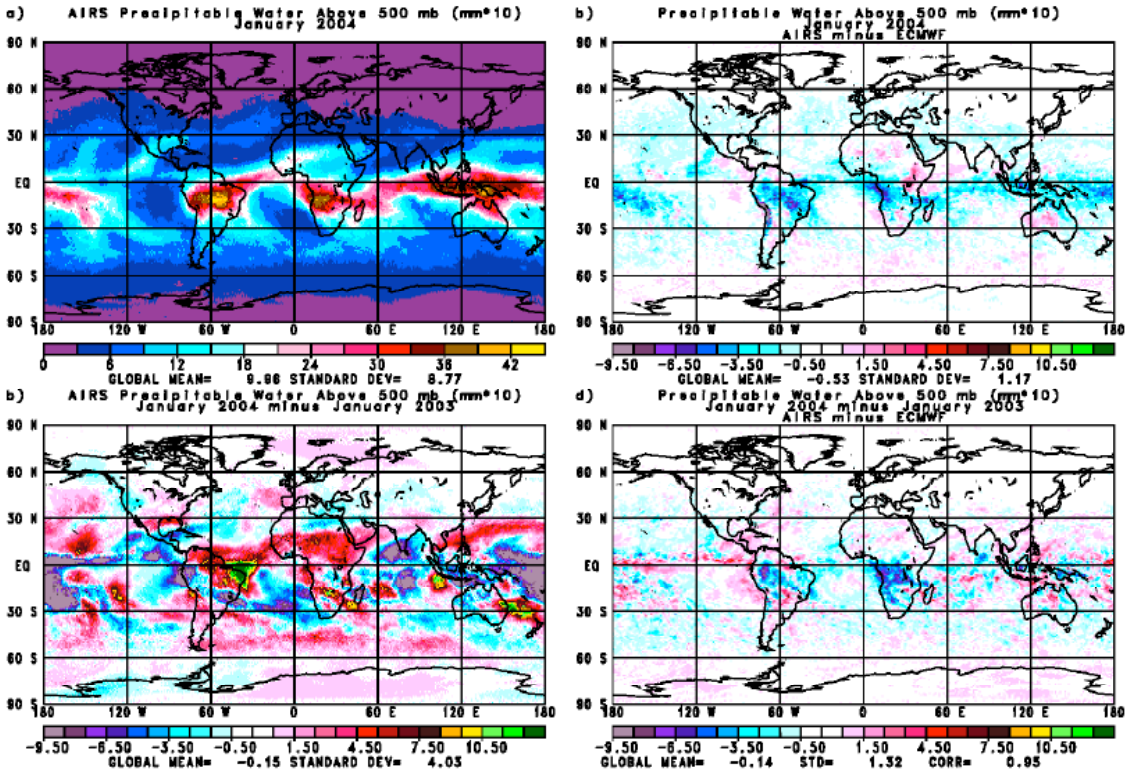

Figure C.18. Precipitable Water above 500 mb (mm*10)

C.2.2.2 Total O_3 Burden

Because AIRS is an infrared sounder, ozone profiles are produced day and night, as well as in polar winter. TOMS (Herman, *et al.*, 1991) produces highly accurate measurements of total ozone, but operates only under sunlight conditions because it is an ultraviolet based instrument. In generating AIRS monthly mean fields of total O_3, all cases passing the Constituent Test were averaged, including both ascending (day) and descending (night) observations. The monthly mean AIRS total ozone field for January 2004 is shown in Figure C.19a. The monthly mean TOMS ozone field, shown in Figure C.19b, is the average of all TOMS daily fields, originally given on a 1.25° longitude by 1.0° latitude grid. We generated the monthly mean TOMS total ozone field by averaging TOMS daily mean fields. The daily TOMS data was obtained from the website http://toms.gsfc.nasa.gov/ftpimage.html. At least 10 days of observations were needed for a given grid point to generate the monthly mean field. Figure C.19c shows the difference between the monthly mean AIRS and TOMS total ozone fields for January

2004. Care should be taken about differences near the TOMS terminator, at about 61°N, because of possible time of month sampling differences.

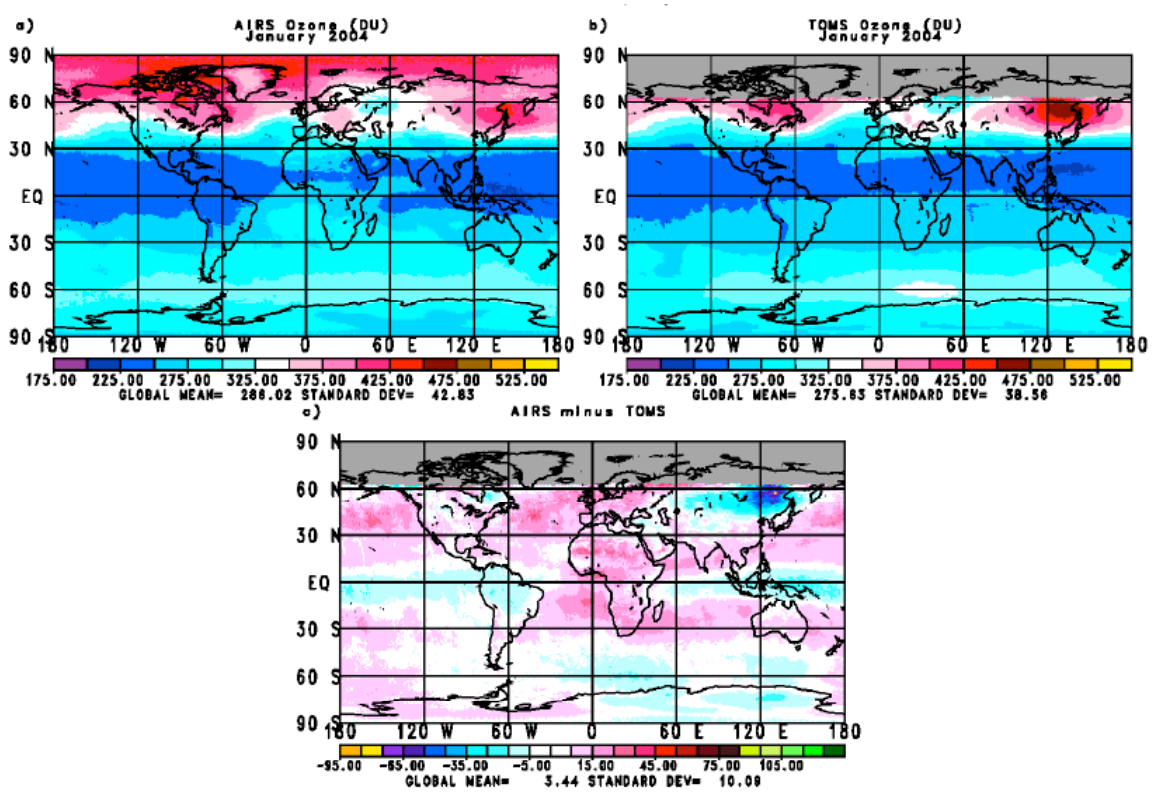

Figure C.19. Monthly Mean Total O_3 (DU)

There is a reasonable agreement between monthly mean AIRS and TOMS total ozone fields. The global mean difference is 3.44 DU (1.3% of the TOMS global mean) and the spatial standard deviation is 10.09 DU (3.7%). It is important to note that AIRS produces reasonable values of total ozone north of the terminator, where no TOMS data exists. It is clear that some large scale spatial systematic differences exist between the AIRS and TOMS fields. The cause of this needs to be understood.

Figures C.20 a-c show analogous results for the difference of monthly mean total ozone between January 2004 and January 2003. Features of the interannual differences of total O_3 are depicted well by AIRS. The spatially coherent differences have cancelled out to some extent, though AIRS appears to show a spurious increase in global total ozone by 5 DU. Over extratropical oceans, spatial patterns of interannual differences in total ozone

are similar to, and in phase with, those of 70-mb temperature (not shown), which are in turn out of phase with those of 500-mb temperature and surface skin temperature.

The spatial standard deviation of the difference of the interannual difference fields is 8.71 DU, compared to 10.09 DU for the monthly mean fields. It is encouraging to see a spatial correlation of 0.80 for the interannual difference fields where they both exist, and a spatially coherent interannual difference field at high latitudes where TOMS data does not exist. We are examining the causes of the systematic differences between AIRS and TOMS and expect an improved O_3 retrieval algorithm in the next version of the AIRS retrieval algorithm to become operational at the Goddard DAAC.

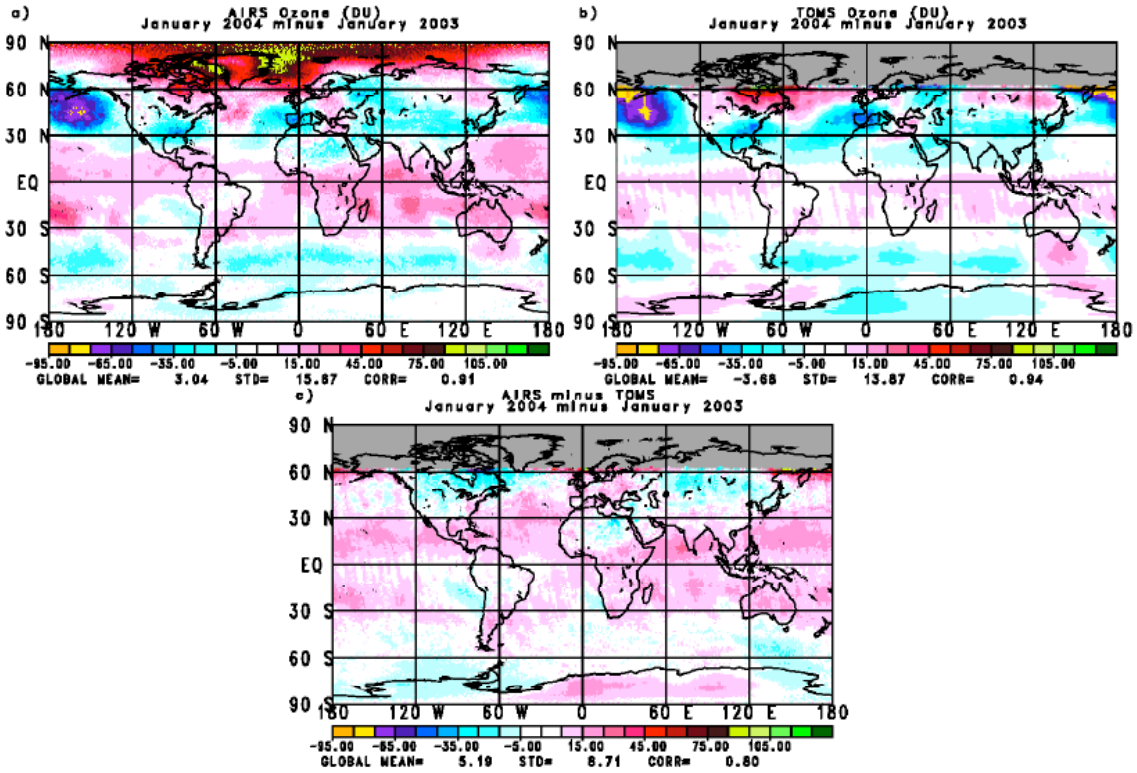

Figure C.20. Monthly Mean Total O_3 (DU), January 2004 minus January 2003

C.3 References

Aumann, H., M. T. Chahine, C. Gautier, M. Goldberg, E. Kalnay, L. McMillin, H. Revercomb, P. Rosenkranz, W. Smith, D. Staelin, L. Strow, and J. Susskind, AIRS/AMSU/HSB on the Aqua mission: Design, science objectives, data products, and processing systems. *IEEE Trans. Geosci. Remote Sensing*, **41**, 253-264, February 2003.

Goldberg, M. D., Y. Qu, L. M. McMillin, W. Wolff, L. Zhou, and M. Divakarla, AIRS near-real-time products and algorithms in support of operational numerical weather prediction. *IEEE Trans. Geosci. Remote Sensing*, **41**, 379-389, February 2003.

Goldberg, M., C. Barnet, and M. Divakarla, Three-way comparisons of AIRS, ATOVS and radiosonde temperature and moisture profiles. Submitted to *JGR*, 2005.

Masuda, K., T. Takashima, and Y. Takayama, Emissivity of pure and sea waters for the model sea surface in the infrared window region. *Remote Sensing of the Environ*., **24**, 313-329, 1988.

McMillin, L. M., and Crone, L. J., and Kleespies, T. J., Atmospheric transmittance of an absorbing gas: Improvements to the OPTRAN approach. *Applied Optics*, **34**, 8396-8399, 1995.

McNally, A., J. Derber, W. Wu, and B. Katz, The use of TOVS level 1B radiances in the NCEP SSI Analysis system. *Q.J.R. Meteorol. Soc*., **126**, 689-724, 2000.

Rosenkranz, P. W., Retrieval of temperature and moisture profiles from AMSU-A and AMSU-B measurements. In *Proc. IGARSS*, 2000.

Strow, L., and Hannon, S., and DeSouza-Machado, S., and Motteler, H., An Overview of the AIRS Radiative Transfer Model. *IEEE Transactions on Geosciences and Remote Sensing*, **41**, No. 2, 303-313, 2003.

Strow, L., S. Hannon, S. De-Souza Machado, and D. Tobin, Validation of the AIRS radiative transfer algorithm. Submitted to *JGR*, 2005.

Susskind, J., and Rosenfield, J., and Reuter, D., An accurate radiative transfer model for use in the physical inversion of HIRS2 and MSU temperature sounding data. *Journal of Geophysical Research*, **88**, No. C13, 8550-8568, 1983.

Susskind and Pfaendtner, Impact of interactive physical retrievals on NWP. Proceedings of a workshop held at ECMWF, May 9-12, 1989, European Center for Medium-Range Weather Forecasts, Shinfield park, Reading TG2 9AX, United Kingdom, 1989.

Susskind, J., P. Piraino, L. Rokke, L. Iredell, and A. Mehta, Characteristics of the TOVS Pathfinder Path A dataset. *Bull. Amer. Meteor. Soc*., **78**, No. 7, 1449-1472, 1997.

Susskind, J., C. D. Barnet, and J. M. Blaisdell, Retrieval of atmospheric and surface parameters from AIRS/AMSU/HSB data in the presence of clouds. *IEEE Trans. Geosci. Remote Sensing*, **41**, 390-409, February 2003.

Susskind, J. and R. Atlas, Atmospheric soundings from AIRS/AMSU/HSB. *Proc. SPIE Conference*, **5425-31**, 311-319, April 12-15, 2004.

Susskind, J., L. Iredell, F. Keita, and G. Molnar, Validatin of interannual differences of AIRS monthly mean parameters. Submitted to *JGR*, 2005.

Wu, X. and W. L. Smith, Emissivity of rough sea surface for 8-13 μm: Modeling and verification, *Appl. Opt.*, **36**, 2609-2619, 1997.